DOE-ER-0313/37
Distribution
Categories
UC-423, -424

FUSION MATERIALS
SEMIANNUAL PROGRESS REPORT
FOR THE PERIOD ENDING
December 31, 2004

Prepared for
DOE Office of Fusion Energy Sciences
(AT 60 20 10 0)

DATE PUBLISHED: MARCH 2005

Prepared for
OAK RIDGE NATIONAL LABORATORY
Oak Ridge, Tennessee 37831
Managed by
UT-Battelle, LLC
For the
U.S. DEPARTMENT OF ENERGY

FOREWORD

This is the thirty-seventh in a series of semiannual technical progress reports on fusion materials science activities supported by the Fusion Energy Sciences Program of the U.S. Department of Energy. This report focuses on research addressing the effects on materials properties and performance from exposure to the neutronic, thermal, and chemical environments anticipated in the chambers of fusion experiments and energy systems. This research is a major element of the national effort to establish the materials knowledge base of an economically and environmentally attractive fusion energy source. Research activities on issues related to the interaction of materials with plasmas are reported separately.

The results reported are the product of a national effort involving a number of national laboratories and universities. A large fraction of this work, particularly in relation to fission reactor irradiations, is carried out collaboratively with partners in Japan, Russia, and the European Union. The purpose of this series of reports is to provide a working technical record for the use of program participants, and to provide a means of communicating the efforts of fusion materials scientists to the broader fusion community, both nationally and worldwide.

This report has been compiled and edited under the guidance of R. L. Klueh and Teresa Roe, Oak Ridge National Laboratory. Their efforts, and the efforts of the many persons who made technical contributions, are gratefully acknowledged.

G. R. Nardella
Research Division
Office of Fusion Energy Sciences

TABLE OF CONTENTS

the last two cycles. The cause has not been determined. The middle capsule has operated at its target temperature of 600°C. A partial blockage of the purge gas line observed in the first cycle of irradiation led to a reduction in the target temperature for the lower capsule to ~425°C (from an original target of 450°C). Further degradation of this blockage has caused some operational difficulties resulting in this capsule running at slightly lower temperatures, ~418°C average, for part of cycle 402.

1.0 VANADIUM ALLOYS

No contributions.

2.0 CERAMIC COMPOSITE MATERIALS

SIC/SIC DESIGN FOR A FLOW CHANNEL INSERT—G. E. Youngblood, R. J. Kurtz, and R. H. Jones (Pacific Northwest National Laboratory)*

OBJECTIVE

The primary objective of this fusion materials research effort is to support component design and future testing of test blanket modules (TBM) for the International Thermonuclear Experimental Reactor (ITER).

SUMMARY

This report will examine the potential for using SiC fiber-reinforced composite (SiC/SiC) as the construction material for making a Flow Channel Insert (FCI) to be used in an ITER test blanket module. A SiC/SiC-FCI component is an attractive feature to enhance safe operations and power conversion efficiency in a D-T fusion reactor blanket that utilizes the dual-coolant flow concept. A SiC/SiC-FCI would act as an insulating layer to electrically and thermally decouple flowing, molten Pb-Li alloy (a combination tritium generation and heat bearing medium) from the structural, load-bearing ferritic steel channel walls of the blanket. The required properties for SiC/SiC-FCI materials are low transverse thermal and electrical conductivity, as well as Pb-Li compatibility and radiation stability. Analysis of these properties suggests that a composite architectural or "engineering" design solution will be necessary to achieve the SiC/SiC-FCI goals.

PROGRESS AND STATUS

Introduction

Over the next 30 years, the construction and operation of the International Thermonuclear Experimental Reactor (ITER) will provide the primary test-bed worldwide for integrated fusion power development. A critical issue that needs to be demonstrated in ITER is predictable and controllable power extraction from a deuterium-tritium (D-T) fusion reaction. This will involve designing and operating a high temperature heat removal and tritium breeding management system. Currently, one of the most attractive systems under consideration is based on the concept of using a Dual Coolant Blanket (DCB). The blanket surrounds the torroidal D-T reaction chamber to absorb and convert the neutron kinetic energy to thermal energy and to generate the tritium fuel. The design and testing of a DCB module in ITER is one of the key elements of the U.S. "ITER Mission" [1].

Actual electrical power will be generated in a fusion reactor for the first time in ITER. The 500 MW ITER fusion test reactor will provide a wide range of relevant material and component tests under combined 14 MeV neutron, heat and particle fluxes. Data from these tests will provide necessary information for the later development and design of a DEMO reactor (a DEMOnstration power reactor, the next step after ITER) [2]. In particular, several blanket designs that are DEMO-relevant will be tested in ITER. A particularly attractive blanket design based on the DCB concept is depicted in Fig. 1 [3].

To breed the tritium fuel, a DCB module would contain a liquid Pb-17 at % Li eutectic metal alloy (melting point ~300°C) with about 90% Li^6 isotope enrichment so that the tritium-breeding ratio is greater than one without the use of a neutron multiplier (such as beryllium). The liquid Pb-Li flows through numerous parallel, helium-cooled ferritic steel channels to carry the generated tritium and heat away. To reduce MHD-induced pressure drop in the flowing Pb-Li, an electrically insulating component called a Flow Channel Insert (FCI) is located within each steel channel. The FCIs also thermally decouple the hot Pb-Li (bulk flow temperature ~800°C max) from the He-cooled ferritic steel wall (temperature ~500°C max). A ceramic, fiber-reinforced silicon carbide composite (SiC/SiC) has been proposed as a promising material for the construction of FCIs [3].

---

*Pacific Northwest National Laboratory (PNNL) is operated for the U.S. Department of Energy by Battelle Memorial Institute under contract DE-AC06-76RLO-1830.

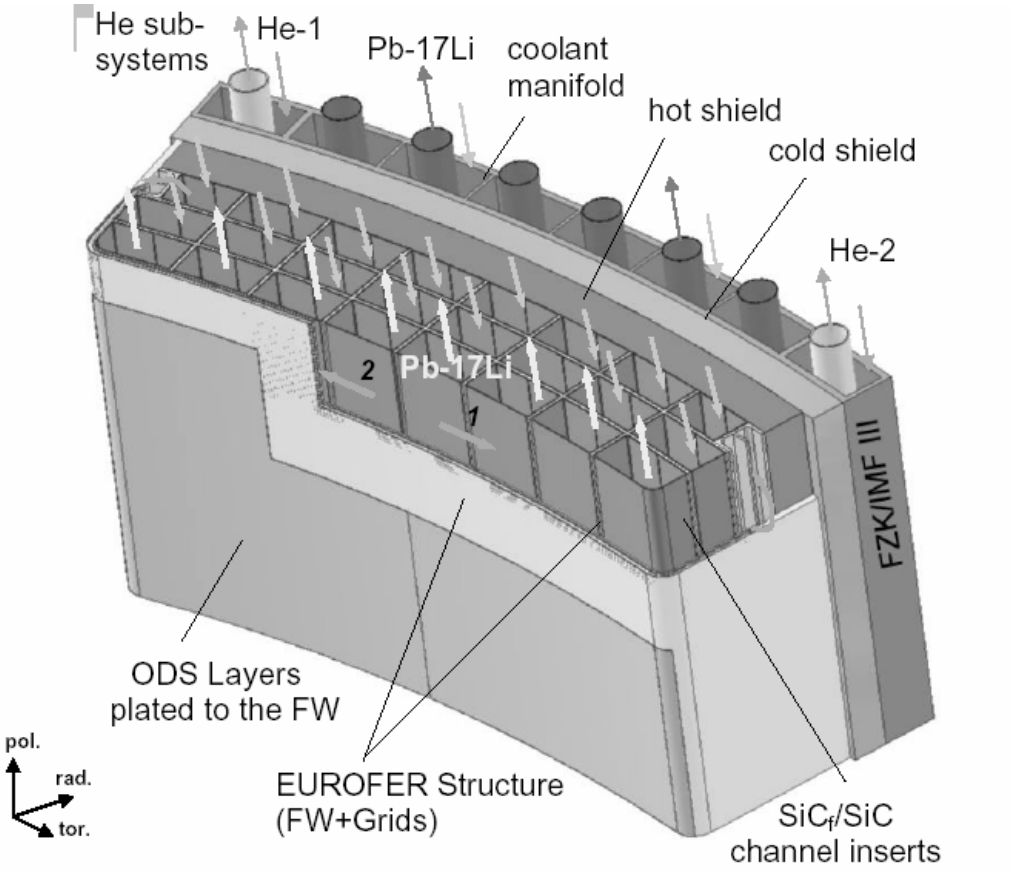

Fig. 1. Schematic of EU advanced dual coolant DEMO blanket section designed for a D-T Tokamak fusion reactor (FZKA 6780), taken from Morley et al. [3].

In Fig. 1, the first wall of the DEMO blanket, and the EUROFER ferritic steel grid structure, are helium-cooled (or heated at start-up) through embedded channels. The grid structure supports numerous (176 blanket modules x 24 FCI/module) SiC/SiC-FCIs through which the liquid metal Pb-17Li flows at low velocity (~0.1 m/s, but up to ~2 m/s in connecting piping). Each channel will have a cross-section of about 0.08 m^2 with lengths in meters. The FCIs (typical thickness ~5 mm) divide the flow channels into two regions. The larger inner region contains the slowly flowing, high temperature (460–700°C) Pb-Li. An advantage for removing heat at high temperature is the potential for obtaining high fusion power conversion efficiency, possibly >50%. The thin (~2–3 mm) outer region contains a cooler stagnant layer of Pb-Li that reduces the potential for erosion/corrosion of the steel walls. However, a torroidal magnetic field induces radial electrical currents in the flowing liquid metal, which in turn may cause a pressure drop along the long flow channels. The FCI interrupts the closed electrical conducting path in the radial (transverse) direction between the conducting steel walls and liquid metal and tends to reduce the MHD-induced pressure drops. To continue consideration of the DCBM-concept, the successful development and testing of FCIs (a key component that would utilize a large volume of SiC/SiC) obviously is necessary.

The primary goal for DCBM-testing in ITER will be the demonstration of effective tritium management, of the ability to generate high temperature heat, and of operation under integrated thermal, mechanical and electromagnetic loads. To carry out these functions in the proposed DCBM temperature operating range

of 500–800°C, according to initial modeling efforts by Morley [3], the SiC/SiC material should have the following properties (listed somewhat in order of timeliness and importance):

(1) Low transverse electrical and thermal conductivity (1–10 S/m and ~1 W/mK, respectively).
(2) Compatible with liquid Pb-17Li alloy at temperatures up to 800°C.
(3) Impermeable to the liquid Pb-Li.
(4) Good thermal shock and thermal cycling behavior (in-plane E ~100 GPa).
(5) Radiation and creep resistance.
(6) Wear resistance (hardness).
(7) Non-magnetic.

This report will examine the potential for obtaining the desired low transverse electrical and thermal conductivity properties in 2D-SiC/SiC, listed as priority (1) above.

Themal Conductivity

In Fig. 2, progress to fabricate SiC/SiC with a high effective (through the wall thickness) thermal conductivity (K_{eff}) is illustrated [4]. A K_{eff} >15 W/mK is recommended for the use of SiC/SiC as a structural fusion material during irradiation.

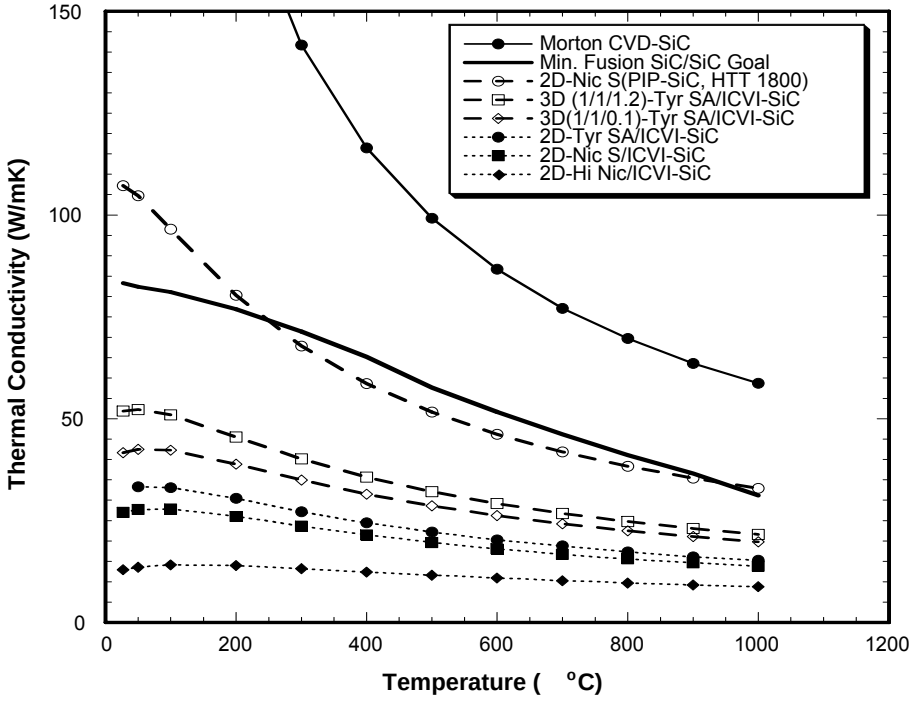

Fig. 2. Progress to attain SiC/SiC with high (K_{eff}. >15 W/mK during irradiation) transverse thermal conductivity [5]. The plotted values are for unirradiated materials.

By the use of advanced Nicalon™ type S or Tyranno™ SA fibers, the K_{eff}-values for 2D-SiC/CVI-SiC composites have more than doubled compared to values exhibited by the original fusion reference SiC/SiC made with Hi-Nicalon™ fiber (lowest curve, ~10–14 W/mK). Furthermore, by using 3D-weaves K_{eff}-values have approximately tripled over that of the 2D-Hi Nic composite. Finally, the K_{eff}-values of a 2D-SiC/SiC (made by MER Corp. with Nicalon S fibers and a polymer infiltrated and pyrolized PIP-SiC matrix given a special high temperature treatment, an HTT >1800°C) approximately match the estimated,

before-irradiation minimum fusion thermal conductivity goals for a SiC/SiC structural material (solid line). For reference, the K_{eff}-values for dense, high-purity Morton CVD-SiC also are given [9].

Although efforts to meet high thermal conductivity goals are continuing, a new goal now is to develop or design a radiation-resistant SiC/SiC-FCI with low K_{eff}. In fact, the new value desired for the FCI-application (~1 W/mK) is a factor of <1/10th of the 2D-Hi Nic reference K_{eff}-values shown in Fig. 2. To date, little research effort has been expended in reducing K_{eff}, but that circumstance has now changed with the advent of the SiC/SiC-FCI concept.

The thermal conductivity of irradiated SiC decreases due to the accumulation of point defects that effectively scatter phonons in SiC. In the 500–800°C range of interest, the degradation could be as much as a factor of 1/5 to 1/3 for SiC/SiC irradiated to saturation doses or above (~1 dpa-SiC) [6]. But for once nature is kind! Because of the decrease of K_{eff} for irradiated SiC, meeting the requirement of low K_{eff} becomes easier as the number of point defects accumulates. Therefore, as far as the SiC/SiC-FCI application is concerned, the critical time is at the beginning of life (BOL) for irradiation exposure, i.e., before SiC has been irradiated. Unfortunately, a SiC/SiC composite made with advanced SiC fibers with a crystalline SiC matrix (to preserve radiation stability) likely will have K_{eff}-values even greater than the Hi-Nic reference values of 10–14 W/mK, values well above those required for a SiC/SiC-FCI at BOL.

To provide the desired extremely low composite K_{eff}-values, it is obvious that architectural means will have to be employed. A 2D-SiC/SiC composite material will have to be specially designed and fabricated ("engineered") to meet the required very low FCI K_{eff}-values.

Electrical Conductivity

The electrical conductivity issue parallels that for thermal conductivity – low values of transverse electrical conductivity (σ_{eff}) are desired. Most measurements of electrical conductivity of 2D-SiC/SiC to date have been made in-plane rather than in the transverse direction. Because of the marked anisotropy in 2D-SiC/SiC composites made with woven fabric layers, experimental as well as modeling efforts to measure and/or to predict σ_{eff} are needed.

In Fig. 3, the electrical conductivity values for several unirradiated SiC-based materials are presented as a function of temperature.

The conductivity data by Weber [7] for high-purity (>99.999%), monolithic CVD-SiC indicate electrical conductivity values increasing with increasing temperature from 18 S/m at RT up to 210 S/m at 1000°C. A logarithmic plot of this data suggests a thermally activated process with an activation energy of ~0.12 eV, which likely corresponds to a shallow N-impurity energy band of 0.06–0.10 eV in β-SiC [8]. Nitrogen is a common trace (a few ppm) impurity even in CVD-fabricated SiC.

The data for the similar Morton CVD-SiC material exhibits somewhat higher electrical conductivity values and a different dependence on temperature [9]. The electrical conductivity of SiC, a wide band-gap (2.3 eV) semiconductor, is extremely sensitive to impurity content and types, which likely accounts for these observed differences between nominally the same materials. Although the electrical conductivity of CVD-SiC is close to the SiC/SiC-FCI goal at room temperature, in the higher 500–800°C temperature range its electrical conductivity values are ~200 S/m, much higher than the desired 1–10 S/m values.

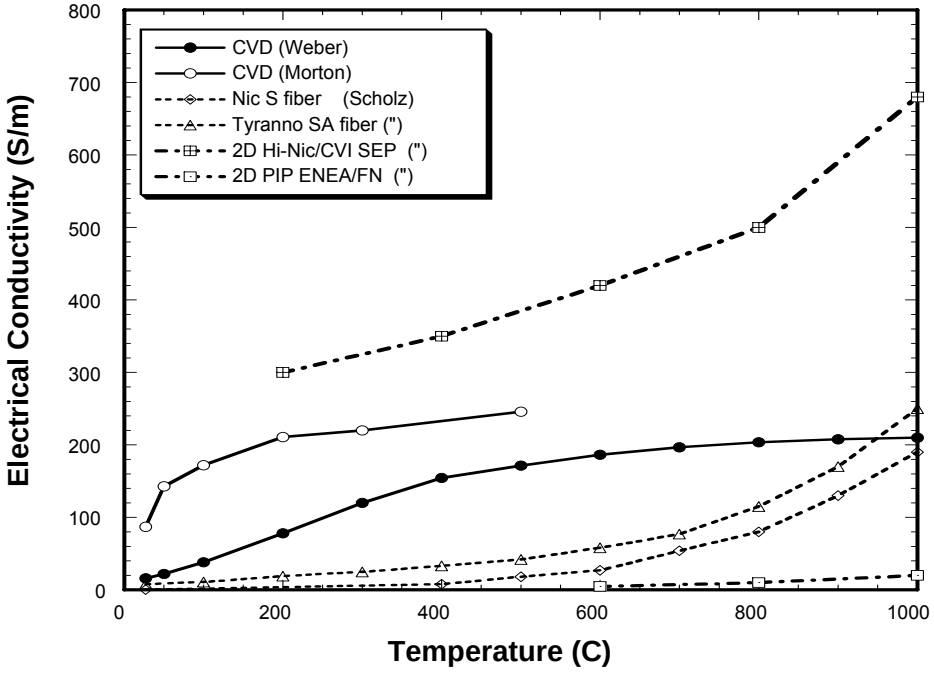

Fig. 3. Electrical conductivity of unirradiated composite, fiber and monolithic SiC-based materials [5].

The dashed lines show data for two types of high-purity, crystalline SiC fibers, Tyranno™ SA and Nicalon™ type S, reported by Scholz et al. [10]. Over the 500–800°C temperature range of interest, the electrical conductivity values increase from 20 to 80 S/m and 40 to 110 S/m for the type S and Tyranno™ SA fibers, respectively. The Tyranno fiber conductivity values are greater than for the type S fiber, but except for temperatures greater than ~1000°C, are less than the CVD-SiC values. The Tyranno fiber is sintered and has a larger grain size than the type S fiber, which may account for the small differences observed between these two fiber types. For both fibers, the electrical conductivity values increase monotonically with temperature in a similar way, but with an entirely different temperature dependence compared to that for the monolithic CVD-SiC. Unfortunately, both of these radiation stable fiber types have conductivity values that exceed the SiC/SiC-FCI goals.

Finally, the electrical conductivity data for the 2D Hi-Nic/CVI-SiC composite are extremely high (>300 S/m). In this composite, the Hi-Nicalon fibers were coated with a thin (~200 nm) pyrocarbon (PyC) layer. Microscopic examination of composite cross-sections indicated many fiber-to-fiber contacts. This is a typical composite structure with considerable electrical continuity through adjoining PyC-layers. Because carbon is an excellent electrical conductor, carbon pathways likely dominate the electrical conduction of SiC/SiC composites with PyC-coated fibers, as suggested by conductivity models. Furthermore, the electrical conductivity of the Hi-Nicalon fiber itself is about x10 that of type S fiber, which is likely due to the excess C in the Hi-Nic fiber with a C/Si ratio of 1.4. In fact, the very low electrical conductivity exhibited by the 2D PIP ENEA SiC/SiC composite (<10 S/m even up to 1000°C) partly results because its fibers were uncoated. In addition, rather than crystalline SiC the PIP-SiC matrix for this material consisted mostly of amorphous Si-C-O. Although such a matrix material exhibits a low electrical conductivity, this non-crystalline form of SiC is very irradiation unstable and not acceptable for the SiC/SiC-FCI application.

Overall, what is called for in a SiC/SiC-FCI is a composite with a nanocrystalline SiC matrix constructed with at least a few thin electrical and thermal insulating layers (perhaps silica) to first decouple the fibers one from another, and second to decouple the fiber bundles and perhaps even fabric layers from each other. The insulating layers must be thin and protected on both surfaces by CVI-SiC to hopefully

preserve radiation resistance. That is, an engineering or architectural design solution is suggested to preserve radiation stability and to provide the desired low K_{eff}- and σ_{eff}-values needed for the SiC/SiC-FCI application.

Conclusions

A composite engineering or architectural design solution is needed to provide the desired low K_{eff}- and σ_{eff}-values for the SiC/SiC-FCI application.

Future Work

A 4-probe DC-method will be used to measure the electrical conductivity as a function of temperature for candidate bar-shaped 2D-SiC/SiC-FCI materials. A 2-probe AC-method will be used to measure the transverse electrical conductivity of candidate disc-shaped 2D-SiC/SiC-FCI materials. Existing 2D-thermal conductivity models will be modified to analyze the measured transverse and parallel electrical conductivity data for the 2D-SiC/SiC materials in terms of the composite matrix, fiber and fiber coating components and the composite architecture.

Acknowledgements

The U.S. Department of Energy, Office of Fusion Energy Sciences, funded this research.

References

[1] M. Abdou and U.S. ITER-TBM Team, U.S. Plans and Strategy for ITER Blanket Testing, presented at the 16th ANS TOFE meeting, September 14, 2004, Madison, Wis.
[2] V. Barabash, Role and contribution of ITER in research of materials and reactor components, J. Nucl. Mater. 329–333 (2004) 156–160.
[3] N. B. Morley et al., Current understanding of feasibility of SiC/SiC composites for flow channel inserts in Dual Coolant Pb-17Li blankets, presented at TBM meeting, June 4, 2004, UCLA.
[4] R. H. Jones et al., Promise and challenges of SiC/SiC composites for fusion applications, J. Nucl. Mater. 307–311 (2002) 1107.
[5] G. E. Youngblood, presented at the 6th IEA SiC/SiC Workshop, Boston, June 10–11, 2004.
[6] G. E. Youngblood, D. J. Senor, and R. H. Jones, Effects of irradiation and post-irradiation annealing on the thermal conductivity/diffusivity of monolithic and f-SiC/SiC composites, J. Nucl. Mater. 329–333 (2004) 507.
[7] W. Weber (unpublished data).
[8] Y. Goldberg, M. Levinshstein, and S. Rumyantsev, In 2001 Silicon Carbide (SiC), Properties of Advanced Semiconductor Materials, John Wiley and Sons, Inc., New York (2001) 93–147.
[9] Technical Bulletin #107, Morton Advanced Materials, Woburn, Mass. (1994).
[10] R. Scholz, F. dos Santos Marques, and B. Riccardi, Electrical conductivity of silicon carbide composites, J. Nucl. Mater. 307–311 (2002) 1098.

COMPATIBILITY OF CVD SIC WITH Pb-Li AT 800°-1200°C—B. A. Pint and J. L. Moser (Oak Ridge National Laboratory)

OBJECTIVE

The objective of this task is to assess the long-term, high-temperature compatibility of SiC/SiC composites and Pb-Li. One proposed fusion reactor concept uses SiC/SiC composites with a self-cooled Pb-17Li blanket. Another concept uses a SiC/SiC flow channel insert with a dual coolant of He and Pb-Li at 800°C. One attractive feature of ceramic composites is their high temperature capabilities (≥1000°C). However, there is limited compatibility data above 800°C for this system. As the first step in the evaluation process, monolithic SiC is being exposed to Pb-17Li in capsule tests at 800°-1200°C.

SUMMARY

The Pb-Li chemistry was analyzed after the first series of static Pb-17Li capsule tests with monolithic SiC specimens. No Si was detected after the 1000h tests at 800° and 1100°C with a detectability limit of 30ppma (5ppmw). These results confirm the prior results of no specimen mass change and provide a promising but still incomplete picture of compatibility in this system. A second series of longer-term capsule tests is underway to examine potential changes in wetting behavior. A 1200°C capsule test also is being planned.

PROGRESS AND STATUS

Introduction

Among the proposed fusion reactor concepts, silicon carbide composites are a structural material option that is thought to allow the highest reactor operating temperature (1000°-1100°C) and thus the highest operating efficiency.[1,2] Both the TAURO and ARIES-AT proposals have Pb-17at.%Li self-cooled blankets which are attractive because the Pb-17Li acts as coolant, neutron multiplier and tritium breeder.[3] (The eutectic Pb-Li composition was chosen because it has a low melting point of 235°C.) Another concept uses SiC/SiC composite flow channel inserts with a dual coolant blanket based on ARIES-ST.[4] The insert serves as an electrical and thermal insulator between Pb-Li at 800°C and He-cooled ferritic steels. Present assessments of the materials feasibility for both of these strategies are incomplete because there is little information available on the high temperature compatibility of SiC with Pb-Li at temperatures of 800°C and higher. In a static exposure at 427°C, SiC composites (but not monolithic SiC) dissolved in unalloyed Li.[5,6] However, the activity of Li in Pb-17Li is greatly reduced (1.2×10^{-4} at 500°C)[7] suggesting that compatibility would be better with the eutectic.

Prior to the start of this task, results at 800°C had shown limited reaction between Pb-17Li and SiC composites.[8-10] An initial series of static Pb-17Li capsule tests were performed on high-purity (99.9995%) CVD β-SiC specimens and the experimental procedure and results are detailed elsewhere.[11,12] (These experiments used monolithic SiC specimens instead of composites as a first step towards evaluating SiC compatibility to avoid the microstructural and microchemistry complexities of composites and the better compatibility found for monolithic material compared to SiC/SiC composites in Li.[5]) To avoid unwanted reactions of the capsule with Pb-Li, the SiC specimens were contained in SiC capsules. After 1000h at 800°C, no wetting was observed between Pb-Li and SiC and therefore no chemical attack would be expected. At 1100°C, there was evidence of only limited wetting after 1000h. After cleaning the specimens, no mass change was measurable at either temperature suggesting that SiC is compatible with static Pb-17Li to at least 1100°C. To follow up on those observations, the Pb-Li was sent for chemical analysis after the test and the starting Pb material also was analyzed.

Results

The Pb-Li was analyzed after both capsule tests (800° and 1100°C) as was the starting Pb, Table 1. (The variation in Li may be an experimental error. It is magnified by the conversion from mass%.) In Pb-Li, the Si detectability limit was 30ppma (5ppmw) and none was detected. This is significantly less Si than was detected by microprobe analysis (350ppmw) after an 800°C exposure by Kleykamp.[9] The major impurities detected were C and O with low levels of some metals, Table 1. These results suggest that monolithic, high-purity SiC is compatible with Pb-17Li to at least 1100°C in a static environment. More interaction may be expected with the SiC fibers or the fiber-matrix interface. However, it is anticipated that a dense CVD SiC seal coat will cover the outer layer of any SiC composite components.

Long-term capsule tests on monolithic SiC are currently underway at 800°C (5,000h) and 1100°C (2,000h) using the same experimental procedure. Longer times are being investigated because of the limited amount of wetting observed in the 1,000h tests. If wetting is due to a native oxide on the SiC samples, longer times may break down this thin surface layer. Observations with stainless steel and mercury indicate that there can be an extended incubation period to develop wetting.[13] A 1200°C test also is being planned. Welding and oxidation studies are being conducted on alloy 602CA (Ni-26at.%Cr-5Al) to verify its applicability as an outer capsule for this very high temperature.

Future work will eventually need to include flowing liquid metal experiments with a temperature gradient. Static capsule experiments can only be expected to produce a limited picture of the compatibility issue where saturation of one or more of the dissolving components can inhibit further reaction. However, the observation of no detectable dissolved Si in the Pb-Li following exposure is a promising result about the compatibility in this system.

References

[1] A. Hasegawa, A. Kohyama, R. H. Jones, L. L. Snead, B. Riccardi, and P. Fenici, J. Nucl. Mater. 283-287 (2000) 128.
[2] R. H. Jones, L. Giancarli, A. Hasegawa, Y. Katoh, A. Kohyama, B. Riccardi, L. L. Snead, and W. J. Weber, J. Nucl. Mater. 307-311 (2002) 1057.
[3] A. R. Raffray et al., Fusion Eng. Des. 55 (2001) 55.
[4] P. Noajitra, L. Buhler, U. Fischer, S. Malang, G. Reimann, and H. Schnauder, Fusion Eng. Des. 61-62 (2002) 449.
[5] T. Terai, T. Yoneoka, and S. Tanaka (unpublished research from reference #2, 2000).
[6] T. Yoneoka, S. Tanaka, and T. Terai, Mater. Trans. 42 (2001) 1019.
[7] P. Hubberstey, J. Nucl. Mater. 247 (1997) 208.
[8] F. Barbier, Ph. Deloffre, and A. Terlain, J. Nucl. Mater. 307-311 (2002) 1351.
[9] H. Kleykamp, J. Nucl. Mater. 321 (2003) 170.
[10] H. Kleykamp, J. Nucl. Mater. 283-287 (2000) 1385.
[11] B. A. Pint, L. D. Chitwood, and J. R. DiStefano, DOE/ER-0313/35 (2003) 13.
[12] B. A. Pint, K. L. More, H. M. Meyer, and J. R. DiStefano, Fusion Sci. Technol. (in press, 2005).
[13] S. J. Pawel, ORNL/TM-2002/280, Oak Ridge National Laboratory, Oak Ridge, Tenn. (2002).

Table 1. Chemical composition using inductively coupled plasma and combustion analysis of the starting Pb and the Pb-Li after capsule exposures at the indicated temperatures for 1000h (in ppma except for Li in atomic%).[12]

Test	Li	Si	C	O	N	Al	Cr	Fe	Mo	Ni	Y
Starting	n.d.	<40	<170	1270	<40	<8	<4	<4	<2	<4	<2
800°C	17.49%	<30	1850	4090	100	6	<3	6	<2	<3	<2
1100°C	16.27%	<30	1160	3550	90	<6	<3	6	<2	<3	<2

CHARACTERIZATION OF CHEMICALLY VAPOR INFILTRATED SILICON CARBIDE COMPOSITES REINFORCED BY VARIOUS HIGH MODULUS FIBERS: I. THERMAL CONDUCTIVITY—T. Nozawa, Y. Katoh, L. L. Snead (Oak Ridge National Laboratory), T. Hinoki and A. Kohyama (Kyoto University, Japan)

OBJECTIVE

The objective in this study is to evaluate in-plane and through-thickness thermal conductivities of various architecture types of the SiC/SiC composites and the hybrid SiC-C/SiC composites incorporated with high-modulus SiC and carbon fibers.

SUMMARY

The Tyranno™-SA fiber composites remarkably improved their thermal conductivity, in particular the through-thickness thermal conductivity in the orthogonal three-dimensional (3D) composite system due to excellent thermal conductivity of Tyranno™-SA fiber itself. The carbon fiber was in general beneficial to obtain high thermal conductivity of the composites. However, many matrix cracks, induced by the mismatch of coefficients of thermal expansion during processing, restricted heat transfer via matrix of carbon fiber containing composites, limiting the improvement of the thermal conductivity.

PROGRESS AND STATUS

Introduction

Silicon carbide fiber reinforced silicon carbide (SiC/SiC) composites are candidate materials for nuclear fusion and advanced fission reactors because of elevated-temperature chemical and mechanical capability, low induced-radioactivity and after-heat [1]. The latest composites fabricated from the high modulus SiC fibers, i.e., highly-crystalline and near-stoichiometric SiC fibers such as Tyranno™-SA and Hi-Nicalon™ Type-S, and the β-SiC matrix provide good geometrical stability and strength retention after neutron irradiation [2–4]. Also, enhanced thermal and thermo-mechanical properties of the highly crystalline SiC composites have the added advantage to providing higher system efficiency. In addition, higher thermal conductivity and strength also allow higher resistance to thermal shock.

Constituent materials are one important factor to maximize the thermal properties of composites. Among various processing techniques, chemical vapor infiltration (CVI) is regarded as the technique that produces the highest crystallinity SiC with inherently high thermal conductivity [5]. Tyranno™-SA and Hi-Nicalon™

Type-S fibers are also beneficial to use due to their crystalline structure. Tyranno™-SA fiber possesses the thermal conductivity of 65 W/m-K, while 18 W/m-K for Hi-Nicalon™ Type-S. Further thermal conductivity improvements have been proposed whereby hybrid composite concepts using carbon fibers as reinforcements mixed with SiC fibers (SiC-C/SiC composites) are utilized [6]. Specifically, pitch-based carbon fibers possess much higher thermal conductivity (22~1000 W/m-K), as compared to SiC or other graphite fibers. For many nuclear applications, heat transport in the direction orthogonal to the plane of the primary stress is required. For this reason, a Z-stitch of high conductivity graphite fiber into an X-Y weave of SiC fibers has been considered. Matrix densification is also important to keep good heat transfer via matrix. The through-thickness thermal conductivity of ~70 W/m-K, which is higher than that of the conventional composites (~20 W/m-K), has been reported for two dimensional (2D) SiC/SiC composite with the density of ~3.1 g/cm^3, fabricated by nano-infiltration transient eutectic phase sintering (NITE) process [7].

Experimental Procedure

Materials

The materials were SiC matrix composites with the highly crystalline and near-stoichiometric SiC fibers: Tyranno™-SA Grade-3 and Hi-Nicalon™ Type-S. Also hybrid SiC matrix composites with Tyranno™-SA Grade-3 and pitch-based carbon (P120S: ~640 W/m-K) fibers was prepared (Table 1). All materials were produced by isothermal/isobaric CVI process. Two types of 2D SiC/SiC composites with plain-weave (P/W) Tyranno™-SA and 5-harness satin-weave (S/W) Hi-Nicalon™ Type-S, two types of orthogonal 3D SiC/SiC composites with differed through-thickness (Z-direction) fiber content: X: Y: Z = 1: 1: 1 and 1: 1: 4, and two types of hybrid composites with a P/W and an orthogonal 3D architecture composed of Tyranno™-SA and P120S fibers (Figure 1) were fabricated, respectively. It is noted that the Z-direction fibers of both 3D SiC/SiC composites were made into SA grade (Si-Al-C) from AM grade (Si-Al-C-O) Tyranno™ fiber at the temperature of ~2073 K in inert environment after weaving. All composites had 150 nm thick pyrolytic carbon (PyC) as fiber/matrix (F/M) interphase.

Thermal Conductivity

Room temperature thermal diffusivity was measured using a xenon flash technique and thermal conductivity was calculated using the measured composite density and specific heat. Specific heat of composites was calculated assuming the rule of mixtures. Microstructures were examined with an optical microscopy and a field emission scanning electron microscopy (FE-SEM).

Table 1. SiC/SiC and hybrid SiC-C/SiC composites under investigation

ID	Fiber	Architecture	X- (and Y-) fiber volume fraction [%]	Z-fiber volume fraction [%]	Density [Mg/m^3]	Porosity [%]
P/W SA	SA[*1]	P/W	20	-	2.51	20
S/W HNLS	HNLS[*2]	5-harness S/W	22	-	2.52	19
3D(1:1:4) SA	SA[*1]	3D(X:Y:Z=1:1:4)	10	40	2.76	10
3D(1:1:1) SA	SA[*1]	3D(X:Y:Z=1:1:1)	15	15	2.78	11
Hybrid 2D	SA[*1]+C[*3]	P/W	SA[*1]:8, C[*3]:18	-	2.25	19
Hybrid 3D	SA[*1], C[*3]	3D(X,Y:SA[*1], Z:C[*3])	SA[*1]:12	C[*3]:21	2.19	25

[*1]SA: Tyranno™-SA Grade 3 fiber, [*2]HNLS: Hi-Nicalon™ Type-S fiber, [*3]C: P120S fiber

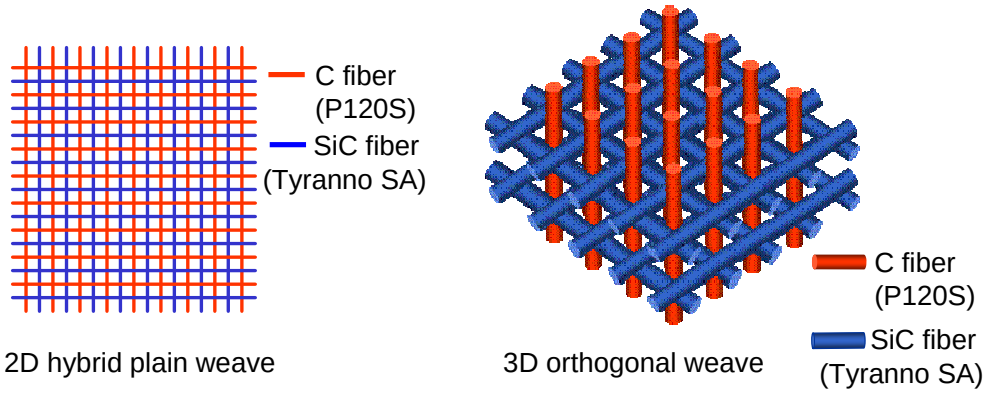

Fig. 1. Schematic illustrations of hybrid 2D and 3D SiC-C/SiC composites.

Results and Discussion

Figure 2 shows the typical cross-sectional images of as-received composites. Two dimensional SiC/SiC composites had large pores in most cases in weaving cross-sectional pockets, resulting in a density of ~2.5 g/cm^3. By contrast, both 3D SiC/SiC composites were well-densified even in the pocket regions, yielding a density of ~2.7 g/cm^3. Both 2D and 3D hybrid composites had large pores in pocket regions. Therefore less densification of the matrix yielded a lower density (~2.2 g/cm^3) than that of ideally densified composites (~2.8 g/cm^3). In addition, the hybrid composites contained transverse matrix cracks around every carbon fiber bundle. Specifically major cracks propagated within laminated plies for some 2D hybrid composites. This is attributed to the large CTE mismatch between the SiC matrix and the carbon fiber.

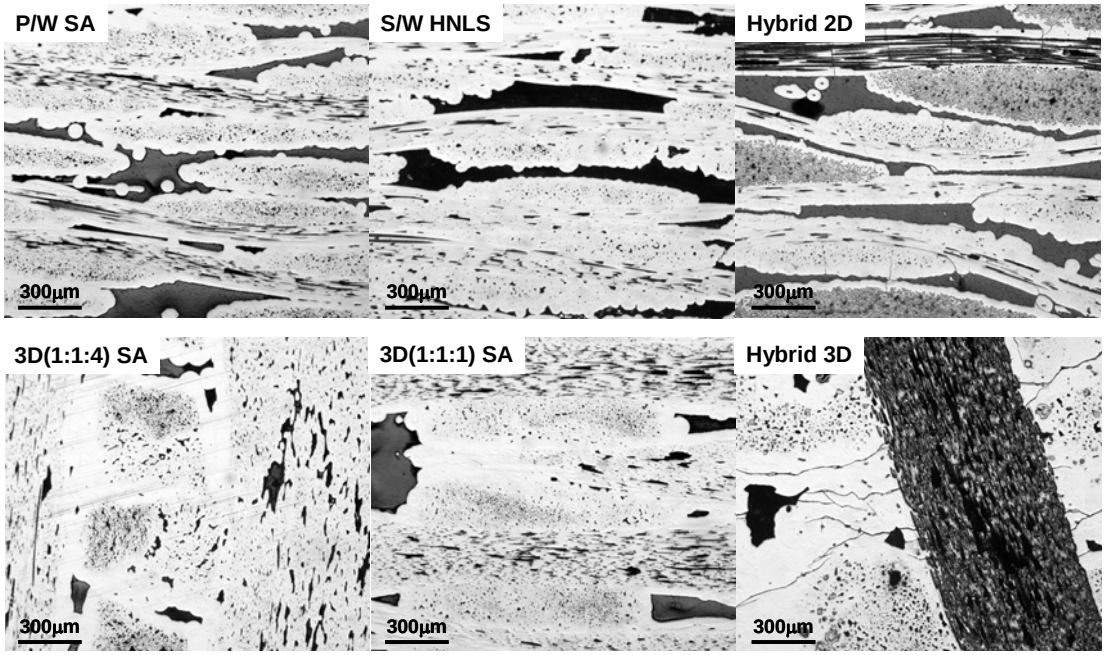

Fig. 2. Typical micrographs of polished cross-sections of various SiC/SiC and SiC-C/SiC composites.

Figure 3 shows a relationship between the axial fiber volume fraction and thermal conductivity. The 3D SiC/SiC composites with the Tyranno™-SA fiber exhibited the highest improvement of the thermal conductivity. Specifically, the presence of continuous Z-direction fibers remarkably improves the through-thickness thermal conductivity. Similarly, the carbon fiber with higher thermal conductivity of 640 W/m-K is, in general, considered effective to provide the high thermal conductivity composite. However many CTE mismatch induced cracks prevented thermal diffusion via matrix of carbon fiber containing composites, resulting in less improvement than the Tyranno™-SA composites. The in-plane thermal conductivity was also high (~50 W/m-K) similar to the through-thickness thermal conductivity due to the presence of continuous X- or Y-direction fibers. In contrast, the SiC/SiC composite of Hi-Nicalon™ Type-S with relatively lower thermal conductivity exhibited less improvement of the in-plane thermal conductivity, though high axial (in-plane) fiber volume fraction.

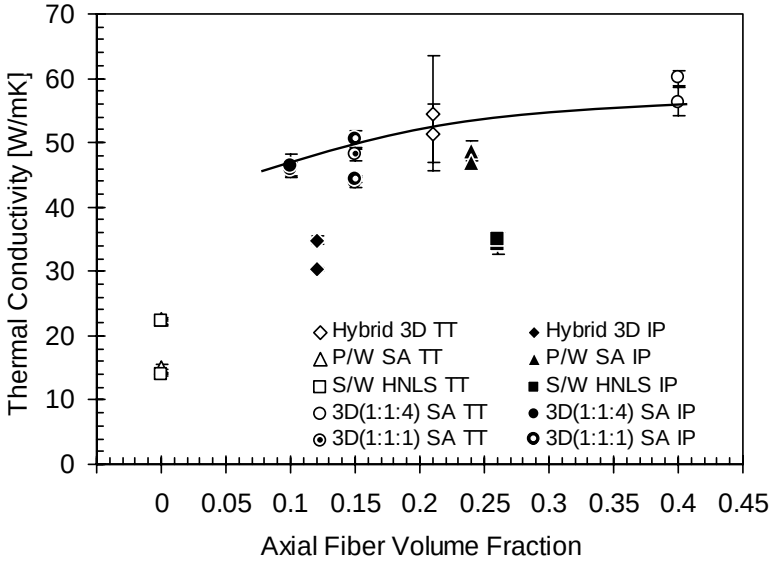

Fig. 3. Through-thickness (TT) and in-plane (IP) thermal conductivity with respective to the axial fiber volume fraction.

Acknowledgements

The authors would like to thank Dr. Hsin Wang at Oak Ridge National Laboratory for thermal conductivity measurement. This research was sponsored by the Office of Fusion Energy Sciences, U.S. Department of Energy under contract DE-AC05-00OR22725 with UT-Battelle, LLC, and "JUPITER-II" U.S.-Department of Energy/Japanese Ministry of Education, Culture, Sports, Science and Technology (MEXT) collaboration for fusion material system research.

References

[1] A. R. Raffray, R. Jones, G. Aiello, M. Billone, L. Giancarli, H. Golfier, A. Hasegawa, Y. Katoh, A. Kohyama, S. Nishio, B. Riccardi, and M.S. Tillack, Fus. Eng. Des. 55 (2001) 55.

[2] L. L. Snead, Y. Katoh, A. Kohyama, J. L. Bailey, N. L. Vaughn, and R. A. Lowden, J. Nucl. Mater. 283–287 (2000) 551.

[3] T. Hinoki, L. L. Snead, Y. Katoh, A. Hasegawa, T. Nozawa, and A. Kohyama, J. Nucl. Mater. 307–311 (2002) 1157.

[4] T. Nozawa, L. L. Snead, Y. Katoh, and A. Kohyama, J. Nucl. Mater. 329–333 (2004) 544.

[5] Y. Katoh, A. Kohyama, T. Hinoki, and L. L. Snead, Fus. Sci. Technol. 44 (2003) 155.

[6] L. L. Snead, M. Balden, R. A. Causey, and H. Atsumi, J. Nucl. Mater. 307–311 (2002) 1200.

[7] Y. Lee, T. Nozawa, T. Hinoki, and A. Kohyama, submitted to Proceedings of the Sixth IEA Workshop on SiC/SiC Composites for Fusion Energy Application, 2004, International Energy Agency.

CHARACTERIZATION OF CHEMICALLY VAPOR INFILTRATED SILICON CARBIDE COMPOSITES REINFORCED BY VARIOUS HIGH MODULUS FIBERS: II. TENSILE PROPERTIES—T. Nozawa, Y. Katoh, L. L. Snead (Oak Ridge National Laboratory), T. Hinoki and A. Kohyama (Kyoto University, Japan)

OBJECTIVE

The objective in this study is to evaluate the fundamental mechanical properties of various architecture types of SiC/SiC and hybrid SiC-C/SiC composites reinforced by high-modulus SiC and carbon fibers, designed to provide high thermal conductivity.

SUMMARY

Tensile properties of SiC/SiC composites were significantly dependent on the axial fiber volume fraction; three-dimensional (3D) SiC/SiC composites with in-plane fiber content <15% exhibited lower tensile strength and proportional limit stress. The composites with high volume fraction of the axial fibers >20% exhibited improved tensile properties. In contrast, the hybrid SiC-C/SiC composites with severe matrix damage induced by the large mismatch of coefficients of thermal expansion between the fiber and the matrix exhibited low tensile tangent modulus and proportional limit stress.

PROGRESS AND STATUS

Introduction

Advanced SiC/SiC composites with the highly-crystalline SiC fibers and the matrix are beneficial to improve system efficiency and allow higher resistance to thermal shock because of their enhanced thermal and thermo-mechanical properties. In Part I [1], it was revealed that the 3D Tyranno™-SA fiber composites showed the excellent thermal transport properties (~55 W/m-K) due to excellent thermal conductivity of Tyranno™-SA, ~65 W/m-K. In contrast, the hybrid SiC-C/SiC composites incorporated with the carbon fibers were prevented heat transport via matrix due to severe damage in the matrix by the large mismatch of coefficients of thermal expansion between the carbon fiber and the SiC matrix.

The latest composites with the high modulus SiC fibers, i.e., highly-crystalline and near-stoichiometric SiC fibers: Tyranno™-SA and Hi-Nicalon™ Type-S, and the β-SiC matrix provide good geometrical stability and strength retention after neutron irradiation [2–4]. However, mechanical property data of the advanced SiC/SiC composites are still insufficient and strongly required to obtain for practical applications.

Experimental Procedure

A plain-weave Tyranno™-SA/CVI-SiC (P/W SA), a satin-weave Hi-Nicalon™ Type-S/SiC (S/W HNLS), and two types of 3D Tyranno™-SA/CVI-SiC composites with the fabric configurations of X:Y:Z=1:1:4 and 1:1:1 (3D(1:1:4) SA and 3D(1:1:1) SA) were prepared. In addition, P/W and 3D hybrid SiC-C/SiC composites incorporated with the P120S carbon fibers (Hybrid 2D and Hybrid 3D) were fabricated to give improved thermal conductivity. All composites had 150 nm-thick pyrolytic carbon as fiber/matrix interphase. Details of materials were summarized in Table 1 of Part I [1].

Tensile specimens were machined from the composite plates so that the longitudinal direction was parallel to either of X or Y fiber directions. Miniature tensile geometry that had been developed for neutron irradiation studies on ceramic composites [5] was employed. The rectangular geometry (length × width × thickness) of 15.0 mm × 4.0 mm × 2.3 mm was used, except for the 3D SiC/SiC composites with 20.0 mm × 6.0 mm × 2.5 mm. Tensile tests were conducted following the general guidelines of ASTM standard C1275. For the testing at room temperature, specimens were clamped by wedge grips with aluminum end tabs on both faces of the gripping sections. The strain was determined by averaging the readings of strain gauges bonded to both faces of the center gauge section. The crosshead displacement rate was 0.5 mm/min for all tests.

Results and Discussion

Figure 1 exhibits the typical tensile stress-strain curves and tensile data are listed in Table 1. Each of the curves for 2D SiC/SiC composites comprises an initial proportional segment that corresponds to the elastic deformation, followed by a second linear portion during which matrix cracks in transverse fiber bundles progressively develop, and a further non-linear portion due to domination of the matrix cracks in the longitudinal fiber bundles and the fiber failures. The tensile strength of 200~300 MPa for 2D SiC/SiC composites is similar to that obtained from conventional 2D CVI-SiC/SiC composites [6]. The higher tensile tangent modulus of ~270 GPa of the 2D SiC/SiC composites is attributed to the use of the highly-crystalline SiC fibers and the β-SiC matrix. The large scatters were due to varied pore content. The 3D SiC/SiC composites exhibited high elastic modulus, though significantly lower tensile strength than the 2D CVI SiC/SiC composites. They are roughly distinguished into two types of fracture patterns: brittle and quasi-ductile with non-linear portion beyond initial linear segment, although both fracture behaviors exhibited limited short fiber pullout. Most of the brittle specimens failed after the first proportional limit stress, resulting in lower tensile strength, ~65 MPa.

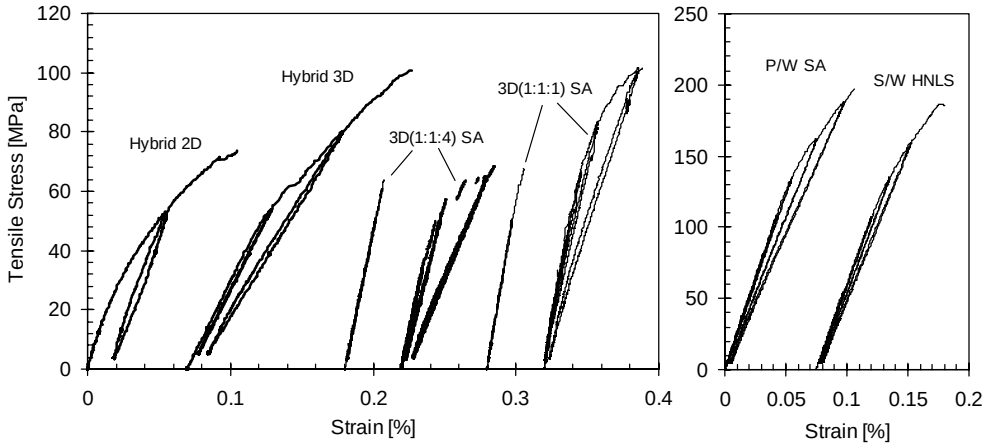

Fig. 1. Typical tensile stress-strain curves of various CVI SiC/SiC and hybrid SiC-C/SiC composites.

Table 1. Reduced tensile data of various SiC/SiC and hybrid SiC-C/SiC composites

Composite ID	Tensile tangent modulus [GPa]	First proportional limit stress [MPa]	Second proportional limit stress [MPa]	Ultimate tensile strength [MPa]	Misfit stress [MPa]
P/W SA	273(23)	103(21)	135(15)	199(2)	24(9)
S/W HNLS	244(6)	101(9)	145(4)	226(50)	15(4)
3D(1:1:4) SA - brittle	213(26)	64	-	64	-
3D(1:1:4) SA	224(5)	35(2)	49(1)	59(13)	4(2)
3D(1:1:1) SA - brittle	264(18)	60(4)	-	65(4)	-
3D(1:1:1) SA	277	53	70	102	2(4)
Hybrid 2D	138(28)	8(1)	23(3)	94(28)	32
Hybrid 3D	95(10)	47(1)	82(14)	98(3)	18(4)

*The numbers in parenthesis indicate standard deviation.

A feature of the hybrid composites is significantly lower elastic moduli, ~140 GPa for 2D and ~100 GPa for 3D, respectively. In contrast, the estimated elastic moduli by parallel-serial approach based on the rule of mixtures [7] yielded ~270 GPa for 2D and ~100 GPa for 3D. It is noted that the elastic modulus of P/W hybrid composites was roughly estimated by replacing with the orthogonal 2D architecture. Therefore the estimated elastic modulus should be influenced by pore distribution and waviness. Processing-induced matrix cracks perpendicular to the loading axis of the 2D hybrid composites severely reduced initial tensile tangent modulus. Damaged matrices also caused less proportional segment, followed by progressive damage accumulations in lower stress level. Contrarily, the 3D hybrid composites with transverse matrix

cracks around Z-stitch carbon fibers, which existed parallel to the axial fibers, exhibited less degradation of the elastic modulus.

The significant difference of tensile strength in the composite types is attributed primarily to the effective fiber volume content in the loading axis. According to Curtin [8], the intact fibers transfer the applied load beyond the fiber failure. In particular, it is simply assumed that intact fibers equally convey the applied load, well known as the global load sharing (GLS) theory. This indicates that the ultimate tensile strength is proportional to the axial fiber volume fraction. Composites tested in this study were designed with varied fiber volume content. As plotted in Fig. 2(a), the large differences in axial fiber content provided the differed tensile strength in each composite. Both 3D SiC/SiC composites with large structural unit, ~3.0 mm, are subjected to change in fiber volume fraction in cutting position. The bare fibers located at the edges of the specimen are mostly damaged, i.e., discontinuous along the gauge length, and those are ineffective in load transfer. In this case, less ability to transfer the applied load resulted in the quasi-brittle failure at the first proportional limit stress. In addition, the possible slight processing damage on reinforcing fibers of 3D SiC/SiC composites during heating up to 2073 K may have degraded the tensile strength.

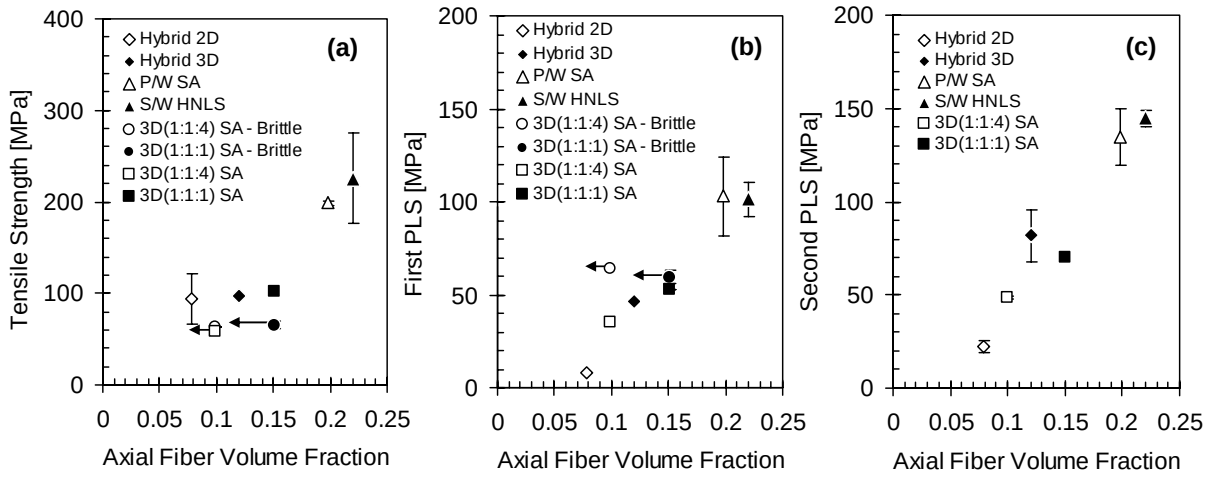

Fig. 2. Relationships among tensile properties and the axial fiber volume fraction.

As with the tensile strength, the difference of the proportional limit stress (PLS) in composite types may be attributed primarily to the axial fiber volume content (Figs. 2(b) and (c)). In particular, the 2D hybrid composites with severe processing-induced matrix damages had lower PLS, although, in many cases, it is very difficult to define the second PLS from the stress-strain curve because of progressive damage

accumulation. Degradation of the reloading modulus at the lower stress level supports progressive damage accumulation.

The residual thermal stress is inevitable when the coefficients of thermal expansion are different between the fibers and the matrix. In the Tyranno™-SA or Hi-Nicalon™ Type-S/PyC/CVI-SiC system, the residual stress should be minimal, because the fibers consist primarily of cubic (beta-phase) SiC, i.e., equivalent to the matrix constituent. The thermal residual stress estimated by the method proposed by Vagaggini et al. [9] exhibits nearly zero for 3D SiC/SiC composites and residual tension of ~20 MPa for 2D SiC/SiC composites (Table 1). The slightly larger residual stress of 2D SiC/SiC composites might be due to restriction by waviness. The hybrid SiC-C/SiC composites exhibited relatively higher tensile residual stress due to large CTE mismatch of the SiC and the carbon.

Acknowledgements

The authors would like to thank Dr. Edgar Lara-Curzio at Oak Ridge National Laboratory for mechanical testing. This research was sponsored by the Office of Fusion Energy Sciences, U.S. Department of Energy under contract DE-AC05-00OR22725 with UT-Battelle, LLC, and 'JUPITER-II' U.S. Department of Energy/Japanese Ministry of Education, Culture, Sports, Science and Technology (MEXT) collaboration for fusion material system research.

References

[1] T. Nozawa, Y. Katoh, L. L. Snead, T. Hinoki, and A. Kohyama, submitted to Fusion Materials Semiannual Progress Report for Period Ending December 31, 2004, DOE/ER-0313/37, U.S. Department of Energy.
[2] L. L. Snead, Y. Katoh, A. Kohyama, J. L. Bailey, N. L. Vaughn, and R. A. Lowden, J. Nucl. Mater. 283–287 (2000) 551.
[3] T. Hinoki, L. L. Snead, Y. Katoh, A. Hasegawa, T. Nozawa, and A. Kohyama, J. Nucl. Mater. 307–311 (2002) 1157.
[4] T. Nozawa, L. L. Snead, Y. Katoh, and A. Kohyama, J. Nucl. Mater. 329–333 (2004) 544.
[5] T. Nozawa, Y. Katoh, A. Kohyama, and E. Lara-Curzio, Proceedings of the Fifth IEA Workshop on SiC/SiC Composites for Fusion Energy Application, International Energy Agency, 74 (2002).
[6] Y. Katoh, A. Kohyama, T. Hinoki, and L. L. Snead, Fus. Sci. Technol. 44 (2003) 155.
[7] T. Ishikawa, K. Bansaku, N. Watanabe, Y. Nomura, M. Shibuya, and T. Hirokawa, Compos. Sci. Technol. 58 (1998) 51.

[8] W. A. Curtin, J. Am. Ceram. Soc. 74 (1991) 2837.

[9] E. Vagaggini, J-M. Domergue, and A. G. Evans, J. Am. Ceram. Soc. 78 (1995) 2709.

EFFECT OF INTERPHASE THICKNESS ON TENSILE PROPERTIES OF HI-NICALON™ TYPE-S FCVI COMPOSITES—Y. Katoh, L. L. Snead, and T. Nozawa (Oak Ridge National Laboratory), T. Hinoki and A. Kohyama (Kyoto University), N. Igawa and T. Taguchi (Japan Atomic Energy Research Institute)

OBJECTIVE

The objective of this work is to determine the influence of interphase thickness on tensile properties of the Hi-Nicalon™ Type-S / pyrolytic carbon interphase / chemically vapor infiltrated SiC composite system, in search of the optimum interphase for the near-stoichiometric SiC fiber-reinforced rigid SiC matrix composites for fusion applications.

SUMMARY

Fast fracture properties of chemically vapor-infiltrated silicon carbide matrix composites with Hi-Nicalon™ Type-S near-stoichiometric silicon carbide fiber reinforcements and thin pyrolytic carbon interphase were studied. The primary emphasis was on preliminary assessment of the applicability of a very thin pyrolytic carbon interphase between fibers and matrices of silicon carbide composites for use in nuclear environments. It appears that the mechanical properties of the present composite system are not subject to strong interphase thickness effects, in contrast to those in conventional non-stoichiometric silicon carbide-based fiber composites. The interphase thickness effects are discussed from the viewpoints of residual thermal stress, fiber damage, and interfacial friction. A preliminary conclusion is that a thin pyrolytic carbon interphase is beneficial for fast fracture properties of stoichiometric silicon carbide composites.

PROGRESS AND STATUS

Introduction

Silicon carbide (SiC) is a unique material that maintains high strength and corrosion resistance at temperatures well beyond the typical high temperature limits for superalloys. More importantly, the excellent thermo-mechanical properties of SiC are maintained after neutron irradiation to medium-to-high fluences at elevated temperatures [1]. Continuous SiC fiber-reinforced SiC matrix composites (SiC/SiC composites) can be used as structural materials, since they possess pseudo-ductile, predictable, and tailorable fracture properties in addition to the unique merits of monolithic SiC [2]. Early generations of SiC/SiC composites failed to demonstrate neutron tolerance due to a rapid irradiation-induced densification of ‘SiC-based’ non-stoichiometric fibers [3–5]. However, as improved SiC fibers became available, experiments started to demonstrate good tolerance of SiC/SiC composites to neutron irradiation [5–7]. Those SiC fibers, which consist primarily of a polycrystalline form of cubic SiC and are termed Generation-III SiC fibers [8], are now commercially available as Hi-Nicalon™ Type-S (Nippon Carbon Co., Tokyo, Japan) [9] and Tyranno™-SA (Ube Industries, Ltd., Ube, Japan) [10]. The Generation-III SiC fiber composites are also considered for application as in-core components of advanced gas thermal reactors [11] and gas fast reactors [12]. Fusion power reactor design studies assume that SiC/SiC composites can be used in gas-cooled solid-breeding blankets [13–16] and helium/Pb-Li dual-coolant blankets [17,18]. Some of the dual-coolant blanket concepts, including the U.S.-proposed Test Blanket Module (TBM) for

the International Thermonuclear Experimental Reactor (ITER), utilize channel inserts made of SiC or SiC/SiC as an electrical and thermal insulator [19].

Among various processing techniques for matrix densification of SiC/SiC composites, chemical vapor infiltration (CVI) is the technique that produces reference materials for nuclear applications [8]. The CVI process is essentially a chemical vapor deposition (CVD) of the matrix material on (coated) fiber surfaces as the substrate. A high purity, stoichiometric, and polycrystalline matrix for SiC/SiC composites can not be efficiently produced by any other industrialized processes. Non-stoichiometric and/or nano-crystalline SiC matrices in melt-infiltrated or polymer-impregnated and pyrolyzed composites are usually prone to deteriorate during irradiation [20,21]. The CVI process is not only effective in producing high strength composites for primary structure applications but is also appropriate for tailoring of trans-thickness thermal and electrical conductivity for the channel insert application, by controlling porosity and inter-fiber spacing.

Another advantage of the CVI technique is that the deposition of fiber-matrix interphases as a CVD coating on the fibers can be incorporated in the matrix densification process. Properties of the interphases are highly tailorable in CVI SiC/SiC composites [22].

The objective of this work is to evaluate the non-irradiated mechanical properties of Generation III SiC fiber-reinforced CVI SiC-matrix composites with a tailored pyrolytic carbon (PyC) interphase. The primary focus was on the influence of interphase thickness, which is a key parameter that controls mechanical properties of ceramic composites. For conventional CVI-SiC/SiC composite systems, an optimum PyC interphase thickness range of 150–300nm is reported for the best fracture behavior [23–26]. However, for application in fusion blankets, the minimum use of carbon constituents is preferred to optimize irradiation stability, chemical compatibility with coolants and/or breeding materials, tritium permeability, and electrical conductivity. The Generation III SiC fibers are significantly different from conventional SiC fibers in physical (coefficient of thermal expansion, elastic modulus), mechanical (fracture strain), chemical (reactivity and bonding at the surface), and topographical (surface roughness) properties. These differences can cause difference in the effect of interphase characteristics on composite properties, so the effects must be quantified.

Experimental Details

The materials studied were Hi-Nicalon™ Type-S fiber-reinforced, PyC interphase, CVI SiC-matrix (Hi-Nicalon Type-S/PyC/CVI-SiC) composites produced at Oak Ridge National Laboratory. Composites with three PyC interphase thicknesses were produced with 2D plain-weave fabric from an early lot of Hi-Nicalon Type-S fibers (Lot# 298201, produced in 1998) with a [0°/30°/60°] stacking sequence (‘0/30/60’, hereafter) [27]. The average interphase thicknesses were 80, 130, and 270nm. Additionally, one composite was produced with 2D plain-weave fabric of a newer lot of fibers (Lot# 320203, 2002) using a [0°/90°] stacking sequence (‘0/90’). The newer Hi-Nicalon Type-S fibers were produced by continuous factory line, including spinning, electron beam curing, and decarbonization, while the older fibers had been produced through a series of batch processes. The specification sheet provided by the manufacturer shows that the newer fibers possess slightly higher nominal tensile strength and very slightly lower tensile modulus than the older fibers. The property differences between the two generations

of Hi-Nicalon Type-S fibers are seen in Table 1, along with the summary of properties of the composites fabricated in this study.

The interphase deposition and matrix densification were carried out in isothermal and temperature gradient [28,29] configurations, respectively, at the High Temperature Materials Laboratory, Oak Ridge National Laboratory (ORNL). Stacks of ~60 fabric sheets of 76 mm-diameters were tightly held in graphite fixtures during the infiltration. The PyC interphase was deposited from propylene precursor (50 cm^3/min) diluted with argon (1000 cm^3/min) at 1373K and 5kPa total pressure. The interphase thickness was controlled by adjusting the time of deposition, since the deposition rate was fairly constant during the coating process. The SiC matrix was infiltrated using methyltrichlorosilane (MTS, Gelest Inc., Morrisville, PA) at a hot surface temperature of 1373–1473K and back pressure of 100kPa. The liquid MTS precursor was carried by hydrogen bubbled through it at a flow rate of 0.3–0.5 g/min. The deposition rate was approximately 30nm/min.

Tensile specimens were machined from the composite discs with the longitudinal direction parallel to one of the fiber directions. Miniature tensile specimen geometry that had been developed for neutron irradiation studies of ceramic composites was employed [30]. The specimen geometry and dimensions are given in Fig. 1. The gauge length of 15mm and the width of 3mm (corresponding to two thread intervals) are within a range where a systematic gauge size effect is observed [31]. The gauge thickness of ~2.3mm accommodates approximately 10 fabric layers. The tensile testing procedure followed general guidelines of ASTM standards C1275-00 and C1359-96. The tensile test incorporated several unloading / reloading sequences in order to allow analysis on the hysteretic response. For the tests at room temperature (RT), the specimens were clamped by wedge grips with aluminum tabs on both faces of the grip sections. The strain was determined by averaging the readings of strain gauges fastened to both faces of the central gauge section during the testing at RT. The elevated temperature tests were performed at 1573K in a flow of commercial ultra-high purity argon. Edge-loaded passive grips recommended in ASTM standard C1359-96 were employed to hold the specimen. The strain was measured on one side of the gauge section by means of reflective laser extensometry. Details of the elevated temperature testing can be found elsewhere [32]. The crosshead displacement rate was 0.5mm/min for all tests. Fracture surfaces were examined using a field emission scanning electron microscope (FE-SEM).

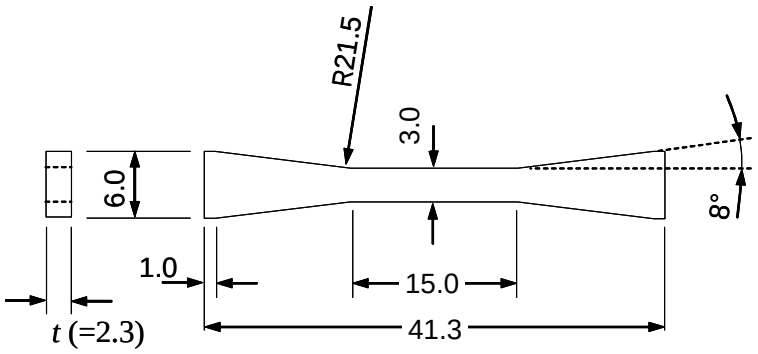

Fig. 1. Geometry of the miniature tensile specimen. Unit of dimensions is millimeter.

Results

The dimensions of the infiltrated composites were 76mm diameter x ~12.7mm thickness. Variations in the interphase coating thickness and porosity within individual discs were both typically ±30%. The interphase thickness was determined by microscopic examination on the polished surfaces using an FE-SEM. Examples of backscattered electron images of the composites with the nominal interphase thickness of 80, 130, and 270nm are presented in Fig. 2. The porosity was calculated based on the measured apparent mass density (= mass / envelope volume), measured interphase thickness, and the estimated fiber volume fraction. Because of the significant variations within the nominally identical materials, both the interphase thickness and the porosity were measured for individual mechanical property specimens. Values summarized in Table 1 are those averaged over the tested tensile specimens. The tensile stress – strain curves obtained at RT for the 0/30/60 composites with three different interphase thicknesses are shown in Fig. 3. Each of the curves contains an initial proportional segment that roughly corresponds to the elastic deformation, followed by a second linear portion during which matrix cracks are progressively developing, and a further non-linear portion due to domination of the fiber failure. Although these three specimens failed at similar stress levels, a distinct difference in the fracture strain and in the hysteresis behavior is noted between the composite with 56nm-thick interphase and those with 178 or 315nm-thick interphases.

Figure 4 compares the tensile behavior of the 0/90 composites with thin (43 and 62nm) PyC interphase at RT and at 1573K. The 0/90 composite exhibited significantly higher strength and larger fracture strain than the 0/30/60 composite that have similar interphase thickness. The tensile behavior at 1573K is apparently different from that at RT. However, since the unloading / reloading moduli for unloading from 75, 100, and 125MPa are almost identical, increase in the matrix crack density is not primarily responsible for the increase in permanent strain. Furthermore, the intersection of unloading and reloading segments at higher stress levels suggests that an artificial drift in the test instrumentation is added to the strain reading. Therefore, the elevated temperature data were used only for comparison of the ultimate strength and the matrix damage parameter.

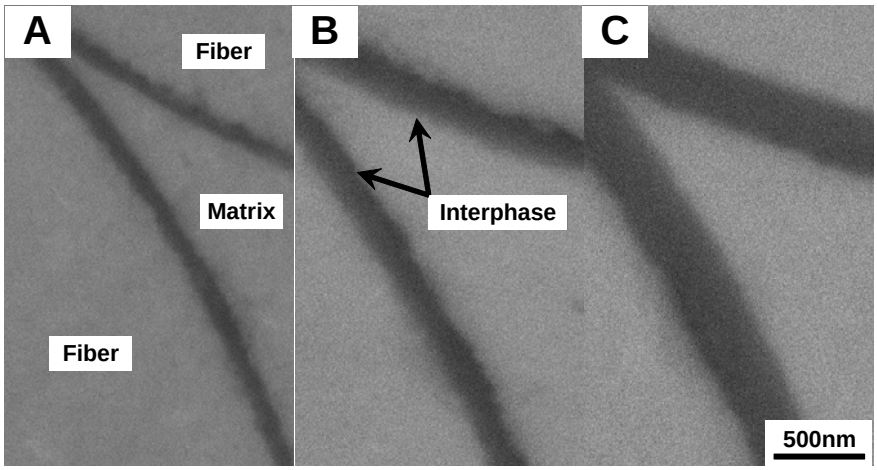

Fig. 2. Backscattered scanning electron images of fiber-matrix interfacial regions of the composites. (A) CVI-1258, 40 < t_{PyC} < 90nm, (B) CVI-1257, 150 < t_{PyC} < 180nm, (C) CVI-1259, 200 < t_{PyC} < 390nm.

An example RT stress – strain curve for Tyranno™-SA SiC-fiber composite, obtained from a companion work [33] is included in Fig. 4. The Tyranno-SA composite has a 2D plain-weave architecture with a thin (25nm) PyC interphase. While the Tyranno-SA and the Hi-Nicalon Type-S composites exhibited similar proportional limit stresses (PLSs) and similar second-stage linear behavior, a major difference is noted in that the Hi-Nicalon Type-S composite failed after matrix crack saturation had been achieved. Additionally, the transition from the proportional to the second linear deformation stage seems to be smoother in the Hi-Nicalon Type-S Composite.

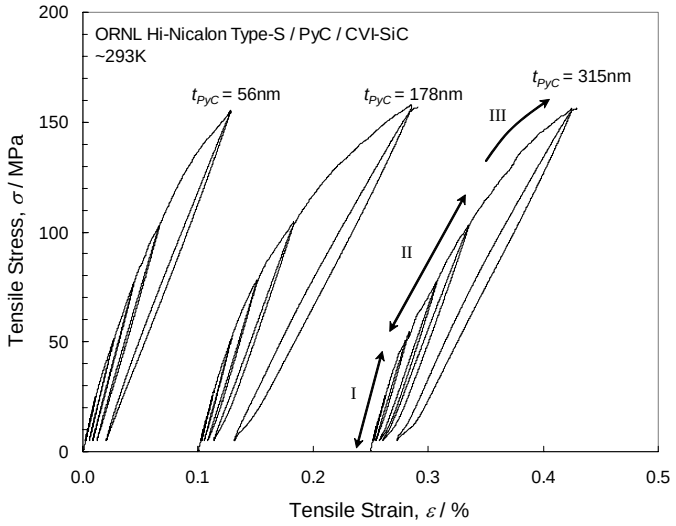

Fig. 3. Representative load – strain curves obtained for Hi-Nicalon™ Type-S (2D-PW, 0°/30°/60°) / PyC / CVI-SiC composites with various PyC interphase thickness. Stages I, II, and III indicate the initial proportional stage, the second linear stage, and the non-linear fiber failure stage, respectively.

The ultimate tensile strength (UTS), PLS, and tensile modulus of the Hi-Nicalon Type-S / PyC / CVI-SiC composites are plotted against the PyC interphase thickness in Figs. 5, 6, and 7, respectively. The PLS was defined as the stress at 5% deviation from the extrapolated linear segment used for the modulus determination. As seen in Fig. 5, the UTS exhibited a slight positive dependence on the interphase thickness, although the dependence might not be statistically significant. No significant difference was shown in UTS, after values were normalized to the longitudinal fiber volume fraction, between the plain-weave 0/30/60 composite and the plain-weave 0/90 composite. The UTS at 1573K appeared lower than that at RT by 10 to 30%.

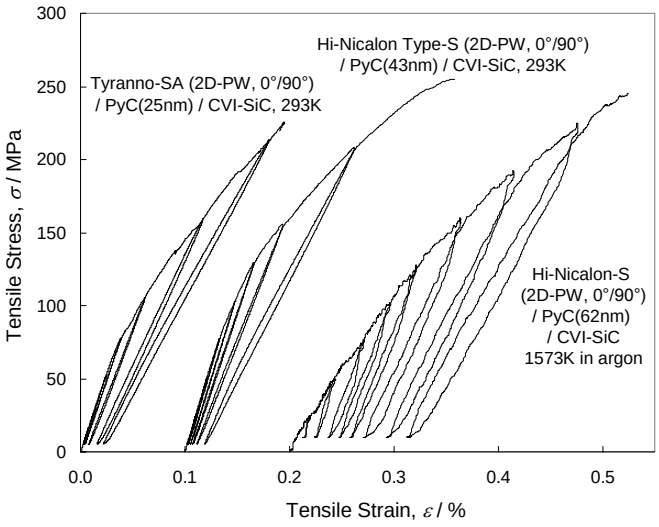

Fig. 4. Comparison of load – strain curves obtained for very thin PyC-interphase Tyranno™-SA composite at room temperature and Hi-Nicalon™ Type-S composite at room temperature and at 1573K in argon.

In contrast to the UTS, the tensile PLS exhibited a negative correlation with the interphase thickness, as shown in Fig. 6. The correlation is significant in this case, as the PLS of 30~40MPa at the interphase

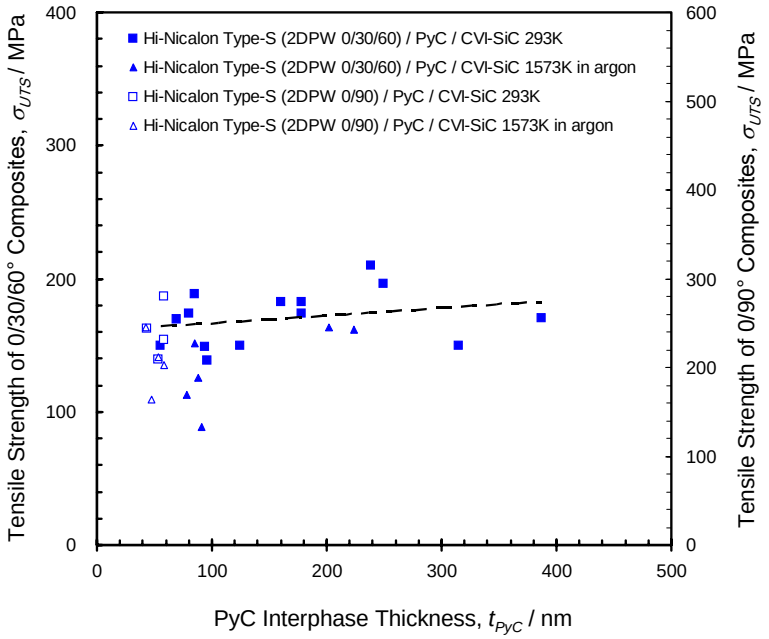

Fig. 5. Ultimate tensile stress of Hi-Nicalon™ Type-S / PyC / CVI-SiC composites at room temperature plotted against PyC interphase thickness

thickness of <100nm decreases to 20~30MPa at >300nm. The plain-weave 0/90 composite exhibited much higher PLS than the plain-weave 0/30/60 composites for similar interphase thickness, even after normalization to the longitudinal fiber fraction. The difference is due most likely to the difference in stacking sequence, since Tyranno-SA 2D-plain weave 0/90 composites with similar interphase features exhibited substantially higher PLS for identical testing condition [33] The PLS could also be affected by the matrix density, but in this case the difference could not be the effect of matrix density, because the porosity in the 0/30/60 composite with interphase thickness <100nm and that in the 0/90 composite are about the same. The influence of 2D fabric architecture on PLS is not known.

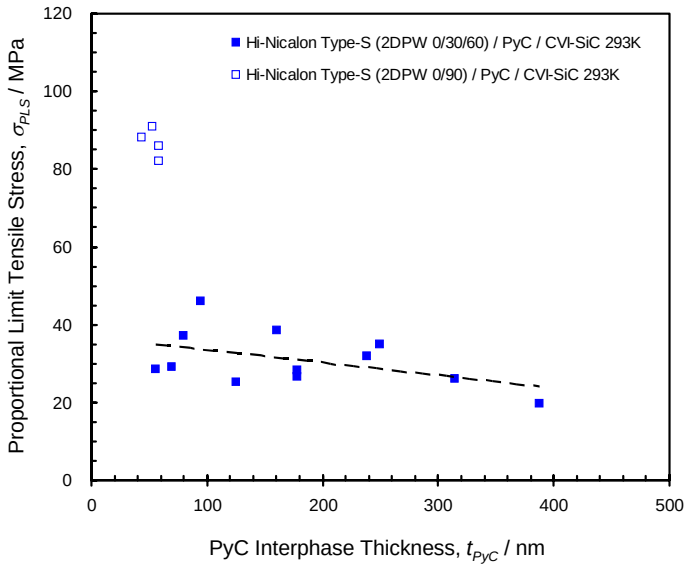

Fig. 6. Proportional limit tensile stress of Hi-Nicalon™ Type-S / PyC / CVI-SiC composites at ambient temperature plotted against PyC interphase thickness.

The tensile tangent modulus was also slightly affected by the interphase thickness. As shown in Fig. 7, the modulus decreases monotonically as the interphase gets thicker. The PyC interphase in these composites consists of near-isotropic glassy carbon. The observed interphase thickness effect on the modulus is primarily a volume effect of the very much less rigid glassy carbon in the rigid silicon carbide. Fitting to a simple model suggests ~10GPa of interphase Young's modulus and ~240GPa of Young's modulus for effective mean medium representing all the other composite constituents including pores [33].

In Figs. 8(A) and (B), typical RT fracture surfaces within the longitudinal fiber bundle regions are compared between composites with 56nm- and 315nm-thick interphases. A substantial population of fibers exhibit pull-out length of 10–30μm for the case of 56nm-thick interphase, whereas similar fiber populations could not be identified in the 315nm-thick interphase composite. The rest of the fibers showed pull-out length of ~100μm or longer. Pairs of representative fracture surfaces of individual fibers are included as subsets in Fig. 8. Fracture origins in the fibers were identified either on the surface (left) or as an internal flaw (right). Frequencies of fractures originating from surface and from an internal flaw were roughly comparable, although a statistical comparison was not made. A fracture surface of the 44nm-thick interphase composite tested at 1573K is presented in Fig. 8(C). The fiber pull-out length at 1573K appeared substantially longer and was typically 200–300μm. The majority of the fibers fractured at the

elevated temperature appeared to have initiated at the surface. It is not known if it is due to an effect of testing temperature or differences between fibers of the two generations.

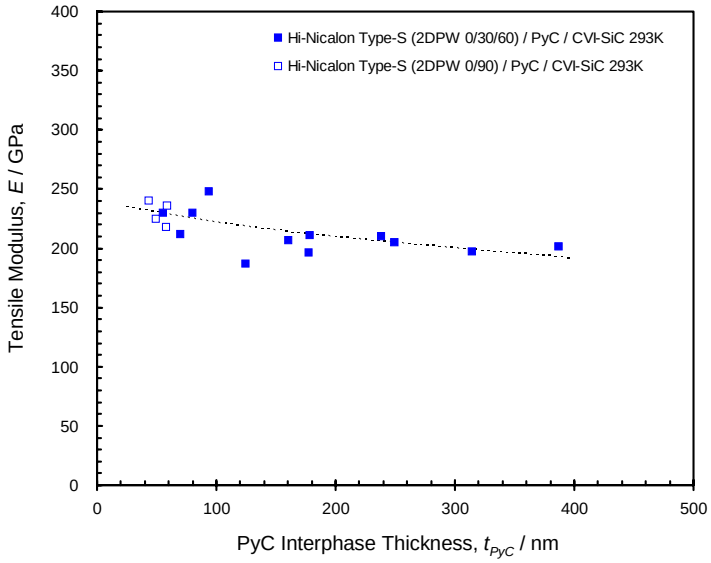

Fig. 7. Influence of PyC interphase thickness on initial tangential modulus of Hi-Nicalon™ Type-S / PyC / CVI-SiC composites.

Discussion

Observations described in the previous section imply that the non-linear tensile behavior could be significantly different between the Hi-Nicalon Type-S composites with PyC interphase < ~100nm or > ~100nm. In contrast, the UTS and modulus exhibited small or negligible dependence on the interphase thickness. The relatively small width of the hysteresis loop for the 56nm-thick interphase composite in Fig. 3 indicates the stronger friction at the sliding interfaces, if the matrix crack density is the same [34]. The shorter average fiber pull-out length on the fracture surface of the same composite indicates the stronger friction, since the pull-out length is inversely proportional to the frictional stress [35]. The larger PLS for thinner interphase might be due partly to the stronger friction, according to the model proposed by Curtin for uni-directional composites [35]. However, it could be more closely related to the higher composite modulus, since a substantial fraction of macroscopic cracks in 2D composites initiate at internal pore surfaces [36].

(1) Matrix damage evolution and in-situ fiber strength

The evolution of matrix damage parameters in four different composites with increasing peak tensile stress is plotted in Fig. 9. The matrix damage parameter was defined as:

$$D = 1 - E^* / E_c \qquad (1)$$

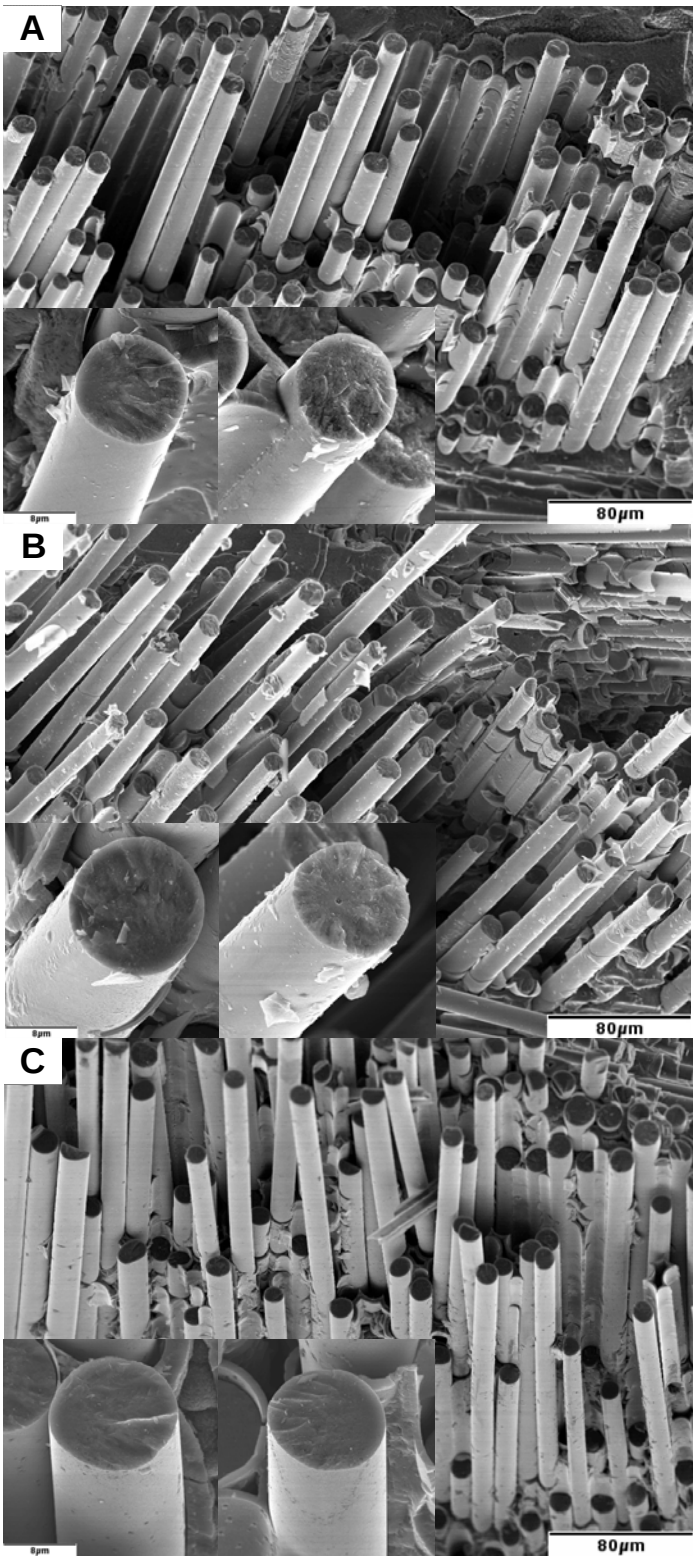

Fig. 8. Longitudinal fiber bundle regions in fracture surfaces of Hi-Nicalon™ Type-S / PyC / CVI-SiC composites. (A) t_{PyC}=56nm, tested at RT, (B) t_{PyC}=315nm, tested at RT, and (C) t_{PyC}=44nm, tested at 1573K in argon. Fiber fracture surfaces are shown in inserts.

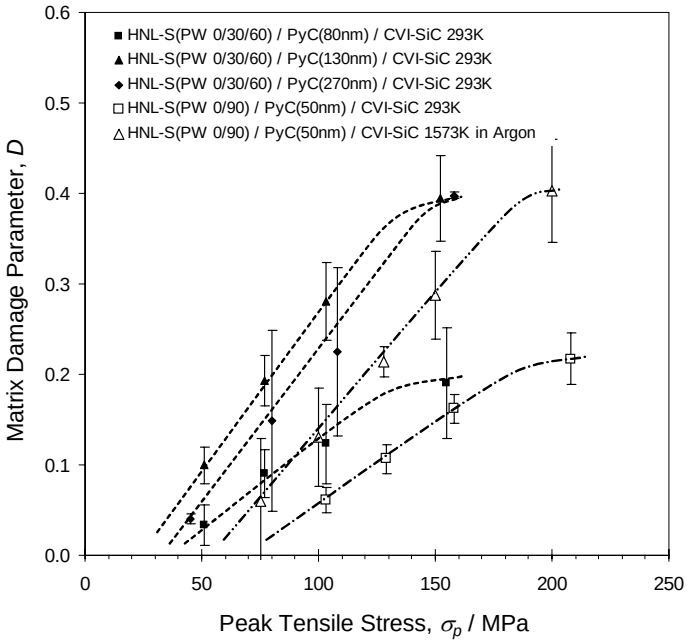

Fig. 9. Peak tensile stress dependence of matrix damage parameter.

where E^* is Young's modulus of the composite with matrix cracks and E_c the initial composite Young's modulus. The matrix damage parameter is approximately proportional to the matrix crack density. The rate of matrix crack accumulation with increasing stress appeared to be significantly different between the composites with nominal interphase thickness of 80nm and those with thickness >120nm. Furthermore, the matrix crack density at composite failure appeared to be significantly lower in the thin interphase materials, including the 0/90 composite, than in the thicker interphase materials. These differences are essential to the apparent dissimilarity seen in stress – strain curves in Fig. 3. The matrix crack accumulation rate at 1573K appeared to be higher than at RT.

Since the matrix crack density in the 0/30/60 composites apparently saturates at slightly below 150MPa of peak stress, as shown in Fig. 3, a linear fit to plots for the peak stress <150MPa intersects the horizontal axis at a matrix cracking stress. Comparison with Fig. 6 confirmed that the matrix cracking stresses at RT agreed well with the average PLS, i.e., 30–35MPa and ~60MPa for the 0/30/60 and 0/90 composites, respectively. The matrix cracking stress at 1573K appeared to be slightly lower than that at RT.

As shown in the inserts of Fig. 8, many of the fiber fracture surfaces exhibited a well-defined hackle and mirror pattern. The fracture strength (σ_f) of each fiber can be estimated using the mirror radius (r_m) measured using the SEM and the following empirical relationship [37].

$$\sigma_f r_m^{1/2} = A_m \qquad (2)$$

where A_m is the mirror constant. Taking A_m as 3.5MPa $m^{-1/2}$ [38], the in-situ strength of individual fibers was calculated to be 1.9–2.8GPa with an average of ~2.3GPa, regardless of the interphase thickness or fabric architecture. These numbers are close to the vender-provided nominal strength (2.6GPa) of Hi-

Nicalon Type-S fibers, which had been measured for fiber bundles. Therefore, the failure of thin interphase composites at a relatively low matrix crack density is not due to the weaker in-situ fiber strength but possibly due to the higher interfacial shear strength.

(2) Hysteresis analysis

In all the hysteresis loops from higher stresses (>75MPa) shown in Fig. 3, each unloading curve consists of an initial parabolic segment followed by a linear segment that continues to <20MPa, and each reloading curve also consists of an initial parabolic segment and the following linear segment that continues until it reaches the stress from which the unloading started. Such behavior can be seen in Fig. 10, in which the reciprocal moduli during the unloading / reloading processes are plotted against stress for three different composites. In the reciprocal modulus plot, the magnitude of the slopes for parabolic unloading and reloading segments are identical in an ideal condition, satisfying the following relationship with the interfacial frictional stress (τ) [39].

$$\left|\frac{d(1/E)}{d\sigma}\right| = \frac{b_2(1-a_1V_f)^2}{2V_f^{\,2}\tau E_m}\cdot\frac{r}{d} \qquad (3)$$

where V_f is volume fraction of the aligned fibers, E_m the effective mean modulus of matrix, pores, non-aligned fibers and interphase ('inside debonding' is assumed here), r the fiber radius, d the mean matrix crack spacing, and a_1 and b_1 the Hutchinson-Jensen parameters [40]. Figure 10 shows an apparently larger frictional stress in the 56nm-thick interphase composite than in the 178nm-thick interphase composite, if similar matrix crack densities at the given peak tensile stress are assumed. For the majority of the unloading and reloading curves, the slope could be determined with reasonable certainty. For the 0/90 composite, only the slope of the reciprocal reloading modulus could be determined, as was the case for the Tyranno-SA 0/90 composites [33].

As the mean matrix crack spacing was not measured in individual tested specimens, the sliding stress parameter, $\tau/(r/d)$, was defined and plotted in Fig. 11 as a function of interphase thickness. The sliding stress parameters were determined upon both unloading and reloading moduli at peak stress of ~150MPa for the 0/30/60 composites, while they were determined only from the reloading moduli at peak stress of ~200MPa for the 0/90 composite. Plots for the 0/30/60 composites in Fig. 11 indicate a transition of the sliding stress parameter at an interphase thickness of ~100nm. However, the transition is due primarily to the difference in matrix crack spacing, as the matrix damage parameters at the peak stress level of ~150MPa of the 0/30/60 composites with thinner (<100nm) interphases are approximately one half of those of the composites with thicker (>100nm) interphases. Therefore, the influence of interphase thickness on the interfacial sliding stress is not very significant in this range.

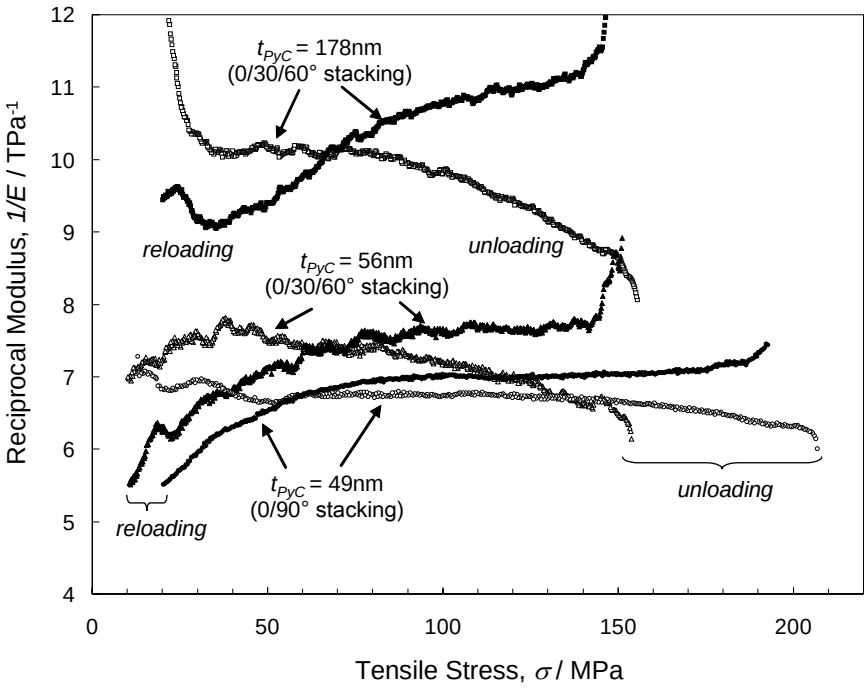

Fig. 10. Reciprocal moduli measured during unloading – reloading sequences incorporated in tensile testing. Material is Hi-Nicalon™ Type-S / PyC (160nm) / CVI-SiC composite.

Transversal matrix cracks in 2D CVI composites initiate mostly at the corners of inter-fiber-bundle pores where a significant stress concentration occurs, thus the saturated crack spacing of one half of the fabric's thread interval can be assumed when the crack initiation in the transversal fiber bundles is neglected. If we assume that is the case and the saturated crack density is achieved at a matrix damage parameter of ~0.4, the interfacial sliding stress τ falls in the range 10 to 20MPa for the composites studied. The sliding stress parameters obtained from the 0/90 composite appeared significantly smaller than those of the 0/30/60 composite with similar interphase thickness, even though the matrix damage parameters (discussed later) were similar at the peak loading stresses applied. This might be attributed to a potential difference in surface conditions between fibers in different generations.

Comparing the sliding stress parameters obtained at 1573K and RT shows a very substantial decrease at the elevated temperature. The same phenomenon is obviously seen in Fig. 4. The absolute values for elevated temperature data points in Fig. 11 are not highly credible due to the low quality of strain data acquisition. However, as the positive drift in strain measurement should have narrowed the hysteresis loops, it is very likely that the much smaller indicated interfacial friction at 1573K is real. The longer fiber pull-out lengths at 1573K also supports this interpretation.

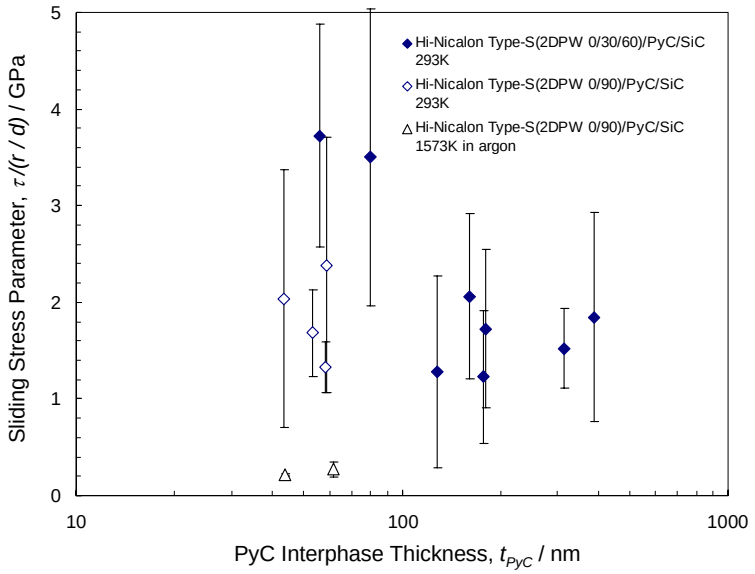

Fig. 11. Influence of PyC interphase thickness on dynamic interfacial sliding stress parameter. Error bars correspond to sum of uncertainty in data interpretation.

(3) Residual stress

The residual thermal stress is inevitable when the coefficients of thermal expansion are different between the fibers and the matrix, as the composites have been cooled down by >1000K after infiltration. In the Hi-Nicalon Type-S / PyC / CVI-SiC system, the residual stress should be minimal, because the fibers consist primarily of cubic (beta-phase) SiC, that is identical with the matrix constituent. The small amount of excess carbon present in the fiber (C/Si = 1.05 according to the specification of the vender) might have affected the thermoelastic properties. Figure 12 presents the residual thermal stress estimated by the method proposed by Vagaggini, et al. [41]. The axial stress in the matrix is approximately comparable to the misfit stress in magnitude and is in tension when the misfit stress is positive. In contrast to the reported positive misfit stress of ~+100MPa in a ceramic grade Nicalon™ / PyC / CVI-SiC composite [39], the average misfit stress in the present system appeared to be ~20MPa. Meanwhile, the extrapolated linear segments of the reloading curves converged at -50 to +5MPa with an average of ~-20MPa, suggesting a similar magnitude of axial tensile stress in the matrix. In the ceramic grade Nicalon composite system, the relatively large CTE mismatch between the fibers and matrix can result in a misfit stress as high as a few hundred MPa. The misfit stress can effectively be mitigated by applying a compliant PyC interphase of an appropriate thickness [42]. If that is the case, the measured misfit stress should exhibit negative correlation with the interphase thickness. However, in the Hi-Nicalon Type-S composite system studied, there is no clear correlation between the misfit stress and interphase thickness. This shows that the residual thermal stress in the composite must be insignificant, although a slight positive misfit stress might exist.

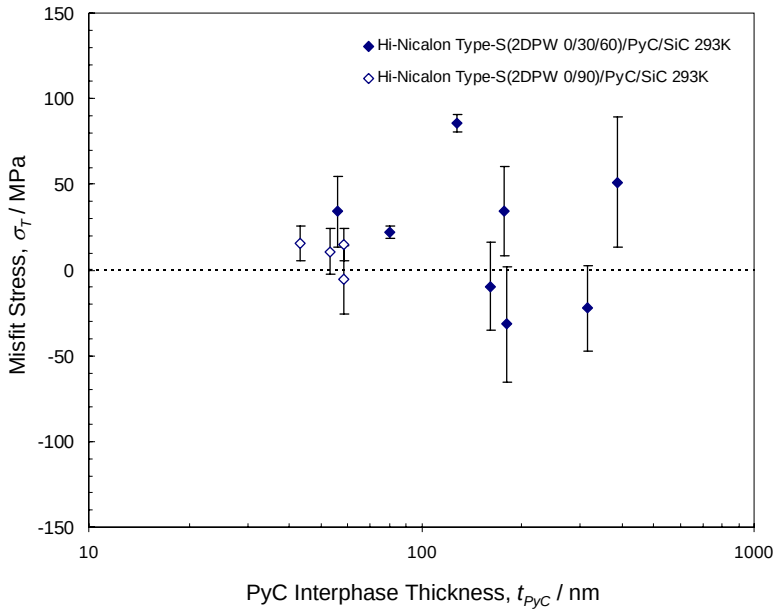

Fig. 12. Thermoelastic misfit stress plotted against PyC interphase thickness for Hi-Nicalon™ Type-S / PyC / CVI-SiC composites. Error bars correspond to sum of uncertainty in data interpretation.

Future Work

The study on PyC interphase thickness effect on tensile properties in the Hi-Nicalon Type-S CVI SiC/SiC composite system is completed. The knowledge obtained in this work have been provided a base in designing the reference SiC/SiC composites for irradiation in HFIR-18J experiment.

References

[1] R. J. Price, Nucl. Technol. 35 (1977) 320–336.
[2] G. R. Hopkins, Proceedings of the First Topical Meeting on Technology of Controlled Nuclear Fusion, CONF-740402-P2, Vol. II, San Diego (1974) 437.
[3] L. L. Snead, S. J. Zinkle, and D. Steiner, J. Nucl. Mater. 191–194 (1992) 560–565.
[4] G. W. Hollenberg, C. H. Henager, Jr., G. E. Youngblood, D. J. Trimble, S. A. Simonson, G. A. Newsome, and E. Lewis, J. Nucl. Mater. 219 (1995) 70.
[5] L. L. Snead, Y. Katoh, A. Kohyama, J. L. Bailey, N. L. Vaughn, and R. A. Lowden, J. Nucl. Mater. 283–287 (2000) 551–555.
[6] Y. Katoh, A. Kohyama, L. L. Snead, T. Hinoki, and A. Hasegawa, Neutron Tolerance of Advanced SiC-Fiber/CVI-SiC Composites, Proceedings of the 19th IAEA Fusion Energy Conference, IAEA-CN-94, International Atomic Energy Agency (2002) FT/P1-03.
[7] T. Hinoki, L. L. Snead, Y. Katoh, A. Hasegawa, T. Nozawa, and A. Kohyama, J. Nucl. Mater. 307–311 (2002) 1157–1162.
[8] Y. Katoh, A. Kohyama, T. Hinoki, and L. L. Snead, Fusion Sci. Technol. 44 (2003) 155.
[9] M. Takeda, J. Sakamoto, A. Saeki, and H. Ichikawa, Ceram. Eng. Sci. Proc. 17 (1996) 35–42.

[10] T. Ishikawa, Y. Kohtoku, K. Kumagawa, T. Yamamura, and T. Nagasawa, Nature 391 (1998) 773–775.
[11] G. O. Hayner et al., Next Generation Nuclear Plant Materials Research and Development Program Plan, INEEL/EXT-04-02347, Idaho National Engineering and Environmental Laboratory (2004).
[12] W. R. Corwin, L. L. Snead, S. J. Zinkle, R. K. Nanstad, A. F. Rowcliffe, L. K. Mansur, R. W. Swindeman, W. Ren, D. F. Wilson, T. E. McGreevy, P. L. Rittenhouse, T. Allen, J. Gan, and K. D. Weaver, The Gas Fast Reactor (GFR) Survey of Materials Experience and R&D Needs to Assess Viability (to be published as Oak Ridge National Laboratory Technical Memorandum, U.S. Department of Energy).
[13] S. Sharafat, F. Najmabadi, and C. Wong, Fusion Eng. Des. 18 (1991) 215–222.
[14] A. S. Perez Ramirez, A. Caso, L. Giancarli, N. Le Bars, G. Chaumat, J. F. Salavy, and J. Szczepanski, J. Nucl. Mater. 233–237 (1996) 1257–1261.
[15] S. Nishio, S. Ueda, I. Aoki, R. Kurihara, T. Kuroda, H. Miura, T. Kunugi, Y. Seki, T. Nagashima, and M. Ohta et al., Fusion Eng. Des. 41 (1998) 357–364.
[16] A. R. Raffray, L. El-Guebaly, S. Gordeev, S. Malang, E. Mogahed, F. Najmabadi, I. Sviatoslavsky, D. K. Sze, M. S. Tillack, X. Wang, and ARIES Team, Fusion Eng. Des. 58–59 (2001) 549–553.
[17] P. Norajitra, L. Buehler, U. Fischer, S. Malang, G. Reimann, and H. Schnauder, Fusion Eng. Des. 61–62 (2002) 449–453.
[18] ARIES Team, M. S. Tillack, X. R. Wang, J. Pulsifer, S. Malang, and D. K. Sze, Fusion Eng. Des. 49–50 (2000) 689–695.
[19] M. Abdou, D. Sze, C. Wong, M. Sawan, A. Ying, and N. Morley, U.S. Plans and Strategy for ITER Blanket Testing, Fusion Science and Technology (in press).
[20] R. J. Price and G. R. Hopkins, J. Nucl. Mater. 108–109 (1982) 732–738.
[21] Y. Katoh, H. Kishimoto, M. Kotani, W. Yang, and A. Kohyama, J. Nucl. Mater. 289 (2002) 42–47.
[22] R. Naslain, Compos. Sci. Technol. 64 (2004) 155–170.
[23] R. A. Lowden, Ceram. Trans. 19 (1991) 619–630.
[24] J. P. Singh, D. Singh, and M. Sutaria, Compos. A30 (1999) 445–450.
[25] J. H. Miller, P. K. Liaw, and J. D. Landes, Mater. Sci. Eng. A 317 (2001) 49–58.
[26] W. Yang, H. Araki, T. Noda, J. Park, Y. Katoh, T. Hinoki, J. Yu, and A. Kohyama, Mater. Trans. 43 (2002) 2568–73.
[27] N. Igawa, T. Taguchi, L. L. Snead, Y. Katoh, S. Jitsukawa, A. Kohyama, and J. C. McLaughlin, J. Nucl. Mater. 307–311 (2002) 1205–1209.
[28] T. M. Besmann, J. C. McLaughlin, and H.-T. Lin, J. Nucl. Mater. 219 (1995) 31–35.
[29] K. J. Probst, T. M. Besmann, D. P. Stinton, R. A. Lowden, T. J. Anderson, and T. L. Starr, Surf. Coat. Technol. 120–121 (1999) 250–258.
[30] T. Nozawa, Y. Katoh, A. Kohyama, and E. Lara-Cruzio, Proceedings of the Fifth IEA Workshop on SiC/SiC Ceramic Composites for Fusion Energy Application, International Energy Agency (2002) 74–86.
[31] T. Nozawa, T. Hinoki, Y. Katoh, A. Kohyama, and E. Lara-Cruzio, Small Specimens Test Techniques: Fourth Volume [ASTM STP 1418, M. A. Sokolov, J. D. Landes, and G. E. Lucas (eds.), ASTM International, West Conshohocken, PA, 2002] 294–305.
[32] K. Hironaka, T. Nozawa, T. Hinoki, N. Igawa, Y. Katoh, L. L. Snead, and A. Kohyama, J. Nucl. Mater. 307–311 (2002) 1093–1097.
[33] Y. Katoh, T. Nozawa, and L. L. Snead, Mechanical Properties of Thin PyC Interphase SiC-Matrix Composites Reinforced with Near-Stoichiometric SiC Fibers (submitted to Journal of the American Ceramic Society).
[34] A. G. Evans, J.-M. Domergue, and E. Vagaggini, J. Am. Ceram. Soc. 77 (1994) 1425–1435.

[35] W. A. Curtin, J. Am. Ceram. Soc. 74 (1991) 2837–45.
[36] S. Zhu, M. Mizuno, Y. Kagawa, and Y. Mutoh, Compos. Sci. Technol. 59 (1999) 833–851.
[37] J. J. Mecholsky, S. W. Freiman, and R. W. Rice, J. Mater. Sci. 11 (1976) 1310–19.
[38] M. D. Thouless, O. Svaizero, L. S. Sigl, and A. G. Evans, J. Am. Ceram. Soc. 72 (1989) 525–532.
[39] J-M. Domergue, E. Vagaggini, and A. G. Evans, J. Am. Ceram. Soc. 78 (1995) 2721–31.
[40] J. W. Hutchinson and H. M. Jensen, Mech. Mater. 9 (1990) 139–163.
[41] E. Vagaggini, J-M. Domergue, and A. G. Evans, J. Am. Ceram. Soc. 78 (1995) 2709–20.
[42] R. A. Lowden, Characterization and Control of the Fiber-Matrix Interface in Ceramic Matrix Composites, ORNL/TM-11039, Oak Ridge National Laboratory (1989).

3.0 FERRITIC/MARTENSITIC STEELS AND ODS STEELS

REDUCED-ACTIVATION BAINITIC AND MARTENSITIC STEELS FOR NUCLEAR FUSION APPLICATIONS—R. L. Klueh (Oak Ridge National Laboratory)*

OBJECTIVE

Since the mid 1980s, research programs have been in progress in Europe, Japan, and the United States to develop reduced-activation steels for fusion applications. This report reviews the recent work in the development of those steels.

SUMMARY

Reduced-activation steels were developed to enhance safety and reduce adverse environmental effects of future fusion power plants. Martensitic and bainitic steels were developed during the 1985–90 timeframe, and the feasibility of their use for fusion was investigated in an international collaboration from 1994 to present. Work continues to improve the steels and understand the effect of neutron irradiation on them.

Introduction

Development programs for materials for future fusion power reactors are being carried out in Japan, the European Union, and the United States. Possible structural materials for the reactor chamber first wall and blanket structure are limited, because the material will operate at elevated temperatures while being exposed to a flux of high-energy neutrons. Ferritic steels were first considered for fusion in the late 1970s, and the first steels considered were commercial 9–12%Cr martensitic steels and 2.25% Cr bainitic steels (all compositions are in wt %) [1].

Beginning in the mid-1980s, fusion reactor materials research programs throughout the world began developing “low-activation” structural materials [2–21]. Low-activation materials were defined as materials that during irradiation would either not activate or any induced radioactivity caused by transmutation of elements in the material by interaction with high-energy (14 MeV) neutrons from the deuterium-tritium fusion reaction would decay rapidly to allow safe operation and hands-on reactor maintenance [2,3]. True low-activation structural materials were not feasible, and “reduced-activation” steels were proposed that would not contain elements that would result in long-lived, transmutation-produced, radioactive elements. This would allow for safer and more economical disposal of radioactive reactor components after service exposure. Radioactivity from reduced-activation steels should decay to low levels in ≈100 y, compared to thousands of years for some non-reduced-activation steels.

The conditions (temperatures, stresses, and environment) reduced-activation steels would be exposed to in an operating fusion reactor are not well established, although simplified design studies have been carried out to investigate various concepts [22]. Coolants for systems in which the ferritic and martensitic steels would be used include helium and liquid lead-lithium (Pb-Li) eutectic alloy. As with all power-generation systems, designers push for high temperatures for increased efficiency. Operating stresses for systems where the steels are generally considered candidates are around 50 MPa, perhaps slightly higher for helium-cooled systems and slightly lower for liquid-metal systems. Under these conditions, the upper operating temperature for the ferritic/martensitic steels would be similar to those of conventional power plants when creep is limiting, about 550–600ºC. Oxidation in the helium system should not be a limiting factor, since oxygen impurities in the helium should be controllable to very low levels. Liquid-metal corrosion by Pb-Li coolant could reduce the upper temperature limit to about 450ºC if the liquid is in direct contact with the steel [23]. Insulating coatings on the exposed steel are proposed to suppress magnetohydrodynamic effects due to the flowing liquid [23]. One proposed design uses silicon-carbide inserts to isolate the steel from the liquid Pb-Li, thus increasing the upper operating temperature back to where creep limits the design stress (550–600ºC) [22].

---

*This contribution is to appear in *Current Opinion in Solid State and Materials Science* 8 (2004) 239.

The other important environmental condition in a fusion reactor is irradiation. Because of its importance for evaluating steels for fusion, this subject will be discussed in some detail prior to the detailed discussion of the development of martensitic and bainitic reduced-activation steels for fusion applications.

Irradiation Effects on Ferritic/martensitic Steels

High-energy neutron irradiation in a fusion reactor displaces atoms from their normal matrix positions to form vacancies and interstitials. It is the disposition of the "displacement damage," measured as displacements per atom (dpa), that affects mechanical properties. The progressive change in microstructure of ferritic steels with irradiation dose and temperature involves the agglomeration of vacancies and interstitials into voids and dislocation loops that cause swelling. Loop size increases and loop number density decreases with increasing temperature, eventually becoming unstable around 400–450ºC [1, 24–28]. In ferritic/martensitic steels, agglomeration of vacancies can lead to void swelling up to about 500ºC.

Ferritic steels became of interest because they are low swelling compared to conventional austenitic stainless steels when irradiated in a fast reactor. Besides swelling, the production of vacancies during irradiation can accelerate recovery and precipitation processes (e.g., coarsening) and induce non-equilibrium phases, which can affect properties [1,24–26,28,29].

Transmutation reactions of neutrons with metal atoms produce a new atom (usually another metal atom) with a smaller atomic number and a gas atom—helium or hydrogen. The small numbers of new non-gaseous atoms that form are generally thought not to affect properties, although these atoms are the source of radioactivity that provided impetus for the development of "low-activation" materials. The effect of hydrogen was generally thought to be minimal, because most of it was expected to migrate out of the lattice at reactor operating temperatures. However, recent ion [30] and proton [31] irradiations have produced evidence for retention of considerable amounts of the hydrogen in austenitic stainless steel and martensitic steel, respectively. Recent neutronic calculations, dosimetry analysis, and gas measurements for proton-irradiated martensitic steels suggested that hydrogen effects should not be an issue above 250ºC [32]. Indications are that helium can affect swelling [25], and this will be discussed below. This is important for a fusion reactor, where high helium concentrations will be produced, although ferritic steels will still remain low swelling relative to austenitic stainless steels.

The effect of irradiation on tensile behavior of the 7–12% Cr ferritic/martensitic steels depends on temperature [33–36]. Hardening caused by irradiation-induced dislocation loops and precipitate changes occurs at irradiation temperatures up to 425–450ºC. It is measured as an increase in yield stress and ultimate tensile strength (Fig. 1) and a decrease in ductility [34]. Hardening saturates with increasing fluence, and saturation occurs by 10 dpa [35]. For irradiation above 425–450ºC, properties are generally unchanged (Fig. 1), but there may be radiation-enhanced softening, depending on fluence [34,35].

Irradiation hardening affects other properties, such as fatigue and toughness, with the latter of greatest concern. The effect on toughness is observed in Charpy impact tests as an increase in ductile-brittle transition temperature (DBTT) and a decrease in upper-shelf energy (USE) [37–42] (Fig. 2). The shift in DBTT varies inversely with irradiation temperature and saturates with neutron fluence for irradiation in a fast reactor, where little helium forms (indicated in Fig. 2, which shows the same shift in DBTT after 10 and 17 dpa). Saturation may not occur under conditions where high-helium concentrations form, as discussed below.

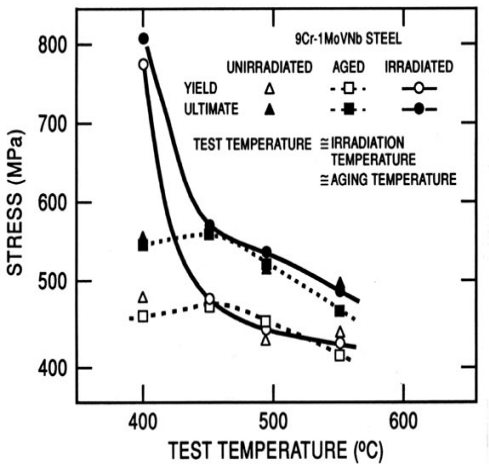

Fig. 1. Yield stress and ultimate tensile strength of normalized-and-tempered, thermally aged, and irradiated modified 9Cr-1Mo (9Cr-1MoVNb) steel. Irradiation was in Experimental Breeder Reactor (EBR-II) to 9 dpa [34].

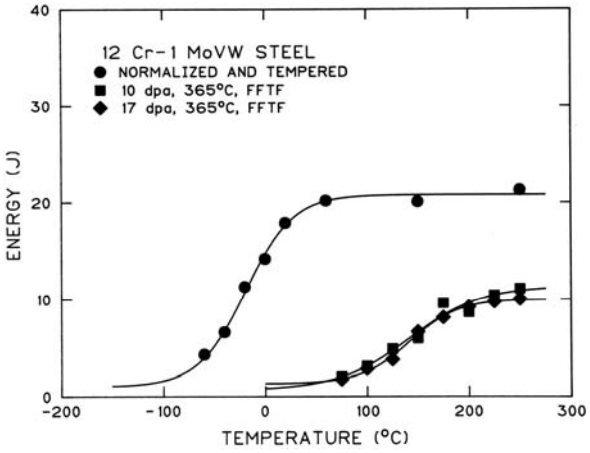

Fig. 2. Charpy curves for half-size specimens of Sandvik HT9 (12Cr-1MoVW) steel before and after irradiation to 10 and 17 dpa at 365ºC in the Fast Flux Test Facility FFTF [35].

Reduced-activation Steels

Martensitic Steels

For steels to meet reduced-activation criteria, calculations indicated that the typical steel-alloying elements Mo, Nb, Ni, Cu, and N must be eliminated or minimized [1–3]. Proposals for reduced-activation ferritic steels involved the replacement of molybdenum in conventional Cr-Mo steels by tungsten [4,6–10] and/or vanadium [7,11]. Niobium was replaced by tantalum.

Research programs in the 1980s in Japan, European Union, and United States developed 7–12% Cr-V and Cr-W-V reduced-activation steels [4–15] to which tantalum are sometimes added as a replacement for niobium [5,7–9,15]. Steels with 7–9% Cr were emphasized over 12% Cr, because of the difficulty of eliminating δ-ferrite in 12% Cr steels without increasing carbon or manganese for austenite stabilization. Nickel is usually used for austenite stabilization (instead of manganese), but it was prohibited by the reduced-activation criteria. Delta-ferrite can lower toughness, and manganese promotes chi-phase precipitation during irradiation, which causes embrittlement [11].

In Japan, nominally Fe-7.5Cr-2.0W-0.2V-0.04Ta-0.10C (F82H) [8,16,17] and Fe-9Cr-2W-0.2V-0.07Ta-0.05N-0.10C (JLF-1) [14,18,19] steels were chosen, and in Europe, an Fe-9.3Cr-1.0W-0.25V-0.04Cu-0.10C (OPTIFER Ia) and Fe-9.4Cr-1.1Ge-0.30V-0.13C (OPTIFER II) were originally chosen and investigated [13,20]. The steel with the best properties in the United States was ORNL 9Cr-2WVTa steel [10,15,21].

Reduced-activation 7–12% Cr steels were patterned after commercial 9–12% Cr steels with the objective that they have properties as good or better than the commercial steels they were to replace. They had microstructures similar to the commercial steels, as seen in Fig. 3, where the ORNL 9Cr-2WVTa steel is compared with modified 9Cr-1Mo steel after which it was patterned [1]. The microstructures consist of tempered martensite, and the predominant precipitates are fairly large $M_{23}C_6$ carbides on prior-austenite grain boundaries and martensite lath (subgrain) boundaries with a few small MX precipitates in the matrix.

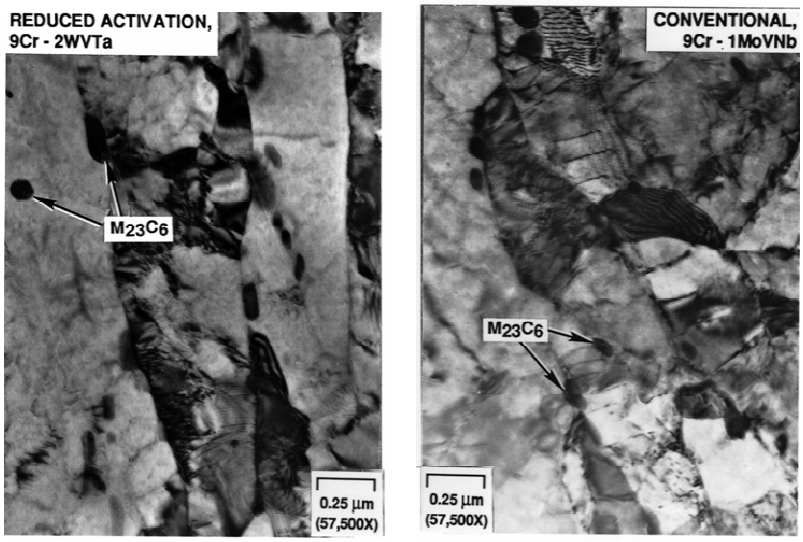

Fig. 3. Electron micrographs of normalized-and-tempered reduced-activation 9Cr-2WVTa and conventional 9Cr-1MoVNb steels [1].

Although all 7–12% Cr conventional and reduced-activation steels irradiated to high displacement damage (>100 dpa) demonstrate the effect of irradiation on toughness (Fig. 2), there are differences among steels, as shown in Fig. 4, where shifts in DBTT for Sandvik HT9 (Fe-12Cr-1Mo-0.5W-0.5Ni-0.25V-0.1C) and ORNL 9Cr-2WVTa are compared after irradiation in a fast reactor at 365ºC [1]. The reduced-activation steel developed much less shift (10ºC vs. 125ºC). Part of this difference was attributed to the larger carbon concentration in HT9 (0.2%) than in 9Cr-2WVTa (0.1%). Modified 9Cr-1Mo has a DBTT shift about half as large as HT9 for similar test conditions, which is still more than twice that for 9Cr-2WVTa. In this case, carbon cannot explain the difference, since these two steels have similar amounts of carbon. The tantalum in 9Cr-2WVTa was shown to have a favorable effect that could be used to explain the difference in these two steels [43].

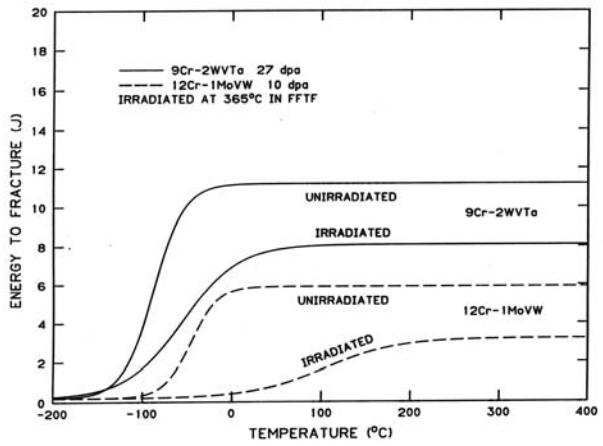

Fig. 4. Comparison of Charpy impact curves for one-third-size specimens of unirradiated and irradiated of HT9 (12Cr-1MoVW) and ORNL 9Cr-2WVTa steels irradiated in FFTF at 365ºC [1].

At an International Energy Agency (IEA) "Workshop for Ferritic/Martensitic Steels for Fusion" in 1992, a proposal was made for an international collaboration to determine the feasibility of using ferritic steels for fusion. The Japanese delegation at the meeting proposed making available large heats of reduced-activation steel for collaboration between Japan, Europe, and the United States under IEA auspices. A modified F82H composition was determined, and two 5-ton heats of this F82H-IEA (Fe-7.5Cr-2W-0.2V-0.04Ta-0.1C) steel were produced by the Japan Atomic Energy Research Institute (JAERI) and NKK Corporation.

Testing of the large heats of F82H-IEA to determine the unirradiated properties was completed during the last two years [44,45]. Physical properties (density, specific heat, thermal expansion, thermal conductivity, Young's modulus, modulus of rigidity, Poisson's ratio, and magnetic hysteresis) and mechanical properties (tensile, creep, Charpy impact, fracture toughness, isothermal fatigue, thermal fatigue, and low-cycle fatigue) were obtained. A computerized database on base metal and welds was developed that is available to the international community on the internet [46].

Besides determining baseline data, F82H-IEA specimens were included in over twenty neutron-irradiation experiments conducted in the High Flux Isotope Reactor (HFIR) in the U.S., in the Japan Research Reactor (JRR-4) and the Japan Materials Test Reactor (JMTR), and the High Flux Reactor (HFR) in The Netherlands. Results were in general agreement with results for other experimental 7–9Cr-WV-type reduced-activation steels that show improved irradiation resistance over conventional Cr-Mo steels [46].

Studies on irradiated F82H-IEA are continuing to determine irradiation effects on a range of properties for base metal and weldments. As discussed above, irradiation embrittlement causes an increase in DBTT in a Charpy test. Charpy data cannot be used for design. Instead, fracture toughness data are required, and such data for irradiated F82H were obtained [47]. In this work, six disk-compact tension [DC(T)] specimens were irradiated in HFIR to ≈3.8 dpa at two temperatures. Three of the specimens in the low-temperature capsule were at an average of 261°C and another three at 240°C. In the high-temperature capsule, all six specimens were irradiated at an average temperature of 377°C. Fracture-toughness-transition temperatures were evaluated, and the master curve concept was used to evaluate the shift of the fracture toughness transition temperature. Specimens irradiated at the higher temperature exhibited a relatively modest shift of about 40°C. However, the shift of fracture-toughness-transition temperature of specimens irradiated below 300°C was much larger—about 180°C. This shift is in general agreement with the DBTT shift observed for F82H Charpy specimens irradiated in HFIR at 300ºC [48].

Reduced-activation steel development began with small experimental heats to determine compositions with mechanical properties as good or better than the Cr-Mo steels they were to replace. Once that was achieved, the large heats of F82H-IEA were used to establish the feasibility of using the steels for fusion. The next step was to use what was learned to produce advanced steels, and the European Union fusion program has taken that step and produced a 3.5-ton heat of a new steel designated EUROFER 97 [49].

Nominal target chemistry for EUROFER (Fe-9.0Cr-1.1W-0.2V-0.07Ta-0.03N-0.11C) differed from that of F82H-IEA (Fe-8.0Cr-2.0W-0.2V-0.04Ta-0.10C). Actual compositions differed from the target composition, and F82H contained less Cr (7.5%), Ta (0.023%), and V (0.14%) than the target composition; the EUROFER contained more tantalum (0.14%) than the target composition [50]. Therefore, major differences in the steels are the Cr, W, and Ta compositions. Lower tungsten was used in the EUROFER specification (1% vs. 2% for F82H) because the tritium breeding rate is higher for the lower tungsten. A higher breeding rate was considered necessary for the reactor design being considered in the European program at the time the steel was ordered. Lower tungsten will also reduce the amount of Laves phase formed relative to steels with higher tungsten. Despite differences in composition, the two steels had similar microstructures and tensile, impact, and creep properties [50–52]. Data on impact properties indicated that the EUROFER has a lower DBTT and a similar to slightly lower USE [50–52].

In addition to studies to determine displacement damage effects, effect of the simultaneous production of displacement damage and transmutation helium in a fusion reactor first wall on swelling and mechanical

properties has been a source of uncertainty, and the subject continues to receive attention. In the absence of a 14 MeV (energy of neutrons from the deuterium-tritium reaction) neutron source, simulation experiments using ion implantation [53], boron-doping [54–58], and nickel-doping [42,59] have been used.

Recent results with boron doping indicated increased swelling due to helium [55,56] when F82H specimens with ≈30 and ≈60 ppm natural boron and ≈65 ppm ^{10}B were irradiated in HFIR at 400ºC up to 52 dpa to produce ≈30, ≈60, and ≈330 appm He, respectively (Fig. 5). Helium is produced by an (n,α) reaction where α is an α-particle (^{4}He). The reaction is:

$$^{10}B + n \rightarrow {}^{4}He + {}^{7}Li \qquad (1)$$

where n is the neutron (fast or thermal†). Natural boron contains ≈20% ^{10}B.

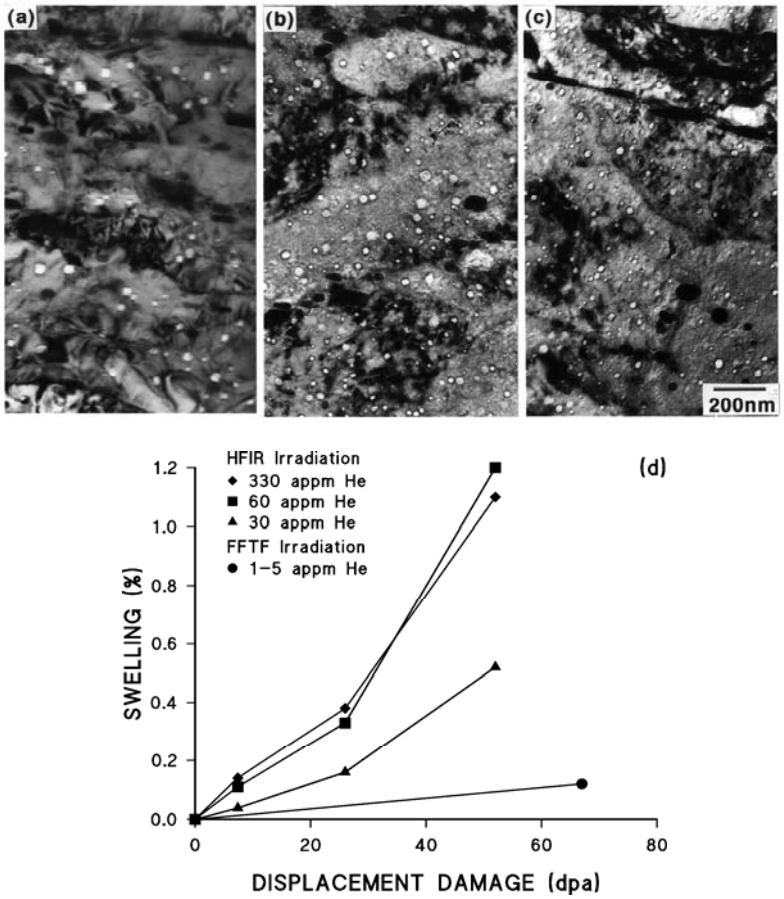

Fig. 5. Cavities in normalized-and-tempered F82H with different boron levels irradiated to 52 dpa in HFIR at 400ºC to produce (a) 30, (b) 60, and (c) 330 appm He. (d) Swelling as a function of displacement damage for the different helium levels for irradiation in HFIR compared to irradiation in the Fast Flux Test Facility (FFTF), where little helium was formed [55].

---

†A thermal neutron is a free neutron with kinetic energy <0.025 eV (≈4.0×10^{-21} J)—the average kinetic energy of a room-temperature gas. A fast neutron is a free neutron with kinetic energy >1MeV. Fast neutrons are produced by nuclear processes such as nuclear fission and fusion.

Cavity size, number density, and swelling after 52 dpa for the three steels were respectively 12.7 nm, 6.1×10^{20} m^{-3}, and 0.52%; 10.6 nm, 2.4×10^{21} m^{-3}, and 1.2%; and 7.6 nm, 6.1×10^{21} m^{-3}, and 1.1%. Swelling of 1.2 and 1.1% after only 52 dpa for the steels with 60 and 330 appm He, respectively, is much larger than generally expected for these steels. The higher number density of smaller cavities for the steel with 330 appm He than the steel with only 60 appm He evidently suppressed swelling by acting as neutral sinks for vacancies and interstitials compared to the lower number density of larger cavities in the steel with 60 appm He. Most previous high-dose data that showed low swelling came from fast reactor irradiation (little helium generated), and as seen in Fig. 5(d), the swelling of F82H irradiated in the Fast Flux Test Facility (FFTF) to 67 dpa (<5 appm He) was about an order of magnitude less (0.12%) [60].

All simulation techniques have problems. Boron, for example, is a reactive element that can be associated with precipitates and prior austenite grain boundaries; also, lithium from the transmutation of ^{10}B could cause problems. Furthermore, during fission reactor irradiation, all the boron is quickly transformed into helium, which differs from what happens in a fusion reactor, where helium forms simultaneously and more gradually with the displacement damage.

When nickel-doped steels are irradiated in a mixed-spectrum reactor such as HFIR, displacement damage and helium form simultaneously. Helium forms by a two-step (n,α) reaction of ^{58}Ni with thermal neutrons in the mixed spectrum: displacement damage forms from fast neutrons in the spectrum [1]. The reactions are:

$$^{58}Ni + n \rightarrow {}^{59}Ni + \gamma \qquad (2)$$

$$^{59}Ni + n \rightarrow {}^{56}Ni + {}^{4}He \qquad (3)$$

where γ is a gamma ray. This technique also has problems [61]. In recent work, a 9Cr-2W reduced-activation steel with and without 1% Ni was irradiated to 2.2 and 3.8 dpa at 270 and 348ºC, respectively, in the Advanced Test Reactor (ATR), a fast reactor where little helium forms.‡ The nickel-containing steel hardened about 20% more than the steel without nickel at 270ºC, but strengths were similar after irradiation at 348ºC [61]. Likewise, there was a larger shift in DBTT for the nickel-containing steel than the one without nickel when irradiated at 270ºC, but not after irradiation at 348ºC. TEM analysis indicated nickel refined the size of defect clusters, which were more numerous in the nickel-containing steel [61].

These results indicated that nickel doping should be used with caution below ≈300ºC. Results with nickel doping that most strongly indicated helium caused an increase in DBTT above that caused by displacement damage alone and without a saturation with fluence were high-dose tests at 400ºC [40]. Tensile tests of specimens irradiated in a fast reactor gave no indication of hardening due to helium (or nickel). TEM studies of nickel-doped steels irradiated in HFIR and FFTF showed a high density of M_6C formed in the nickel-doped steel but not in the undoped steel [25]. Since the DBTT shift in HFIR, where helium forms, was larger than in FFTF, where little helium forms, the results indicated that helium caused the shift [42,59].

---

‡A fast reactor neutron spectrum does not contain a significant number of thermal neutrons relative to a mixed-spectrum reactor, which contains both fast and thermal neutrons, nor does it contain the high-energy 14.1 MeV neutrons of a fusion spectrum. The average creation energy of neutrons in a fast reactor is about 2 MeV, and the energy spectrum contains neutrons mainly in the range above about 10 keV. Little transmutation helium is produced in ferritic steels by neutrons in that energy range.

Another method used recently to study helium effects is irradiation with 600–750 MeV protons in PIREX (Proton Irradiation Experiment) and SINQ (Swiss Spallation Neutron Source) at the Paul Scherrer Institute in Switzerland [62,63]. Microstructural observations indicated that during the simultaneous production of displacement damage and helium, helium is distributed in the pre-existing cavities produced by displacement damage [62]. Therefore, helium does not produce hardening above that due to displacement damage alone. Finally, irradiation in SINQ of Charpy specimens of F82H, modified 9Cr-1Mo, and OPTIFER produced an increase in DBTT that had a linear dependence on helium concentration up to 600 appm He, demonstrating the importance of helium on embrittlement [63]. For the irradiation conditions examined, there was no indication of saturation with dose.

These recent results on helium effects on swelling [57,58,62] and toughness [63] of reduced-activation steels are disturbing, given the large amount of helium that will form in a fusion reactor first wall. Furthermore, the observations agrees with those in nickel- [42,59] and boron-doping [56] experiments that indicated increased swelling with increased helium and an increase in DBTT with increased helium above that observed by displacement damage alone with no increase in strength attributable to helium. More work on helium effects is required to validate the ferritic/martensitic steels for fusion applications.

Bainitic Steels

Although reduced-activation 7–9% Cr martensitic steels were eventually chosen for further development, low-chromium bainitic steels were also studied [4, 5,11,14,15] during the original development phase. Steel development programs in the United States and Japan examined chromium concentrations over the range 2.25 to 12% [11,14,15]. An Fe- 2.25Cr-2.0W-0.25V-0.07Ta-0.1C (2¼Cr-2WVTa) steel had a higher strength than the ORNL 9Cr-2WVTa steel for similar heat treatment conditions [21], but the 9Cr-2WVTa steel had better toughness [37]. Similar results were obtained in Japan [14]. In this case, irradiation in the JMTR resulted in essentially no shift in DBTT for the 2.25Cr steel compared to a shift of 22ºC for the 9Cr steels. However, the 9Cr steels still had the lowest DBTT after irradiation because of the lower value before irradiation [14].

The Oak Ridge National Laboratory (ORNL) reduced-activation steel development program was the only one that pursued bainitic steels beyond the first iteration [64,65]. Prior to work on reduced-activation steels, work at ORNL demonstrated that quenched-and-tempered plates of an Fe-3Cr-1.5Mo-0.25V-0.1C steel unexpectedly had better Charpy properties than normalized (air-cooled)-and-tempered plates [66]. Different tempered bainitic microstructures were observed (Fig. 6), and they were related to microstructures observed by Habraken and Economopoulos (H&E) [67], who found morphological variations in the bainite transformation products that differed from classical upper and lower bainite, although they formed in the bainite transformation temperature regime.

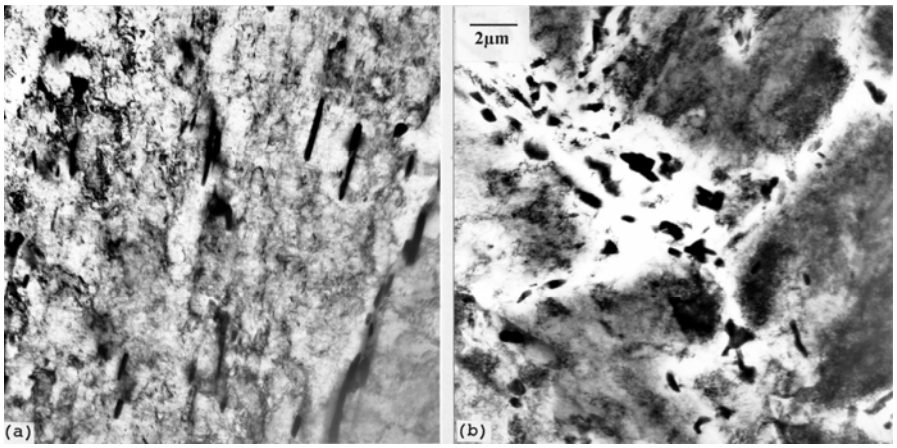

Fig. 6. Microstructures of (a) quenched-and-tempered and (b) normalized-and-tempered 3Cr-1.5MoV steel [64].

The bainite transformation region of an isothermal-transformation diagram (≈250–550ºC) can be divided into two temperature regimes by a horizontal line, above which upper bainite forms and below which lower bainite forms. For the non-classical bainites that formed during continuous cooling, H&E showed that a continuous cooling transformation diagram could be divided into three vertical regimes (Fig. 7). A steel cooled through zone I produced a “carbide-free acicular” structure, consisting of side-by-side plates or laths. When cooled through zone II, a carbide-free "massive or granular” structure resulted, referred to as granular bainite. It was determined that granular bainite consists of a bainitic ferrite matrix with a high dislocation density containing martensite-austenite (M-A) “islands” enriched in carbon during formation of the bainite [67]. Microstructures formed in zone III are not relevant to this discussion.

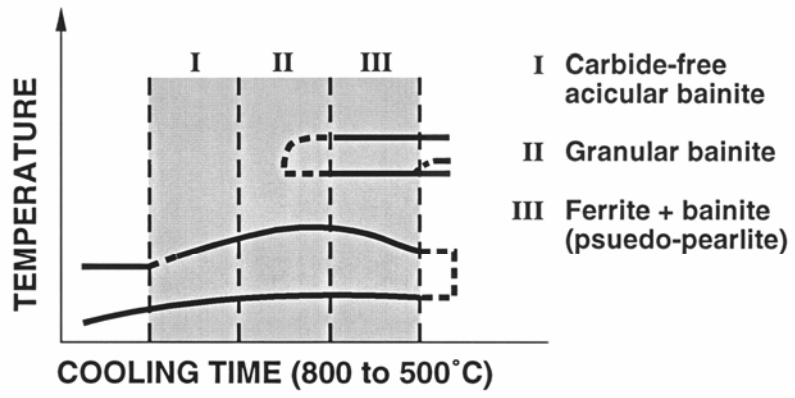

Fig. 7. Schematic representation from Habraken and Economopoulos of a continuous-cooling transformation diagram with cooling zones for the formation of three morphological variations of bainite during continuous cooling.

The microstructure of slowly cooled reduced-activation 2¼Cr-2WVTa [Fig. 8(a)] steel was characteristic of granular bainite; the dark areas are the M-A islands. The microstructure of the specimen cooled rapidly [Fig. 8(b)] was characteristic of carbide-free acicular bainite, as defined by H&E [67]. When granular bainite is tempered, large globular carbides form in the high-carbon M-A islands [Fig. 6(b)], whereas elongated carbides form on lath boundaries of acicular bainite [Fig. 6(a)] [65]. It is these different carbide microstructures that give rise to the different Charpy properties (the globular carbides of the normalized-and-tempered steel lower the toughness relative to the quenched-and-tempered steel) [66].

If the understanding of the effects of cooling rate on microstructure is correct, then toughness of the bainitic steels could be improved by cooling rapidly—quenching instead of normalizing (air cooling). It was reasoned, therefore, that another possibility to promote carbide-free acicular bainite is by improving hardenability [65]. Hardenability is the relative ability of a steel to avoid forming the soft ferrite phase when cooled from the austenitizing temperature. Increasing hardenability has the same relative effect as increasing the cooling rate: it moves the transformation of ferrite to longer times so the steel can be cooled more slowly and still obtain bainite. This should also move the zone for the formation of acicular bainite to longer times and allow it to form at slower cooling rates.

Hardenability can be altered by changing chemical composition, and based on the 2¼Cr-2WVTa having excellent tensile properties but reduced toughness after normalizing and tempering, the composition was varied to demonstrate how the properties could be improved based on the above reasoning [65]. This

eventually led to two nominal compositions that have been investigated in some detail: Fe-3.0Cr-3.0W-0.50Mn-0.25Si-0.25%V (3Cr-3WV) and this composition with 0.1% Ta (3Cr-3WVTa).

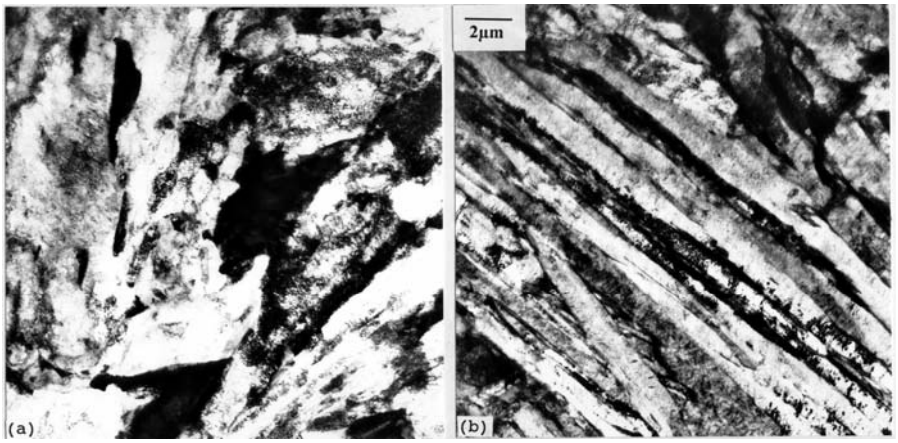

Fig. 8. Microstructure of a 2¼Cr-2WVTa steel after (a) a slow cool to develop granular bainite and after (b) a fast cool to produce carbide-free acicular bainite.

The 3Cr-3WV and 3Cr-3WVTa steels have strengths from room temperature to 600ºC that exceed those of the advanced commercial 2.25Cr steels T23 (Fe-2.25Cr-1.6W-0.25V-0.05Nb-0.07C) and T24 (Fe-2.25Cr-1.0Mo-0.25V-0.07Ti-0.005B-0.07C). The 3Cr-3WVTa also has strength approaching and exceeding that of some of the high-chromium steels such as F82H and modified 9Cr-1Mo. A similar advantage is exhibited during creep at 600ºC [Fig. 9(a)]. Creep tests at 650ºC [Fig. 9(b)] showed that the 3Cr-3WVTa steel has properties comparable to modified 9Cr-1Mo (T91) (no data were available for T23 at this temperature).

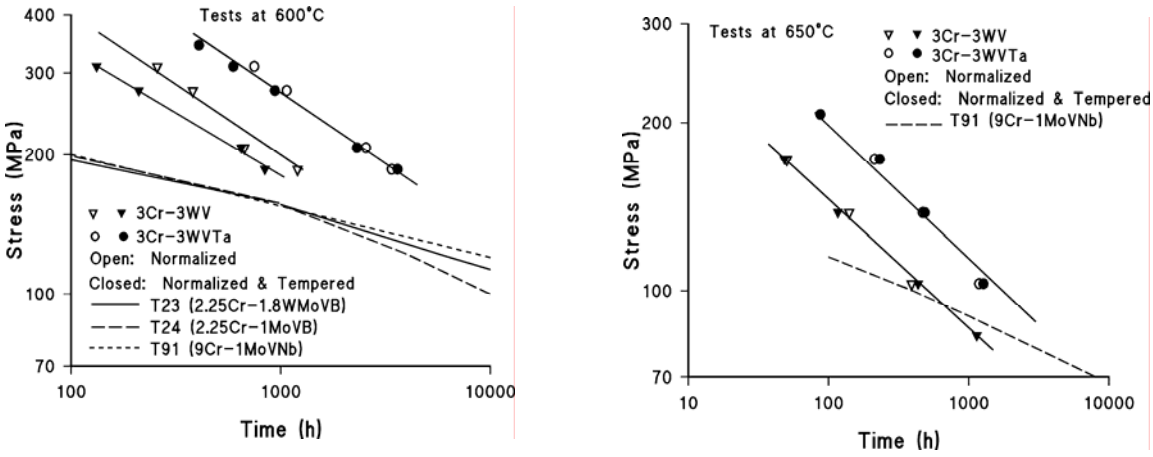

Fig. 9. Creep-rupture curves for 3Cr-3WV and 3Cr-3WVTa steels in the normalized and normalized-and-tempered conditions (a) at 600ºC compared to T23 (2.25Cr-1.6WVNb), T24 (2.25Cr-1MoVTi), and modified 9Cr-1Mo (9Cr-1MoVNb) steels and (b) at 650ºC compared to modified 9Cr-1Mo steel.

Elevated-temperature strength in these steels is obtained from a bainitic microstructure with a high number density of fine MX precipitates in the matrix (Fig. 10). Both the 3Cr-3WV and 3Cr-3WVTa steels contain needle-like precipitates, but the precipitates are considerably finer in the latter steel, indicating an

effect of the tantalum. Indications are that during creep, coarsening of these fine matrix precipitates is more rapid in the steel without tantalum.

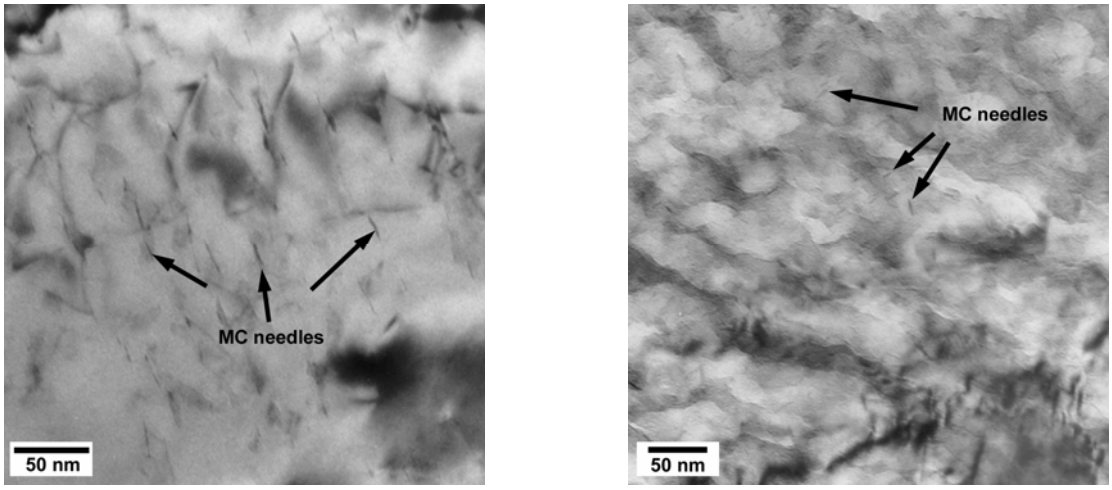

Fig. 10. Photomicrographs of (a) 3Cr-3WV and (b) 3Cr-3WVTa steels showing the fine needle precipitates that provide creep strength.

Conclusions

Reduced-activation steels for fusion applications were developed as replacements for conventional steels for reduced radioactivity for waste disposal after service. New 7–9% Cr martensitic steels with molybdenum replaced by tungsten and niobium replaced by tantalum were developed with microstructures and properties equivalent to or better than the conventional steels they replaced. Emphasis was on 7–9% Cr martensitic steels because 9–12% Cr conventional Cr-Mo steels had been considered primary candidate materials for fusion prior to the development of reduced-activation steels.

Although 2–3% Cr bainitic steels were studied in the early stages of the development program, with one exception, they were abandoned for high-chromium steels. A nominally Fe-3.0Cr-3.0W-0.25V-0.10Ta-0.10C bainitic steel was developed with excellent high-temperature strength. Depending on the design temperatures for fusion reactors, a low-chromium steel could offer advantages, especially for fabrication of the complicated structures envisioned. Low-chromium steels are more easily welded, since the welds and heat-affected zones will not contain hard and brittle martensite.

Reactor designers may push to higher operating temperatures for increased efficiency. The original conventional steels (e.g., modified 9Cr-1Mo) considered were developed for fossil-fired power plants with a maximum operating temperature of 550-600ºC. Reduced-activation steels were patterned after these steels and generally have creep and tensile properties similar to modified 9Cr-1Mo. In recent years, improved conventional steels for fossil-fired plants have been developed with maximum temperatures of 600-630ºC [68]. Therefore, methods used to improve the conventional steels need to be examined to determine if similar improvements can be made in reduced-activation steels.

In addition to the elevated-temperature requirements, steels for fusion also require resistance to high-energy neutron irradiation. Martensitic and bainitic steels appear sufficiently resistant to radiation damage in the absence of large amounts of helium. Because high-energy neutrons produced by the fusion reaction will also produce large amounts of transmutation helium, it is important to understand the effect of simultaneous helium and displacement damage production in a steel reactor first wall. There are

indications that helium can affect toughness of martensitic and bainitic steels, and more work is required to understand that potential problem.

References

[1] R. L. Klueh and D. R. Harries, High-chromium ferritic and martensitic steels for nuclear applications, American Society for Testing and Materials, West Conshohocken, Pa. (2002).
[2] R. W. Conn, E. E. Bloom, J. W. Davis, R. E. Gold, R. Little, K. R. Schultz, D. L. Smith, and F. W. Wiffen, Report on Low Activation Materials for Fusion Applications, Nucl. Technol./Fusion 5 (1984) 291–310.
[3] G. W. Butterworth and O. N. Jarvis, Comparison of transmutation and activation effects in five ferritic alloys and AISI 316 stainless steel, J. Nucl. Mater. 122&123 (1984) 982–988.
[4] N. M. Ghoniem, A. Shabaik, and M. Z. Youssef, Development of low activation vanadium steel for fusion applications, In J. W. Davis and D. J. Michel (eds.), Proceedings of Topical Conference for Ferritic Steels for Use in Nuclear Energy Technologies, The Metallurgical Society of AIME, Warrendale, Pa. (1984) 201–208.
[5] R. L. Klueh and E. E. Bloom, The development of ferritic steels for fast induced-radioactivity decay for fusion reactor applications, Nucl. Eng. Des./Fusion 2 (1985) 383–389.
[6] D. S. Gelles, Optimization of martensitic stainless steels for nuclear reactor applications, In F. A. Garner, D. S. Gelles, and F. W. Wiffen (eds.), Optimizing Materials for Nuclear Applications, The Metallurgical Society of AIME, Warrendale, Pa. (1985) 63–71.
[7] D. Dulieu, K. W. Tupholme, and G. J. Butterworth, Development of low-activation martensitic stainless steels, J. Nucl. Mater. 141–143 (1986) 1097–1101.
[8] M. Tamura, H. Hayakawa, M. Tanimura, A. Hishinuma, and T. Kondo, Development of potential low activation ferritic and austenitic steels, J. Nucl. Mater. 141–143 (1986) 1067–1073.
[9] T. Noda, F. Abe, H. Araki, and M. Okada, Development of low activation ferritic steels, J. Nucl. Mater. 141–143 (1986) 1102–1106.
[10] R. L. Klueh, D. S. Gelles, and T. A. Lechtenberg, Development of ferritic steels for reduced activation: The U.S. program, J. Nucl. Mater. 141–143 (1986) 1081–1087.
[11] D. S. Gelles, Effects of irradiation on low activation ferritic alloys: A review, In R. L. Klueh, D. S. Gelles, M. Okada, and N. H. Packan (eds.), Reduced Activation Materials for Fusion Reactors, ASTM STP 1047, Philadelphia: American Society for Testing and Materials (1990) 113–129.
[12] C. Y Hsu and T. A. Lechtenberg, Microstructure and mechanical properties of unirradiated low activation ferritic steel, J. Nucl. Mater. 141–143 (1986) 1107–1112.
[13] K. Anderko, K. Ehrlich, L. Schäfer, and M. Schirra, CETA-EinEntwicklungsschritt zu einem Schwach Activierbaren martensitischen Chromstahl, Kernforschungszentrum Karlsruhe, KfK Report 5060 (June 1993).
[14] H. Kayano, H. Kurishita, A. Kimura, M. Narui, M. Yamazaki, and Y. Suzuki, Charpy impact testing using miniature specimens and its application to the study of irradiation behavior of low-activation ferritic steels, J. Nucl. Mater. 179–181 (1991) 425–428.
[15] R. L. Klueh and P. J. Maziasz, Microstructure of Cr-W steels, Met. Trans. 20A (1989) 373–381.
[16] M. Tamura, H. Hayakawa, M. Tanimura, A. Hishinuma, and T. Kondo, Phase stability of reduced activation ferritic steel: 8%Cr-2%V-0.04%Ta-Fe, J. Nucl. Mater. 155–157 (1988) 620–625.
[17] M. Yamanouchi, M. Tamura, H. Hayakawa, A. Hishinuma, and T. Kondo, Accumulation of engineering data for practical use of reduced activation ferritic steel: 8%Cr-2%W-0.2%V-0.04%Ta-Fe, J. Nucl. Mater. 191–194 (1992) 822–826.
[18] F. Abe, T. Noda, H. Araki, and S. Nakazawa, Alloy composition selection for improving strength and toughness of reduced activation 9Cr-W steels, J. Nucl. Mater. 179–181 (1991) 663–666.
[19] A. Kohyama, Y. Kohno, K. Asakura, and H. Kayano, R&D of low activation ferritic steels for fusion in Japanese universities, J. Nucl. Mater. 212–215 (1994) 684–689.
[20] K. Ehrlich, S. Kelzenberg, H. D. Röhrig, L. Schäfer, and M. Schirra, The development of ferritic-martensitic steels with reduced long-term activation, J. Nucl. Mater. 212–215 (1994) 678–683.
[21] R. L. Klueh, Heat treatment behavior and tensile behavior of Cr-W steels, Met. Trans. 20A (1989) 463–469.

[22] M. S. Tillack, X. R. Wang, J. Pulsifer, S. Malang, and D. K. Sze, ARIES-ST breeding blanket design and analysis, Fus. Eng. Des. 49–50 (2000) 689–695.
[23] H. U. Borgstedt, H. Glasbrenner, and Z. Peric, Corrosion of insulating layers on MANET steel in flowing Pb-Li, J. Nucl. Mater. 212–215 (1994) 1501–1503.
[24] V. S. Agueev, V. N. Bykov, A. M. Dvoryashin, V. N. Golovanov, E. A. Medvendeva, V. V. Romaneev, V. K. Sharmardin, and A. N. Vorobiev, Influence of structure and phase composition on 1Cr13Mo2NbVB steel mechanical properties in initial, aged, and irradiated states, In N. E. Packan, R. E. Stoller, and A. S. Kumar (eds.), Effects of Radiation on Materials: 14th International Symposium, ASTM STP 1046, Vol. I, Philadelphia: American Society for Testing and Materials (1989) 98–113.
[25] P. J. Maziasz, R. L. Klueh, and J. M. Vitek, Helium effects on void formation in 9Cr-1MoVNb and 12Cr-1MoVW irradiated in HFIR, J. Nucl. Mater. 141–143 (1986) 929–937.
[26] J. J. Kai and R. L. Klueh, Microstructural analysis of neutron-irradiated martensitic steels, J. Nucl. Mater. 230 (1996) 116–123.
[27] D. S. Gelles, Microstructural development in reduced activation ferritic alloys irradiated to 200 dpa at 420ºC, J. Nucl. Mater. 212–215 (1994) 714–719.
[28] E. A. Little and L. P. Stoter, In H. R. Brager and J. S. Perrin (eds.), Effects of Irradiation on Materials: Eleventh Conference, ASTM STP 782, Philadelphia: American Society for Testing and Materials (1982) 207–233.
[29] D. S. Gelles and L. E. Thomas, Effects of neutron irradiation on microstructure in experimental and commercial ferritic alloys, In J. W. Davis and D. J. Michel (eds.), Proceedings of Topical Conference for Ferritic Steels for Use in Nuclear Energy Technologies, Warrendale, Pa.: The Metallurgical Society of AIME (1984) 559–567.
[30] J. D. Hunn, M. B. Lewis, and E. H. Lee, Hydrogen retention in ion-irradiated steels, In Second International Topical Meeting on Nuclear Applications of Accelerator Technology, La Grange Park, Ill.: American Nuclear Society (1998) 375–381.
[31] P. Marmy and B. M. Oliver, High strain fatigue properties of F82H ferritic-martensitic steel under proton irradiation, J. Nucl. Mater. 318 (2003) 132–142.
[32] Y. Dai, Y. Foucher, M. R. James, and B. M. Oliver, Neutronics calculation, dosimetry analysis and gas measurements of the first SINQ target irradiation experiment, STIP-I, J. Nucl. Mater. 318 (2003) 167–175.
[33] C. Wassilew, K. Herschbach, E. Materna-Morris, and K. Ehrlich, Irradiation behaviour of 12% Cr martensitic steels, In J. W. Davis and D. J. Michel (eds.), Proceedings of Topical Conference for Ferritic Steels for Use in Nuclear Energy Technologies, Warrendale, Pa.: The Metallurgical Society of AIME, (1984) 607–614.
[34] R. L. Klueh and J. M. Vitek, Elevated-temperature tensile properties of 9Cr-1MoVNb steel, J. Nucl. Mater. 132 (1985) 27–31.
[35] R. L. Klueh and J. M. Vitek, Tensile properties of 9Cr-1MoVNb and 12Cr-1MoVW steels irradiated to 23 dpa at 390 to 550ºC, J. Nucl. Mater. 182 (1991) 230–239.
[36] R. L. Klueh and J. M. Vitek, Fluence and helium effects on the tensile properties of ferritic steels at low temperatures, J. Nucl. Mater. 161 (1989) 13–23.
[37] R. L. Klueh and D. J. Alexander, Irradiation Effects on Impact Behavior of 12Cr-1MoVW and 2¼Cr-1Mo Steels, In R. E. Stoller, A. S. Kumar, and D. S. Gelles (eds.), Effects of Radiation on Materials: 15th International Symposium, ASTM STP 1125, Philadelphia: American Society for Testing and Materials, (1992) 1256–1266.
[38] W. L. Hu and D. S. Gelles, The ductile-to-brittle transition behavior of martensitic steels neutron irradiated to 26 dpa, In F. A. Garner, C. H. Henager, and N. Igata (eds.), Influence of Radiation on Material Properties: 13th International Symposium (Part II), ASTM STP 956, Philadelphia: American Society for Testing and Materials (1987) 83–97.
[39] V. K. Shamardin, A. M. Pecherin, O. M. Vishkarev, V. P. Borisov, and G. A. Tulyakov, Investigation of the radiation-induced embrittlement of chromium steels, In Proceedings of the International Conference on Radiation Materials Science, Alushta, USSR (1990) 3–11.
[40] R. L. Klueh and D. J. Alexander, Impact behavior of 9Cr-1MoVNb and 12Cr-1MoVW steels, J. Nucl. Mater. 179–181 (1991) 733–736.

[41] C. Wassilew and K. Ehrlich, Effect of neutron irradiation on the dynamic fracture toughness behaviour of the 12% Cr steel MANET-1 investigated using subsize V-notch specimens, J. Nucl. Mater. 191–194 (1992) 850–854.
[42] R. L. Klueh and D. J. Alexander, Effect of irradiation in HFIR on tensile properties of Cr-Mo steels, J. Nucl. Mater. 187 (1992) 60–69.
[43] R. L. Klueh, D. J. Alexander, and M. Rieth, The effect of tantalum on the mechanical properties of a 9Cr-2W-0.25V-0.07Ta-0.1C steel, J. Nucl. Mater. 273 (1999) 146–154.
[44] R. L. Klueh, D. S. Gelles, S. Jitsukawa, A. Kimura, G. R. Odette, B. van der Schaaf, and M. Victoria, Ferritic/martensitic steels—overview of recent results, J. Nucl. Mater. 307–311 (2002) 455–465.
[45] S. Jitsukawa, A. Kimura, A. Kohyama, R. L. Klueh, A. A. Tavassoli, B. Van der Schaaf, G. R. Odette, J. W. Rensman, M. Victoria, and C. Petersen, Recent results of the reduced activation ferritic/martensitic steel development, J. Nucl. Mater. 329–333 (2004) 243.
[46]] S. Jitsukawa, M. Tamura, B. van der Schaaf, R. L. Klueh, A. Alamo, C. Petersen, M. Schirra, P. Spaetig, G. R. Odette, A. A. Tavassoli, K. Shiba, A. Kimura, and A. Kohyama, Development of an extensive database of mechanical and physical properties for reduced-activation martensitic steel F82H, J. Nucl. Mater. 307–311 (2002) 179–186.
[47] M. A. Sokolov, R. L. Klueh, G. R. Odette, K. Shiba, and H. Tanigawa, Fracture toughness characterization of irradiated F82H in the transition region, In M. L. Grossbeck, T. R. Allen, R. G. Lott, and A. S. Kumar (eds.), Effects of Radiation on Material: 21st International Symposium, ASTM STP 1447, West Conshohocken, Pa.: ASTM International (2003) 408–418.
[48] R. L. Klueh, M. A. Sokolov, K. Shiba, Y. Miwa, and J. P. Robertson, Embrittlement of reduced-activation ferritic/martensitic steels irradiated in HFIR at 300ºC and 400ºC, J. Nucl. Mater. 283–287 (2000) 478–482.
[49] B. van der Schaaf, D. S. Gelles, S. Jitsukawa, A. Kimura, R. L. Klueh, A. Moslang, and G. R. Odette, Progress and critical issues of reduced activation ferritic/martensitic steel development, J. Nucl. Mater. 283–287 (2000) 52–59.
[50] Fusion Technology: Annual Report of the Association CEA/EURATOM (2000) 199–200.
[51] Nuclear Fusion Programme Annual Report of the Association Forschungszentrum Karlsruhe/EURATOM, October 1999–September 2000, Forschungszentrum Karlsruhe, FZKA 6550 and EUR 19707 EN (December 2000) 138–142.
[52] Fusion Technology: Annual Report of the Association, CEA/EURATOM (2000) 203–204.
[53] R. Lindau, A. Möslang, D. Preininger, M. Rieth, and H. D. Röhrig, Influence of helium on impact properties of reduced-activation ferritic/martensitic Cr-steels, J. Nucl. Mater. 271&272 (1999) 450–454.
[54] E. V. van Osch, M. G. Horsten, G. E. Lucas, and G. R. Odette, Mechanical properties of four 7-9%Cr reduced activation martensitic steels after 2.5 dpa, 300ºC irradiation, In M. L. Hamilton, A. S. Kumar, S. T. Rosinski, and M. L. Grossbeck (eds.), Effects of Irradiation on Materials: 19th International Symposium, ASTM STP 1366, West Conshohocken, Pa.: American Society for Testing and Materials (2000) 612–625.
[55] E. L. Materna-Morris, M. Rieth, and K. Ehrlich, Irradiation behavior of ferritic/martensitic 9-12%Cr steels, In M. L. Hamilton, A. S. Kumar, S. T. Rosinski, and M. L. Grossbeck (eds.), Effects of Irradiation on Materials: 19th International Symposium, ASTM STP 1366, West Conshohocken, Pa.: American Society for Testing and Materials (2000) 597–611.
[56] K. Shiba and A. Hishinuma, Low-temperature irradiation effects on tensile and Charpy properties of low-activation ferritic steels, J. Nucl. Mater. 283–287 (2000) 474–477.
[57] E. Wakai, N. Hashimoto, Y. Miwa, J. P. Robertson, R. L. Klueh, K. Shiba, and S. Jitsukawa, Effect of helium production on swelling of F82H irradiated in HFIR, J. Nucl. Mater. 283–287 (2000) 799–805.
[58] Y. Miwa, E. Wakai, K. Shiba, N. Hashimoto, J. P. Robertson, A. F. Rowcliffe, and A. Hishinuma, Swelling of F82H irradiated at 673 K up to 51 dpa in HFIR, J. Nucl. Mater. 283–287 (2000) 334–338.
[59] R. L. Klueh and D. J. Alexander, Embrittlement of 9Cr-1MoVNb and 12Cr-1MoVW steels irradiated in HFIR, J. Nucl. Mater. 187 (1992) 60–69.
[60] T. Morimura, A. Kimura, and H. Matsui, Void swelling of Japanese candidate martensitic steels under FFTF/MOTA irradiation, J. Nucl. Mater. 239 (1996) 118–125.
[61] R. Kasada, A. Kimura, H. Matsui, and M. Narui, Enhancement of irradiation hardening by nickel addition in the reduced-activation 9Cr-2W martensitic steel, J. Nucl. Mater. 258–263 (1998) 1199–1203.

[62] X. Jia, Y. Dia, and M. Victoria, The impact of irradiation temperature on the microstructure of F82H martensitic/ferritic steel irradiated in a proton and neutron mixed spectrum, J. Nucl. Mater. 305 (2002) 1–7.
[63] Y. Dia and X. Jai, The behavior of martensitic steels after irradiation in SINQ target 3, In Proceedings of Conference on Accelerator Applications in a Nuclear Renaissance, La Grange Park, Ill., American Nuclear Society (2004) 857–863.
[64] R. L. Klueh, D. J. Alexander, and E. A. Kenik, Development of low-chromium, chromium-tungsten steels for fusion, J. Nucl. Mater. 227 (1995) 11–23.
[65] R. L. Klueh, D. J. Alexander, and P. J. Maziasz, Bainitic chromium-tungsten steels with 3% chromium, Met. Trans. 28A (1977) 335–343.
[66] R. L. Klueh and A. M. Nasreldin, Microstructure and mechanical properties of a 3Cr-1.5Mo steel, Met. Trans. 18A (1987) 1279–1290.
[67] L. J. Habraken and M. Economopoulos, Bainitic microstructures in low-carbon alloy steels and their mechanical properties, In Transformation and Hardenability in Steels, Ann Arbor, Mich., Climax Molybdenum Company (1967) 69–107.
[68] R. Viswanathan and W. Bakker, Materials for ultrasupercritical coal power plants—boiler materials: Part 1, J. Mater. Eng. Perform. 10 (2000) 81–95.

FRICTION STIR WELDING OF MA957 OXIDE DISPERSION STRENGTHENED FERRITIC STEEL—S. M. Howard, B. K. Jasthi, and W. J. Arbegast (South Dakota School of Mines and Technology), G. J. Grant, S. Koduri, D. R. Herling, and D. S. Gelles (Pacific Northwest National Laboratory)*

OBJECTIVE

The objective of this effort is to investigate friction stir welding technology for application to oxide dispersion strengthened ferritic steels.

SUMMARY

A 1-in. (25.4 mm) diameter yttria-dispersion-strengthened MA957 ferritic steel alloy tube with a 0.125" (3.18 mm) wall thickness was successfully plasticized by friction stir welding. The pin tool was a W-Re tool with 0.125" (3.17 mm) diameter tip. It showed no discernable wear for the total 12" (305 mm) of weld. Weld conditions were 1000 and 1400 RPM, 4 in/min (101 mm/min), with and without preheating to 135ºC. Metallographic analysis of the post friction-stir welded material showed a decrease in material hardness to 225±22 H_V compared to the parent material at 373±21 H_V. All weld conditions produced plasticization; however, improved plasticization was observed for preheated samples.

PROGRESS AND STATUS

Introduction

In the last 15 years a new joining technology, Friction Stir Joining has emerged that has the potential to join many complex materials. This process, invented by TWI, Ltd.[1], is a solid state process that employs severe plastic deformation to create joints between a wide variety of different materials. The weld is created by clamping the materials to be joined, and plunging a spinning tool into the surface. The spinning tool is then translated down the joint line leaving behind a weld zone characterized by a fine-grained, dynamically recrystallized microstructure. Typically, the tool is spun at 400 rpm to 2000 rpm, and translated down the joint line at a rate of 4 in/min to 300 in/min depending on tool design, base material, and thickness. As the tool rotates and translates, complex flow patterns develop in the base material that creates an intimate mixing of materials from both sides of the weld. Heat input during plastic deformation generally creates a temperature in the weld between 0.6 and 0.8 of the absolute melting temperature, so no liquid phase is generated.

The objective of this investigation is to determine if MA957 oxide dispersion strengthened (ODS) ferritic steel could be plasticized by friction stir welding. MA957 is a commercial yttria (Y_2O_3) dispersion-strengthened ferritic steel alloy that represents the class of oxide dispersion strengthened alloys that may be used as advanced ferritic steels for first wall applications. Conventional welding of such materials disturbs the extremely fine oxide particles within the alloy, because the less dense particles rise to the surface of the molten weld pool. A means for joining such alloys that preserves the dispersion and its concomitant properties would extend the alloy's usefulness and offer important additional applications. One method by which the alloy might be joined while preserving the dispersion structure is friction stir welding. Since fiction stir welding is a solid phase technique for joining metals and alloys, the problem of dispersoid rising to the weld pool surface in fusion welding might be avoided. The primary advantage of friction stir welding of steels compared to most other welding techniques is the lower heat input and avoidance of the liquid-to-solid transformation. This creates less severe metallurgical changes in the weld's heat affected zone (HAZ), less residual stress, and avoidance of problems arising from hydrogen embrittlement and gas entrapment.

The material used for this study was from the National Cladding and Duct Materials Development Program material stockpile. A batch of MA957 bars was purchased for fabrication into fuel cladding[2],

*Pacific Northwest National Laboratory (PNNL) is operated for the U.S. Department of Energy by Battelle Memorial Institute under contract DE-AC06-76RLO-1830.

and one gun-drilled bar remained. It was decided that that bar could be used for initial friction stir joining studies.

Experimental Procedure

The material used in this work consisted of an MA957 cylinder 1.00" (25.4 mm) OD, 0.75" (19.0 mm) ID and 9" (229 mm) length. It was fitted tightly with an Inconel 625 rod as shown in Fig. 1. This ODS MA957 steel clad bar was friction stir welded according to the selected processing parameters shown in Table 1. The processing included with- and without-preheating to avoid a possible ductile-to-brittle transition temperature which is near room temperature for this alloy. The rod was clamped into a V-groove fixture as shown in Fig. 2, but no attempt was made to restrain the material radially as is possible naturally in the welding of a flat plate. Therefore, considerable flash was expected on either side of the weld as well as poor backfilling of the pin tool track. Even so, a determination of plasticization extent was believed possible by this arrangement. The pin tool used was a W-Re tool with 1/8" tip. The specimen was preheating using a hot air gun. Hardness measurements were performed on the completed specimens in selected zones using a Vickers hardness tester. Each weld was approximately 3 inches (76.2 mm) long. After the four welds were completed, the resulting friction stir processed cylindrical specimens were sectioned perpendicular to the axis with water cooling. The samples were mounted and polished for metallographic examination. An etching solution of 2 g $CuCl_2$, 40 ml HCl, and 40-80 ml ethanol was used.

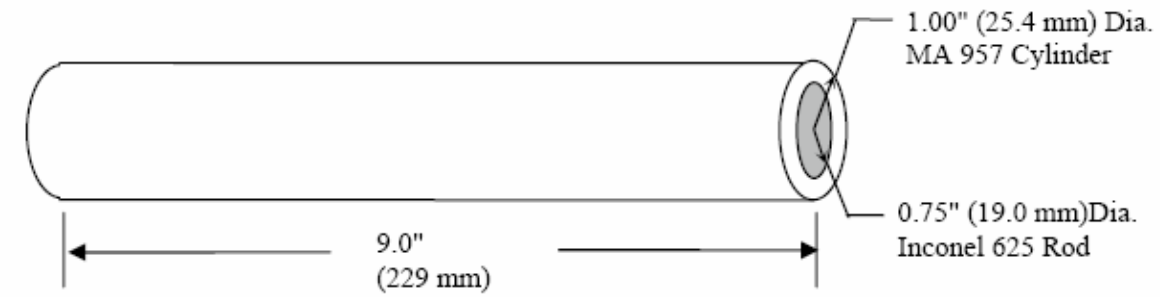

Fig. 1. Dimensions of MA957 ODS steel specimen.

Table 1. Weld process parameters

Weld No	Weld Speed in./min. (IPM)	Spindle speed (rpm)	Condition
1	4	1400	No preheating
2	4	1000	No preheating
3	4	1400	Preheating (135°C)
4	4	1000	Preheating (135°C)

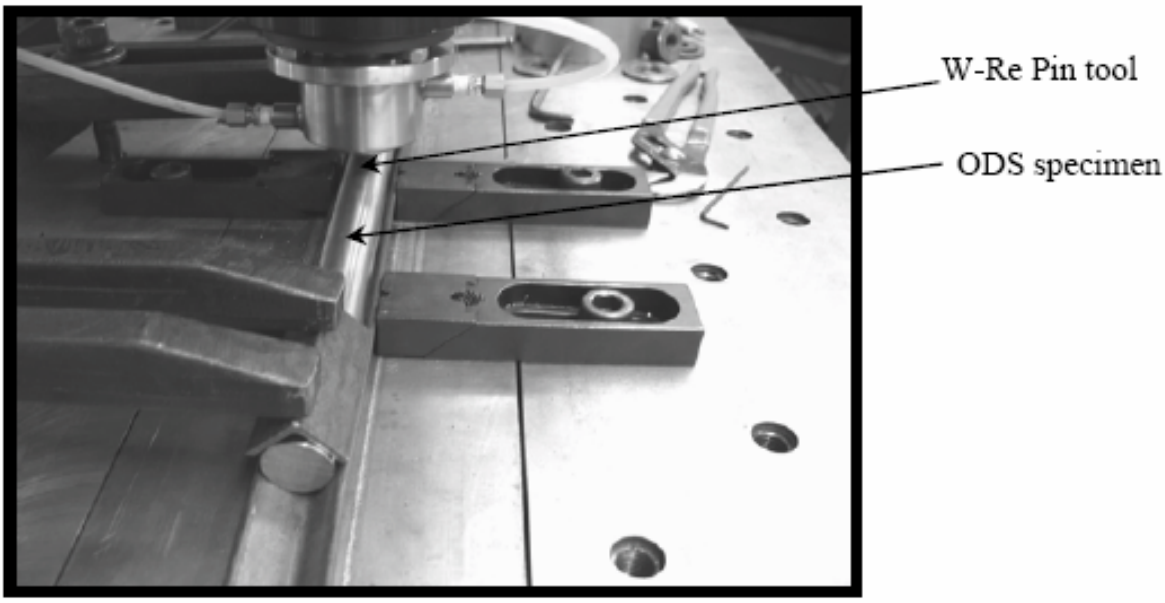

Fig. 2. Friction stir welding setup for MA957.

Results

Plasticization was achieved for all weld conditions. The W-Re pin tool showed no noticeable damage or wear; however, some ODS MA957 metal adhered to the pin tool. Figure 3 shows plasticized material in the processed region. The processed region is not consolidated due to tool-part mismatch arising from the tube curvature. However, the plasticized region shows the nature of flow and confirms that ODS alloys can be processed using friction stir welding. Figure 4 shows micrographs of the parent and the nugget zones created by friction stir welding. All of the figures are at the same magnification and have a size bar that is 200 microns in length. Hardness measurements of the plasticized, parent, and HAZ materials are provided in Table 2. Some of the measurements are averages. The table also shows the number of measurements included in each average (#) and the corresponding standard deviations. The results demonstrate that the hardness is reduced by friction stir welding from 373±21 H_V for the parent material to 225±22 H_V in the nugget and ~317±11 H_V in the HAZ.

All welding conditions resulted in considerable plasticity of the ODS MA957 alloy. This work largely dispels concerns that a dispersion-hardened material such as MA957 cannot be plasticized by friction stir welding. It remains undetermined if friction stir welded ODS material retains its valued mechanical properties. However, the hardness measurements do offer some information worth summarizing here.

It was observed that the degree of plasticization was greatest when the material was preheated (to 135°C) and welded at 1400 RPM. Also, higher rotational speed resulted in more plasticization regardless of preheating. Hardness measurements indicated a significant decrease in the plasticized zone compared to the parent material. Furthermore, the nugget hardness is directly related to the weld pitch as shown in Fig. 5. Weld pitch is likely related to the weld temperature, in which case the nugget hardness is directly related to weld temperature.

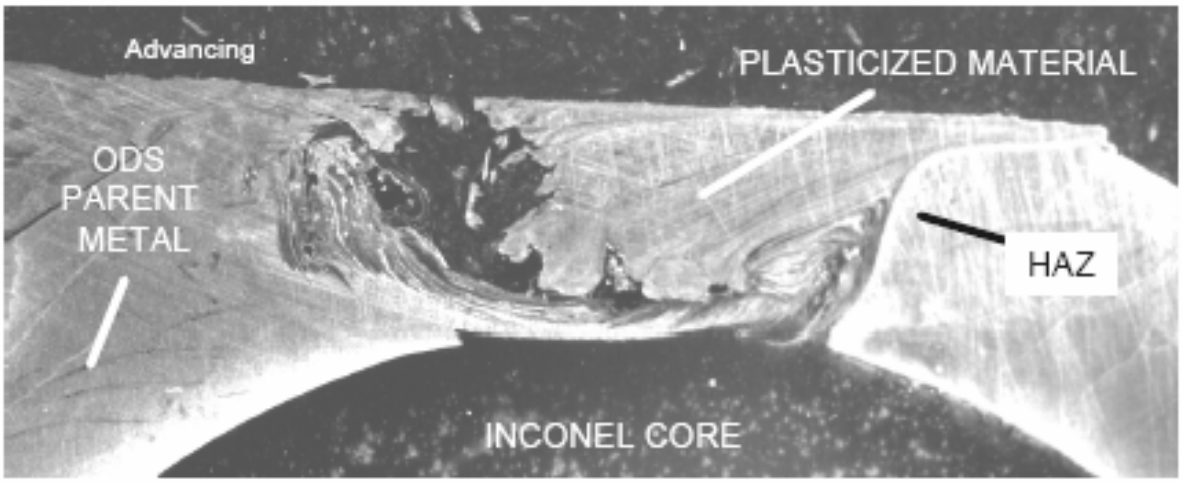

Fig. 3. Cross section of ODS alloy tube plasticized by friction stir processing. Processed region is not consolidated due to tool-part mismatch, but the plasticized region shows the nature of flow and confirms that ODS alloys can be processed using FSP.

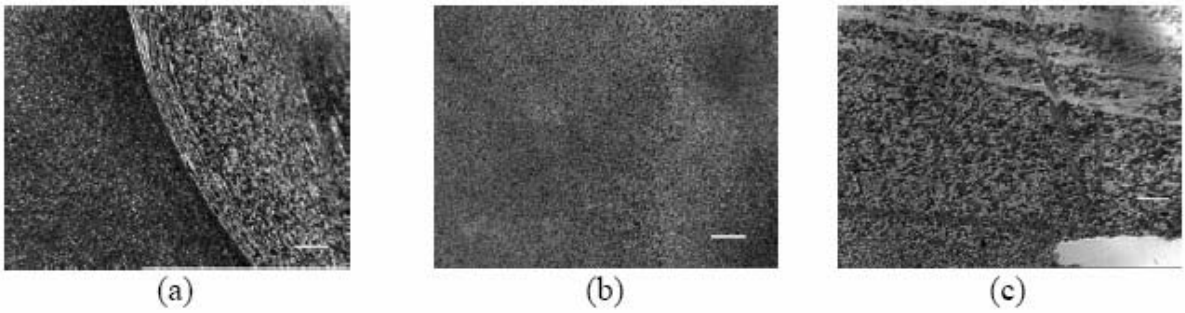

Fig. 4. Micrographs of ODS MA957: (a) nugget (right)-TMZ interface, (b) parent, and (c) nugget zone.

Table 2. Hardness measurements

Weld No	Zone	Hardness, H_V	Standard Dev.	#
1	Nugget	223	17	4
	HAZ	284		1
2	Nugget	240	21	6
	HAZ	339		1
3	Nugget	206	9	3
	HAZ	307		1
4	Nugget	232	25	7
	HAZ	339		1
Parent Material		373	21	4
All HAZ		317	27	4

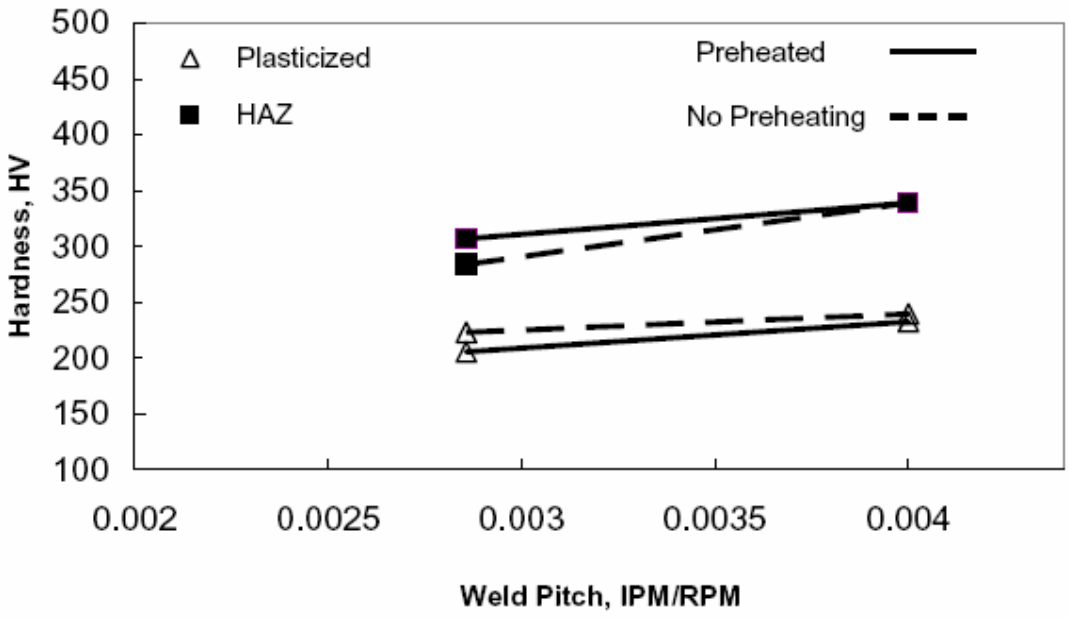

Fig. 5. Dependence of hardness on weld pitch.

Discussion

A decrease in the average weld nugget hardness was observed compared to the parent material from approximately 373±21 H_V to 225±22 H_V. Greater weld pitch, and likely related weld temperature, resulted in more plasticization and slightly greater nugget hardness. No definitive grain size determination was made but morphology suggests an increase in grain size in the nugget. The observed decrease in hardness resulting from friction stir processing may be related to this apparent increase in grain size in the nugget, and is likely is due to yttria redistribution. TEM work is needed to determine the yttria morphology and distribution in the nugget. However, an explanation is possible based on experience with recrystallization of MA957[3], where it was found that hardness was considerably reduced with an accompanying large increase in dispersoid size. The change was attributed to the presence of alumina stringers in the material which allowed replacement of the yttria with a coarser ruby structure. If additional investigation confirms this presumed increase in grain size, one might control such growth by liquid

nitrogen quenching behind the weld. Also, hardness may be regained by doing post weld heat-treatment. However, it may be more beneficial to use alternate material for future work. Unfortunately, ODS ferritic steel in quantities needed for friction stir welding is very limited in availability.

Conclusions

ODS MA957 ferritic steel is plasticized without difficulty when stirred with a W-Re pin tool. Preheating to 135°C improves the plasticization compared to not preheating. Preheating has little effect on the resulting weld. The value of preheating the material above the ductile-brittle transition temperature to prevent pin tool damage was not established.

Future Work

The effort will be continued as opportunities become available.

References

[1] W. M. Thomas et al., Friction Stir Welding, International Patent Application PCT/GB92, Patent Application GB9125978.9, December 6, 1991.
[2] M. L. Hamilton, D. S. Gelles, R. J. Lobsinger, G. D. Johnson, W. F. Brown, M. M. Paxton, R. J. Puigh, C. R. Eiholzer, C. Martinez, and M. A. Blotter, Fabrication Technological Development of the Oxide Dispersion Strengthened Alloy MA957 for Fast Reactor Applications, PNL-13168 (2000).
[3] M. L. Hamilton, D. S. Gelles, R. J. Lobsinger, M. M. Paxton, and W. F. Brown, Fabrication Technology for ODS Alloy MA957, PNL-13165 (2000) 10.
[4] S. M. Howard, B. K. Jasthi, W. J. Arbegast, G. J. Grant, S. Koduri, and D. R. Herling in Friction Stir Welding and Processing III, edited by K. V. Jata et al., TMS, The Minerals, Metals & Materials Society (2005) (to be published).

ON THE PRECIPITATION KINETICS, THERMAL STABILITY AND STRENGTHENING MECHANISMS OF NANOMETER SCALE Y-Ti-O CLUSTERS IN NANOSTRUCTURED FERRITIC ALLOYS—M. J. Alinger and G. R. Odette (University of California, Santa Barbara)

OBJECTIVE

The objective of this study was to explore the factors that control the formation and stability of Y-Ti-O nanoclusters (NCs) in nanostructured ferritic alloys (NFAs).

SUMMARY

A systematic matrix of annealing times and temperatures were used to assess the kinetics of NC precipitation in Fe-14Cr powders mechanically alloyed (MA) with Ti and Y_20_3 (U14YWT). The MA dissolves the Y, O, and Ti as supersaturated solutes that subsequently precipitate during hot powder consolidation, or annealing, in the form of nm-scale solute clusters (NCs). The NCs evolve extremely rapidly due to high diffusion rates and excess vacancies produced by MA. The non-equilibrium kinetics of NC evolution is nucleation controlled, with the number density (N) scaling with an effective activation energy of ≈53±15kJ/mole. The stability of the NCs during high-temperate annealing of MA957 was also characterized. The NCs coarsen and transform to nearer-to-equilibrium oxide phases at radii >≈3.5 nm, with a high effective activation energy of ≈880 kJ/mole and a time dependence characteristic of a dislocation pipe diffusion mechanism, with $r(t) - r(o) \alpha t^{1/5}$. The effect of the micro-nanostructure on the alloy strength was assessed by microhardness measurements. The NCs can be sheared by dislocations and have an obstacle strength (α) that increases with r (nm) as $\alpha \approx 0.37\log(r/2b)$ (≈0.1 to 0.5).

PROGRESS AND STATUS

Introduction

The objective of this work is to develop a fundamental understanding of the kinetics of NC nucleation, growth, coarsening and transformations, as well as their strengthening contributions, to provide a basis for tailoring NFA microstructures to specific applications; and to predict their thermal their stability during extended, high temperature service.

Experimental Procedure

Materials, Annealing Conditions, and Characterization Methods

NC precipitation kinetics were studied using milled and annealed U14YWT powders described in a previous report [1]. Note the NCs that form in the annealed powders are similar to those observed in hot consolidated alloys that experience the same time-temperature history. The powder anneals were performed using two different heat-up rates: a ramp anneal (RA) to mimic HIP consolidation; and an isothermal anneal (IA) with very rapid heating and cooling to observe short time processes. The annealing was carried out at selected combinations of times (t) and temperatures (T) that ranged from 1/3 to 81 h and 600 to 1150°C, respectively. Due to the relatively large supply of available material, thermal aging treatments were carried out on MA957 to evaluate the stability of the NCs at selected t-T combinations that ranged from 1/3 to 480 h and 1150 to 1400°C. Small angle neutron scattering (SANS) was used to characterize the NCs in both cases, and Vickers microhardness was used to measure the strength of consolidated alloys and annealed MA 957. Additional details can be found in the dissertation of the lead author [2].

Results

NC Formation and Growth

Figure 1 shows an example of the NC evolution at 1000°C as a function t for both RA and IA powders, in terms of the NC radius (r), volume fraction (f), number density (N), and magnetic to nuclear scattering ratio (M/N). The formation of Y-Ti-O rich NCs is very rapid (almost time-independent) at all T. This is believed to be due to the high diffusion rates at higher T and large super-saturations of excess vacancies produced by MA at lower T. Figure 2 shows a corresponding example of the T-dependence of the NC parameters at t = 1/3 h. The NC N, f, and M/N decrease and the r increases with higher T. The NC N, f, and M/N are also higher for the RA compared to the IA powders, since the alloys spend considerable time at lower temperatures in the former case. These results suggest that the kinetics of non-equilibrium NC precipitation are primarily nucleation-controlled.

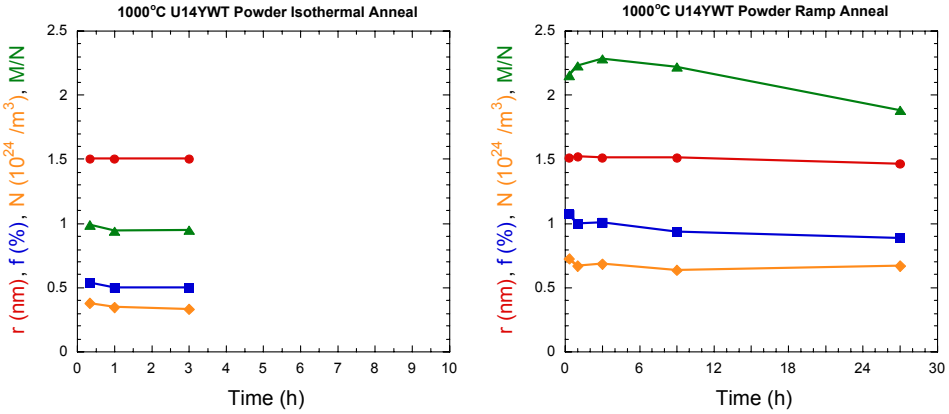

Fig. 1. An example of the NC evolution at 1000°C in annealed powders as a function t.

If the NC atomic solute densities are ≈1.1 to 1.2 times higher than the matrix Fe-Cr phase, the M/N ratio which is a measure of the composition of the NCs, is generally consistent with data from 3D atom probe tomography (APT) studies reported by Miller et al. [3], as well as limited measurements we have made on the consolidated UCSB model alloy U14YWT. These atom densities, and the observed solute (Y+Ti) to O ratios, that are >1, are inconsistent with the properties of known equilibrium oxide phases. The increases in the M/N indicate that the NCs loose Ti (and Y?) and gain Fe with decreasing T. The RA T-t history, and effectively lower T, also increases the apparent Fe content (higher M/N) of the NC compared to the IA treatment.

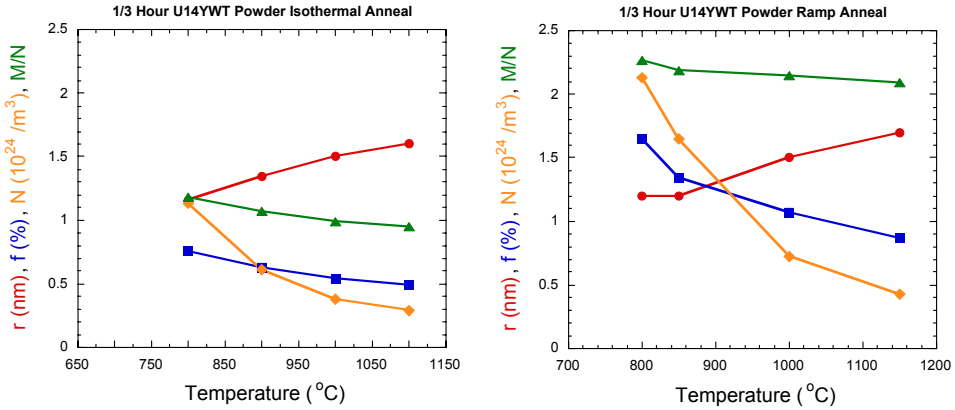

Fig. 2. An example of the NC evolution at 1/3 h as a function T.

The non-equilibrium kinetics of NC evolution is nucleation controlled, with the number density (N) scaling with an effective activation energy of ≈53±15kJ/mole as shown in Fig. 3.

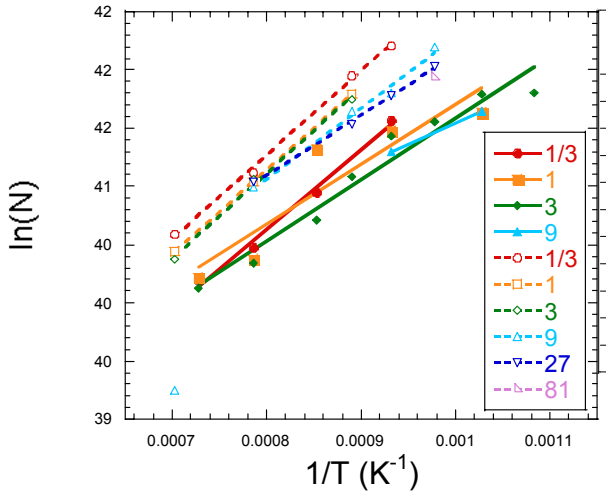

Time (h)	Anneal Type	Q_{en} (kJ/mole)
1/3	Isothermal	56.83
1	Isothermal	42.78
3	Isothermal	44.00
9	Isothermal	30.81
1/3	Ramp	59.71
1	Ramp	59.99
3	Ramp	60.60
9	Ramp	82.28
27	Ramp	42.80
Average		53.31
Standard Deviation		15.02

Fig. 3. ln[N] (N in units of NCs/m^3) versus 1/T (in units of 1/°K). The N(T) can be described by a simple time-independent rapid nucleation model, with an effective activation energy of ≈53 ±15 kJ/ mole.

NC Thermal Stability in MA957

As shown in Fig. 4a and b, the NCs in the MA957 alloy extruded at 1150°C are very stable and initially coarsen by a dislocation pipe diffusion mechanism as $r = r_o[k_c t + 1]^{1/5}$, where r_o is the as-processed NC radius and $k_c = k_{co}\exp(-Q_c/RT)$ is a temperature-dependent rate constant.

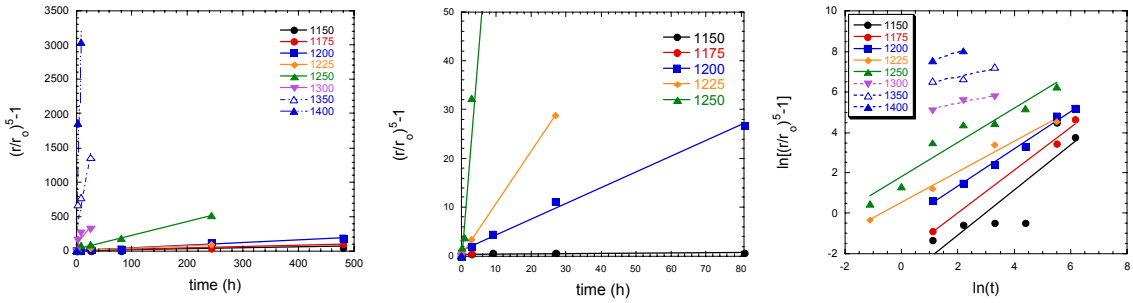

Fig. 4. Plots of $(r/r_o)^5$-1 versus annealing time a) all T versus all t; b) for all T versus short t prior to transformation to nearer-to-equilibrium oxide phases; and c) $\ln[r/r_o^5\text{-}1]$ versus ln(t) data and fits to evaluate the p-dependence of $r = r_o[k_c t + 1]^p$, yielding p ≈1/5 for the shorter t data with r <3.5 nm (solid lines).

The NCs transform to nearer-to-equilibrium oxide phases at r >≈3.5 nm. Analysis of the data T-dependence of the NC (r <3.5 nm) coarsening data a number of different ways, including as shown in Fig. 5, yields an average effective activation energy of Q_c ≈880±125 kJ/mole, and k_{co} ≈2.95×10^{27}/s. The very high value of Q_c is believed to be associated with the combination of low solubility of Y in ferrite (with large atomic size differences) and the high strength of Y-Ti-O bonds. As shown in Fig. 6, extrapolating the model to lower service temperatures predicts that the NCs will resist coarsening, for example, up to t >10^5 h at 1000°C.

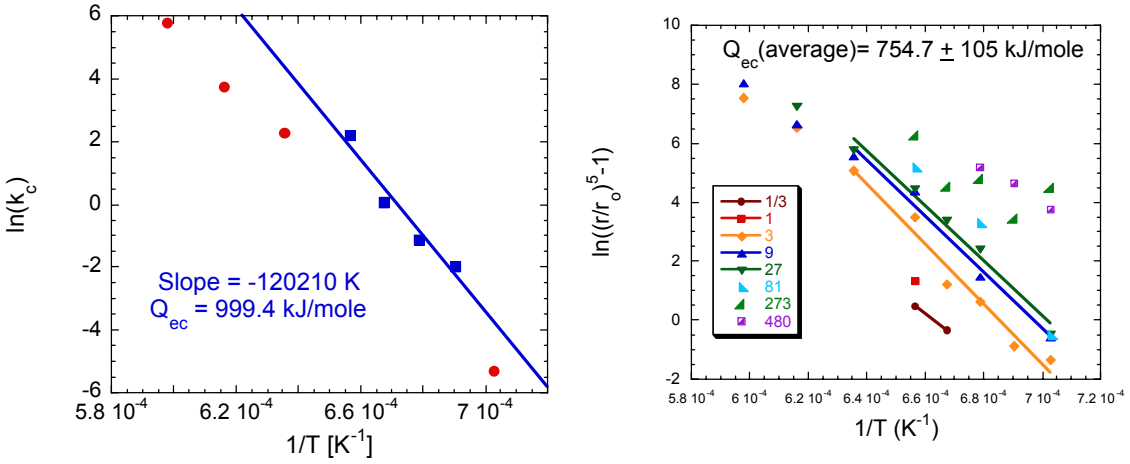

Fig. 5. Effective coarsening activation energy, Q_{ec}, of a) 999.4 kJ/mole from a plot of $\ln(k_c(T))$ versus 1/T and b) 754.7 kJ/mole from a plot of least squares fit of $\ln((r/r_o)^n\text{-}1)$ vs. t_a against 1/T.

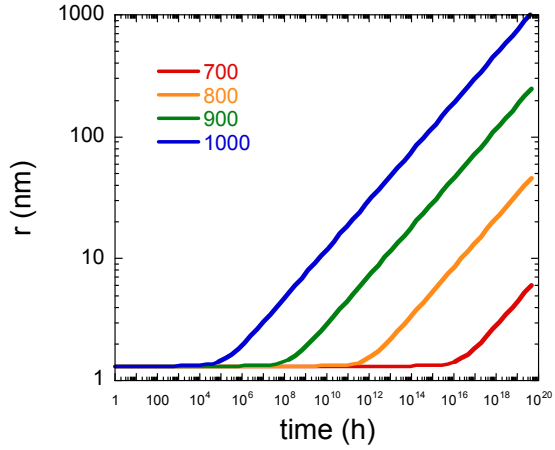

Fig. 6. The predicted r as a function of time for various temperatures.

NFA Strengthening Contributions

The total yield stress (σ_y) of NFAs includes 'baseline' (σ_b) contributions from the lattice resistance of 'impure' unalloyed Fe, polycrystalline grains or nanograins, substitutional alloy solutes and dislocations, as well as hardening due to NCs that act as dispersed barriers to dislocation slip. The baseline strength depends on the alloy composition and heat treatment history and ranges from σ_b ≈600 to 950 MPa. Assuming the NCs contribution to σ_y is given by $\sigma_o = \sigma_y - \sigma_b$, the obstacle strength α can be estimated as, $\alpha(r) = \lambda\sigma_o/[2.45Gb]$, where $\lambda(=1.81r/\sqrt{f}-1.63r)$ is the NC spacing on the slip plane, G is the shear modulus, and b is the Burger's vector. Here r, f, and, hence, λ, are determined from the SANS measurements.

Figure 7 shows that $\alpha(r)$ is the same for MA 957 and the UCSB model alloys and increases linearly as α ≈log[r/2b]. Thus the NC and small oxides act as weak to moderately strong (α ≈0.1 to 0.5) obstacles that can be sheared by dislocations.

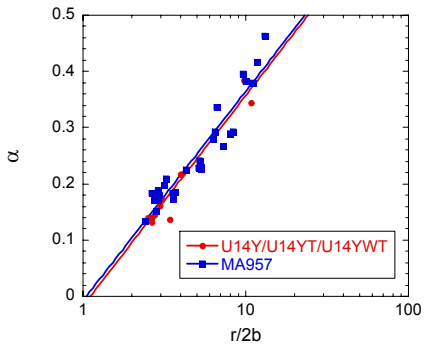

Fig. 7. Plot of α versus log(r/2b) for the U14 alloys containing Y or Ti and Y and the annealed MA957.

As shown in Fig. 8, for a given volume fraction, f, of NC obstacles, the peak hardening occurs at r ≈1.4nm, with a maximum value of $\sigma_o/\sqrt{f}$ of about 7600 MPa. The log(r/2b) size scaling is consistent with a

modulus interaction mechanism. This mechanism has been modeled by Russell and Brown [2] for nm-scale coherent Cu precipitates. The peak strength of the NC is more than 2 times that for Cu clusters.

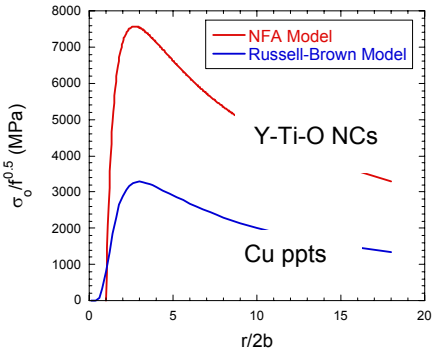

Fig. 8. The predicted $\sigma_o/\sqrt{f}$ (f = 0.01) versus r/2b for NCs and for the Russell-Brown model, showing the peak hardening occurs r/2b ≈1.4 nm.

Future Work

Future work will focus on the following items:

1. Better identification of the character of the NCs using a variety of techniques, including additional ATP studies, as well as transmission electron microscopy and positron annihilation spectroscopy.

2. Extension of the NC thermal stability studies to lower temperatures and longer times.

3. Comprehensive characterization of the coupled evolutions of the NC, dislocation and nano-grain structures during processing and thermal service.

4. Assessment of alternative alloys and processing paths.

5. Evaluating and hopefully resolving of the issue of inhomogeneous microstructures and NC distributions in the UCSB model alloys.

6. Characterization of the constitutive and fracture toughness properties of NFAs and their relation to the overall microstructure.

7. Modeling the thermo-kinetics of micro-nanostructural evolutions in NFAs as well as the structure-property relations.

Acknowledgements

The authors gratefully acknowledge the supply of Fe-14Cr powders provided by and many helpful discussions with Dr. D. Hoelzer of ORNL. We also thank Doug Klingensmith (UCSB) for his contributions to the SANS experiments and Professor Brian Wirth (UC Berkeley) for his help in analysis of the SANS data. We acknowledge the support of the National Institute of Standards and Technology, U.S. Department of Commerce, in providing facilities used in this work. This research was supported by DOE Office of Fusion Energy Science (Grant # DE-FG03-94ER54275) and the INERI DOE Office of Nuclear Energy through a subcontract with ORNL (Grant # 400014112).

References

[1] M. J. Alinger, G. R. Odette, and D. T. Hoelzer, Fusion Materials Semiannual Progress Report DOE/ER 0310/35 (December 2003) 129–134.
[2] M. J. Alinger, On the Formation and Stability of Nanometer Scale Precipitates in Ferritic Alloys During Processing and High Temperature Service, dissertation submitted in partial fulfillment of Ph.D. degree in Materials from the University of California, Santa Barbara (September 2004).
[3] M. K. Miller et al., Mater. Sci. Engr. A V353 (2003) 140–145.
[4] K. C. Russell and L. M. Brown, Acta Metall. V20 (1972) 969.

POSITRON ANNIHILATION CHARACTERIZATION OF NANOSTRUCTURED FERRITIC ALLOYS—M. J. Alinger and G. R. Odette (University of California, Santa Barbara), S. C. Glade and B. D. Wirth (University of California, Berkeley), Y. Nagai and M. Hasegawa (Tohoku University, Sendai Japan)

OBJECTIVE

The objective of this research was to probe nm-scale precipitates as well as the defect structure of nanostructured ferritic alloys (NFAs) using positron annihilation spectroscopy to provide further understanding of microstructure development during processing.

SUMMARY

Positron annihilation spectroscopy lifetime and orbital electron momentum spectroscopy (OEMS) data are in qualitative agreement with small angle neutron scattering (SANS) observations for NCs in NFAs. In the U14WT alloys, which do not contain yttrium, the positrons primarily annihilate in the matrix and matrix features like dislocations or small solute clusters. A small fraction of the positrons annihilate at large vacancy clusters or gas bubbles. In the case of the Y containing alloy, U14YWT, up to ≈50% of the positrons annihilate at non-magnetic features characteristic of Y-Ti-O NCs and, perhaps, smaller vacancy cluster-bubble type features.

PROGRESS AND STATUS

Introduction

Structural alloys used in the intense neutron fields of first wall and blanket structures of fusion reactors must minimize residual radioactivity arising from nuclear reactions as well as provide long-term stability of both the microstructure and mechanical properties. Microstructural stability includes the ability to successfully manage high levels of both transmutation products like helium and displacement of atoms from their lattice positions, creating excess concentrations of vacancies and self-interstitial atoms. In combination, these requirements present a unique material challenge within a materials science based approach to advanced alloy design and development [1,2,3,4,5].

A significant effort has been devoted to achieving high creep strength, radiation damage resistant alloys by creating a very high number density of fine-scale features that act as dislocation obstacles, serve as the dominant nucleation site for small helium bubbles and promote vacancy-interstitial recombination. Such fine-scale features have been observed in alloys traditionally classified as oxide dispersion strengthened (ODS) alloys. The aim of ODS alloys is to create a fine dispersion of oxide particles for enhanced creep strength. Traditionally it was believed that oxide particles are refined and homogeneously dispersed throughout the microstructure through mechanical alloying (MA) [6]. The MA powders are then consolidated using techniques such as hot extrusion and hot isostatic pressing (HIPing). However, it has recently been shown that, for specific alloy chemistries and processing routes, a high number density of coherent, nm-scale Y-Ti-O nanoclusters (NCs) can be produced by MA of Fe-Cr-Ti powders with Y_2O_3 followed by precipitation of Y, Ti, and O from solid solution during hot consolidation [7,8,9,10]. Such alloys have been described as nano-dispersion-strengthened ferritic alloys (NFAs).

In this study, positron annihilation lifetime spectroscopy (PALS) is used to detect open volume regions in NFAs. The chemical identity of the elements at the annihilation sites was also assessed by measuring the coincident Doppler broadening of the annihilation photons, referred to as orbital electron momentum spectroscopy (OEMS) [11]. In addition to probing open volume regions, positrons will preferentially localize, or ‘trap,’ in regions of stronger affinity. In contrast, elements or phases with a lower affinity tend to repel positrons. Through the use of these techniques, quantitative (or semi-quantitative) information on precipitate evolution, akin to results for age hardenable alloys, can be obtained [12].

Experimental Procedure

Materials

Gas atomized master alloy powders containing ≈14-wt% Cr, 0.4-wt% Ti and 3-wt% W were MA with and without 0.25-wt% Y_2O_3 by SPEX ball milling in argon for 8 hours. The milled powders were then degassed at 200°C for 24 hours, canned in seamless low carbon steel tubes and consolidated by hot isostatic pressing (HIPing) at 200 MPa for 3 h at 850, 1000, and 1150°C. The alloy codes used in this investigation are U14YWT (Fe-14Cr-3W-0.4Ti-0.25Y_2O_3) for alloys containing Y_2O_3 and U14WT without Y_2O_3 (Fe-14Cr-3W-0.4Ti). Additional details can be found in Ref. [13].

Small Angle Neutron Scattering (SANS)

Small angle neutron scattering (SANS) was performed on the 8 m SANS instrument (NG1) at the National Institute of Standards and Technology. With a neutron wavelength of 0.5 nm, the instrumental configuration yielded a maximum scattering vector, q ≈3.0 nm^{-1}. A strong ≈1.7 T magnetic field applied in the horizontal direction permitted measurement of both nuclear, $d\Sigma/d\Omega(q)_n$, and magnetic, $d\Sigma/d\Omega(q)_m$, neutron scattering cross sections, where:

$$\frac{d\Sigma}{d\Omega}(q,\phi) = \frac{d\Sigma}{d\Omega}(q)_n + \sin^2\phi \frac{d\Sigma}{d\Omega}(q)_m \qquad (1)$$

Here ϕ is the angle with respect to the magnetic field direction. Subtraction of parasitic background counts and normalization of the sample counts, transmissions and masses to a water standard were carried out to measure the absolute $d\Sigma/d\Omega(q,\phi)$. These absolute cross-sections were averaged over specified detector q and ϕ ranges, typically at ϕ = 0±30, 45±15, and 80±10, and used to evaluate the magnetic-to-nuclear scattering ratio (M/N). Note that the M/N is typically determined from scattering over the entire detector.

The scattering cross sections for the nanometer features associated with the variable of interest, $d\Sigma/d\Omega_f$, were determined by subtracting the control cross section (see reference 14 for a detailed description of the SANS data reduction and analysis procedures). For example, subtracting the $d\Sigma/d\Omega$ for U14WT from that for U14YWT was used to assess the effect of Y_2O_3. The $d\Sigma/d\Omega(q,\phi)$ specify the average size (<r>), size distribution ($\Delta r/r$), volume fraction (f) and number density (N) of scattering features. For features with a specified size (r):

$$\frac{d\Sigma}{d\Omega}_{mag}(q) = NV^2\left(\rho_f^{mag} - \rho_m^{mag}\right)^2 S(qr) \qquad (2)$$

Here, ρ_f^{mag} and ρ_m^{mag} are the feature and matrix magnetic coherent scattering length densities and S(qr) is a form factor that depends on the features shape and size [15]. We determined <r>, f, and N by fitting computed $d\Sigma/d\Omega(q)_m$ curves to the $d\Sigma/d\Omega(q)$ data assuming a log-normal distribution, parameterized by mode radius, r_m, $\Delta r/r$, and $d\Sigma/d\Omega(0)_m$ [14]. However, measuring f and N requires *knowledge* of the ρ_f and ρ_m. This is possible for magnetically saturated ferromagnetic alloys, where the matrix magnetic coherent scattering length density, ρ_m^{mag}, is known from the magnetic moment of the alloy (in this case accounting for Cr and other solutes) [16]. Assuming the features are primarily Y, Ti, and O, and non-magnetic, $\rho_f^{mag} \approx 0$.

Positron Annihilation Spectroscopy (PAS)

Positron Annihilation Spectroscopy (PAS) is a useful complementary tool for characterizing NCs and other key components of NFA microstructures. In a pure defect free crystal, positrons migrate by thermal

diffusion until they annihilate with an electron in the crystal. The annihilation occurs over a characteristic mean lifetime, which varies from element to element and is approximately 110 ps in pure iron [17].

However, during diffusion, positrons are trapped by various open-volume defects such as vacancy clusters, dislocations, and different types of interfaces. Additionally, positrons localize ('trap') within clusters of elements (or compound phases) that have a higher positron affinity than that of the matrix. The positron affinities for the most pertinent elements in NFAs are: Fe=-3.84, Cr=-2.62, Y=-5.31, W=-1.31, and Ti=-4.06, in units of eV [18]. The affinity differences essentially represent the trapping energy for a positron. Thus, for example, a positron would be trapped in a pure Y phase in an iron matrix with a binding energy of about 1.5 eV. While both Y and Ti will trap positrons, the affinity for O is not known, nor is it well established for the nanoclusters.

If the electron density is lower at a trapping site, the positron lifetime will increase relative to the lifetime in a defect-free bulk. Further, well-defined open-volume trapping features have a unique characteristic lifetime. For example in Fe, the lifetime associated with a dislocation is about 140 to 160 ps and a single vacancy 175 to 185 ps [19,20,21]. Positrons are strongly trapped in vacancy clusters and the lifetime initially increases rapidly with cluster size but saturates at ≈500 ps for clusters with more than ≈60 vacancies [22,23]. It is also known that positron lifetimes are longer in some insulating oxide compounds, which may form positronium with characteristic annihilation lifetimes that may exceed 1000 ps. The lifetime of Al_2O_3 is 150 ps [24] and in TiO_2 is 180 ps [25], but to our knowledge, is not known for the other oxides of interest.

The overall positron lifetime spectrum obtained for a situation where positron trapping and annihilation occurs at two defects as well as annihilation in the bulk material (3 lifetime components) is [26]:

$$D(t) = I_1 \exp\left(\frac{-t}{\tau_1}\right) + I_2 \exp\left(\frac{-t}{\tau_2}\right) + I_3 \exp\left(\frac{-t}{\tau_3}\right) \tag{3}$$

where t is time, I_1, I_2, and I_3 are the relative intensities of the three life time components τ_1, τ_2, and τ_3 and [17]:

$$\begin{aligned} \tau_1 &= \frac{1}{\lambda_b + \kappa_{d1} + \kappa_{d2}} \\ \tau_2 &= \frac{1}{\lambda_{d1}} \\ \tau_3 &= \frac{1}{\lambda_{d2}} \end{aligned} \tag{4}$$

where κ_{d1} and κ_{d2} are the trapping rates of the shorter and longer lifetime defects, respectively. λ_b, λ_{d1}, and λ_{d2} are the positron annihilation rates in the bulk material and defects, respectively. In turn, the relative intensities are:

$$\begin{aligned} I_1 &= 1 - I_2 - I_3 \\ I_2 &= \frac{\kappa_{d1}}{\lambda_b - \lambda_{d1} + \kappa_{d1} + \kappa_{d2}} \\ I_3 &= \frac{\kappa_{d2}}{\lambda_b - \lambda_{d2} + \kappa_{d1} + \kappa_{d2}} \end{aligned} \tag{5}$$

The trapping rates can be evaluated through the expression:

$$\kappa_i = \mu_i N_i \tag{6}$$

where μ_i is the trapping coefficient and N_i is the concentration of trapping sites (number density). In reality, a distribution of positron lifetimes reflecting a competition between a number of different trapping sites exist and the measured positron lifetime distribution reflects the competition between the dominant traps.

The two or three lifetime positron trapping model requires one additional assumption, namely the 'trapping regime.' Positrons can be trapped in either the diffusion or transition limited regimes, or a combination of both. Positron localization at trapping sites is complex and not well understood and it is possible that, in some cases, positron transition to a trapped state governs over diffusion trapping. The diffusion limited regime assumes that the probability of the positron diffusing to a trap prior to annihilation in the bulk governs positron behavior. In this case, the trapping coefficients for spherical traps (μ_{sphere}) and dislocations ($\mu_{\perp}$) are:

$$\mu_{sphere} = 4\pi r D_{+}$$
$$\mu_{\perp} = \frac{\rho_{\perp} D_{+}}{N} \qquad (7)$$

where r is the radius of the precipitate, $\rho_{\perp}$ is the dislocation density, D_{+} is the diffusivity of the positron (~2 cm^2s^{-1} in Fe-14Cr), and N is the effective number density which cancels out in Equation 6 for trapping at a dislocation. For the NFA materials in this investigation, the precipitate r and N have been obtained by SANS measurements. In a perfect crystal, all of the positron annihilation occurs in the matrix. However, at sufficient sink densities the lifetime of the positron in the trapping site(s) becomes a significant (measurable) fraction of the total annihilation events. Thus, positron lifetime analysis can provide information on the character, size, and number density of the trapping site(s).

Another feature of the annihilation process that can be exploited is the fact that momentum is conserved during the event that converts the positron-electron pair to two photons moving in approximately opposite directions. While the thermal positron itself has little momentum, that of the orbital electrons is much larger and varies both within a particular element (e.g., valence versus core electrons) and between elements. Thus, the distribution of momentum carries information about the chemistry of the annihilation site. By measuring both annihilation photons in coincidence, very high resolution measurements of the linear momentum of the electron-positron pair can be obtained, which provides the orbital electron momentum spectra (OEMS) (often called coincidence Doppler broadening, CDB spectroscopy). Typically, OEMS data are presented as the ratio of the amplitude of the photon counts [$I(p_L)$] at a particular value of momentum, p_L, to that for a reference material, in this case Fe. A common unit of p_L is the electron rest mass (m_o) multiplied by the speed of light (c). Each element or defect trapping feature has a characteristic [$I(p_L)$] normalized shape. For example vacancy clusters have a high intensity $I(p_L)$ at low momentum $p_L \approx 0$ while the $I(p_L)$ is lower at intermediate p_L compared with Fe. In an actual material $I(p_L)$ is determined by the weighted combination of individual annihilation sites.

The OEMS was measured using an experimental setup in which positrons emitted from a radioactive ^{22}Na source are confined and transported to the sample using a strong magnetic field (~1.0 kG). By reversing the orientation of the magnetic field (e.g., from up to down in a vertical direction), the positrons are still transported to the sample, but the majority and minority electron populations in a magnetic material is reversed. This enables spin-polarized, magnetic positron annihilation measurements [27], yielding data on the magnetic character of the positron annihilation site. When the normalized fraction of positron annihilations with high-momentum electrons versus low-momentum electrons is plotted for each magnetic field orientation, magnetic character of the positron annihilation site is revealed as a splitting of the two data points. In contrast, the data points and OEMS spectra are unchanged (superimposed) for positron annihilation in non-magnetic materials. This technique has been successfully used to confirm the non-magnetic behavior of embedded, nanometer-sized copper-rich precipitates in irradiated reactor pressure vessel steels [27] and has also been used in this investigation.

Results

The SANS results are summarized in Fig. 1 and are discussed in detail elsewhere for the HIP consolidated U14YWT alloys [28]. With increasing HIP consolidation temperature from 850 to 1150°C, the mean radius (r) increases from 1.25 to 1.71 nm, the volume fraction (f) decreases from 2.15 to 0.65%, and the number density (N) decreases from 2.57 to 0.30 x10^{24} m^{-3}.

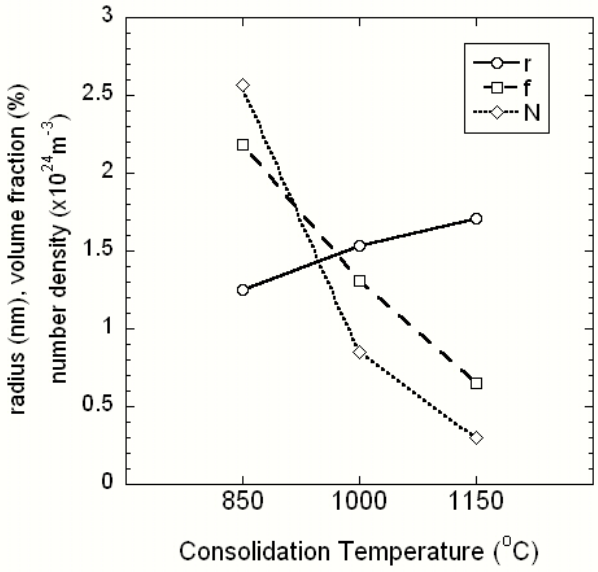

Fig. 1. Results of SANS data analysis for radius (r), volume fraction (f), number density (N), and magnetic to nuclear scattering ratio (M/N).

Positron OEMS

Fig. 2 shows the measured I(p_L) curves characteristic of Y_2O_3, Ti_2O_3, and TiO_2, normalized by dividing with the I(p_L) for unalloyed Fe providing characteristic annihilation momentum signatures for positrons which (might) trap in oxides embedded in the Fe matrix. The curves for the three oxides are generally similar with a substantial dip at intermediate p_L ≈5-30 (m_oc); Y_2O_3 has the deepest minimum.

Fig. 3 shows the corresponding normalized I(p_L)curves for U14WT (filled symbols) and U14YWT (open symbols) for HIPing at 850, 1000, and 1150°C. The I(p_L) dips for all of the HIPed alloys, except U14WT1150, at intermediate p_L with much larger decreases for the Y-containing alloys. The spectra, especially for U14YWT are qualitatively similar to, but weaker, than those for the pure oxides. With the exception of U14WT HIPed at 1150°C, all the alloys also show an I(p_L) peak at low p_L, indicative of open volume vacancy-bubble annihilation or, perhaps, an oxide type feature. The U14WT alloy HIPed at 1150°C shows the least evidence of annihilation in a Ti-O rich phase. Indeed in this case, the predominant annihilation is in the Fe-Cr-W-Ti matrix showing the effects of solutes or small solute clusters. The corresponding I(p_L) curves for Ti and Cr are shown in Fig. 4.

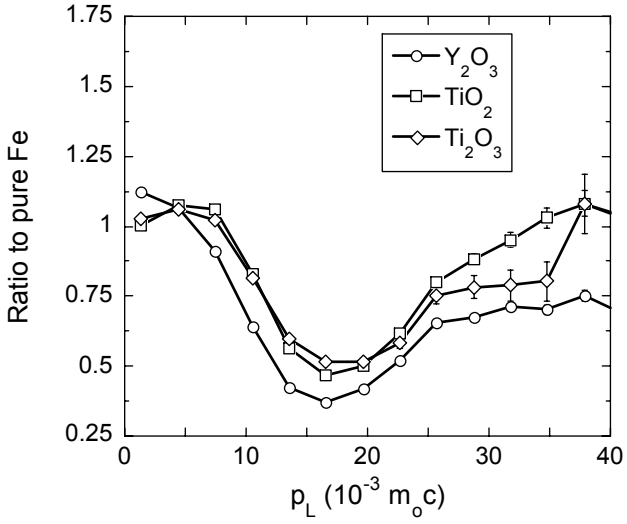

Fig. 2. Measured $I(p_L)$ curves characteristic of oxides Y_2O_3, Ti_2O_3, and TiO_2 normalized by dividing with the $I(p_L)$ for unalloyed Fe.

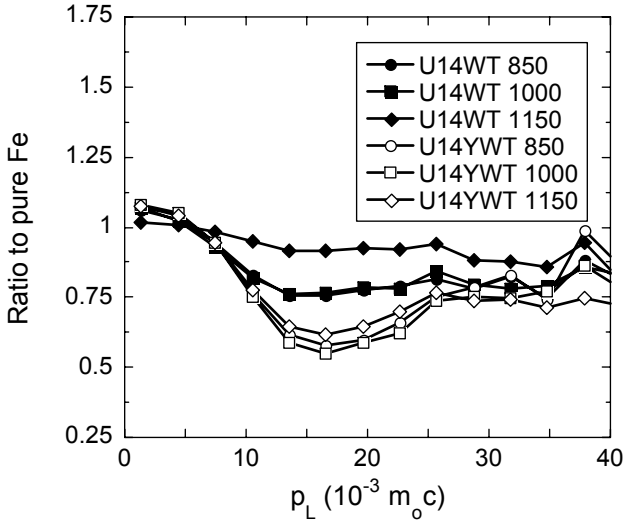

Fig. 3. PAS OEMS plot normalized to Fe.

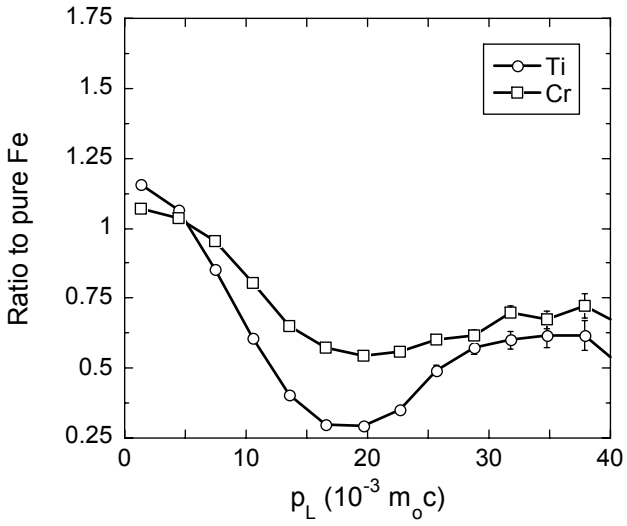

Fig. 4. I(p_L) curves for Ti and Cr.

The I(p_L) curves for the alloys containing both Ti and Y (U14YWT) are appreciably deeper than for those with only Ti (U14WT), and the depths increase at the lower HIPing temperatures. The deeper dips in the U14YWT versus U14WT alloys, as well as the trend with HIPing temperature, are consistent with an increasing trap sink strength for NC (U14YWT) and vacancy-bubble clusters and Ti-oxides (U14WT). Overall, the I(p_L) curves are consistent with a mixed set of annihilation sites in the matrix, likely to include NCs, vacancy clusters, and dislocations.

It is common to plot the OEMS data in terms of the relative fractions of high (W) versus low momentum (S) annihilations. The S and W parameters are determined by integrating the I(p_L) curves between specified p_L limits and dividing by the corresponding integration over the entire p_L range. The limits used in this work were 0.0 to 2.8 x$10^{-3}$$m_o$c (S) and 7.2 to 29.0 x$10^{-3}$$m_o$c (W), respectively, which is shown in Fig. 5.

Fig. 5 also shows the corresponding S-W points for various oxides and elemental Fe, Cr, and Ti. The W is lower and S is higher in the U14WT alloys compared to Fe, likely due to a combination of alloying effects and annihilation at vacancy clusters, or perhaps oxide-type features. However, from the relative positions on the S-W plot, the TiO and TiO_2 oxides themselves do not appear to be good candidates for the secondary annihilation sites. Indeed, the U14WT alloys fall along a tie line established in previous measurements between Fe and irradiated iron containing large vacancy clusters as well as Ti itself. The S-W position in the U14WT alloys is also consistent with annihilation at Ti clusters.

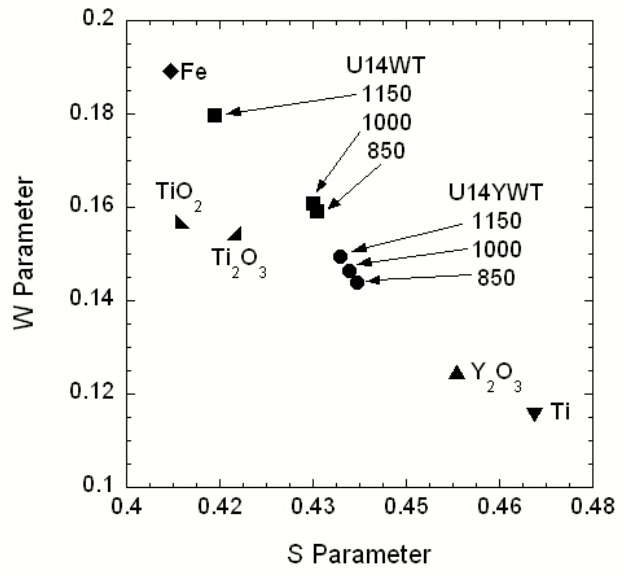

Fig. 5. PAS S-W analysis of the NFAs compared to several reference materials.

Fig. 6 is an expanded plot of Fig. 5 focusing on the U14WT and U14YWT alloys. The dashed lines connect the Fe data point to the measured values for the oxides (TiO_2, Ti_2O_3, and Y_2O_3) as well as Ti. The U14YWT alloys are shifted further to lower W and higher S and in the direction of Y_2O_3. The paired filled and unfilled symbols for each material represent the effects of magnetic polarization. Thus, there is a substantial splitting in ferromagnetic Fe and essentially no splitting in the oxides or paramagnetic Cr and Ti. The splitting is reduced to some extent in the U14WT alloys compared to Fe. However, the splitting is substantially reduced in the U14YWT alloys. This indicates a sizeable fraction of the annihilations take place in non-magnetic features.

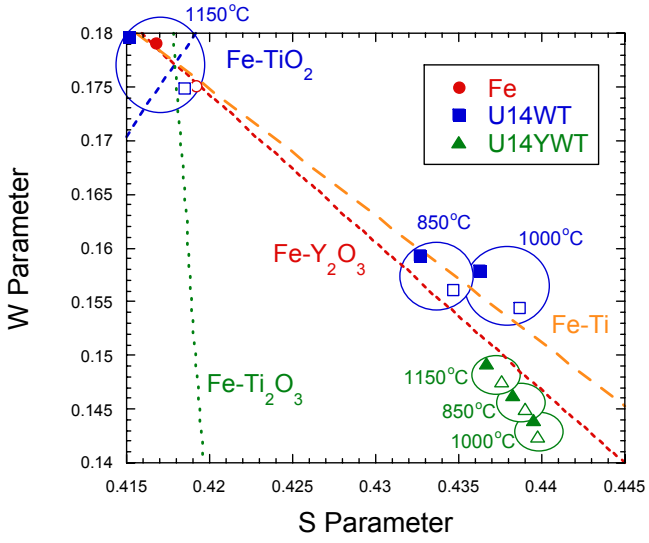

Fig. 6. Expanded plot of S-W analysis performed at LLNL with a line fit to Fe and Y_2O_3.

Positron Lifetime

The PAS lifetime data are shown in Fig. 7 and listed in Table 1. The right hand side of the lifetime plot shows the results of calculations for vacancy cluster and listed in lifetimes in iron [22]. In both alloys, short (τ_1) and long (τ_2) annihilation lifetimes are discernable. However, the lifetime in the U14WT alloys is dominated by a fraction I_1 of the annihilations in the matrix ≥85% with τ_1 ≈107 to 140 ps, reasonably characteristic with defect-free pure Fe (≈110 ps), and a fraction of annihilation at dislocations (≈140 ps) [29]. There is a small fraction of long lifetime annihilations (I_2 < 15%) with τ_2 ≈360 to 380 ps, characteristic of large vacancy clusters or gas bubbles; or even, perhaps, an oxide type feature. Notably, Schaefer and co-workers measured a similar long lifetime (360 ± 30 ps) component in nanocrystalline and nominally pure Fe with a mean grain size of 6 nm, but with a slightly larger intensity (≈33%) [20]. As well, Ohkubo and co-workers observe vacancy clusters with a lifetime of ≈340 ps in nominally pure Fe subject to high-speed deformation [30]. The predicted positron lifetime of vacancy clusters containing between 10 and 15 vacancies ranges from 330 to 380 ps [30]. The similarity of the lifetimes in the U14WT alloys and previous measurements on nanocrystalline iron indicate vacancy clusters as the likely positron trapping site. Notably, the fraction of τ_2 annihilations for U14YWT HIPed at 1150°C is only ≈4%.

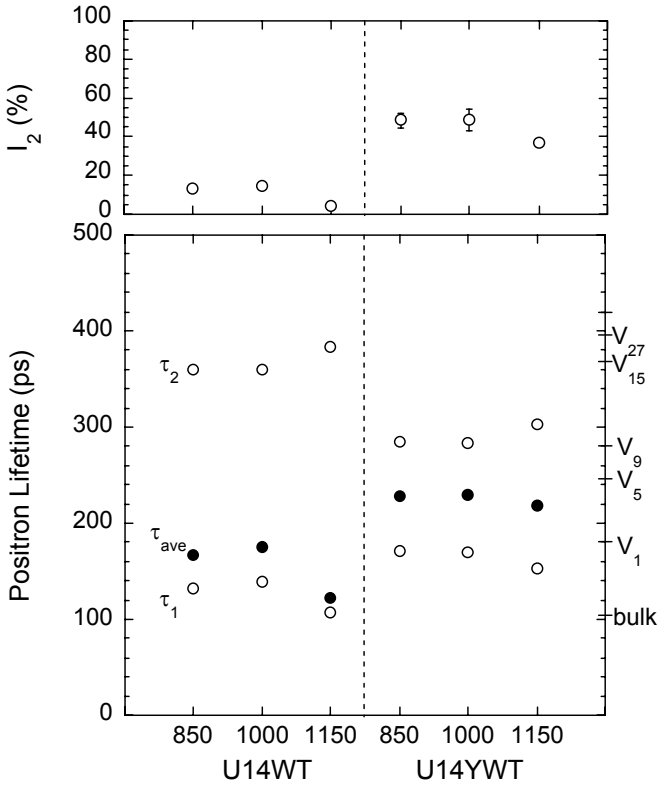

Fig. 7. PAS measured lifetimes and relative intensities for the controls and yttria containing alloys. The calculated lifetimes in Fe for V_x, where x is the number of vacancies in a cluster, are shown on the right axis [22].

Table 1. PAS lifetime data

Alloy	HIP Temp	τ_{av}	$\Delta\tau_{av}$	τ_1	$\Delta\tau_1$	τ_2	$\Delta\tau_2$	I_2	ΔI_2
	(°C)	(ps)	(ps)	(ps)	(ps)	(ps)	(ps)	(%)	(%)
U14WT	850	166.9	0.2	132.1	0.5	360.4	5.2	13.0	0.5
U14WT	1000	175.4	0.2	139.0	1.0	359.1	5.7	14.3	1.1
U14WT	1150	121.8	0.3	107.1	0.9	383.2	22.3	4.1	1.0
U14YWT	850	228.5	0.3	171.0	3.0	284.6	6.7	48.4	3.9
U14YWT	1000	229.5	0.2	169.6	4.6	283.1	5.3	48.6	5.3
U14YWT	1150	218.4	0.2	153.5	1.6	302.9	2.1	37.0	1.5

In contrast, the τ_1 annihilation lifetimes of 154 to 172 ps are longer in the case of the U14YWT alloys, consistent with a mixture of annihilation at dislocations (≈140–160 ps) and vacancies (≈175 ps). The longer τ_2 annihilation lifetimes are shorter than in U14WT, ranging from ≈280 to 300 ps, but represent a much higher I_2 fraction from ≈37 to 49% of the total. The τ_2 increases and the intensity-fraction decreases slightly for the 1150°C HIP. Note these trends are similar to those in the OEMS data and suggest that a large fraction of annihilations take place in Y-Ti-O rich NCs.

Discussion

The lifetime data can be analyzed using the simplified rate theory approach outlined above. The potential positron trapping sites considered in this investigation are vacancies, vacancy clusters, fine scale precipitates and dislocations.

U14WT Alloys

As discussed above, the alloys that did not contain Y had a minor long lifetime component, τ_2, as indicated by a small I_2. A majority of the positrons annihilated in the bulk material, however, some (≈5–15%) annihilated in open volume or low electron density traps. These alloys did not contain a significant density of nm-scale precipitates, but TEM showed that they had a high dislocation density and fine grain size [31]. The severe deformation resulting from mechanical alloying also produces a high non-equilibrium concentration of vacancies [32]. In addition, the gas atmosphere used during milling (typically Ar for iron alloys) can be incorporated into the powders and has been shown to precipitate in fine bubbles associated with precipitates [33].

The U14WT alloy HIPed at 1150°C had a short lifetime component equivalent to that of bulk iron and a small (I_2≈4%) long lifetime component corresponding to a vacancy cluster size of ≈22 vacancies. This leads to an estimated cluster density of 4.05×10^{20} m^{-3}. Assuming an average vacancy formation energy from the literature of 175 kJ/mole this prediction would yield a total vacancy concentration equal to that of the thermal equilibrium concentration in Fe at 1025°C [34].

For the alloys HIPed at 850 and 1000°C, the short lifetime components are longer than that of pure iron, but shorter than for a single vacancy. A lifetime value in this range is generally attributed to annihilation at a dislocation [19]. This data can be analyzed by assuming a high but not unreasonable value for MA materials, dislocation density (≈10^{15} m^{-2}), and with τ_2 produced by trapping at vacancy clusters-bubbles as seen in the alloy HIPed at 1150°C. From the positron lifetime, the cluster sizes for the 1000 and 850°C HIPed U14WT are both ≈15 vacancies. The resulting calculated densities of vacancy clusters are 3.8 and 3.4 $\times 10^{22}$ m^{-3} for 1000 and 850°C, respectively. These densities correspond approximately to the thermal equilibrium vacancy concentration expected at the melting point of iron.

U14YWT Alloys

In contrast, the τ_1 annihilation lifetimes (154 to 172 ps) are longer in the case of the U14YWT alloys. The τ_2 annihilation lifetimes are shorter than in U14WT, ranging from (280 to 300 ps), but represent a much higher I_2 fraction of the total. These trends are similar to those in the measured OEMS and suggest that a large fraction of annihilations take place in Y-Ti-O rich NCs.

Measured lifetimes for Al_2O_3 and TiO_2 are in the range of 150 to 180 ps, and it is unclear what lifetime to expect from the NC; especially considering that they are likely not fully formed oxides, may be complexed with vacancies and/or associated with dislocations. Fig. 8 shows the U14YWT OEMS curves normalized by the corresponding 'baseline' curve for the U14WT alloy HIPed at 1150°C, along with the corresponding curves for the oxides. The heavy dashed line in Fig. 8a is the Y_2O_3 data weighted by 0.45, corresponding to the average value of I_2 assuming that the NC annihilation component corresponds to the lifetime τ_2. The longer lifetime can be attributed to either a much longer lifetime in the Y_2O_3 than Al_2O_3 or TiO_2 or because of trapping in vacancy cluster-nanocluster complexes. Fig. 8b shows the results of using a Y_2O_3 weighting fraction of 0.65, obtained by fitting to the average U14YWT spectra at 850, 1000, and 1150°C, over the range of 10–40 x10^{-3} m_oc. Notably, the weighting fraction value of 0.65 corresponds most closely to the intensity values associated with τ_1 at a lifetime of 165 ps. This lifetime is within the expected regime from the other oxides.

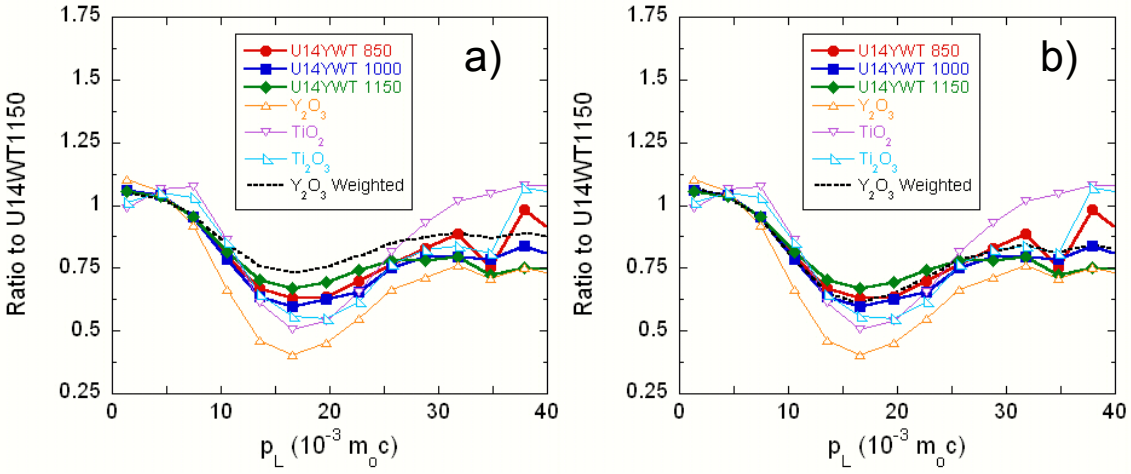

Fig. 8. I(p_L) curves for the U14YWT alloys for the 3 HIPing temperatures normalized by the corresponding 'baseline' curve for the U14WT alloy HIPed at 1150°C, along with the corresponding curves for the oxides. The heavy black dashed line is the Y_2O_3 weighted average and is 0.45 in Fig. a and 0.65 in Fig. b.

Thus, if we are to assume instead that τ_1 is due to annihilation at NCs, consistent with the analysis leading to Fig. 8b, then τ_2 is attributed to annihilation in vacancy clusters. In such a scenario, vacancy cluster sizes, estimated from the lifetime, would contain 9–10 vacancies, smaller than those in the U14WT. The required number density of such clusters, as calculated from the simplified trapping model are 1.1x10^{24}, 4.2x10^{24}, and 1.0x10^{25} m^{-3} for 1150, 1000, and 850°C, respectively. These vacancy concentrations are very high and appear to be somewhat unrealistic, though MA is capable of creating very high dislocation densities.

An alternate assumption is that the long lifetime component is associated with annihilation in nanoclusters (as in Fig. 8a), and the short lifetime component is at dislocations; a dislocation density of 1.1x10^{16} m^{-2} is estimated from the simplified trapping model for the U14YWT HIPed at 1150°C. At 1000 and 850 the

corresponding dislocation densities would be 1.7×10^{16} and 4.3×10^{16}, respectively. The high dislocation density from this analysis is problematic, but implies that the NCs are effective at pinning dislocations and inhibiting recovery with respect to the U14WT alloys without NCs. Note the vacancy clusters, present in the U14WT alloy, may also exist in the U14YWT alloy. However, the NC number densities are an order of magnitude greater and thus have a much larger effective positron sink strength.

Of course, the microstructure of these alloys is very complex, with multiple positron trapping sites, and this simplified analysis neglects consideration of the electronic structure of the nanoclusters, which is likely different than Y_2O_3. However, the results clearly show positron annihilation spectra consistent with Y-Ti-O and vacancy cluster lifetimes as well as with other nanocrystalline Fe and fast-deformation Fe [20,22]. Further clarification of the trapping sites in these alloys requires additional research.

Summary and Conclusions

In summary, the PAS lifetime and OEMS data are in qualitative agreement with the SANS observations. In the U14WT alloys, which do not contain Y, the positrons primarily annihilate in the matrix as well as features like dislocations or small solute clusters. A small fraction of the positrons annihilate at large vacancy clusters (or gas bubbles) that are also probably complexed with solutes. The simplified positron lifetime trapping (rate theory) analysis indicates high dislocation densities and vacancy concentrations are (reasonably) consistent with that anticipated in MA and HIPed alloys.

In the case of U14YWT alloys, which contained Y, up to $\approx$50% of the positrons annihilate at non-magnetic features associated with an S-W position indicating the presence of Y-Ti-O NCs and, perhaps, smaller vacancy cluster type features. Interpretation of the lifetime data for these alloys is difficult and depends on which positron lifetime is assumed to be associated with the NCs. Regardless, these alloys have a high concentration of defects, whether they are dislocations or vacancy clusters. Further investigation is required to better understand these relationships.

Future Work

Future work will focus on collecting and analyzing positron lifetime data for a series of thermally annealed MA957 specimens for which SANS data on the NC evolution exists as well as lifetime measurements for Y_2O_3. Also, we plan to perform Monte-Carlo simulations of the diffusion of positrons in alloys incorporating their effective trapping strength for the trapping limited regime as well as the effects of multiple positron trapping sites.

Acknowledgements

The authors gratefully acknowledge the supply of the Fe-14Cr powders and many helpful discussions with Dr. D. Hoelzer of ORNL. We also thank Doug Klingensmith (UCSB) for his contributions to the SANS experiments. We acknowledge the support of the National Institute of Standards and Technology, U.S. Department of Commerce, in providing facilities used in this work. This research was supported by DOE Office of Fusion Energy Science (Grant # DE-FG03-94ER54275) and the INERI DOE Office of Nuclear Energy through a subcontract with ORNL (Grant # 400014112).

References

[1] S. Yamashita, K. Oka, S. Ohnuki, N. Akasaka, and S. Ukai, Phase Stability of Oxide Dispersion-Strengthened Ferritic Steels in Neutron Irradiation, J. Nucl. Mater. 307–311 (2002) 283–288.
[2] J. Saito, T. Suda, S. Yamashita, S. Ohnuki, H. Takahashi, N. Akasaka, M. Nishida, and S. Ukai, Void Formation and Microstructural Development in Oxide Dispersion Strengthened Ferritic Steels During Electron-Irradiation, J. Nucl. Mater. 258–263 (1998) 1264–1268.

[3] K. Asano, Y. Kohno, A. Kohyama, T. Suzuki, and H. Kusanagi, Microstructural Evolution of an Oxide Dispersion Strengthened Steel under Charged Particle Irradiation, J. Nucl. Mater. 155–157 (1988) 928–934.
[4] H. Kinoshita, N. Akasaka, H. Takahashi, I. Shibahara, and S. Onose, Microstructural Change on Electron Irradiated Oxide Dispersion Strengthened Ferritic Steels, J. Nucl. Mater. 191–194 (1992) 874–878.
[5] V. V. Sagaradze, V. I. Shalaev, V. L. Arbuzov, B. N. Goshchitskii, Y. Tian, W. Qun, and S. Jiguang, Radiation Resistance and Thermal Creep of ODS Ferritic Steels, J. Nucl. Mater. 295 (2001) 265–272.
[6] J. S. Benjamin, Dispersion Strengthened Superalloys by Mechanical Alloying, Metall. Trans. (1970) 2943–2951.
[7] T. Okuda and M. Fujiwara, Dispersion Behavior of Oxide Particles in Mechanically Alloyed ODS Steel, J. Mater. Sci. Lett. 14 (1995) 1600–1603.
[8] S. Ukai, T. Nishida, and H. Okada, Development of Oxide Dispersion Strengthened Ferritic Steels for FBR Core Application, (I), J. Nucl. Sci. Technol. 34 (3) (1997) 256–263.
[9] S. Ukai, T. Nishida, T. Okuda, and T. Yoshitake, R&D of Oxide Dispersion Strengthened Ferritic Martensitic Steels for FBR, J. Nucl. Mater. 258–263 (1998) 1745–1749.
[10] M. J. Alinger, G. R. Odette, and D. T. Hoelzer, The Development and Stability of Y-Ti-O Nanoclusters in Mechanically Alloyed Fe-Cr Based Ferritic Alloys, J. Nucl. Mater. 329–333 (2004) 382.
[11] R. W. Siegel, Positron Annihilation Spectroscopy, Annu. Rev. Mater. Sci. 10 (1980) 393–425.
[12] A. Dupasquier, P. Folegati, N. de Diego, and A. Somoza, Current positron studies of structural modifications in age-hardenable metallic systems, J. Phys., Condens. Matter 10 (1998) 10409–10422.
[13] M. J. Alinger, On the Formation and Stability of Nanometer Scale Precipitates in Ferritic Alloys During Processing and High Temperature Service, Ph.D. Thesis, University of California, Santa Barbara (2004) 341.
[14] E. Mader, Ph.D. Thesis, University of California, Santa Barbara (1995).
[15] G. Kostorz, Treatise on Materials Science and Technology - Neutron Scattering, Vol. 15, New York: Academic Press (1979).
[16] ILL Neutron Data Booklet, A.-J. Dianoux and G. Lander (eds.), Institute Laue-Langevin (2001).
[17] T. E. M. Staab, R. Krause-Rehberg, and B. Kieback, Positron annihilation in fine-grained materials and fine powders -an application to the sintering of metal powders, J. Mater. Sci. 34 (1999) 3833–3851.
[18] M. J. Puska, P. Lanki, and R. M. Nieminen, Positron affinities for elemental metals, J. Phys.,: Condens. Matter (1989) 6081–6093.
[19] Y. Kamimura, T. Tsutsumi, and E. Kuramoto, Calculations of positron lifetimes in a jog and vacancies on an edge-dislocation line in Fe, Phy. Rev. B 52 (1995) 879–885.
[20] H.-E. Schaefer, R. Wurschum, R. Birringer, and H. Gleiter, Structure of nanometer-sized polycrystalline iron investigated by positron lifetime spectroscopy, Phy. Rev. B 38 (1988) 9545–9554.
[21] C. Hidalgo, G. Gonzalez-Doncel, S. Linderoth, and J. San Juan, Structure of dislocations in Al and Fe as studied by positron-annihilation spectroscopy, Phys. Rev. B 45 (1992) 7017–7021.
[22] H. Ohkubo, Z. Tang, Y. Nagai, M. Hasegawa, T. Tawara, and M. Kiritani, Positron annihilation study of vacancy-type defects in high-speed deformed Ni, Cu and Fe, Mater. Sci. Eng. A 350 (2003) 95–101.
[23] P. A. Sterne (personal communication 2004).
[24] M. Hasegawa, Y. Nagashima, K. Kawashima, T. Hyodo, S. Yamaguchi, M. Forster, and H.-E. Schaefer, Irradiation-induced voids in alumina single crystal studied by positron annihilation, Nucl. Instrum. Methods B 91 (1994) 263.
[25] Y. Nagai (personal communication 2004).
[26] R. Krause-Rehberg and H. S. Leipner, Positron Annihilation in Semiconductors, Springer, New York (1999).
[27] P. Asoka-Kumar, B. D. Wirth, P. A. Sterne, R. H. Howell, and G. R. Odette, Composition and magnetic character of nanometer-size Cu precipitates in reactor pressure vessel steels: Implications for nuclear power plant lifetime extension, Philos. Mag. Lett. 82 (2002) 609–615.
[28] M. J. Alinger, G. R. Odette, and D. T. Hoelzer, Processing Optimization for Nanocluster Formation in Nanostructured Ferritic Alloys, Metallurgical and Materials Transactions A (to be submitted).

[29] Y. K. Park, J. T. Waber, M. Meshii, C. L. Snead, and C. G. Park, Dislocation studies on deformed single crystals of high-purity iron using positron annihilation: Determination of dislocation densities, Phys.l Rev. B 34 (1986) 823–836.
[30] H. Ohkubo, Z. Tang, Y. Nagai, M. Hasegawa, T. Tawara, and M. Kiritani, Positron annihilation study of vacancy-type defects in high-speed deformed Ni, Cu and Fe, Mater. Sci. Eng. A 350 (2003) 95–101.
[31] H. Kishimoto, M. J. Alinger, G. R. Odette, and T. Yamamoto, TEM Examination of Microstructural Evolution During Processing of 14CrYWTi Nanostructured Ferritic Alloys, J. Nucl. Mater. 329–333 (2004) 369–371.
[32] H. H. Tian and M. Atzmon, Kinetics of Microstructure Evolution in Nanocrystalline Fe Powder During Mechanical Alloying, Acta Mater. 47 (1999) 1255–1261.
[33] M. Klimiankou, R. Lindau, and A. Moslang, Energy-filtered TEM imaging and EELS study of ODS particles and Argon-filled cavities in ferritic-martensitic steels, Micron 36 (2005) 1–8.
[34] H. Schultz, Defect parameters of b.c.c. metals: Group-specific trends, Mater. Sci. Eng. A 141 (1991) 149–167.

A STATISTICAL APPROACH TO FRACTURE TOUGHNESS MODELING OF MA957 USING A σ*-A* CONCEPT—W. J. Yang, M. J. Alinger, T. Yamamoto, and G. R. Odette (University of California, Santa Barbara)

OBJECTIVE

The objective of this study was to model the fracture toughness of MA957 in the cleavage transition with a modified critical stress-critical stressed area (σ*-A*) model to gain insight on the mechanisms leading to the highly anisotropic fracture properties and the very low toughness for crack with fracture planes containing directions parallel to the extrusion direction.

SUMMARY

We modeled the temperature (T) dependent fracture toughness $K_{Jc}(T)$ of MA957 based on a statistically modified critical stress-critical stressed area (σ*-A*) concept. The finite element (FE) method was used to simulate the stress-strain fields as a function of the applied loading K_J at different T in terms of the area (A) encompassed by a specified normal stress contour (σ). Ideally the critical stress (σ*) is defined by the point of intersection of A(σ) plots at various T. However, a statistically mediated range of A* was recognized in our model, corresponding to the intrinsic distribution of K_{Jc}: thus the point at which the A(σ) at various T experience the maximum number of intersections was used to define σ*. The fracture toughness of MA957 is strongly dependent on the specimen orientation. Analysis of cleavage initiation in the L-R orientation, with the highest K_{Jc} yielded the highest σ* ≈3600 MPa. In contrast, the σ* for the C-L orientation, with the lowest K_{Jc}, yielded the lowest σ* ≈2850 MPa, while for the C-R orientation with intermediate K_{Jc}, σ* ≈3000 MPa. In the latter two cases, the ligament planes contain directions parallel to the extrusion direction. However, the A* were roughly similar for all orientations ranging from ≈30 to 400 μm^2. This is probably a result of a common distribution of cleavage initiation sites in the form of μm-scale Al_2O_3 particles aligned in the extrusion direction. The A*-σ*, was used to model median $K_{Jc}(T)$ and the corresponding curves at high and low fracture probabilities determined from a Weibull analysis. The model is in good agreement with previously measured K_{Jc} data, but requires a K_{min} of 10 MPa√m in the C-L orientation, which less than the standard Master Curve (MC) value of 20 MPa√m. We conclude that the low toughness direction is due to both intrinsic crystallographic and microstructurally mediated factors.

PROGRESS AND STATUS

Introduction

Iron-chromium based alloys, strengthened with a high number density of nanometer-scale yttrium-titanium-oxygen clusters (NCs) have demonstrated outstanding high temperature creep strength [1]. Mechanical alloying (MA) ferritic powders with Y_2O_3 and Ti by high-energy ball milling, followed by consolidation at elevated temperature produces nm-scale, coherent Y-O-Ti solute clusters (NCs), as well as a more typical fine-to-coarser scale incoherent dispersed oxide particles [2,3]. We refer to these materials as nanostructured ferritic alloys (NFAs). The NCs are generally believed to be responsible for the high creep strength of NFAs. This high strength, coupled with high corrosion resistance, offers great promise for elevated temperature applications to fusion and advanced fission structures [4,5]. However, a challenge in the development of these alloys is maintaining adequate fracture toughness in combination with the high creep strength. Low toughness is a potential problem with these alloys since, in common with other BCC alloys, NFAs exhibit a ductile-to-brittle fracture mode transition over a characteristic range of T; and the very high strength of NFAs would be expected to result in decreased toughness relative to that of conventional steels.

We have previously characterized the tensile and fracture toughness of as-hot extruded NFA MA957, showing that this alloy has highly anisotropic properties and very low fracture toughness in the C-L and C-R orientations [6]. MA957 is hot extruded at 1150°C resulting in both anisotropic grains (≈0.5 - 5 μm) elongated in the extrusion direction and crystallographic texturing. Further Al_2O_3 impurity inclusions are

aligned as stringer particles in the extrusion direction. Thus a basic understanding of the micromechanical mechanisms controlling cleavage fracture, and how they relate to the underlying alloy structures, is critical to developing NFAs with adequate toughness. Three possible explanations for the anisotropy in the fracture properties and low toughness are proposed: 1) impurity alumina (Al_2O_3) particles from the ferrochrome powder source of the master alloy aligned in the extrusion direction provide geometrically favorable cleavage initiation sites; 2) the anisotropic grain size is effectively larger in the extrusion direction reducing the critical stress for microcracking; and 3) high degree of (-11-1)[110] and (-111)[110] crystallographic texture imparted by hot extrusion produces a intrinsically brittle cleavage orientation.

Experimental Procedures and FE Stress Field Simulations

The fracture toughness and tensile data for MA957 were reported in an earlier publication [6]. Fracture tests were performed at various temperatures on pre-cracked a/W≈0.5, W = B 1/3, Charpy sized (3.33x3.33x18.33 mm) bend bars in three orientations with respect to the extrusion direction shown in Fig. 1: L-R - longitudinal/length-radial crack plane; C-R - circumferential-transverse/length-radial crack plane; and C-L - circumferential-transverse/length longitudinal crack plane. The elastic and elastic-plastic $K_{Jc}(T)$ were evaluated in accordance with ASTM standard E 1921.

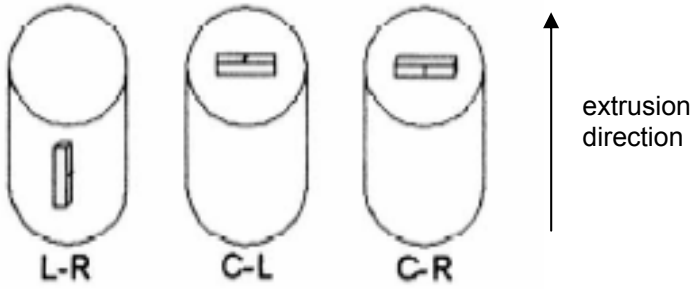

Fig. 1. The fracture specimen orientations reference to the extrusion direction.

Cleavage fracture initiates by the rapid propagation of a cleavage microcrack from a broken brittle cleavage trigger particle in the highly stressed volume ahead of the crack tip. Microcrack propagation requires a local critical Griffith type stress that depends on: a) the cracked particle size; b) its orientation with respect to the adjacent ferrite grain; and c) the corresponding orientation-dependent ferrite micro-crack arrest toughness. The cleavage trigger particles are statistically distributed in size and orientation; thus specimen-to-specimen sampling variations lead to intrinsic scatter in K_{Jc}. The greater the stressed volume, V = BA(σ), the higher the likelihood of activating a weakest link trigger particle leading to cleavage fracture. For this work, a modified critical stress-statistical stressed area (σ*-A*) concept was used to model $K_{Jc}(T)$ [7,8].

Plane strain 2D-FE calculations were used to simulate the stress distribution in front of a blunting semi-circular crack tip using the commercial ABAQUS code and the measured true stress-strain constitutive data fit to simple analytic functions. The quarter symmetry mesh was composed of 826 8-node isoparametric elements with a total of 2607 nodes. The mesh was highly refined crack tip with an initial radius of 1 μm. Post processing codes were used to evaluate A(σ,T) for normal to yield stress ratios σ/σ_y from ≈2.4 to 3.6. Plots of A(σ,T) versus σ were used to define σ* for each orientation.

Results and Discussion

Figure 2 shows the A(σ,T) versus σ. Recognizing that the K_{Jc} data are statistically distributed, we defined σ* at the point of the maximum number of intersections of the A(σ,T) curves. The A*-σ* varied with orientation, as shown by the vertical lines in Fig. 2. In the L-R orientation (Fig. 2a) σ* ≈3600 MPa, while σ* ≈2850 MPa in the C-L orientation (Fig. 2b) and σ* ≈3000 MPa (Fig. 2c) in the C-R orientation. The fracture toughness was found from A(J = J_c) = A* trajectories for each orientation. The cleavage fracture probability, F, for a three-parameter Weibull distribution is:

$$F = 1 - \exp\left[-\left(\frac{K_{JC} - K_{\min}}{K_O - K_{\min}} \right)^4 \right] \qquad (1)$$

Here K_{min} is the minimum fracture toughness and K_O is the K_J at F = 0.632. The points labeled a are for a high F, while those labeled c are for a low F. The intermediate points, labeled b, was taken as the nominal median value of K_{Jc} at F = 0.5. The values of A* for a, b, and c and the various orientations are summarized in Table 1.

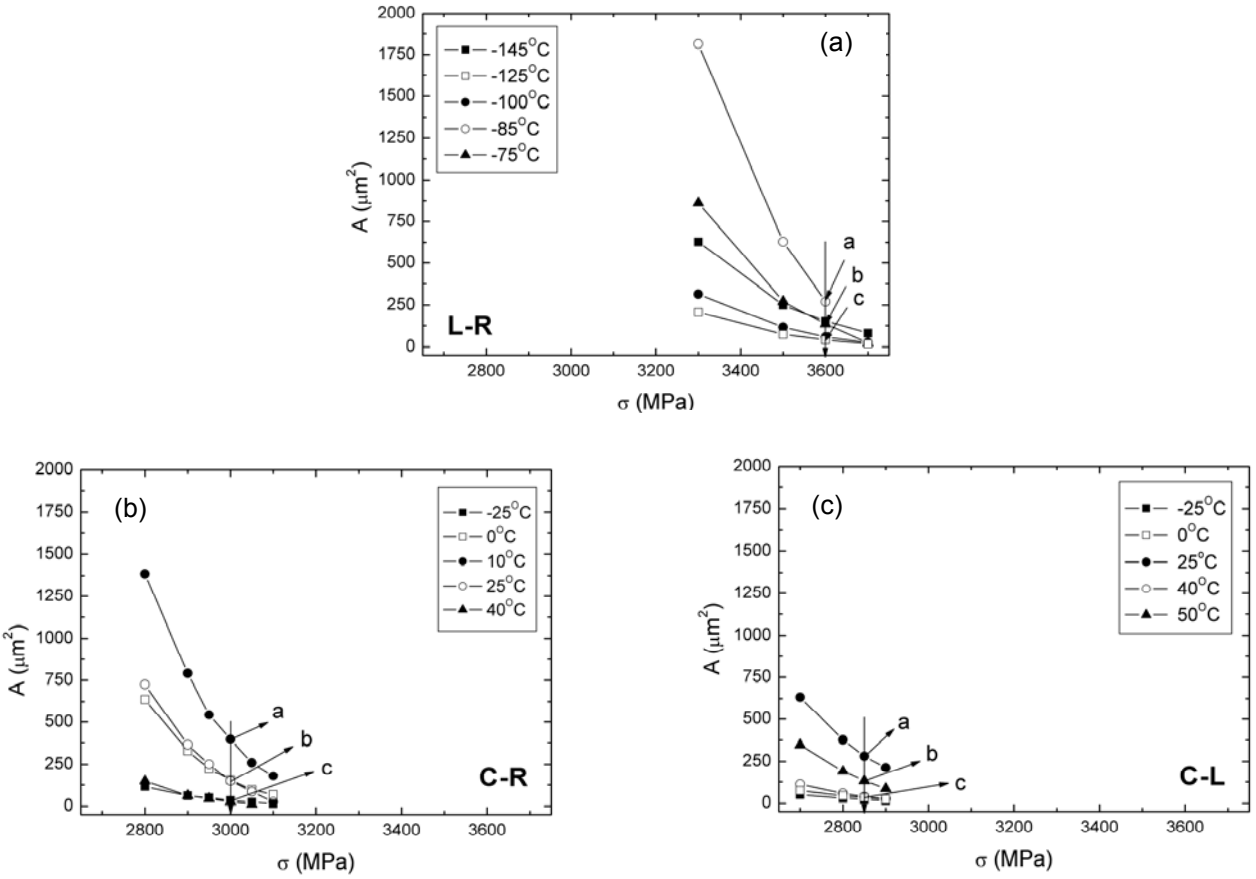

Fig. 2. The A(σ,T) versus σ for each orientation and the points of maximum intersection defining σ* (lines) for: (a) L-R; (b) C-R, and (c) C-L.

Table 1. The local σ* (MPa) and A* (μm^2) for cleavage fracture properties for each orientation

	σ*, MPa	A* for a	A* for b	A* for c
L-R	3600	270	144	49
C-R	3000	397	151	29
C-L	2850	281	132	30

The corresponding K_{Jc}(T) curves cleavage for a, b, and c are shown in Fig. 3 along with a master curve for comparison. As shown in Fig. 3a, the data for the L-R orientation is consistent with K_{min} = 20MPa√m with the high (a) and low (c) fracture probability curves falling at F = 0.89 and 0.09, respectively. A K_{min} = 20MPa√m also provides a reasonable fit to the C-R data shown in Fig. 3b, with the a and c points falling at F = 0.98 and 0.01, respectively. However, fitting the C-L data (Fig. 3c) requires a lower K_{min} = 10MPa√m with the a and c points falling at F = 0.97 and 0.07, respectively. These results suggest modified σ*-A* models and the master curve (MC) concept can be applied to NFAs.

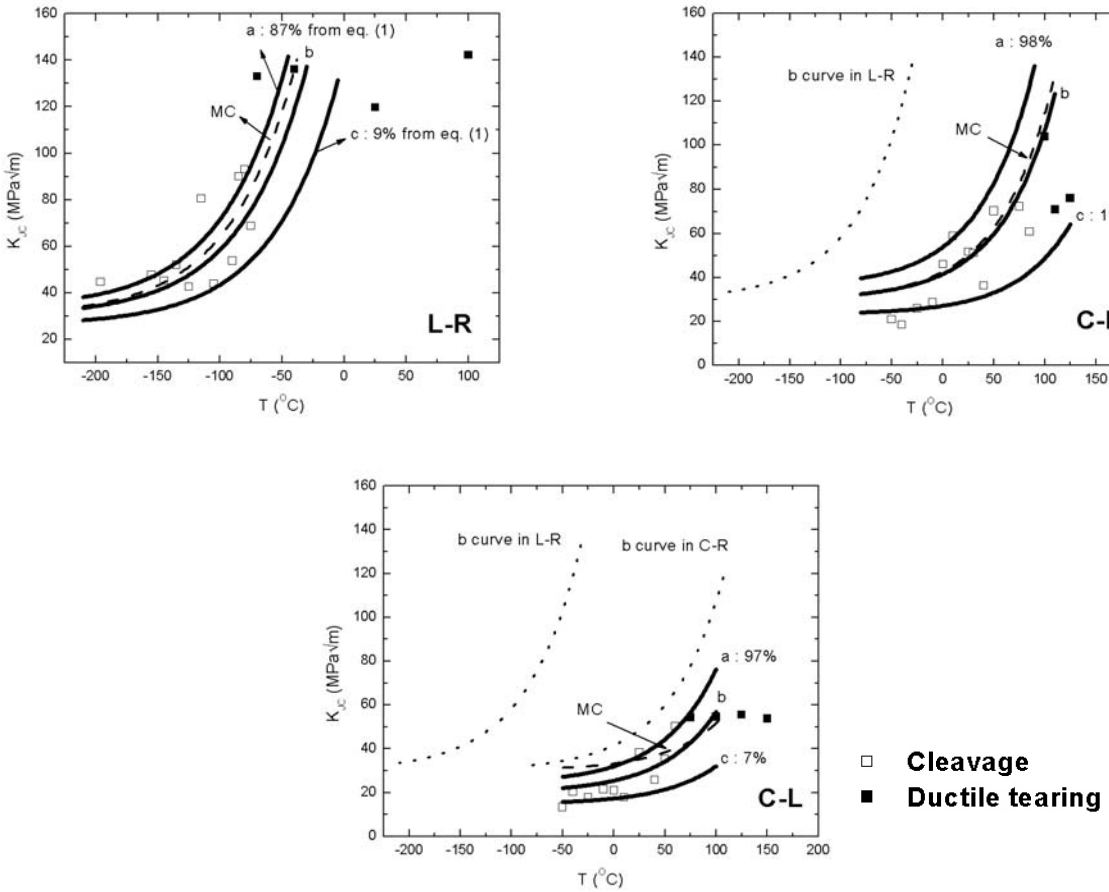

Fig. 3. Predicted K_{Jc}(T) curves for the σ*-A* model for the median and specified fracture probability (F) conditions for the: a) L-R; b) C-R, and c) C-L orientations.

Discussion - The Physical Basis for Anisotropic and Low Toughness Orientations

The model-based analysis of the MA957 fracture data provides new insight regarding the challenges facing developing NFAs with adequate fracture toughness. We had previously argued that the low toughness in the C-L and, to a slightly lesser extent, in the C-R orientations was due to the stringers of impurity Al_2O_3 particles aligned in the extrusion direction. Thus if this were the sole reason for low toughness, the challenge would simply be to develop cleaner, inclusion free alloys. However this explanation does not rationalize the high toughness in the L-R direction which, as illustrated in Fig. 4a, is at least partially due to the tendency of the cracks to diverge out of the nominal ligament crack plane. This is in contrast to the planar cleavage fracture surfaces in the C-R and C-L orientations shown in Figs. 4b and c. The torturous fracture path in the L-R orientation results in higher K_{Jc}, but the underlying reason for the out-of plane cracking is likely due to the existence of an easy cleavage system oriented for crack propagation in the extrusion direction die to texturing.

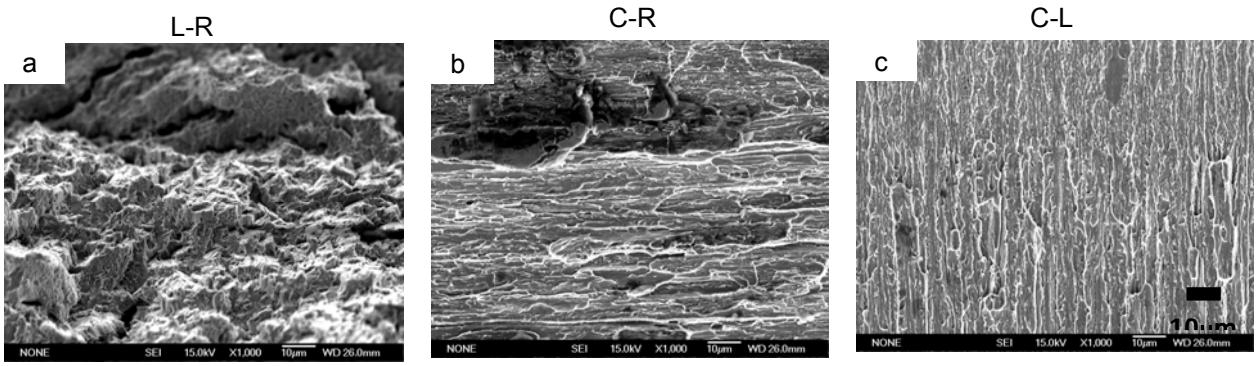

Fig. 4. Fracture surfaces for the: a) L-R; b) C-R; and c) C-L orientations.

Figure 5 schematically illustrates the concept of crack propagation on the easy cleavage system, which is the (100) plane in [010] and [011] directions in ferrite, and trigger particle-effective grain size effects. More detailed crystallographic descriptions along with quantitative analysis of the microstructure σ^* relations will be given in future reports. The particle-stringer and elongated grain orientations are shown by the colored elliptical (C-R and C-L) and circular (L-R) shaped symbols. The easy cleavage plane is shaded with blue and the ligament fracture plane in grey. Qualitatively, the larger grain particle and grain dimensions in the C-L orientation in the direction of crack propagation are expected to lead to the lowest σ^*. While the effective scale of the microstructure is smaller, the C-R orientation still has access to the easy cleavage system in with a extrusion direction lying in the ligament plane, thus has an intermediate σ^*. However, in the L-R orientation the cracks must kink out of the ligament plane to access the easy cleavage system. In combination with the smallest effective microstructure size, this leads to the highest σ^*. The strong tendency for propagation in the extrusion direction is shown in Fig. 6 for cracks produced by Knoop microhardness indentations at –196°C.

If verified by additional research, these concepts have important implications to the potential to develop NFAs with a combination of high strength and adequate toughness. In particular, while the clean alloy, inclusion and carbide free approach is still attractive extruded product form may still have intrinsically low toughness due to the presence of elongated grains and crystallographic texturing. The toughness may be improved with equiaxed and randomly oriented grains in HIPed product forms, but may still be limited by high levels of alloy strength.

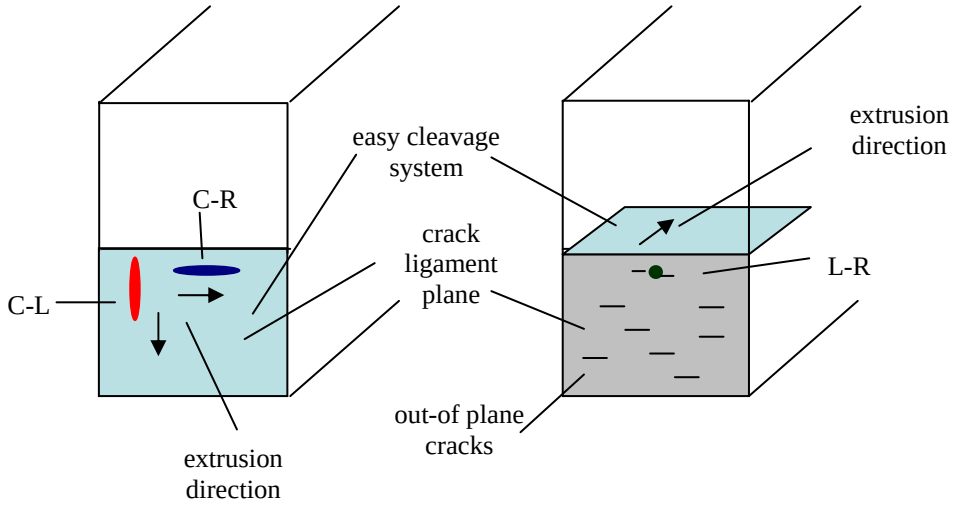

Fig. 5. Schematic illustration of the possible mechanisms leading to the strong orientation dependence and low values of C-R and especially C-L K_{Jc}.

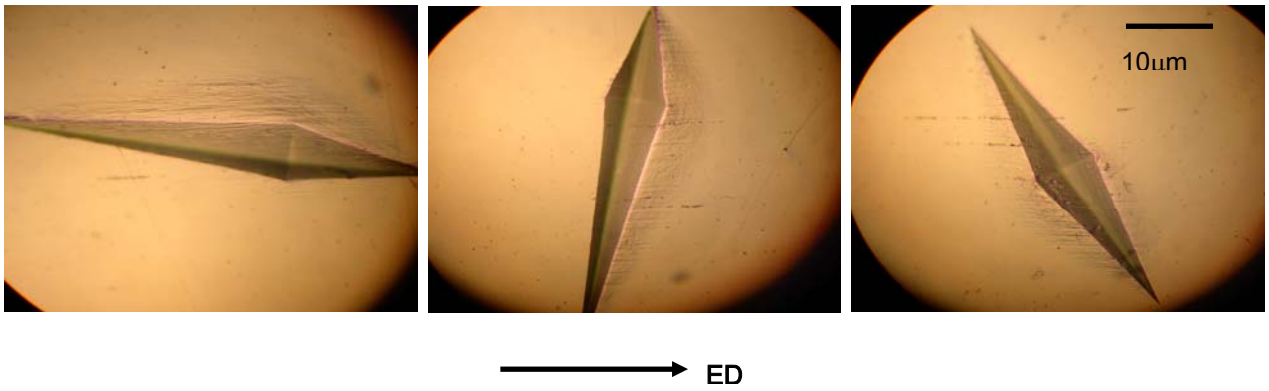

Fig. 6. Microcracks produced by various Knoop hardness indentations at -196°C, all propagating in the extrusion direction.

Future Research

The validity of the concepts proposed in this report will be evaluated in detail in future studies, including:

TEM assessments of the fracture surface crystallographic orientations, trigger particle sites and dislocation structures on FIBed specimens taken from the crack tip process zone.

Confocal microscopy quantification of the topology of the fracture surfaces and corresponding fracture reconstruction studies of initiation sites.

Analysis of the alumina inclusion size, shape, and orientation distributions.

Quantitative analysis of the relationship between the trigger particles, crack tip stress fields, and ferrite micro-arrest toughness.

Analysis of fracture toughness in simple Fe and model NFAs alloys produced by HIPing and hot extrusion.

Acknowledgements

The authors would like to thank Dr. D. Gelles of PNNL for supplying the MA957 and would like to acknowledge D. Gragg and M. L. Hribernik of UCSB for their experimental assistance and valuable discussion.

References

[1] S. Ukai, M. Harada, H. Okada, M. Inoue, S. Nomura, S. Shikakura, K. Asabe, T. Nishida, and M. Fujiwara, Nucl. Mater. 204 (1993) 65.
[2] T. Okuda and M. Fujiwara, J. Mater. Sci. Lett. 14 (1995) 1600.
[3] M. J. Alinger, G. R. Odette, and D. T. Hoelzer, J. Nucl. Mater. 329–333 (2004) 382.
[4] J. J. Fisher, US patent 4,075,010, Dispersion Strengthened Ferritic Alloy for use in Liquid Metal Fast Breeder Reactors (February 21, 1978).
[5] G. D. Smith and J. J. deBarbadillo, in J. J. deBarbadillo et al. (eds.), Structural Applications of Mechanical Alloying, International, Materials Park, Ohio (1994) 117.
[6] M. J. Alinger, G. R. Odette, and G. E. Lucas, J. Nucl. Mater. 307–311 (2002) 484.
[7] H. J. Rathbun, G. R. Odette, M. Y. He, G. E. Lucas, and T. Yamamoto, NUREG/CR-6790.
[8] G. R. Odette, T. Yamamoto, H. J. Rathbun, M. Y. He, M. L. Hribernik, and J. W. Rensman, J. Nucl. Mater. 323 (2003) 313.

4.0 COPPER ALLOYS

No contributions.

5.0 REFRACTORY METALS AND ALLOYS

MICROSTRUCTURAL ANALYSIS ON HELIUM RETENTION OF ION-IRRADIATED AND ANNEALED TUNGSTEN FOILS—N. Hashimoto and J. D. Hunn (Oak Ridge National Laboratory), N. Parikh, S. Gilliam, S. Gidcumb, and B. Patnaik (University of North Carolina at Chapel Hill), and L. L. Snead (Oak Ridge National Laboratory)

OBJECTIVE

In order to investigate helium retention characteristics and helium bubble distribution in tungsten, $^{3}He(d,p)^{4}He$ nuclear reaction analysis (NRA), transmission electron microscopy (TEM) and scanning electron microscopy (SEM) were performed. Two forms of tungsten were used, single crystal and polycrystalline, implanted with to $1x10^{19}$ $^{3}He/m^{2}$ and annealed at 2000°C.

SUMMARY

The helium retention characteristics and helium bubble distribution in tungsten were studied using $^{3}He(d,p)^{4}He$ nuclear reaction analysis (NRA) and transmission electron microscopy (TEM) on two forms of tungsten: single crystal and polycrystalline, implanted to $1x10^{19}$ $^{3}He/m^{2}$ at 850°C and annealed at 2000°C. The NRA results revealed that as-implanted single crystal and polycrystalline tungsten exhibited similar helium retention characteristics. Stepwise annealing reduced the helium retention in both single crystal and polycrystalline tungsten when the number of implantation steps and annealing time were increased. The TEM results indicated that microstructure played a large role in helium trapping; the existence of grain boundaries led to significant cavity formation and greater cavity growth. Single crystal tungsten had less trapping sites for helium, allowing long range He diffusion during annealing. The decrease of He retention in polycrystalline tungsten during stepwise annealing was probably due to significant recrystallization, resulting in decrease of grain boundary density.

PROGRESS AND STATUS

Introduction

In an inertial fusion energy (IFE) reactor chamber, the tungsten armor on the first wall will be subjected not only to X-rays and neutrons, but also to significant ion fluxes. These fluxes vary in type, energy, and intensity and fall into roughly two categories: High-energy ions in the 1-10's of MeV range (C, ^{4}He) and ions in the 0.1-1 MeV range (He, D, T, H). While the chamber designs to date have focused on evaporative losses of first wall or armor due to the impinging X-ray flux from the target fusion, they have largely ignored degradation of mechanical properties due to neutron or ion induced compositional change and displacement damage as well as losses of material at the surface due to sputtering (chemical and physical), blistering, and exfoliation. The present paper focuses on potential damage arising from the helium ion flux.

The most deleterious ions are helium (and hydrogen, with potential synergistic effects) in the energy range 0.1-1MeV, for which the stopping range is on the order of 0.1-1 μm. These ions cause formation of blisters with skin thickness on the order of 0.1-1 μm as well, and hence exfoliation of μm thick layers occurs above a threshold fluence. Studies on ceramics [1] and metals [2-4] show that blistering occurs in all He-implanted materials at room temperature and fluences around ~$3x10^{21}/m^{2}$, and exfoliation occurs for fluences around ~$10^{22}/m^{2}$. These critical fluences decrease with increasing temperature. The critical fluence also increases slightly with increasing penetration depth (ion energy), due to range straggling effects. For a He flux of ~$2x10^{18}$ $/m^{2}s$ this implies that an exfoliation layer equal to the range of the He ions (~1 micron for the 1 MeV He ions) would form about once per hour and a surface erosion loss of about ~1 cm per year would result for the 1 MeV He ions. At 100% duty factor, this is equal to a surface erosion loss of ~2 cm per year. This implies that the He ions should be stopped from reaching the bare wall in order to avoid unacceptable wall erosion.

In an IFE chamber (drywall option), the tungsten first wall (T_M=3410°C) is expected to reach ~2500°C for ~1 μs after each pulse. Helium ion bombardment creates vacancies within W that trap He and act as nucleation sites for He bubble growth. Considerable data are available on blistering due to low energy He ion implantation near room temperature [5]. Trapped He concentration and bubble sizes increases with dose and irradiation temperature due to increasing defect density and thermal mobility. At room temperature, growth of He bubbles beneath the surface causes blistering and surface exfoliation. The critical doses decrease with temperature and increase with ion energy (in ~1-2 MeV He range). However, there is insufficient information on the effects for pulsed implantation and anneal conditions for tungsten.

Helium retention characteristics and helium bubble distribution in tungsten were studied using ^{3}He(d,p)^{4}He nuclear reaction analysis (NRA), transmission electron microscopy (TEM) and scanning electron microscopy (SEM). Two forms of tungsten were used, single crystal and polycrystalline, implanted with to 1x10^{19} ^{3}He/m^2 and annealed at 2000°C.

Experimental

Two forms of tungsten were used in this study: single crystal and polycrystalline. They were implanted at 850°C with 1.3 MeV ^{3}He (range is ~1.67 μm, obtained from TRIM code) to 1x10^{19} ^{3}He/m^2 (flux was 1x10^{15} ~10^{16} ^{3}He/m^{2}s) at the University of North Carolina at Chapel Hill. Nuclear reaction analysis (NRA) using the *^{3}He(d,p)^{4}He* reaction [6] was performed to analyze the *^{3}He* content in the implanted specimens. Deuterons of 780 keV incident on W foils implanted with ^{3}He at a depth of 1.7 microns produces a spectrum of ~13 MeV protons, alphas, and backscattered deuterons. Due to overlap of the energy spectra of alphas and backscattered deuterons, the use of alphas for profiling ^{3}He was not possible. Mylar foils were used to stop the lower energy alphas and backscattered deuterons, but allowed transmission of the higher energy protons. Figure 1 shows the resulting spectrum from NRA, indicating the higher energy proton peak from the *^{3}He(d,p)^{4}He* reaction and other peaks at low energy from a reaction on the surface [7]. After implantation and NRA, flash annealing at ~2000°C was performed for each specimen. The flash annealing consisted of heating to 2000°C within 5 seconds, annealing at 2000°C for 2 seconds, and cool down to 850°C in 5 seconds. Also, implantation in small steps with annealing between steps was performed using a computer automated system that allowed for 1000-step runs to be completed in 30 hours.

TEM specimens were prepared using focused ion beam micromachining (FIB). The FIB used a focused ion beam for controlled removal of material by sputtering. The FIB preparation involved sputter-coating the sample with Pt then depositing a thick protective layer of Pt using the FIB. Machining of the TEM specimen was then performed using 30 keV Ga^+ ions at room temperature.

Results

Nuclear Reaction Analysis (NRA)

Figure 1 shows He retention profiles of the single crystal and polycrystalline tungsten implanted with 10^{19} He/m^2 at 850°C with intermittent annealing at 2000°C [7]. In this experiment, '1 step' means annealing just once after implantation with 10^{19} He/m^2 and '100 steps' and "1000 steps" denotes annealing after each implantation of 10^{17} or 10^{16} He/m^2 and repeating this cycle 100 or 1000 times, respectively. The larger number of steps better simulate the condition of an IFE chamber. As seen in Fig. 1, as-implanted single crystal and polycrystalline tungsten exhibited similar helium retention characteristics. In addition, a flash anneal at 2000°C had no effect on the retention of helium. It also appears that stepwise annealing reduces the helium retention for 100 steps and even more for 1000 steps. Actually, He implantation in 1000 cycles resulted in a decrease of the retained helium by 95% of the implanted amount for single crystal compared to

70% of that for polycrystalline tungsten. This result suggests a preference for single crystal over polycrystalline tungsten due to less He retention. For this implantation condition, neither specimen showed any blistering or exfoliation.

(a) (b)

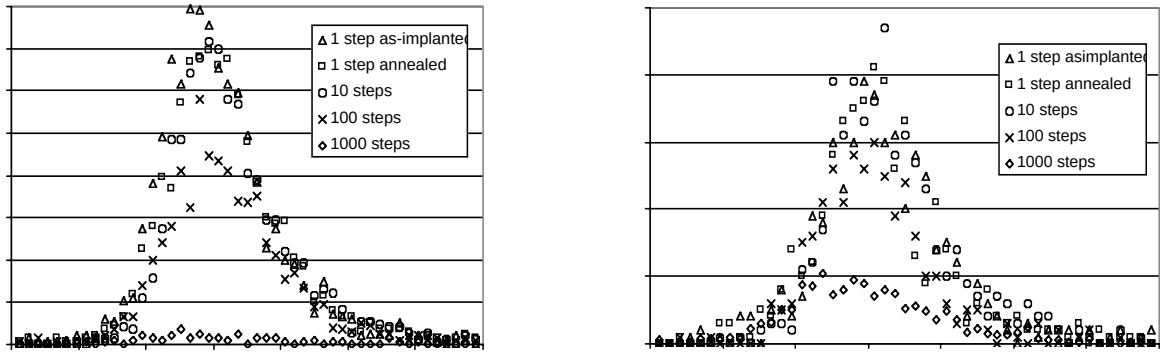

Fig 1. Proton spectra for (a) single crystal and (b) polycrystalline tungsten implanted at 850°C and flash annealed at 2000°C in 1, 10, 100, and 1000 cycles to reach a total dose of 10^{19} He/m^2. The sample implanted with the total dose in one cycle was analyzed before and after the 2000°C anneal [7].

Microstructural Analysis

Single Crystal Tungsten

Figures 2(a) and (b) show microstructures (cross section views) of single crystal tungsten implanted with 10^{19} He/m^2 at 850°C followed by annealing at 2000°C in a single step and in 1000 steps, respectively. No precipitates were observed in either case. Figure 2 (a) shows many tiny cavities (2~3 nm in diameter). The cavity distribution seemed to correspond to the profile of helium retention. Large numbers of cavities were distributed at a depth of 1.67 μm from the surface. In this implanted condition, no cavities were observed in the region from the surface to 1 μm depth. In contract, no visible cavities were observed in the 1000 step annealed single crystal, shown in Fig. 2(b). This observation is in good agreement with the NRA result (Fig. 1).

Polycrystalline Tungsten

Figure 3 shows the microstructures of polycrystalline tungsten implanted with 10^{19} He/m^2 at 850°C followed by annealing at 2000°C in single step. No precipitate was observed in these cases. Single step annealing led to significant cavity growth at grain boundaries, which act as nucleation sites for He bubbles. Cavities were distributed at a depth of 1.0-1.8 μm from the surface.

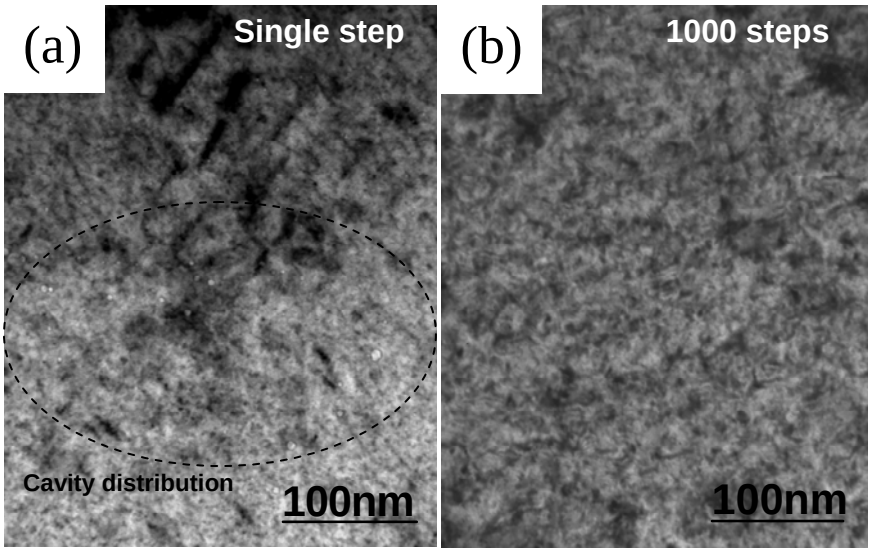

Fig. 2. Microstructures (cross section view) of single crystal tungsten implanted with 10^{19} He/m^2 at 850 °C followed by annealing to 2000 °C in (a) single step and (b) 1000 steps.

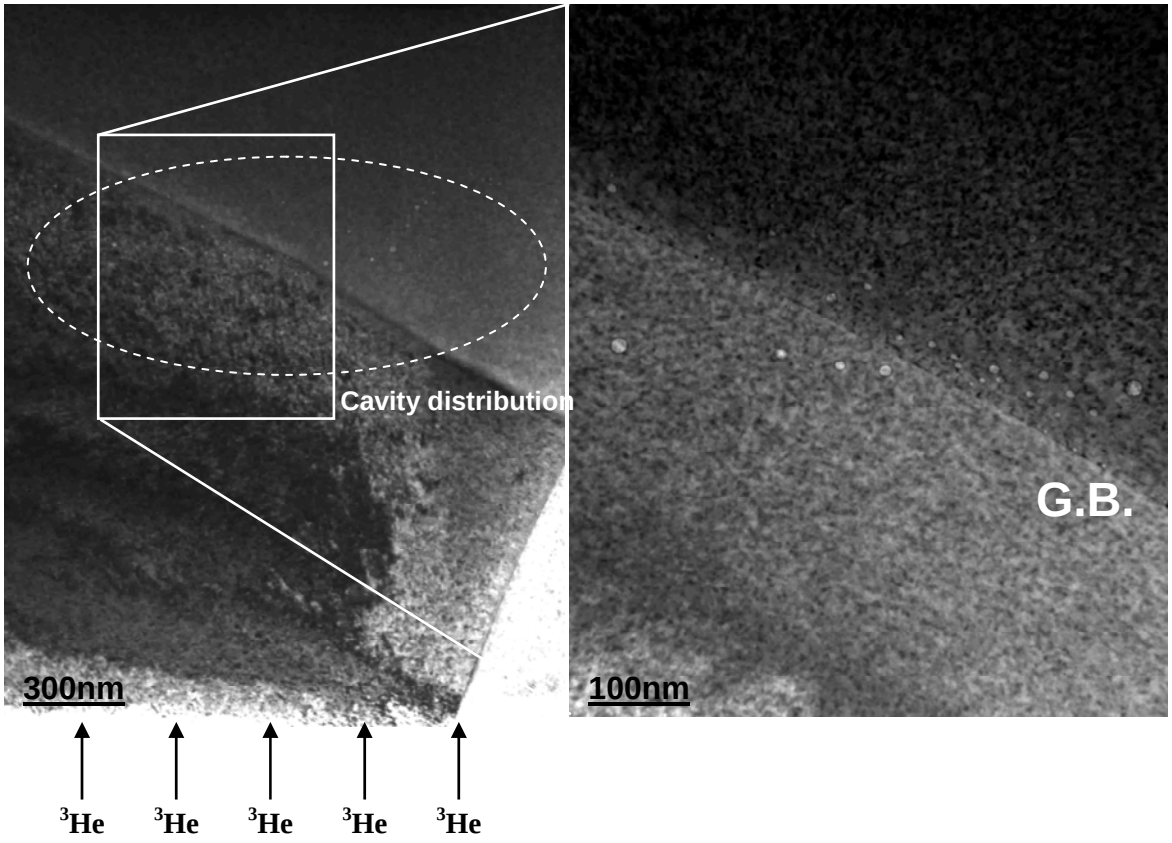

Fig. 3. Microstructures of polycrystalline tungsten implanted with 10^{19} He/m^2 at 850°C followed by annealing at 2000°C in single step.

Figure 4 compares microstructures of polycrystalline tungsten He-implanted and annealed (a) in a single step and (b) in 1000 steps. Annealing in 1000 steps resulted in no visible cavity formation even though the NRA results found polycrystalline tungsten had more He retention than single crystal tungsten. One possible reason is that the amount of helium retention in polycrystalline tungsten during 1000 steps annealing was not enough to form visible cavities (at least 1 nm in diameter).

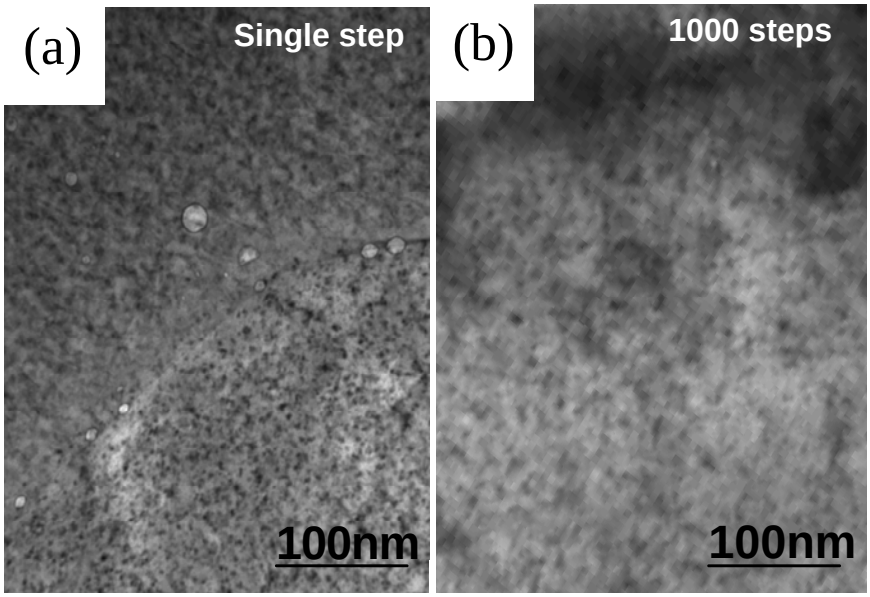

Fig. 4. Microstructures (cross section view) of polycrystalline tungsten implanted with 10^{19} He/m^2 at 850°C followed by annealing to 2000°C in (a) single step and (b) 1000 steps.

Discussion

In general, helium diffusion in a metal matrix is strongly influenced by traps. These traps may be atomic scale defects like impurities and vacancies or extended defects like dislocations, solid precipitates and He bubbles formed at interfaces or in the matrix. It is well known that helium drastically enhances the formation of cavities due to the strong interaction with lattice defects, vacancies and vacancy clusters [8-11]. In order to understand helium retention and/or cavity distribution in tungsten, it is important to have an idea of the cavity development in the grain interior as a function of He generation rate, He content, temperature, time and microstructure. In this experiment, the total helium content, implantation temperature and annealing temperature are constant, while He generation rate, implantation time and annealing time were varied.

Previously, the mechanism for He transport and formation of intense swelling in tungsten was reported [12,13]. With the assumption that the binding energy of a He atom to a vacancy is so high that it never leaves its substitutional site in the lattice, the diffusion coefficient of He atom in single crystal tungsten at 2100°C was estimated to be 10^{-14} m^2/s; annealing at 2000°C for 1 second would result in a He atom diffusion distance of 0.1μm.

The implantation with 10^{19} He/m^2 followed by annealing at 2000°C for 2 sec. resulted in the formation of a large number of tiny cavities in single crystal tungsten [Fig. 2(a)]. Assuming that strong trap sites for He atoms are He-vacancy clusters only, each He atom would diffuse at most 0.2 μm away during annealing. In this case, almost all implanted He would remain in the matrix

and/or form cavities with vacancies. Actually, the single step annealed single crystal tungsten indicated no cavities in the region from the surface to 1 μm in depth, supporting this model. On the other hand, no visible cavities were observed in the 1000 step annealed single crystal tungsten [Fig. 2(b)]. The 1000 step He-implantation and annealing induced very small amount (10^{16} He/m^2) of He atoms and annealed at 2000°C for 2 seconds in each step. During each annealing step, implanted He can diffuse up to ~0.1mm. Since the implanted concentration of He is relatively low, the probability of forming helium bubble nuclei is rather low (few He-He encounters). During 1000 steps, the implanted He can diffuse up to ~100mm which is much greater than the implant depth of 1.7mm. Therefore, most of the implanted He can diffuse to the surface of specimen interior and very few bubbles are nucleated.

Single step annealing of polycrystalline tungsten also allowed implanted He atoms to remain in the matrix and form cavities just as the case for single crystal tungsten. The polycrystalline tungsten includes many grain boundaries, which could act as nucleation sites for cavities with vacancies around the area He remained when grain boundary diffusion is not dominant. The existence of grain boundary actually led to significant cavity formation and greater cavity growth than in single crystal tungsten. The 1000 step implantation and annealing of polycrystalline tungsten resulted in no visible cavities observed. One of the reasons would be due to insufficient He amount in each step for cavity formation that is the same as the case of single crystal tungsten. The other possible reason is any grain growth of the polycrystalline tungsten during annealing at 2000°C for total 50 minutes.

Figure 5 shows scanning electron microscope (SEM) images of polycrystalline tungsten as-implanted (a) and implanted with 10^{19} He/m^2 at 850°C followed by annealing at 2000°C in single step (b) and 1000 steps (c). As seen in Fig. 5(a), the average grain size of as-implanted polycrystalline tungsten is about 1μm, while the polycrystalline tungsten implanted and annealed at 2000°C in a single step indicated larger grain (3~10 μm in diameter). Figure 5 shows that the 1000 step annealing of polycrystalline tungsten resulted in significant grain growth (30~50 μm in size). TEM samples prepared by FIB were 3x5 μm in size, meaning that there was a very low probability to observe grain boundaries within the depth of He distribution. This would be the other reason why polycrystalline tungsten annealed in 1000 steps showed no visible cavities. However, the NRA results showed more He retention in polycrystalline tungsten compared to single crystal tungsten. This is probably because some of the implanted He remained in the matrix during recrystallization and formed cavities in the vicinity of recrystallized grain boundaries.

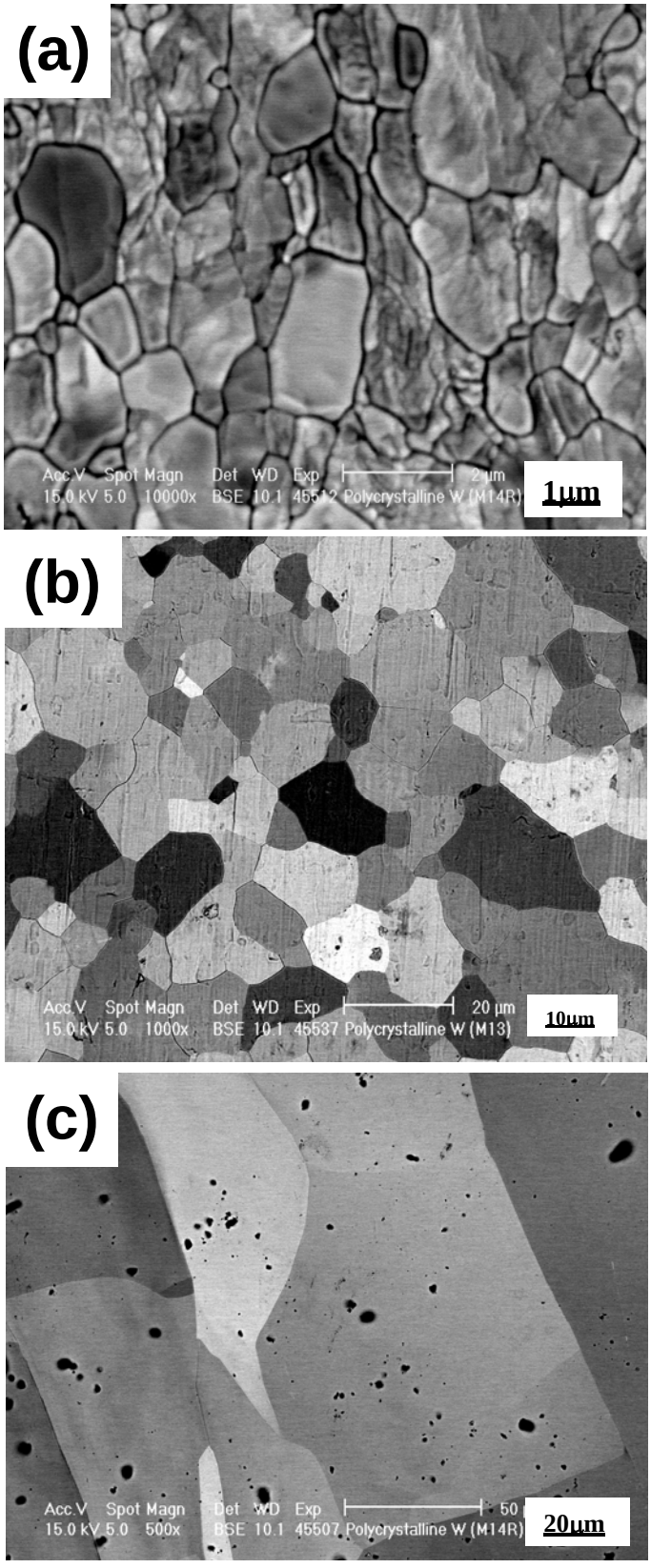

Fig. 5. SEM micrographs polycrystalline tungsten (a) as-implanted and implanted with 1 at 850°C followed by annealing to 2000°C in (b) single step and (c) 1000 steps.

Acknowledgements

This research was sponsored by the U.S. Department of Energy High Average Power Laser Program, under contract No. DE-AC05-00OR22725 with UT-Battelle, LLC.

References

[1] S. J. Zinkle, Gas assisted cavity formation and blistering in ceramics, in Fusion Materials Semiannual Progress Report for Period Ending June 30, 2000, DOE/ER-0313/28, 187–197.
[2] G. M. McCracken, The behavior of surfaces under ion bombardment, Rep. Prog. Phys. 38 (1975) 241–327.
[3] K. L. Wilson, Data compendium for plasma-surface interactions: Section 8. Blistering, Nuclear Fusion special issue (1984) 85–94.
[4] E. L. Fleischer and M. G. Norton, Noble gas inclusions in materials, Heterogeneous Chemistry Review 3 (1996) 171–201.
[5] H. Iwakiri, K. Yasunaga, K. Morishita, and N. Yoshida, J. Nucl. Mater. 283–287 (2000) 1134–1138.
[6] W. H. Geist, The $^{3}He(d,p)^{4}He$ reaction at low energies: Doctoral dissertation, UNC-Chapel Hill, 1998.
[7] S. Gilliam, S. Gidcumb, N. Parikh, B. Patnaik, J. D. Hunn, and L. L. Snead (to be published in the Journal of Nuclear Materials).
[8] A. A. Haasz, J. W. Davis, M. Poon, and R. G. Macaulay-Newcombe, J. Nucl. Mater. 258–263 (1998) 889.
[9] M. Kaminsky, Radiation Effects on Solid Surfaces, American Chemical Society, Washington, D.C., 1986.
[10] K. Shinohara, A. Kawakami, S. Kitajima, Y. Nakamura, and M. Kutsuwada, J. Nucl. Mater. 179–181 (1991) 246.
[11] H. Iwakiri, H. Wakimoto, H. Watanabe, and N. Yoshida, J. Nucl. Mater. 258–263 (1998) 873.
[12] V. N. Chernikov and A. P. Zakharov, J. Nucl. Mater. 165 (1989) 89–100.
[13] V. N. Chernikov, Ju. V. Lakhotkin, H. Ullmaier, H. Trikaus, P. Jung, and H. J. Bierfeld, J. Nucl. Mater. 212–215 (1994) 375–381.

6.0 AUSTENITIC STAINLESS STEELS

No contributions.

7.0 MHD INSULATORS, INSULATING CERAMICS, AND OPTICAL MATERIALS

STUDY OF THE LONG-TERM STABILITY OF MULTI-LAYER MHD COATINGS FOR FUSION REACTOR APPLICATIONS – B. A. Pint, K. L. More, J. L. Moser (Oak Ridge National Laboratory), A. Jankowski (Lawrence Livermore National Laboratory), and A. Suzuki (University of Tokyo, Japan)

OBJECTIVE

The objective of this task is to assess the long-term, high-temperature compatibility of high electrical resistance, multi-layer coatings with lithium at high temperatures. Electrically insulating coatings on the first wall of magnetic confinement reactors are essential to reduce the magnetohydrodynamic (MHD) force that would otherwise inhibit the flow of the lithium coolant. An assessment of the crack tolerance for these coatings determined that a multi-layer coating with metal and ceramic layers was needed to prevent Li from wetting cracks or defects in a single-layer ceramic coating. Experimental compatibility tests are being conducted on bulk materials and single and multi-layer coatings.

SUMMARY

Characterization of electron beam physical vapor deposition (EB-PVD) Y_2O_3 coatings after exposure to Li showed significant changes in the microstructure. Single and bi-layer PVD coatings of Er_2O_3 and Er_2O_3/vanadium have been fabricated and initial characterization has started. A new test rig was constructed for measuring coating resistivity during contact with Li at temperatures up to 500°C. Initial performance of the Er_2O_3 coatings in an in-situ test showed loss of insulating behavior after the Li became liquid (180°C) and significant degradation after exposure to Li at 500°C.

PROGRESS AND STATUS

Introduction

The current focus of the U.S. MHD coating program is the fabrication and testing of multi-layer coatings with a combination of ceramic, high-resistance layers and vanadium layers to prevent interaction between Li and the ceramic layer. A recent evaluation of the effects of cracks and defects on the performance of single-layer MHD coatings concluded that only a very small fraction of through-thickness cracks could be tolerated, assuming that Li will wet the cracks and short the coating.[1] Besides wetting, Li ions also could dope the ceramic layer, thereby increasing its conductivity. Thus, a more robust flaw-tolerant coating system would have a dense metallic layer in contact with the flowing Li. Vanadium would be the prime metallic coating candidate among refractory metals with good Li compatibility at 700°C. This strategy switches the main lithium compatibility requirement from the ceramic layer to the metallic layer and thereby increases the number of candidate materials. However, the ceramic layer must have some degree of compatibility in case the metallic layer has a defect or fails in service.

The results presented in this report include the final characterization work for the EB-PVD Y_2O_3 coatings before and after capsule exposures to Li at 800°C. The compatibility results for these coatings have been presented previously.[1-3] Initial results for a new batch of single layer Er_2O_3 coatings and two layer Er_2O_3/V coatings fabricated in late 2004 also are included.

Experimental Procedure

Current work focused on V-4Cr-4Ti 15mm diameter substrates with Y_2O_3 , Er_2O_3 or Er_2O_3/V coatings made by EB-PVD at Lawrence Livermore National Laboratory (LLNL). Before and after exposure to Li, Y_2O_3 coated specimens were sectioned by focused ion beam (FIB) thinning and examined by scanning electron microscopy (SEM) and analytical transmission electron microscopy (TEM). Additional information

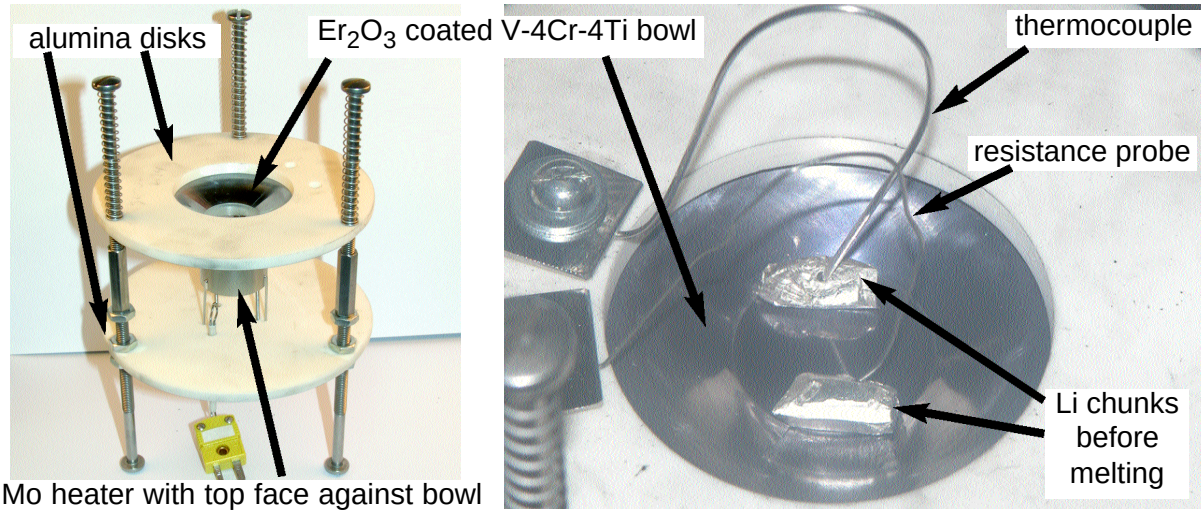

Fig. 1. Photographs of the in-situ rig in an ORNL glove box used to measure resistance of the coatings in contact with liquid Li at temperatures up to 500°C.

about the as-deposited Y_2O_3 coatings are included elsewhere.[1-3] Coatings of Er_2O_3 and Er_2O_3/V were received in late 2004 and characterization is currently underway. An initial test was performed to evaluate a new in-situ test rig shown in Fig. 1. The unit was designed to measure resistance of a coating on a bowl shaped specimen filled with 0.5g of Li at temperatures up to 500°C in a glove box (to minimize Li reaction with O and N). Springs hold the bowl in contact with an alumina disk and a Mo heater. The unit was tested with an uncoated bowl and it was found that Li vaporization was excessive above 500°C, and after 48h at 500°C the Li began to react significantly with impurities (1-2ppm O_2, N_2, H_2O, etc.) in the Ar glove box atmosphere.

Results and Discussion

TEM Characterization. In order to better understand the previously reported[1,4] interaction between Y_2O_3 and Li, characterization work has continued to include polished cross-sections of the 12.5µm thick EB-PVD Y_2O_3 coatings and TEM cross-sections near the substrate-coating interface. The as-deposited EB-PVD coating is shown in Fig. 2. The microstructure is typical of the EB-PVD process. The TEM image in Fig. 2b shows a clean interface between the coating and V-4Cr-4Ti substrate and a coating with a columnar morphology and limited porosity along some grain boundaries.

A very different microstructure was observed after exposure to Li at 800°C. Figure 3 shows polished cross-sections of coatings exposed for 100h and 1000h. After 100h, the original coating microstructure was not retained and gaps between the coating and substrate are apparent, Fig. 3a. After 1000h, the coating crumbled during specimen preparation, Fig. 3b. However, remnants of the Au electrode that was applied after exposure to measure the resistivity were observed. Cross-sections for TEM were made of these specimens near the coating-substrate interface. Unlike the as-deposited columnar micro-structure (Fig. 2b), the grains near the interface were much larger and equiaxed after 100h at 800°C in Li with a few large intergranular pores, Fig. 4a. (Before exposure, only fine intergranular pores were observed, Fig. 2b.) Near the coating-substrate interface, a fine-grained layer was observed with a porous layer above and below it. Energy dispersive x-ray analysis (EDX) showed that the Y/O ratio was slightly higher in this layer. It is not certain if this is because of Li incorporation in the outer layer (which is undetectable by EDX) or O depletion due to interdiffusion with the vanadium alloy substrate. (Vanadium has a high O solubility and will dissolve surface oxides during annealing.[5,6]) Both the inner and outer layers had a cubic structure

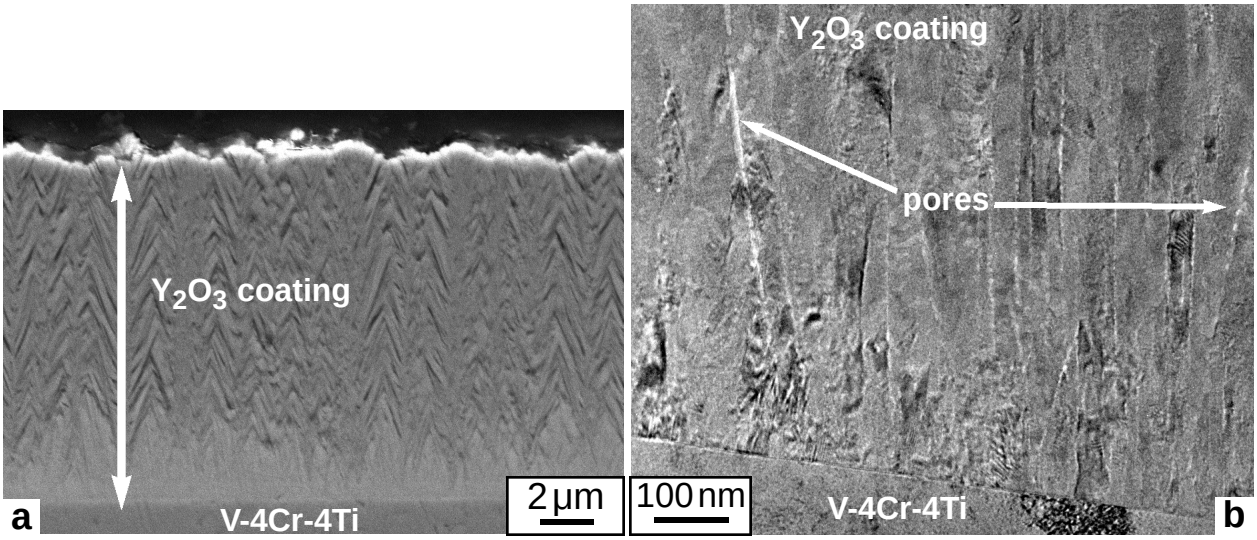

Fig. 2. Cross-sections of the as-received Y_2O_3 coatings. (a) secondary electron image of a polished section and (b) bright-field TEM image of FIB-thinned section near the coating-substrate interface. Arrows mark pores along some grain boundaries.

with a measured d-spacing of 3.12Å, identical to the as-deposited coating.

After 1000h at 800°C in Li, the general equiaxed microstructure was similar but the distinct inner layer was no longer observed, Fig. 4b. In this case, a thin interfacial layer was observed to be rich in vanadium (peak concentration of 6 at.%) and contain small Ti-rich oxide particles. Further characterization of the FIB cross-sections by Auger electron spectroscopy (AES) will be performed to detect Li within the coating.

Er_2O_3 Coatings. Twelve coatings on V-4Cr-4Ti coupons were fabricated in 4 batches in an initial attempt to assess the performance of EB-PVD Er_2O_3 coatings. The coupons were polished to a 600 grit surface before deposition. Two of the batches had a ≈8µm Er_2O_3 layer and two had a ≈20µm layer. The coatings were deposited at elevated substrate temperatures in anticipation of subsequent high-temperature exposures in Li. Substrate temperatures were incrementally varied from 550° to 720°C. One coating from each batch was then coated with 2µm of V in the center of the coupon to prevent the metallic coating from contacting the substrate. X-ray diffraction (XRD) of coated specimens showed that the coatings were poly-crystalline Er_2O_3. For example, Fig. 5 shows an XRD scan of a 21µm thick Er_2O_3 coating deposited at

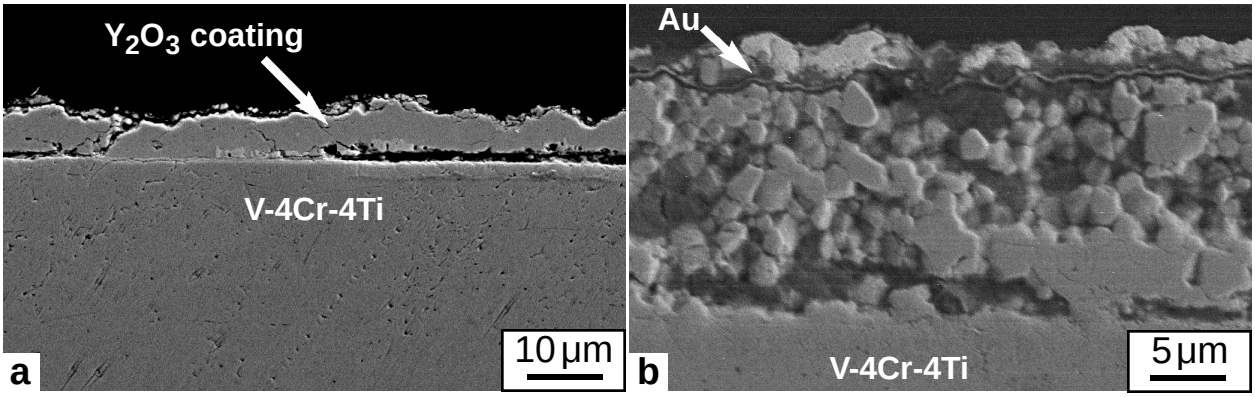

Fig. 3. Secondary electron images of polished cross-sections of the Y_2O_3 coatings after 800°C capsule exposures to Li for (a) 100h and (b) 1000h.

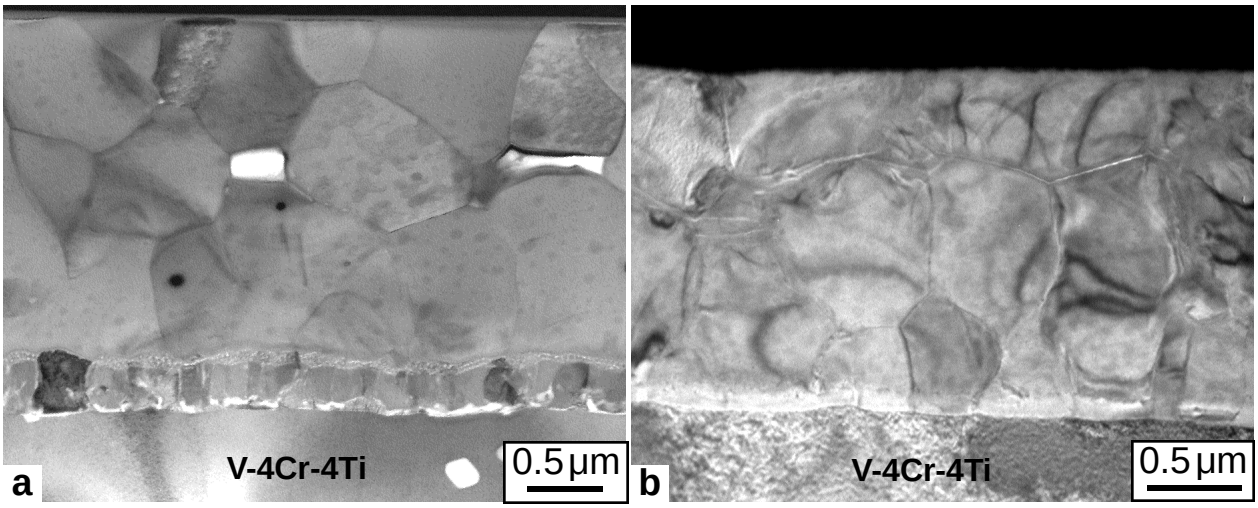

Fig. 4. TEM bright field images of cross-sections of the Y_2O_3 coatings near the coating-substrate interface after 800°C capsule exposures to Li for (a) 100h and (b) 1000h.

720°C. The peaks are consistent with all of and only those reflections reported for polycrystalline Er_2O_3. The morphology of one of the two layer coatings with 8µm of Er_2O_3 and a center region coated with 2µm of V was examined by SEM. Figure 6a shows the Er_2O_3 morphology without the V layer. Figure 6b shows the same specimen in the region coated with V. The roughness of this underlying Er_2O_3 layer leads to a convoluted and likely porous V layer.

Two bowl-shaped specimens were EB-PVD deposited at coating temperatures of 545° and 555°C. These specimens were used to test the performance of the in-situ test rig. One bowl specimen had only a ≈8µm Er_2O_3 coating. At room temperature, chunks of Li weighing 0.5g were placed in the bowl, Fig. 1, and it showed high resistance, effectively an open circuit. The bowl was heated slowly to 500°C. At 180°C, when the Li became liquid, the coating shorted and the resistance was ≈8Ω up to 500°C. Before the Li solidified on cooling, the excess Li was poured out of the bowl and the bowl was cleaned by immersion in methanol for 5h. Figure 7 shows the bowl after cleaning. The coating was removed everywhere the liquid Li touched it. The residue looked like fine black flakes.

The second bowl specimen had ≈11µm Er_2O_3 and a 2µm V layer. It was heated in the test rig to 500°C in the glove box without Li and held for 2h to check the coating resistance. An open circuit (high

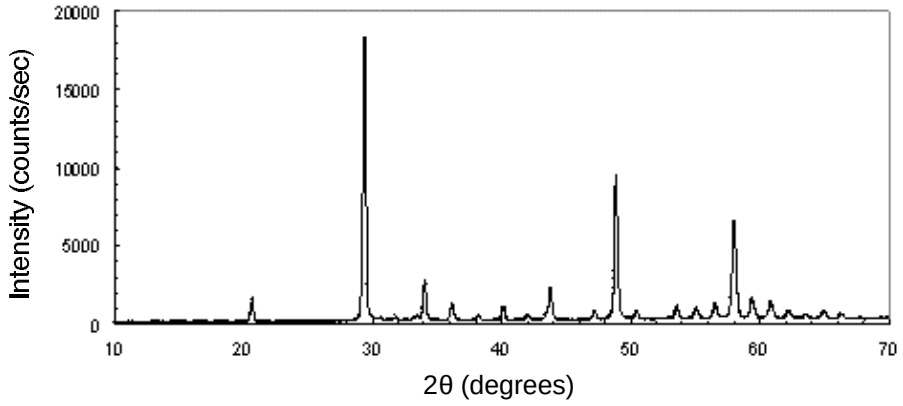

Fig. 5. XRD scan of a 21µm thick EB-PVD Er_2O_3 coating deposited at 720°C.

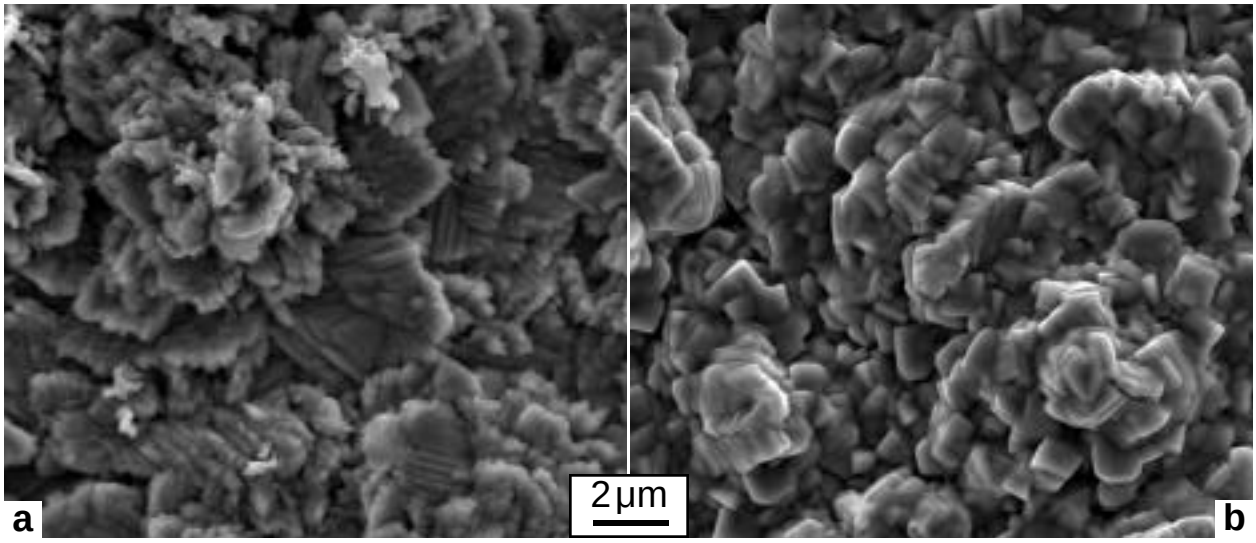

Fig. 6. SEM secondary electron plan-view image of the as-received EB-PVD Er_2O_3 bi-layer coating (a) outside region with only 8µm Er_2O_3 coating and (b) inner region with overlying 2µm vanadium layer.

resistance) was measured throughout heating and cooling to room temperature. However, when Li was added to this specimen, a similar result was observed with the coating shorting at 180°C. This specimen was cleaned by distillation. It had a similar appearance as the specimen shown in Fig. 7 with the coating removed as black flakes where it was in contact with Li. The residual coating and flakes will be characterized by Auger electron spectroscopy and XRD.

Several Li capsule tests with the Er_2O_3 and Er_2O_3/V coatings have been started at 800°C. Additional characterization of the as-deposited Er_2O_3 coatings also will be performed. Based on the morphology in Fig. 6b, a thicker V coating will be fabricated in the future to provide a dense, continuous Li barrier. Different insulating layer materials that have shown potential to meet the MHD coating performance metrics [7] (e.g., Y_2O_3) also may be evaluated in combination with a V overcoat.

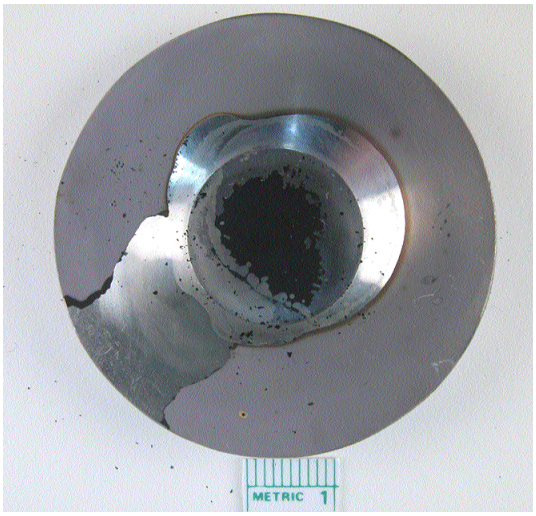

Fig. 7. Photograph of the Er_2O_3 coated specimen after exposure to Li. A pool of liquid Li was in the center of the bowl at up to 500°C. After cooling, excess Li was poured off before it solidified.

References

[1] B. A. Pint, P. F. Tortorelli, A. Jankowski, J. Hays, T. Muroga, A. Suzuki, O. I. Yeliseyeva, and V. M. Chernov, J. Nucl. Mater. 329-333 (2004) 119.
[2] B. A. Pint, L. D. Chitwood, and A. Suzuki, DOE-ER-0313/34 (2003) 96.
[3] B. A. Pint and L. D. Chitwood, DOE-ER-0313/33 (2002) 129.
[4] T. Terai, T. Yoneoka, H. Tanaka, A. Suzuki, S. Tanaka, M. Nakamichi, H. Kawamura, K. Miyajima, and Y. Harada, J. Nucl. Mater. 233-237 (1996) 421.
[5] B. A. Pint and J. R. DiStefano, J. Nucl. Mater. 307-311 (2002) 560.
[6] B. A. Pint and J. R. DiStefano, Oxid. Met. 62 (2005) 33.
[7] B. A. Pint and J. R. DiStefano, DOE/ER-0313/32 (2002) 87.

8.0 BREEDING MATERIALS

No contributions.

9.0 RADIATION EFFECTS, MECHANISTIC STUDIES, AND EXPERIMENTAL METHODS

ON THE RELATION BETWEEN INDENTATION HARDNESS AND THE TRUE STRESS-STRAIN CONSTITUTIVE BEHAVIOR OF A MATERIAL—G. R. Odette, M. Y. He, and D. Klingensmith (University of California, Santa Barbara)

OBJECTIVE

Our objective is to develop a rigorous general relation between indentation hardness (H) and the true stress-strain constitutive $\sigma(\varepsilon)$ laws governing the plastic deformation of metals and alloys.

SUMMARY

A new and powerful indentation hardness (H) approach to evaluating the true stress (σ)-true plastic strain (ε), $\sigma(\varepsilon)$, constitutive behavior of materials is described. Since measurements of H intrinsically probe a wide-range of ε (up to ≈0.5), accurate assessment of the corresponding yield (σ_y) stress and strain hardening [$\sigma_{sh}(\varepsilon)$] pose a significant challenge. Extensive elastic-plastic finite element (FE) simulations have been carried out to assess the relation between H and $\sigma(\varepsilon)$. The simulations were based on both a wide variety of analytical $\sigma(\varepsilon)$ relations, in the form of $\sigma(\varepsilon) = \sigma_y + \sigma_{sh}(\varepsilon)$, as well as actual $\sigma(\varepsilon)$ derived from data on a large number of alloys with a very wide range of constitutive behavior. The analysis led to derivation of a remarkable *universal relation* between H and $\sigma(\varepsilon)$ given by $H \approx 4.05(1 + 34.6\sigma_{flow}/E)\sigma_{flow}$, where $\sigma_{flow} = \sigma_y + <\sigma_{sh}>$, $<\sigma_{sh}>$ is the average strain hardening between ε = 0 and 10%, and E is the elastic modulus. Note we use consistent MKS units of MPa for both H and σ_{flow}. The expression for $H(\sigma_{flow})$ also can be inverted to one describing $\sigma_{flow}(H)$. Experimental σ_{flow}- H data pairs based on this definition of σ_{flow} for the large set of alloys noted above with a very diverse range of $\sigma(\varepsilon)$ are in excellent agreement with the model predictions. The σ_{flow}- H relation provides insight into the large variation of the H/σ_y ratios that are observed for different materials, as well as the corresponding variation in the $\Delta H/\Delta\sigma_y$ ratios used to estimate $\Delta\sigma_y$ due to irradiation based on measurements of ΔH. Applications of the H/σ_{flow} relation, including both evaluating $<\sigma_{sh}>$ in materials that have very low uniform strain capacity in standard tensile tests and measuring at $\sigma(\varepsilon)$ high ε.

PROGRESS AND STATUS

Introduction

Microhardness (H) measurements provide a convenient, non-destructive means to evaluate the strength of materials, as well as to characterize effects such as irradiation hardening. However the relation of H to more quantitative measures of true stress-strain $\sigma(\varepsilon)$ constitutive properties, such as the yield stress (σ_y) and post-yield strain hardening (σ_{sh}), have remained ambiguous, and to a large extent semi-empirical. This is in large part due to the fact that H intrinsically probes a wide range of ε, hence, represents some average measure of an effective flow stress, $\sigma_{flow} = \sigma_y + \sigma_{sh}$. In principle, the decomposition of into σ_y and σ_{sh}, which is an appropriate physical form as proposed by Kocks and Mecking, as well as Zerrelli and Armstrong and others, provides a basis to better quantify the H-$\sigma(\varepsilon)$ relation. For a specified geometry, from a continuum perspective the H-$\sigma(\varepsilon)$ relation can depend only on σ_y, σ_{sh} averaged over some undefined and perhaps variable ε-range, E (or the indenter and material modulus) and the friction coefficient, μ. For example, in the case of a perfectly plastic material, the H/σ_y ratio would be expected to depend only weakly on E and μ. Further, while indentations produce a large range of ε (≈0 to 50%), they are finite and very small regions of high ε would be expected to have little effect on σ_{sh}. Thus we carried out and extensive series of finite element (FE) simulations of the relation between H and σ_y plus $\sigma_{sh}(\varepsilon)$ averaged over different strain ranges for a very wide range of $\sigma(\varepsilon)$ to assess the possibility of obtaining a of a universal master H-$\sigma(\varepsilon)$ relation.

We found such a relation in the form $H = 4.05(1 + 34.6\sigma_{flow}/E)\sigma_{flow}$, where $\sigma_{flow} = \sigma_y + <\sigma_{sh}>$, $<\sigma_{sh}>$ is the average strain hardening between ε = 0 and 10% and E is the elastic modulus. We show that the master relation provides insight into the large variation of the H/σ_y ratios that are observed for different materials, as well as the corresponding variation in the $\Delta H/\Delta\sigma_y$ ratios used to assess effects such as hardening due

to irradiation. We also show that useful applications of the H/σ_{flow} relation are to evaluate $<\sigma_{sh}>$ in materials that have very low uniform strain capacity in standard tensile tests as well as to measure $\sigma(\varepsilon)$ high ε.

Finite Element Modeling of Indentation Harness (H)

Cone indentations were simulated using the general purpose FE code ABAQUS. The plasticity model in ABAQUS is based on J_2-incremental flow theory. The inputs to ABAQUS are E, σ_y, $\sigma_{sh}(\varepsilon)$ and the contact interface friction coefficient (μ). The cone indenter, with an angle of 68.2°, was treated as two-dimensional (z, r, symmetric in θ) rigid body. The two-dimensional half space mesh had 3021 four-node quadrilateral axisymmetric elements with 3232 nodes. The radial (R) and depth (z) dimensions of the mesh were ≈ $50D_{max}$ and $20D_{max}$, respectively, where D_{max} is the maximum penetration depth of the cone. The mesh was refined in the area under the indenter (Fig. 1) and there were more than 20 elements in the contact area under the indenter at maximum load. The calculations were carried out for a prescribed loading/unloading cycle to a maximum load P. Hardness, H, was calculated as P/A, where A is the area of the permanent indentation, $\pi D^2/4$, where D is the diameter of the indentation at the plane of the undeformed specimen surface. Test calculations were carried out to demonstrate that H was independent of the mesh size and a convergence study showed that the meshes provided accurate results for displacements and the pile-up shape.

The friction between the specimen and the indenter affects the shape of the pile-up. For μ <0.2, the effects of μ are significant. However, the pile-up shape is insensitive to $\mu \geq 0.2$. Since the nominal μ for such contacts is ≈0.2 to 0.3, μ = 0.2 was used in the FE simulations. The calculated H values are also insensitive to the load P between 40 and 200g. The effective plastic strain reached 0.5 directly underneath the indenter, so this was used as an upper bound for the strain range (Fig. 2).

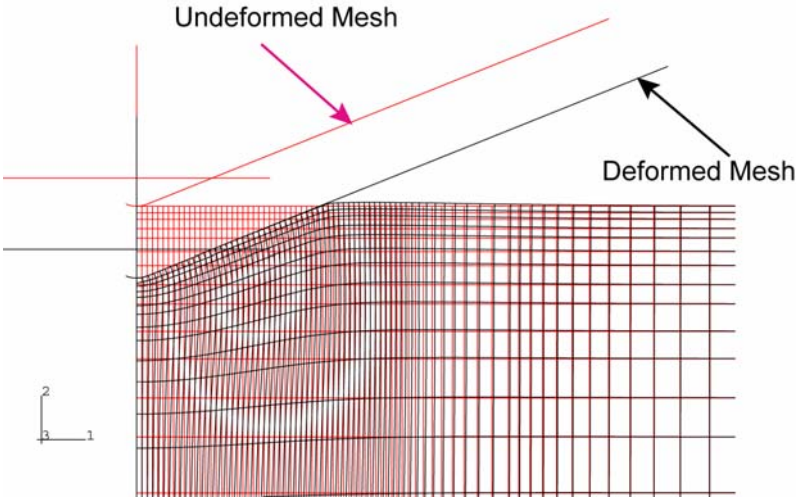

Fig. 1. Section of the mesh used in the FE simulations of H.

One large set of simulations were carried out for E = 200 GPa and constitutive laws in the form:

$$\sigma(\varepsilon) = \sigma_y \qquad \varepsilon \leq \varepsilon_y \qquad \text{(1a)}$$

$$\sigma(\varepsilon) = \sigma_y + \sigma_{sh} = \sigma_y + \sigma_{shm}[1-\exp(-\gamma(\varepsilon-\varepsilon_y)] \qquad \varepsilon > \varepsilon_y \qquad \text{(1b)}$$

The H were calculated for a Luder's-yield strain (ε_y = 0.005) and a wide range of σ_y (100–850), maximum saturated strain hardening levels (σ_{shm} = 125–500) and pre-saturation hardening rates (γ = 3 to 15) (Fig. 3). The calculations were also carried out for actual $\sigma_{sh}(\varepsilon)$ curves derived from tensile tests on a large number of alloys with a very diverse range of constitutive properties ranging from annealed stainless

steels with low σ_y and γ and high σ_{shm}, to martensitic steels with intermediate σ_y and σ_{shm} and high γ, to TiNb with very low σ_{shm}. The materials also included unirradiated and irradiated Mn-Mo reactor pressure vessel (RPV) steels, as well as alloys with large Luders strain regions up to ε_l ≈10% and pre-strained materials.

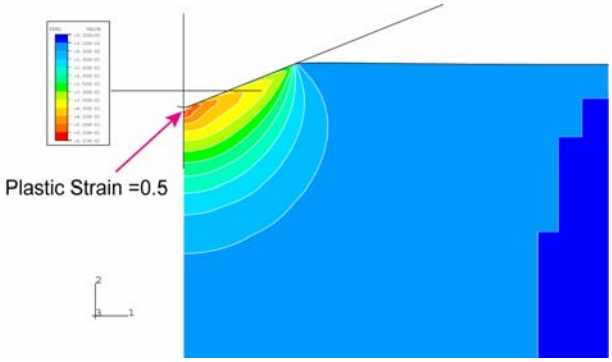

Fig. 2. A typical example of the effective strain distribution under the indenter.

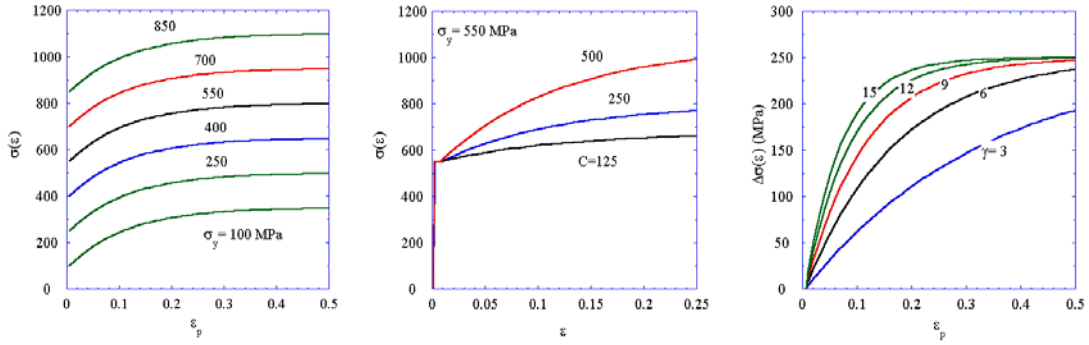

Fig. 3. Analytical σ(ε) laws used in the FE simulations of H.

Results

The σ_y versus H for σ_{shm} =0, 250, and 500 MPa and γ = 9 are shown in Fig. 4. The σ_y increases with H as $\sigma_y \approx A + 0.3H$, with A ≈25, 100 and 170 MPa for σ_{shm} = 0, 250, and 500 MPa, respectively. The corresponding positive offsets on the H axis primarily reflect a contribution to H of the $\sigma_{sh}(\varepsilon)$ averaged over some effective increment of effective plastic strain, ε, under the indent. In other words the σ_{flow} probed by H is larger than σ_y by an effective ε-averaged $<\sigma_{sh}>$.

Thus the FE H data for the various $\sigma(\varepsilon)$ were analyzed by calculating the $<\sigma_{sh}>$ between various lower (ε_l) and upper (ε_u) limits and fitting the corresponding $\sigma_{flow} = \sigma_y + <\sigma_{sh}>$ versus H data with a function in the form:

$$H = C_1(1 + C_2\sigma_{flow})\sigma_{flow} \qquad (2)$$

Here C_1 and C_2 are weak functions of ε_l and ε_u. An optimum set of ε_u and ε_l can be determined by minimizing the standard deviation (δH) of the fit for the predicted H_p from Equation 2 to the FE simulations H_c as a function of ε_l and ε_u as:

$$\delta H = [\Sigma_j (H_{pn} - H_m)^2]^{1/2} \qquad (3)$$

for all values of H for the j different $\sigma(\varepsilon)$. We found that values of $\varepsilon_l \approx 0.0$ and $\varepsilon_u \approx 10\%$ gives a very good fit as shown by the solid line in Fig. 5 given by:

$$H=4.05(1 - 0.000173\sigma_{flow})\sigma_{flow} \quad (4)$$

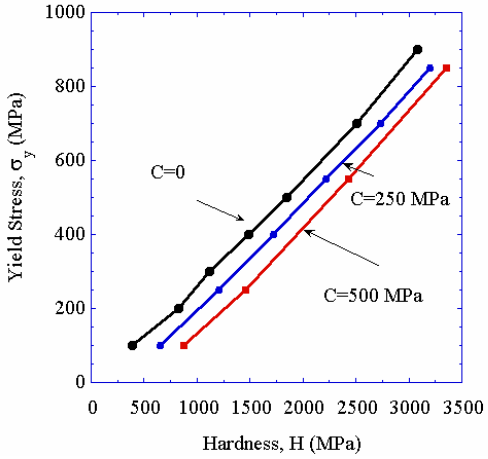

Fig. 4. The σ_y versus the FE simulations of H for different σ_{shm} (= C).

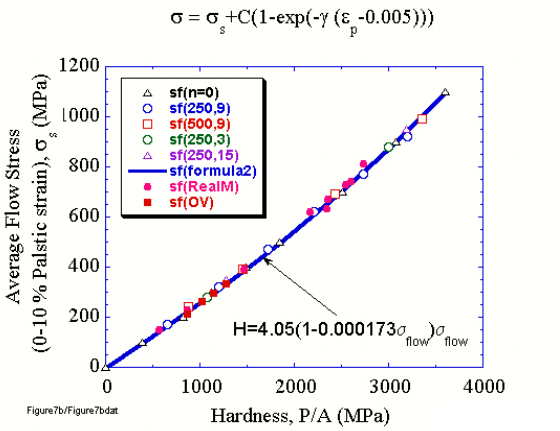

Fig. 5. The $\sigma_{flow} = \sigma_y + \langle\sigma_{sh}\rangle$ versus H for a wide range of $\sigma(\varepsilon)$.

These results are all for E = 200GPa. Thus the curvature in the σ_{flow} versus H relation is likely due to the corresponding variation in σ_{flow}/E. The H/σ_{flow} ratio would be expected to decrease with increasing σ_{flow}/E due to effects such as the constraint on the region of plastic deformation and reverse plasticity. Figure 6 shows the H/σ_{flow} for versus σ_{flow}/E, including additional calculations for E = 50, 100, and 400 GPa for the same $\sigma(\varepsilon)$. As expected, the variation in H/σ_{flow} in the initial calculations is consistent with variations in σ_{flow}/E. Thus Equation 4 can be rewritten as:

$$H=4.05(1 - 34.6\sigma_{flow}/E)\sigma_{flow} \quad (5)$$

However, the results in Fig. 6 show that the linear relation breaks down at $\sigma_{flow}/E > 0.006$. A second order polynomial fit to the σ_{flow}/H for versus σ_{flow}/E data yields:

$$H=4.08(1 + 1755[\sigma_{flow}/E]^2 - 44.1[\sigma_{flow}/E])\sigma_{flow} \quad (6)$$

Additional calculations will be needed between $\sigma_{flow}/E = 0.006$ and 0.012 to confirm the non-linear fit. However, for most materials of interest, $\sigma_{flow}/E < 0.006$; hence, Equation 4 gives an adequate representation of the FE results.

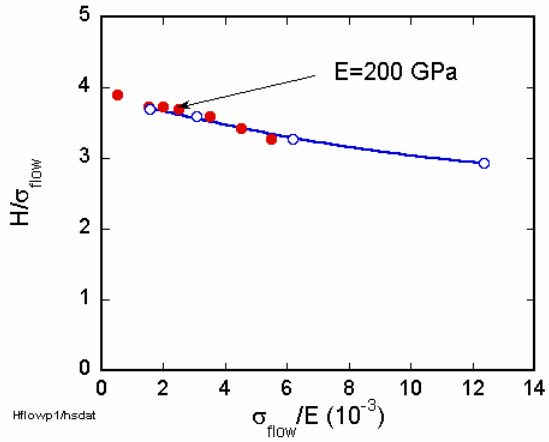

Fig. 6. The σ_{flow}/H versus σ_{flow}/E.

Comparison with Experiment

As noted above, tensile tests were conducted on a large number of materials with a very diverse range of $\sigma(\varepsilon)$. Vickers diamond pyramid hardness (DPH) measurements were also made on these same materials in order to evaluate the FE predictions. The $\sigma_{flow} = \sigma_y + <\sigma_{sh}>$ were directly assessed based on the experimental $\sigma_{sh}(\varepsilon) = \sigma(\varepsilon) - \sigma_y$ converted from engineering stress strain curves up to the onset of necking and averaged between $\varepsilon = 0$ and 10%. Figure 7 compares the experimental σ_{flow} versus H data to the predictions of Equation 4. The agreement is generally very good, although the experimental data tends to fall slightly above the prediction line, especially at lower H; and overall the experimental σ_{flow} versus H relation is more linear than the FE results. FE simulations of diamond pyramid indenter hardness (DPH) show that H_{DPH} are only slightly larger than for cone in indentation, thus variations in the indenter geometry do not explain the modest differences between experimental data and FE predictions of σ_{flow}. We plan to evaluate the effect of a non-rigid indenter next to see if this makes a difference. However, considering the uncertainties in the data and simplicity of the model, we believe the agreement between experiment observations and the FE based universal σ_{flow} - H relation is excellent and provides strong support for use of Equations 4 or 5.

Discussion and Applications

The universal master σ_{flow} - H relation is remarkable in view of the much larger ε-range created by the indentation (see Fig. 3). However, it permits a quantitative understanding of a number of empirical trends, such as:

1. That there is a large variation in the observed H/σ_y ratios due to the effects of both $<\sigma_{sh}>$ and σ_{flow}/E.

2. That the ratio of H/σ_y tends to be higher for steels with low σ_y due to the effect of σ_{flow}/E.

3. That the $\Delta H/\Delta\sigma_y$ following irradiation is generally lower than the unirradiated H/σ_y with irradiation due to reduction in $<\sigma_{sh}>$.

In addition, the universal relation allows combining H and σ_y measurements from a tensile test to estimation of strain hardening in alloys with very low uniform tensile strain as:

$<\sigma_{sh}> = \sigma_{flow}$(from H) - σ_y(from a tensile test)

The universal relation also permits a convenient method to evaluate $\sigma(\varepsilon)$ high ε regions by making H measurements on pre-strained materials. An effective way to do this is to make hardness transverses on sections of a bent beam that undergoes stable plastic deformation over a wide range of effective ε. Indeed, such transverses from regions of high deformation across the neutral axis not only assess regions with ≈0 to very high ε, but also involve complex and varying stress that yield information of plasticity flow laws and tensile to compressive deformation effects on $\sigma(\varepsilon)$j.

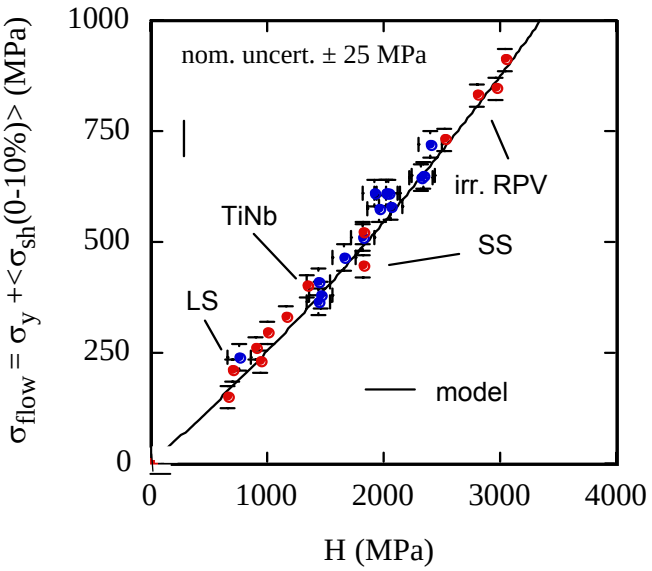

Fig. 7. Pairs of σ_{flow}-H data points for materials with a wide range of compared to the FE model prediction.

Future Research

Future research will focus on the following items:

1. Assessment of the effect of the elastic modulus of the indenter.

2. Additional experimental verification of the σ_{flow}-H relation with an even wider range of materials.

3. Application of the method to assessing $<\sigma_{sh}>$ in materials that undergo immediate necking.

4. Assessing the $\sigma(\varepsilon)$ at high ε in pre-deformed materials.

5. Evaluation of the effects of variations in stress state history on $<\sigma_{sh}>$.

THE INTERACTION OF HELIUM ATOMS WITH EDGE DISLOCATIONS IN α-Fe—H. L. Heinisch, F. Gao, R. J. Kurtz, and E. A. Le (Pacific Northwest National Laboratory)

OBJECTIVE

The objective of this research is to understand the fate of He atoms produced in metals and alloys by fusion neutron induced transmutation reactions. In the present work we study the migration and diffusion mechanisms of He atoms in dislocations in α-Fe using atomic-scale methods of molecular dynamics and statics.

SUMMARY

Formation energies, binding energies, and migration energies of interstitial He atoms in and near the core of an a/2<111>{110} edge dislocation in α-Fe are determined in atomistic simulations using conjugate gradient relaxation and the Dimer method for determining saddle point energies. Results are compared as a function of the proximity of the He to the dislocation core and the excess interstitial volume in regions around the dislocation. Interstitial He atoms have negative binding energy on the compression side of the dislocation and strong positive binding energy on the tension side. Even at low temperatures, interstitial He atoms in the vicinity of the dislocation easily migrate to the dislocation core, where they form crowdion interstitials oriented along the close-packed slip direction, with binding energies in excess of 2 eV. Crowdion interstitial He atoms diffuse along the core, transverse to the crowdion direction, with a migration energy of 0.4–0.5 eV.

PROGRESS AND STATUS

Introduction

Over time He atoms will partition among various sinks in the microstructure such as dislocations, grain boundaries and particle/matrix interfaces. Detailed knowledge of how He interacts with these microstructural features is needed to develop improved kinetic Monte Carlo and rate theory models for prediction of long-time material behavior. Molecular statics, molecular dynamics and the dimer method of potential surface mapping are being used to study the fate of He atoms in the vicinity of dislocations in alpha-iron, which we consider to be a first-order model for ferritic steels. We report here on the calculation of formation energies of He atoms in interstitial positions about the dislocation, which are used to map the locations of the most stable configurations of the He atom-dislocation interaction. Also, the Dimer method was used to determine migration energies of He atoms trapped within the dislocation core. The correlation of this information with the spatial distribution of excess volume around the dislocation is discussed.

Modeling

An a/2<111>{110} edge dislocation was created along the axis of a cylindrical cell of body-centered cubic Fe atoms by displacing the atoms according to the anisotropic elastic displacement field of the dislocation, then relaxing the entire model. The model is periodic along the dislocation line. Binding energy calculations were performed for He atoms placed at substitutional and interstitial positions in the dislocation-distorted lattice on both the tension and compression sides of the dislocation slip plane. Conjugate gradient relaxations were performed to determine the relaxed configurations of the He and surrounding Fe atoms, as well as the energy of the relaxed configuration. In all cases the set of interatomic potentials due to Ackland [1], Wilson and Johnson [2], and Beck [3] were used for the Fe-Fe, Fe-He and He-He interactions, respectively. Excess interstitial volumes associated with interstitial sites in the vicinity of the dislocation were determined using a variation of the Voronoi volume technique, where the volume is located at the center of an interstitial site.

The Dimer method [4] was used to determine saddle point energies for possible transitions of interstitial He atoms to other locations, starting from several positions near the dislocation. The Dimer results give the migration energies and saddle point atom configurations for He interstitials as they migrate from one equilibrium position to another. In a single run the Dimer method can find saddle points for more than one transition from a given starting configuration, not just the transition of lowest energy. Thus, it is useful for locating unexpected and competing transitions, which can be especially important in exploring a complicated potential energy landscape such as near a dislocation or grain boundary.

Results

The binding energies of interstitial He atoms to the dislocation are shown in Fig. 1b, plotted as a function of their initial unrelaxed positions as shown in Fig. 1a. Helium atoms initially within the dislocation core region relax to crowdion interstitial positions and have binding energies in excess of about 1–2 eV, depending on their location, with a maximum binding energy of 2.3 eV for (crowdion) interstitial He atoms in the core of the dislocation. Helium atoms placed farther away from the dislocation core relax to positions near their original octahedral interstitial sites, and they have significantly smaller binding energies that decrease with distance from the dislocation. However, MD simulations at a lattice temperature of 100 K show that interstitial He atoms beginning well away from the dislocation core migrate to the layer of atoms nearest the slip plane, and become crowdion interstitial defects [5]. Near the core the binding energies decrease more rapidly perpendicular to the slip plane than along the slip plane.

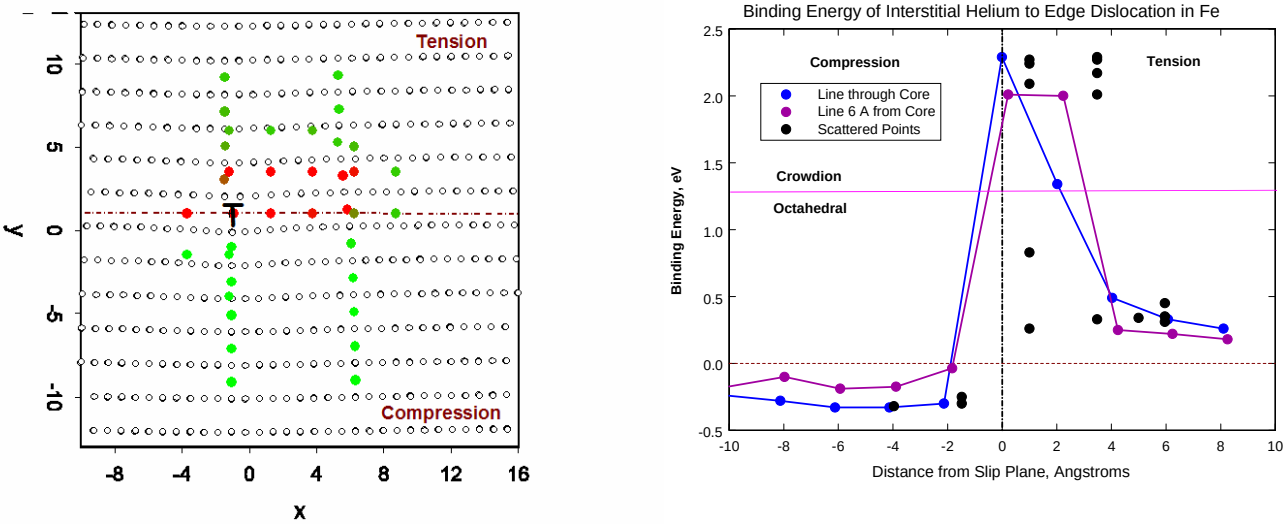

(a) (b)

Fig. 1. a) Locations of the initial position of a single interstitial He atom prior to relaxation. The open circles are Fe atom rows, and the filled, colored circles are the initial He atom positions. The dislocation line (T) is along the z-direction (into the page), and the z-components of all the He locations are approximately the same. b) Binding energies of relaxed interstitial He atoms as a function of their distance from the dislocation slip plane (dashed line in 1a) at the locations in 1a. The points connected by lines are those lying along the two vertical lines of atom positions through the dislocation core and 0.5–0.6 nm from the core, respectively.

The binding energies of relaxed interstitial He atoms to the dislocation can be associated with the excess interstitial volume at the various initial interstitial locations. In Fig. 2 the He binding energy is plotted as a function of excess interstitial volume for locations lying on the line through the dislocation core and along the line about 0.5–0.6 nm from the core, as depicted in Fig. 1a. There is apparently a strong correlation

between excess volume and binding energy for nearly all of the interstitial locations tested. However, in two of the tested locations with excess volume less than 0.0002 nm^3 the binding energy is greater than 2 eV, much higher than the correlation implied by the other data points would predict. These two outlying data points correspond to initial interstitial locations on and near the slip plane at 0.5–0.6 nm from the dislocation core.

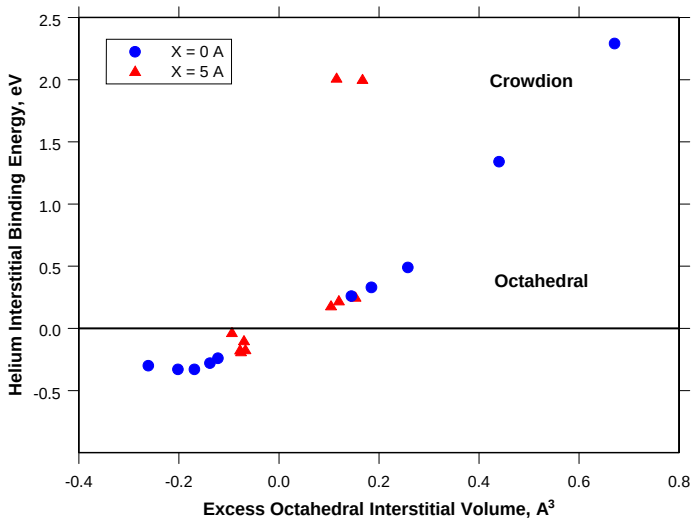

Fig. 2. Binding energy in eV of an interstitial He atom to an edge dislocation in α-Fe as a function of excess interstitial volume in Å^3. Values are shown for He atoms at positions along a line through the core (X=0) and at 5–6 A from the core (X=5) as depicted in Fig. 1a.

It is clear that He interstitials are strongly trapped on the tension side of edge dislocations, so it is unlikely they can easily migrate away from the dislocation except at very high temperatures. However, it may be possible for interstitial He atoms to migrate along the dislocation core. The Dimer method was applied to trapped He interstitials to determine the migration pathways and migration energies for diffusion near the edge dislocation. An interstitial He, initially in the crowdion configuration very near or in the dislocation core, is found to migrate along the dislocation line by jumping to a crowdion position in an adjacent close-packed row with a migration energy of about 0.4–0.5 eV, depending on its initial position and the jump direction.

Table 1 contains a summary of interaction energies of He-related point defects with <112> edge dislocations in α-Fe. Binding energies of substitutional He atoms near the edge dislocation were also calculated, and the maximum binding to the dislocation is 0.5 eV relative to substitutional He in the perfect Fe lattice. The migration energy of substitutional He bound to a dislocation has not been determined. In the perfect Fe lattice the migration energy of substitutional He is quite high, but our Dimer simulations show that a nearby Fe crowdion interstitial can easily "kick out" a substitutional He atom from its lattice site to become an interstitial He having high mobility with a migration energy of 0.08 eV. On the other hand, near the core of the edge dislocation the reverse of this reaction (an interstitial He atom "kicks out" an Fe lattice atom into a crowdion position) is energetically favorable. Thus, substitutional He atoms in or near an edge dislocation are likely to be relatively immobile, facilitating the formation of He clusters. Crowdion interstitial He atoms are strongly bound to the dislocation with a maximum binding energy of 2.3 eV in these simulations. Thus, for some of the highly mobile He interstitials produced under irradiation, once they are created, they will be quickly trapped at edge dislocations where they can migrate along the dislocations at fairly low temperatures in so-called "pipe diffusion." It is interesting to note that their migration energy of 0.4–0.5 eV is in the same range as the migration energy for interstitial He atoms

within $\Sigma 3$ and $\Sigma 11$ grain boundaries (0.3–0.4 eV) determined from results of long-time molecular dynamics simulations [6]. Such grain boundaries also have significant regions of excess volume.

Table 1. Helium interaction energies with edge dislocations in α-iron

Binding Energy, eV Defect	Migration Energy, eV to Edge Dislocation	Perfect Fe	Dislocation
Substitutional He	0.50	--	--
Interstitial He	2.3	0.08	0.4–0.5
He_1V_2	1.2	> 1.1	--

Conclusions

The results of these simulations indicate that interstitial He atoms are either repelled from or trapped at edge dislocations in α-Fe, depending on the direction of approach. Near the dislocation core on the tension side He is strongly trapped as a crowdion with 1–2 eV greater binding energy than as an octahedral interstitial, and in this form He atoms can migrate along the dislocation with a migration energy of 0.4–0.5 eV. Helium binding to dislocations and He migration along dislocations can be at least qualitatively correlated with excess interstitial volume in the dislocation core.

Acknowledgements

The participation of Edward A. Le in this research was supported in part by the U.S. Department of Energy, Office of Fusion Energy Sciences, and in part by the Pacific Northwest National Laboratory's Summer Research Institute on Interfacial and Condensed Phase Chemical Physics, sponsored by the U.S. Department of Energy, Office of Basic Energy Sciences, under U.S. DOE Contract DE-AC06-76L01830.

References

[1] G. J. Ackland, D. J. Bacon, A. F. Calder, and T. Harry, Philos. Mag. A75 (1997) 713.
[2] W. D. Wilson and R. D. Johnson: Interatomic Potential and Simulation of Lattice Defects, Plenum, (1972) 375.
[3] D. E. Beck, Mol. Phys. 14 (1968) 311.
[4] G. Henkelman and H. Jónsson, J. Chem. Phys. 111 (1999) 7010.
[5] H. L. Heinisch, F. Gao, and R. J. Kurtz, Fusion Materials Semiannual Progress Report for the Period Ending June 30, 2004, submitted to the Journal of Nuclear Materials.
[6] F. Gao, H. L. Heinisch, and R. J. Kurtz, Fusion Materials Semiannual Progress Report for the Period Ending December 31, 2004; submitted to the Journal of Nuclear Materials.

MOLECULAR DYNAMICS SIMULATION OF PRIMARY IRRADIATION DEFECT FORMATION IN FE-CR ALLOYS—J.-H. Shim, H.-J. Lee, and B. D. Wirth (University of California, Berkeley)

OBJECTIVE

The objective of this work was to determine the effect of Cr on primary defect production in high-energy displacement cascades in Fe-10%Cr alloys, using two different parameterizations for the Fe-Cr interatomic potential that effectively treated the Cr atom as an oversized and undersized substitutional solute atom, respectively.

SUMMARY

Molecular dynamics simulations of displacement cascades up to 20 keV have been performed in Fe and Fe-10%Cr using two different parameterizations of Finnis-Sinclair type interatomic potentials. The two different potentials describe the extremes of positive (attractive) and negative (repulsive) binding between substitutional Cr atoms and Fe self-interstitial atoms. The effect of Cr, regardless of potential, has a minimal effect on the collisional stage of cascade and on the distribution and number of vacancy and self-interstitial atom clusters. The quantity of mixed Fe-Cr dumbbells is sensitive to the choice of potential, however.

PROGRESS AND STATUS

Introduction

9–12% Cr ferritic/martensitic steels are strong candidates for first-wall and breeding-blanket structural materials in future fusion reactor systems. Therefore, fundamental understanding of microstructural evolution under conditions of fusion neutron irradiation is important, since microstructural changes control mechanical behavior and performance. The modeling of primary defect formation by displacement cascades is a natural starting point in predicting neutron irradiation damage. Molecular dynamics (MD) simulations based on reliable semi-empirical many-body interatomic potentials have long been recognized as the most appropriate tool for the study of displacement cascades. To date many investigations have performed MD cascade simulations in pure Fe using a variety of interatomic potentials [1–4]. Cascade simulations in Fe alloys have seldom been studied, because reliable interatomic potentials for Fe alloys are limited.

Specifically considering the Fe-Cr system, there are a couple of displacement cascade simulation studies that have been recently performed [5,6]. Malerba et al. [5] performed MD cascade simulations of pure Fe and Fe-10%Cr with kinetic energies of primary knock-on atom (PKA) E_p of up to 15 keV. They employed embedded atom method (EAM) potentials to simulate the cascades. While they took the Cr potential from the work of Farkas et al. [8], they fit new Fe and Fe-Cr cross potentials to available physical properties. Their results show that Cr atoms do not have a significant influence on the collision stage of cascades and the number of surviving defects. But on the other hand, they observed mixed Fe-Cr dumbbells form preferentially in Fe-10%Cr alloys. However, the Fe potential used in that work makes the <111> dumbbell more stable than <110> dumbbell [9], opposite to experimental observations [10], recent ab-initio [11,12] and most semi-empirical potential calculations[13–15]. Meanwhile, Wallenius et al. [6] recently fit Fe-Cr EAM potentials to various physical properties of pure Fe, pure Cr and Fe-Cr alloys and simulated displacement cascades of pure Fe, Fe-5%Cr and Fe-20%Cr with E_p of up to 20 keV. Though the potentials of Wallenius et al. [6] are evidently improved by correctly predicting the stability of the dumbbells, the calculated formation energy of the Fe <110> and <111> dumbbells is more than two times larger than the recent ab-initio calculations [11,12] and the experimental data [16].

The purpose of this study is to construct two different Fe-Cr potentials, with a systematic variation in Cr behavior, and to perform MD simulations to elucidate the effect of Cr atoms in Fe on primary irradiation defect formation in displacement cascades.

Interatomic Potentials and Simulation Methods

The Finnis-Sinclair (F-S) potential [17], which provides a similar framework to the EAM potential [7], was chosen to construct the Fe-Cr potentials. In the framework of the Finis-Sinclair formalism, the total energy of the system of the *n* atom system is given by:

$$E_{tot} = \frac{1}{2}\sum_{i\neq j}^{n} V_{ij}(R_{ij}) - \sum_{i}^{n}\left\{\sum_{j}^{n}\phi_{ij}(R_{ij})\right\}^{1/2} \qquad (1)$$

where V_{ij} and f_{ij} are the pairwise repulsive and the many-body cohesive interactions, respectively, between atoms *i* and *j* separated by a distance R_{ij}.

The potentials for the pure elements were taken from the literature [14,17]. For Fe and Cr, the potentials of Ackland et al. [14] and Finnis and Sinclair [17], respectively, were employed. For radiation damage studies, it is important to validate a potential at very short atomic separations as well as at equilibrium separation, because atoms tend to become very close in high-energy cascades. For instance, it is known that the Fe potential developed by Finnis and Sinclair [17] is too 'soft' at short atomic separations for high-energy cascades. Calder and Bacon [1], therefore, modified this potential to make it 'stiffer' in their cascade simulations. Fortunately, the F-S Fe potential proposed later by Ackland et al. [14] was already proven to be in good agreement with the universal equation of state [18] at short atomic separations. It also turned out that the potential of Ackland et al. [14] correctly predict the stability and defect formation energy of Fe dumbbells. The volume-energy curve of the Cr potential by Finnis and Sinclair [17] is plotted in order to decide whether or not this Cr potential is relevant for high-energy cascades (Fig. 1). The agreement with the universal equation of state is quite good. Therefore, there is no need to modify the Cr potential at short atomic distances. It is also beneficial that the F-S Cr potential shows a smaller positive Cauchy pressure compared to the previous EAM Cr potentials, since it is experimentally known that Cr has a negative Cauchy pressure [6].

To construct the Fe-Cr cross potential, the two terms V_{FeCr} and f_{FeCr} must be determined. The scheme proposed by Konishi et al. [19] was adopted from the various cross potential schemes. According to this approach, the two terms are given by:

$$\phi_{FeCr} = \alpha\sqrt{\phi_{FeFe}\phi_{CrCr}} \qquad (2)$$

$$V_{FeCr} = \frac{\beta}{2}\left(\frac{\phi_{FeCr}}{\phi_{FeFe}}V_{FeFe} + \frac{\phi_{FeCr}}{\phi_{CrCr}}V_{CrCr}\right) \qquad (3)$$

where α and β are adjustable parameters.

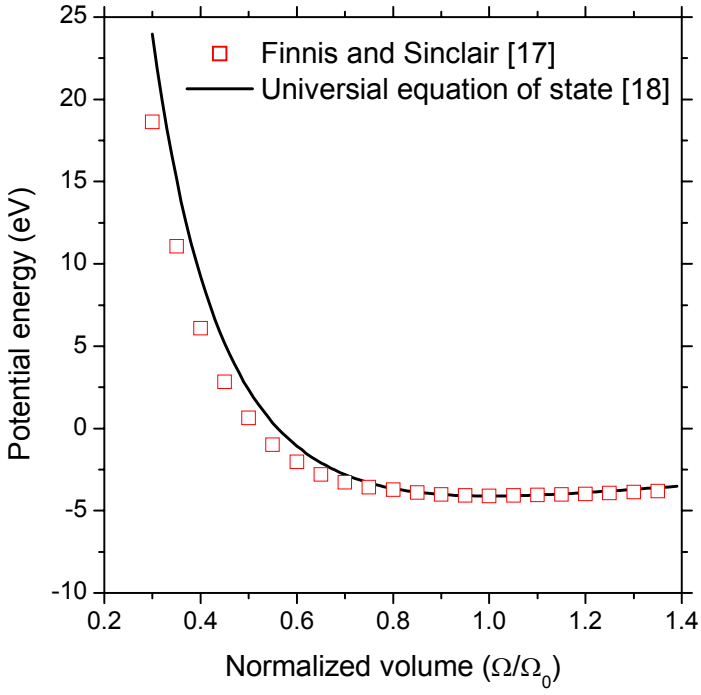

Fig. 1. Calculated potential energy versus normalized volume for Cr by the F-S potential in comparison with the universal equation of state.

Table 1. Parameters for the Fe-Cr potential fitted in this study

	α	β
FeCr I	1.00	1.25
FeCr II	0.94	0.90

In this study, *α* and *β* were fit to experimental data, including the enthalpy of mixing and lattice constants in Fe-Cr alloys. The fit parameters are provided in Table 1. The first cross-potential involved only a fit of β with α fixed equal to 1, because it is more similar to the original F-S alloy scheme proposed by Ackland and Vitek [20]. This potential was named FeCr I. FeCr I shows very good agreement with the CALPHAD calculation for the enthalpy of mixing [21], which is derived from experimental data [22], as shown in Fig. 2. Concerning the lattice constants of Fe-Cr alloys, the FeCr I potential is in agreement with experimental measurements [23–25], as shown in Fig. 3. The binding energies of various point defects are presented in Table 2. The binding energies of Fe-Cr <110> and <111> mixed dumbbells, with respect to an isolated Fe dumbbell and a well-separated Cr atom, are negative, which means that these dumbbells are not energetically stable compared to the Fe-Fe dumbbells. However, this is opposite to the recent ab-initio calculation predicting zero and positive binding energies for the <110> and <111> mixed dumbbells, respectively [26]. The Fe-Cr potential of Wallenius et al. [6] predicts a relatively large positive binding energy of 0.27 eV for the <110> mixed dumbbell. Further, Maury and co-workers have suggested a small (≈<0.15 eV) positive binding energy for mixed Fe-Cr dumbbells in Fe-Cr alloys, based on experimentally

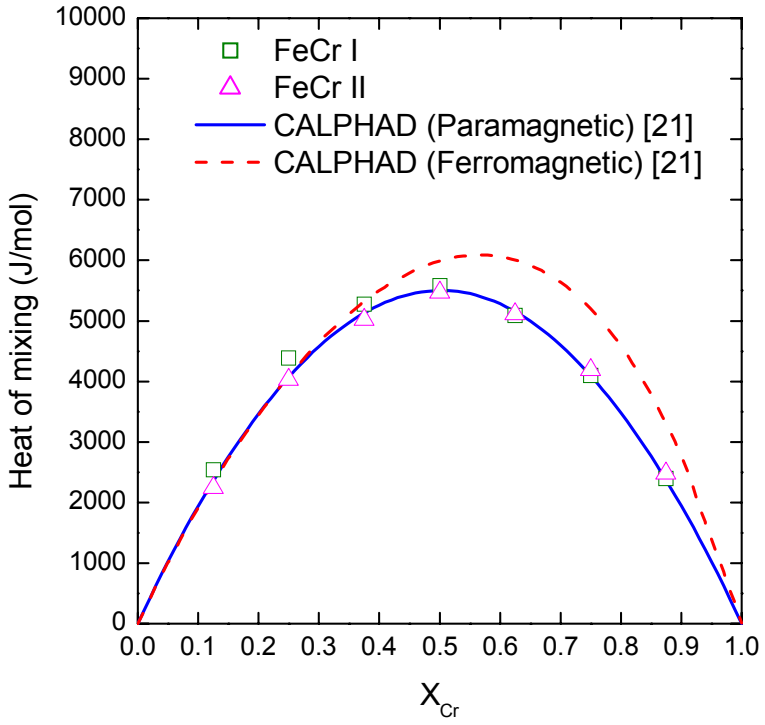

Fig. 2. Calculated heat of mixing in Fe-Cr bcc alloys by the present Fe-Cr potentials in comparison with the CALPHAD calculations.

measured changes in isochronal annealing recovery [34]. Thus, it was decided to fit another Fe-Cr potential, which provided a positive Cr – SIA binding energy, by fitting α and β simultaneously. This potential was named FeCr II. FeCr II does predict positive binding energies for the mixed dumbbells, as shown in Table 2, in addition to also providing good agreement with the enthalpy of mixing and the lattice constants, as shown in Figs. 2 and 3.

In order to validate these two different Fe-Cr potentials, a simple ab-initio calculation was performed using the SeqQuest code [27], which is based on the linear combination of atomic orbitals (LCAO) formulation. A substitutional Cr atom was placed in the bcc Fe matrix consisting of 54 atoms. Although a Cr atom should be slightly oversized compared to Fe, the first nearest neighbor Fe atoms constrict toward the Cr atom by 0.1% in the SeqQuest code. This is in better agreement with the prediction of FeCr II as shown in Table 3 and seems to be closely associated with the stable mixed dumbbells in Fe-Cr alloys predicted by the ab-initio calculation [26]. However, it is not well understood why the mixed dumbbells are energetically stable since Cr is slightly oversized, as well as elastically stiffer than Fe [17]. Possibly, this results from a strong electronic interaction between Fe and Cr atoms in a Fe-rich region, which may also be influenced by magnetic spin effects.

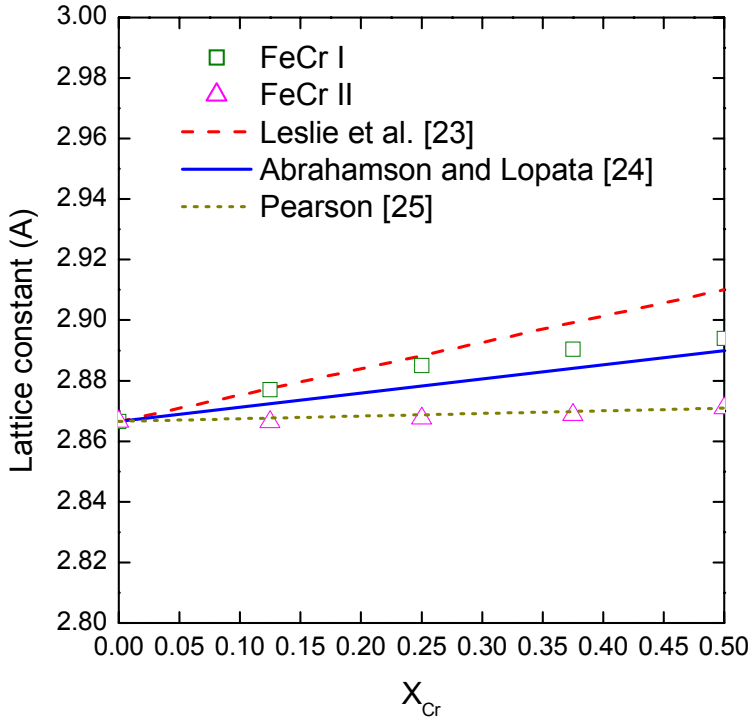

Fig. 3. Calculated lattice constants in Fe-Cr bcc alloys by the present Fe-Cr potentials in comparison with the experimental data.

Table 2. Calculated binding energies of Cr-vacancy, Cr-Cr and Cr-dumbbells in bcc Fe relative to well-separated Cr/vacancy (eV)

	F-S FeCr I	**F-S FeCr II**	**EAM Wallenius [6]**	**Ab-initio Domain [11]**
Cr-V 1NN	0.0386	-0.0016	-	-
Cr-V 2NN	-0.0369	-0.0130	-	-
Cr-Cr 1NN	0.0695	0.0285	-	-
Cr-Cr 2NN	0.0004	0.0289	-	-
$<110>I_{FeCr}$	-0.4037	0.1015	0.27	0
$<111>I_{FeCr}$	-0.2540	0.1950	-	0.3
$<110>I_{FeFe}$-Cr (parallel)	-0.1634	0.0625	-	-
$<110>I_{FeFe}$-Cr (perpendicular)	0.0165	-0.0072	-	-

Table 3. Change in first nearest neighbor distance around a substitutional Cr atom in bcc Fe

	Change (%)
FeCr I	+0.532
FeCr II	-0.316
Ab-initio (SeqQuest)	-0.292

The developed Fe-Cr potentials were implemented in the MDCASK code [28]. The MD simulations were performed using a constant pressure periodic boundary condition based on the Parrinello-Rahman method [29]. The computational cell consisted of 60x60x60 bcc unit cells (432,000 atoms). The cell was thermally equilibrated at 673 K for 30 ps prior to the cascades. The cascades were initiated by giving a primary knock-on atom (PKA) a kinetic energy E_p ranging from 1 to 20 keV along <135> directions, consistent with the approach of other researchers [1,2], in pure Fe and Fe-10%Cr alloys with both FeCr I and FeCr II. The MD simulations continued for 40 ps after cascade introduction without temperature rescaling. In order to obtain defect production statistics, 5–10 MD simulations were performed at each kinetic energy, while changing the specific PKA directions. The Wigner-Seitz cell method was adopted to analyze the number and distribution of produced defects. Second nearest neighbor (NN) criterion for vacancies and third NN criterion for self-interstitial atoms (SIAs) were used for the definition of clusters.

Results

Figure 4 plots the variation in the average number of Frenkel pairs with time for pure Fe and Fe-10%Cr (FeCr I and FeCr II) for the 20 keV cascades. Very similar behavior is shown for pure Fe and Fe-10%Cr (FeCr I and FeCr II). As seen by other research groups [1,2,4–6], the number of Frenkel pairs increases rapidly until reaching a peak around 0.5 ps after initiating the PKA, during the so-called collision stage. The number of Frenkel pairs at the peak varies between 800 and 900. Following the peak, the number of Frenkel pairs quickly decreases due to the recombination of SIAs and vacancies and then about 5 ps after the cascade start, begins to decrease more slowly.

The average number of Frenkel pairs surviving 40 ps after initiating the cascade is plotted in Fig. 5 as a function of PKA energy, E_p. A similar tendency with the power law for pure Fe proposed by Bacon et al. [30] is observed, though with a smaller prefactor of 3.5 vs. 5.7 and a slightly increased power law exponent of 0.82 vs. 0.78. The defect production efficiency is presented in Fig. 6 by dividing the number of surviving Frenkel pairs into the number of displacements predicted by the Norgett-Robinson-Torrens (NRT) model [31], $0.8E_p/2E_d$. The recommended value of the average threshold displacement energy, E_d, of 40 eV was used for bcc Fe [2]. In agreement with other work [1,2,4,5], the efficiency decreases slowly as E_p increases and remains almost constant from 10 to 20 keV. The asymptotic value is about 0.22, which is slightly lower than the previous works for pure Fe [2] and Fe-10%Cr [5]. These results indicate that Cr atoms in Fe do not have a significant effect on the number of primary irradiation defects forming during cascades.

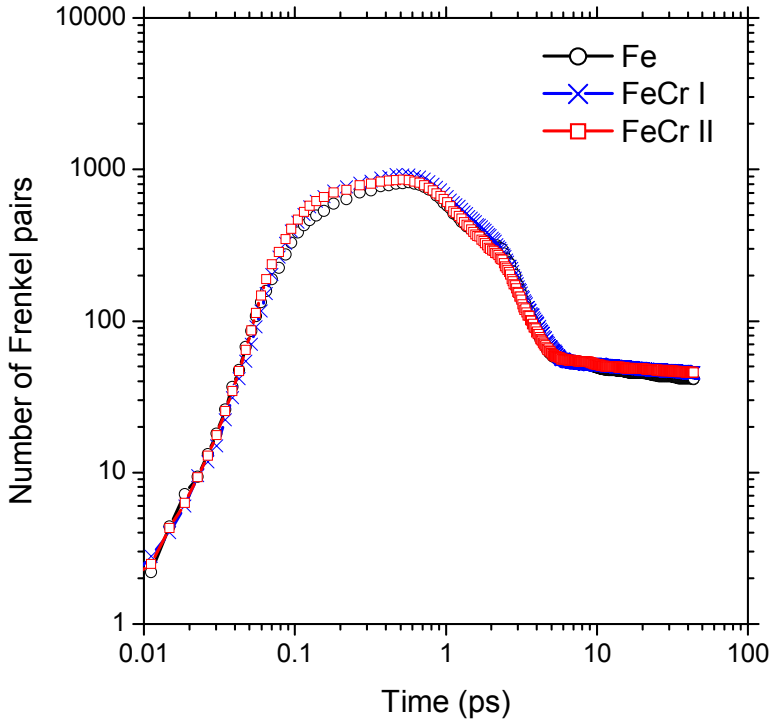

Fig. 4. Number of Frenkel pairs versus time at 20 keV cascades.

Figure 7 shows the typical defect distribution for pure Fe and Fe-10%Cr at 40 ps after initiating the 20 keV cascades. Notably, no significant difference in the defect distribution between pure Fe and Fe-10%Cr is found. While most vacancies are single vacancies, many of the SIAs form clusters containing more than 2 SIAs. Very large clusters containing more than 10 SIAs are often found in all cases. The results from the FeCr I and FeCr II potentials exhibit an opposite feature with respect to the binding (local chemistry) around the defects. As shown in Fig. 8, many Fe-Cr mixed dumbbells (crowdions) and even Cr-Cr dumbbells are produced using the FeCr II potential, whereas mixed dumbbells (crowdions) are not stable in FeCr I and most of the SIA dumbbells involve only Fe atoms. This result is expected from the negative and positive binding energies of the Fe-Cr mixed dumbbell in FeCr I and FeCr II, respectively, as previously shown in Table 2. The fraction of mixed dumbbells observed with the FeCr II potential is larger than that expected of a Fe-10%Cr alloy, assuming that Cr atoms are randomly distributed and there is no interaction between dumbbells and Cr atoms, which would be 0.2 and again, is indicative of the strong binding energy between Cr atoms and SIA from this potential. For the case of larger SIA clusters, Cr atoms are often found associated with the clusters, independent of the choice of interatomic potentials.

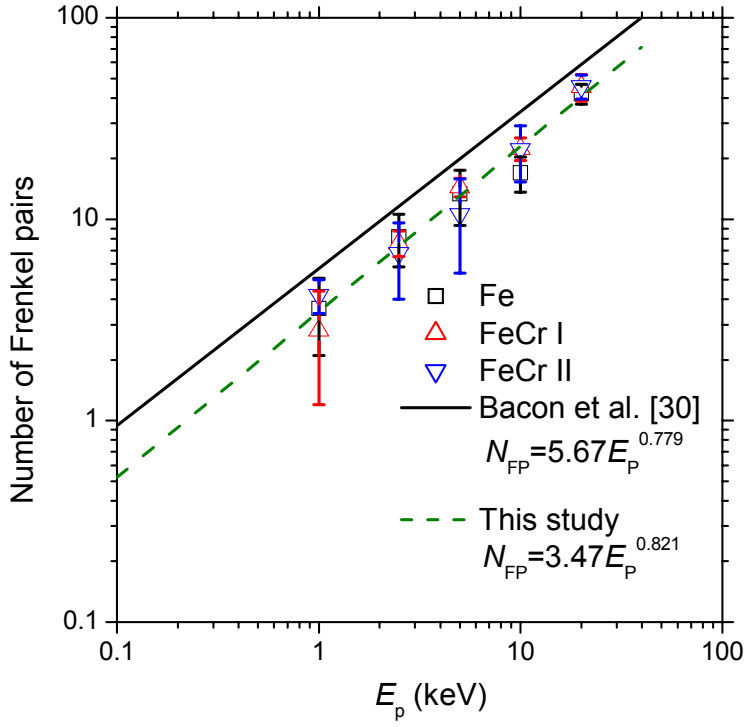

Fig. 5. Number of Frenkel pairs versus E_p.

The results of vacancy and SIA cluster size analysis at 20 keV are summarized in Fig. 9. Consistent with previous work on pure Fe [4], most vacancy clusters consist of 2 and 3 vacancies. In Fe-10%Cr, the number of di-vacancy clusters appears slightly larger than in pure Fe. But, it is not clear at this time whether this is a statistically significant result. For SIA clusters, various cluster sizes are observed, though largest population consists of di-SIA clusters. Figure 10 shows the fractions of vacancies and SIAs in clusters as a function of E_p. The data for vacancy clustering has a large amount of scatter, with cluster fractions varying between 5 and 25%, as Becquart et al. [4] found in their Fe-Cu cascade simulations. The fraction of SIAs in clusters rapidly increases with increasing E_p at the low energy cascades and then exhibits a saturation tendency of about 65% from 5 keV. This tendency is in agreement with pure Fe cascade simulations by Stoller et al. [2] using the original F-S Fe potential. However, the fraction of SIAs in clusters is slightly larger compared to Fe-Cr cascades simulations of Malerba et al. [5]. On the whole, Cr atoms in Fe are unlikely to have a large effect on the clustering tendency of either vacancies or SIA during cascade timescales on the order of tens of picoseconds.

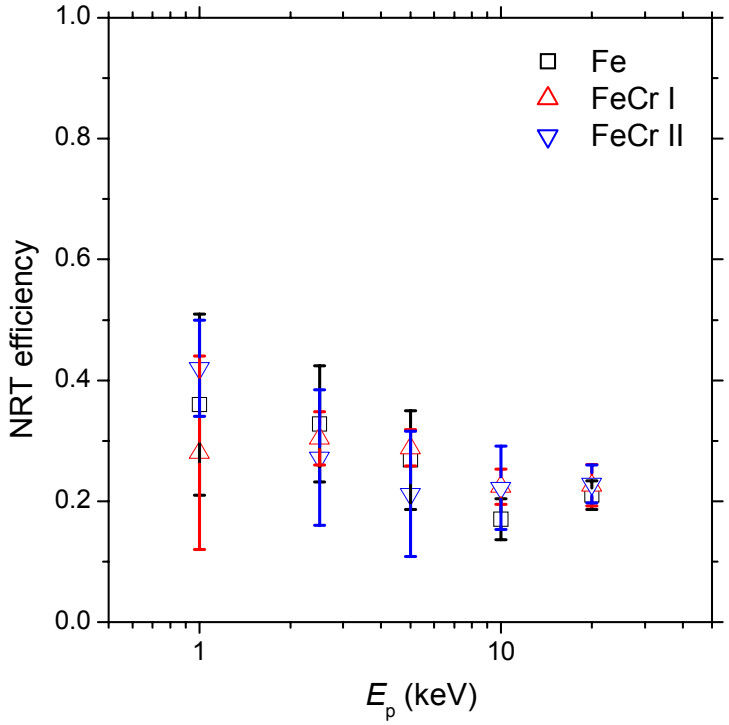

Fig. 6. Defect production efficiency versus E_p.

Discussion

In this study, it is found that Cr atoms in Fe do not have a significant effect on the number of defects produced nor on the formation of clusters during cascades, consistent with other cascade simulations of Fe alloys [5,6]. However, the long-time defect formation and the subsequent microstructural evolution during the annealing stages of cascade aging are more likely to be influenced by the presence of Cr atoms, since Cr atoms can have a more significant impact on defect mobility, particularly for single SIAs and SIA clusters. According to recent MD simulations in Fe-Cr [9] and Fe-Cu [32] alloys, the diffusivity of SIAs are influenced by the presence of solute atoms, especially at low temperatures. In addition, there are experimental observations of a small positive binding energy between Cr and self-interstitial atoms in Fe-Cr alloys, including the possible formation of Fe-Cr mixed dumbbells [34] and that Cr atoms retard the one-dimensional motion of interstitials loops in Fe [33]. It is thought that the binding between SIAs and Cr atoms is the main factor controlling the SIA diffusivity. The two interatomic Fe-Cr potentials proposed in this study show opposite binding interactions for Fe-Cr mixed dumbbells. At present it is quite difficult to decide which potential is more accurate, although the recent ab-initio calculations and the experimental work of Maury support FeCr II. Sufficient experimental investigations of the stability of mixed dumbbells, along with models to compare these results to previous experimental studies of isochronal annealing recovery [34,35], are required to further validate these potentials.

Fe

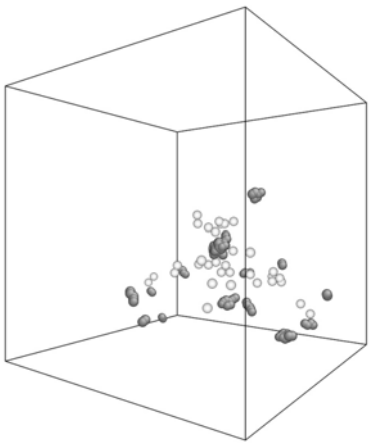

FeCr I

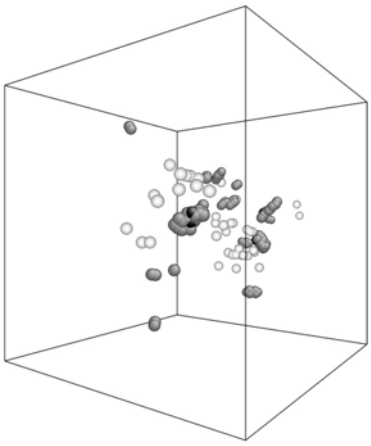

FeCr II

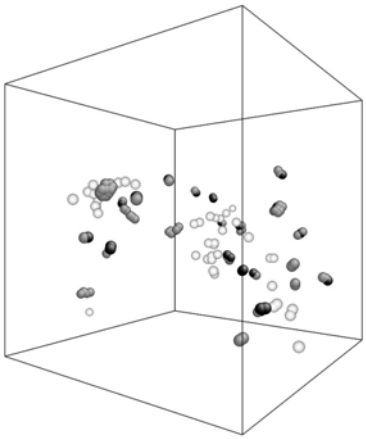

Fig. 7. Typical defect distributions at 40 ps after 20 keV cascades. The empty, gray and black circles represent vacancies, Fe SIAs and Cr SIAs, respectively.

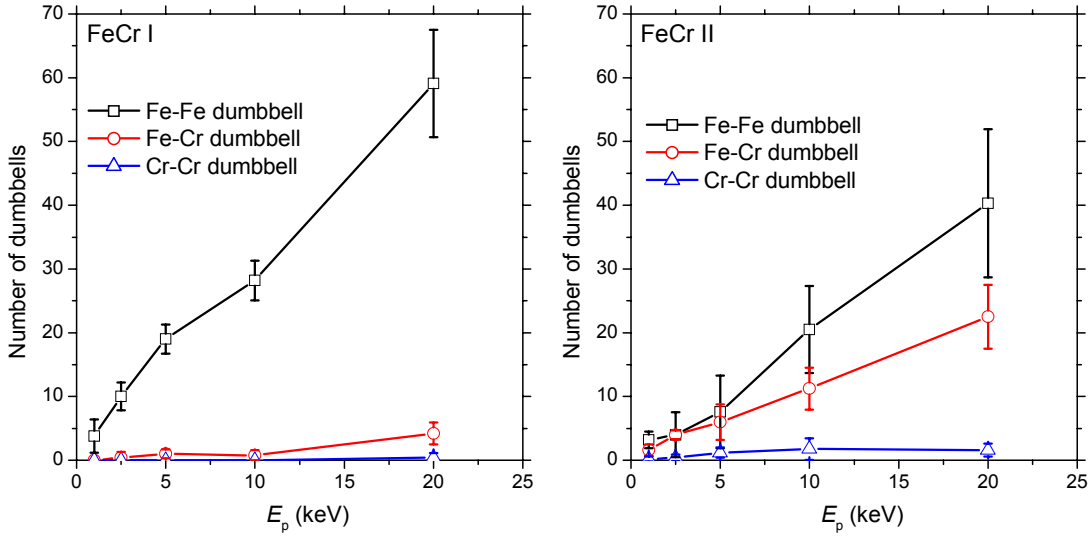

Fig. 8. Number of Fe-Fe, Fe-Cr and Cr-Cr dumbbells in Fe-10%Cr alloys after 20 keV cascades.

Conclusions

MD simulations of displacement cascades with kinetic energy up to 20 keV have been performed in Fe and Fe-10%Cr with potentials based on the Finnis-Sinclair formalism. Two different cross potentials for Fe-Cr, FeCr I and FeCr II are fit to the experimental information available in Fe-Cr alloys, including the heat of mixing and lattice constants. These two potentials exhibit very different behavior for the Cr-SIA interaction; the FeCr I potential predicts unstable Fe-Cr mixed dumbbells while FeCr II predicts stable mixed dumbbells. The potentials used in this study show good agreement, but with slightly lower NRT efficiency than compared to previous works for Fe and Fe-Cr alloys. It is found that Cr atoms do not greatly influence the defect population during the collisional stage of cascades independent of which Fe-Cr potential is selected. However, with FeCr II, many mixed dumbbells are produced after the collisional stage of cascades, well beyond the concentration of Cr. Interesting, the fraction of mixed dumbbells is lower than the results of Malerba et al. [5], possibly due to the lower binding energy derived from the potentials in this work. On the whole, Cr atoms in Fe do not have a significant effect on the production nor distribution of vacancy and SIA clusters right after the collisional cascade stage, independent of the chosen Fe-Cr potential. However, it is expected that the presence of Cr atoms will influence the mobility of SIAs and subsequently damage accumulation and microstructural evolution.

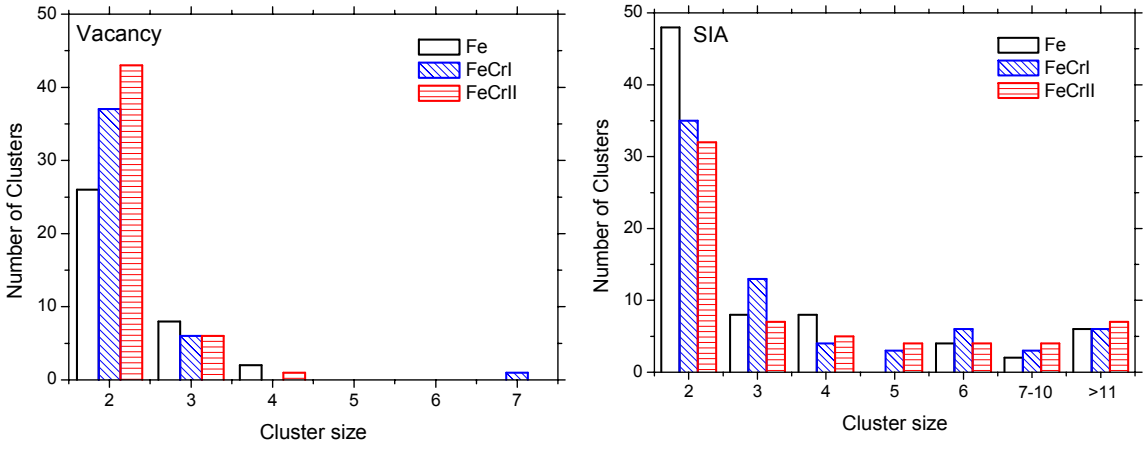

Fig. 9. Size distributions of vacancy and SIA clusters after 20 keV cascades.

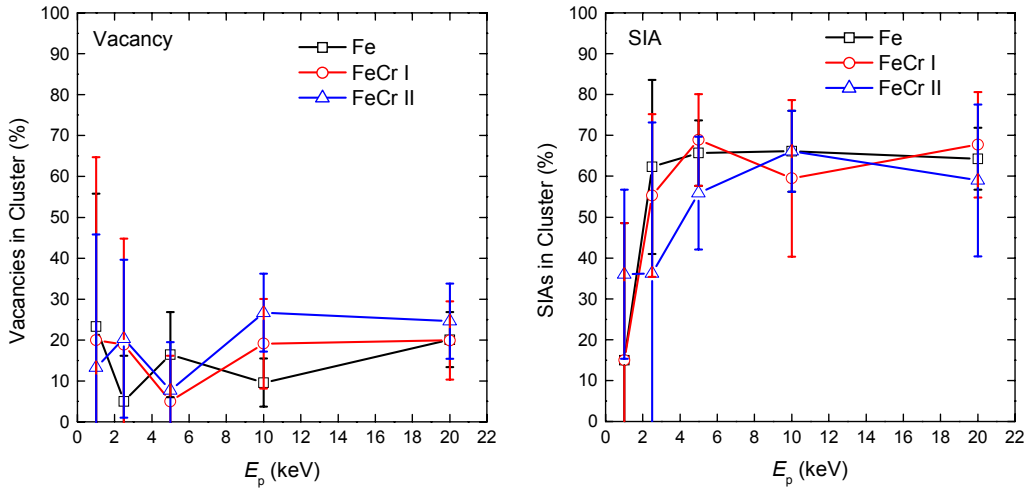

Fig. 10. Fraction of vacancies and SIAs in clusters versus E_p.

Acknowledgements

This work has been supported by the Office of Fusion Energy Sciences, US Department of Energy, under Grant DE-FG02-04ER54750.

References

[1] A. F. Calder and D. J. Bacon, J. Nucl. Mater. 207 (1993) 25.
[2] R. E. Stoller, G. R. Odette, and B. D. Wirth, J. Nucl. Mater. 251 (1997) 49.

[3] N. Soneda and T. Diaz de la Rubia, Philos. Mag. A 78 (1998) 995.
[4] C. S. Becquart, C. Domain, A. Legis, and J. C. Van Duysen, J. Nucl. Mater. 280 (2000) 73.
[5] L. Malerba, D. Terentyev, P. Olsson, R. Chakarova, and J. Wallenius, J. Nucl. Mater. 329–333 (2004) 1156.
[6] J. Wallenius, P. Olsson, C. Lagerstedt, N. Sandbers, R. Chakarova, and V. Pontikis, Phys. Rev. B. 69 (2004) 094103.
[7] M. S. Daw and M. I. Baskes, Phys. Rev. Lett. 50 (1983) 1285.
[8] D. Farkas, C. G. Schon, M. S. F. de Lima, and H. Goldstein, Acta Mater. 44 (1996) 409.
[9] D. Terentyev and L. Malerba, J. Nucl. Mater. 329–333 (2004) 1161.
[10] H. Maeta, F. Ono, and T. Kittaka, J. Phys. Soc. Japan 53 (1984) 4353.
[11] C. Domain and C. S. Becquart, Phys. Rev. B. 65 (2001) 024103.
[12] C.-C. Fu, F. Willaime, and P. Ordejón, Phys. Rev. Lett. 92 (2004) 175503.
[13] B. D. Wirth, G. R. Odette, D. Maroudas, and G. E. Lucas, J. Nucl. Mater. 244 (1997) 185.
[14] G. J. Ackland, D. J. Bacon, A. F. Calder, and T. Harry, Philos. Mag. A 75 (1997) 713.
[15] M. I. Mendelev, S. Han, D. J. Srolovitz, G. J. Ackland, D. Y. Sun, and M. Asta, Philos. Mag. 83 (2003) 3977.
[16] H. J. Wollenberger, In R. W. Cahn and P. Haasen (eds.), Phys. Metall., Third Edition, Elsevier, Amsterdam (1983) 1139–1221.
[17] M. W. Finnis and J. E. Sinclair, Philos. Mag. A 50 (1984) 45.
[18] J. H. Rose, J. R. Smith, F. Guinea, and J. Ferrante, Phys. Rev. B 29 (1984) 2963.
[19] T. Konishi, K. Ohsawa, H. Abe, and E. Kuramoto, Comput. Mater. Sci. 14 (1999) 108.
[20] G. J. Ackland and V. Vitek, Phys. Rev. B 41 (1990) 10324.
[21] J.-O. Andersson and B. Sundman, Calphad 11 (1987) 83.
[22] W. A. Dench, Trans. Faraday Soc. 59 (1963) 1279.
[23] W. Leslie, R. J. Sober, S. G. Babcock, and S. J. Green, Trans. Am. Soc. Metall. 62 (1969) 690.
[24] E. P. Abrahamson and S. L. Lopata, Trans. Metall. Soc. AIME 236 (1966) 76.
[25] W. B. Pearson, A Handbook of Lattice Spacings and Structures of Metals and Alloys, Pergamon Press, New York (1958) 532.
[26] C. Domain, (private communication).
[27] http://www.cs.sandia.gov/~paschul/Quest.
[28] T. Diaz de la Rubia and M. W. Guinan, J. Nucl. Mater. 174 (1990) 151.
[29] M. Parrinello and A. Rahman, Phys. Rev. Lett. 45 (1980) 1196.
[30] D. J. Bacon, A. F. Calder, F. Gao, V. G. Kapinos, and S. J. Wooding, Nucl. Instrum. Methods B 102 (1995) 37.
[31] M. J. Norgett, M. T. Robinson, and I. M. Torrens, Nucl. Eng. Des. 33 (1975) 50.
[32] J. Marian, B. D. Wirth, J. M. Perlado, G. R. Odette, and T. Diaz de la Rubia, Phys. Rev. B 64 (2001) 094303.
[33] K. Arakawa, M. Hatanaka, H. Mori, and K. Ono, J. Nucl. Mater. 329–333 (2004) 1194–1198.
[34] F. Maury, P. Lucasson, A. Lucasson, F. Faudot, and J. Bigot, J. Phys. F: Met. Phys. 17 (1987) 1143.
[35] H. Abe and E. Kuramoto, J. Nucl. Mater. 271–272 (1999) 209–213.

MODELLING THERMODYNAMICS OF ALLOYS FOR FUSION APPLICATION—A. Caro (Lawrence Livermore National Laboratory) (Work done in collaboration with B. Sadigh, P. E. A. Turchi, and M. Caro, Lawrence Livermore National Laboratory)

OBJECTIVE

The research has two main lines. On one side is the development of computational thermodynamic tools to evaluate alloy properties, in particular, free energies, and from these to assess the phase stability and microstructure evolution of model systems under irradiation; with them, to use the information on thermodynamic functions to improve the potentials to the extent that it can be done within the classic approach. On the other hand, to use the tools so developed to predict properties of alloys under irradiation.

SUMMARY

The real problem of microstructure evolution of steels under irradiation involves complex thermodynamics of non-equilibrium and kinetic processes in multicomponent–multiphase alloys. Empirical simulations have a long history addressing Fe and, in particular, with one impurity relevant in fission reactor pressure vessels steels: Cu. However no realistic assessment of the accuracy of the model predictions has been available until very recently. The classic computational approach deals with an oversimplified description of alloys.

The aim of the proposed work is to develop theoretical and numerical methodologies that are directly applicable to multi-scale modeling addressing the specific issues related to multi-component multi-phase systems in non-equilibrium states, such as solid-solution hardening, point defect-solute interactions, stoichiometry effects, static and dynamic strain aging, dislocation-solute interactions, and in general, the aspects of microstructure evolution that are affected by irradiation.

In recent times, several new algorithms appeared showing procedures to numerically evaluate free energies, using both *ab-initio* and empirical descriptions for the total energy, either in molecular dynamics (MD) or Monte Carlo frames (MC). Frenkel and Ladd introduced a method to calculate absolute free energies of arbitrary solids based on the construction of a reversible path from the solid phase under consideration to a reference system whose free energy is known through an analytic expression. Their reversible path method, with some modifications, is one of the most common methods used today, either in MC and MD. This is the method we have implemented in the first phase of this work and applied it to the study of several model systems, Au-Ni, Fe-Cu, and Fe-Cr. In recent papers we reported on the phase diagram calculations for some of these systems. We found they show unexpected differences with the known assessed one.

We concluded from this study that alloys in the framework of empirical potentials require a different treatment of the hetero-atomic interactions if the concentrated cases are to be correctly described. The cases we studied show that adjusting the heat of solution of a single impurity is not enough to describe the complex behavior of concentrated systems. This problem can be addressed by further modifications to the EAM formalism to incorporate concentration dependent interactions that will reproduce the magnitude of excess enthalpy of mixing, as well as the asymmetry around equi-atomic composition.

PROGRESS AND STATUS

We have completed the development of a numerical tool that allows us to study alloys microstructure. In particular, we finished a quite unique code to perform Monte Carlo calculations in multimillion-size samples that would allow us to uncover and explore the microstructure of alloys, either in bulk, as well as in the presence of defects like grain boundaries, isolated dislocations, dislocations cells, etc. It is important to mention that it is not a lattice Monte Carlo code, but a fully relaxed one in the transmutation ensemble. It will provide size, shape, and composition of precipitates, as well as interface energies and structure.

Early examples of application are reported in Figs. 1 and 2.

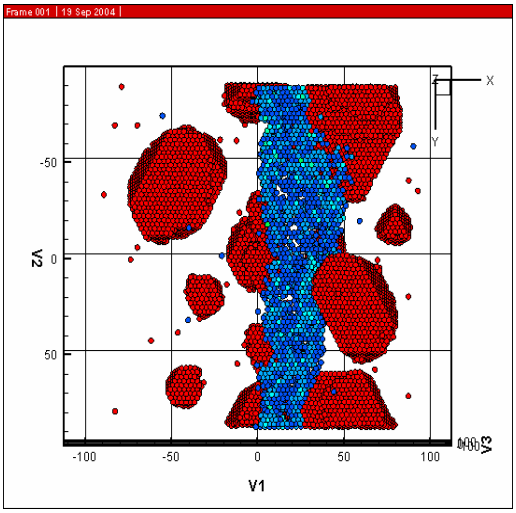

Fig. 1. As an example of application of the newly developed Monte Carlo code, this figure shows a perfect dislocation in fcc Cu (characterized by the ribbon of stacking fault, blue atoms) and nanometer size Fe precipitates, in a dilute $Cu_{99}Fe_1$ alloy.

Having finished in FY04 the development of codes to obtain free energy of alloys, and having studied several potentials available in the literature, highlighting their strength and limitations, we entered the second stage of this research, i.e., the development of improved EAM potentials for alloys with the right thermodynamic behavior. In this goal, we are doing substantial progress in the Fe-Cr system.

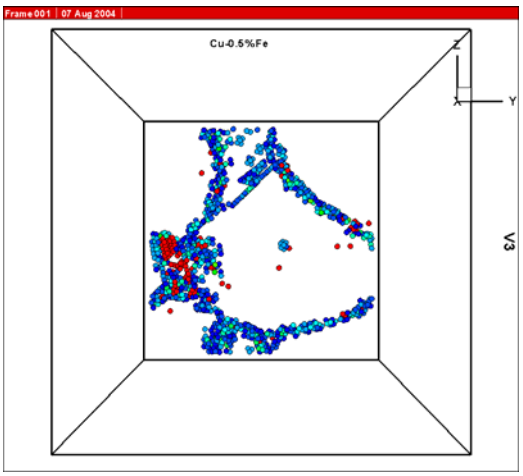

Fig. 2. In polycrystalline materials solute segregation to grain boundaries plays a significant role in affecting the mechanical properties. In this figure we observe Fe precipitation (red atoms) in a nanocrystalline Cu sample where only atoms at grain boundaries (blue circles) are shown. A segregation tendency is clearly observed.

The ability to predict microstructures would be of significant value to effectively make progress in the field of alloys under irradiation. For the particular problem of Fe-Cr alloys, experimental evidence suggests the presence of a negative heat of mixing for concentrations below the solubility limit. This would imply an

ordering tendency in the ferromagnetic phase, a feature which is hard to model simultaneously with the presence of a miscibility gap.

We have developed a generalization of the EAM formalism for concentrated alloys that allows reproducing an arbitrarily complex heat of solution. This was achieved by further modifying the EAM formalism to incorporate concentration dependent interactions that reproduce the magnitude of excess enthalpy of mixing, as well as the asymmetry around equi-atomic composition. Figure 3 shows the agreement between the reported heat of solution of Fe-Cr and the values obtained with the modified EAM scheme. Both curves are indistinguishable. Bulk modulus and lattice parameters, predicted by the model, are not available in the literature for comparison purposes.

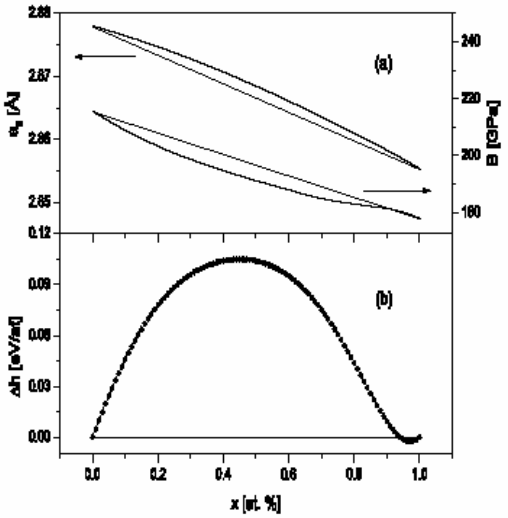

Fig. 3. Variations of bulk modulus B, lattice parameter (a), and formation energy of the Fe-Cr alloy (b), predicted by the modified EAM description of Fe-Cr alloys. Thin straight lines represent the linear interpolation corresponding to the ideal solution. Maximum departures for B and a0 from ideal behavior are 0.25% and 0.1 %, respectively.

The numerical tool we developed and this new potential combined are expected to help us in studying the complex behavior of this alloy in a unique way.

The strategy that we follow is that as new and better potentials for Fe are developed, and new properties for the Fe-Cr system are characterized, either by *ab initio* or experiments, we then focus into their incorporation on better classic potentials for the alloy.

References

[1] A. Caro, P. E. A. Turchi, M. Caro, and E. M. Lopasso, Thermodynamics of an empirical potential description of Fe-Cu alloys, J. Nucl. Mater. 336 (2005) 233–242.
[2] A. Caro, M. Caro, E. M. Lopasso, P. E. A. Turchi, and D. Farkas, Thermodynamics of Fe-Cu Alloys as Described by the Ludwig-Farkas EAM Potential (submitted).
[3] A. Caro and D. Crowson, Classic many body potential for concentrated alloys (in preparation).

HELIUM BEHAVIOR IN METALS CHARACTERIZED BY THERMAL HELIUM DESORPTION SPECTROSCOPY—S. C. Glade and B. D. Wirth (University of California, Berkeley) and H. Schut (Interfaculty Reactor Institute, Delft University of Technology, Delft, The Netherlands)

OBJECTIVE

To construct and operate a thermal helium desorption spectroscopy experimental characterization system for use in analyzing helium behavior in iron and related fusion materials.

SUMMARY

A facility to perform thermal helium desorption spectroscopy is under construction at the University of California, Berkeley. The facility is scheduled to be validated and in operation in early June 2005. Experiments are currently being designed to provide data on helium diffusion, trapping mechanisms and energetics in iron and iron alloys.

PROGRESS AND STATUS

Introduction

The behavior of helium in metals must be understood for future use in fusion applications. In fusion reactors, the helium concentration in metals increases by direct implantation of helium and by nuclear transmutation reactions. Helium has extremely low solubility in most metallic alloys and interacts (traps) strongly with preexisting and radiation produced microstructural defects. At high concentrations, helium precipitates to form helium bubbles which can cause high-temperature intergranular embrittlement and swelling. Of particular interest is the behavior of helium in iron, for which there is very little experimental data [1–3].

A thermal helium desorption spectrometer (THDS) is under construction at the University of California, Berkeley. Its design is based on THDS systems at the Delft University of Technology. The THDS method and information that can be obtained from analyses of the desorption spectra are presented in this progress report.

Experimental Design

Conceptually, thermal helium desorption spectroscopy is simple: heat the material of interest and measure the amount of helium released. The design requirements for a thermal helium desorption spectrometer are presented in Refs. [4–6], and an example of an operating system is provided in Ref. [7]. A schematic of the system at U.C. Berkeley is shown in Fig. 1.

Vacuum System

The THDS system is constructed with commercial stainless steel vacuum components and all-metal valves. The total chamber volume is approximately 2.5 L, pumped with two turbo-drag pumps backed by roughing pumps. The two turbo-drag pump setup allows the mass spectrometer to always remain under vacuum, with only the sample holder and heating system brought to atmospheric pressure for sample changes. Bayard-Albert type hot cathode ionization gauges are used for pressure measurement, with the expected vacuum level of the system to be 10^{-8} Pa (7.5×10^{-11} torr). A liquid nitrogen cooling coil in the sample chamber (not shown in Fig. 1) will be used to prevent heating of chamber walls as well as to condense gases other than He that are desorbed from the sample.

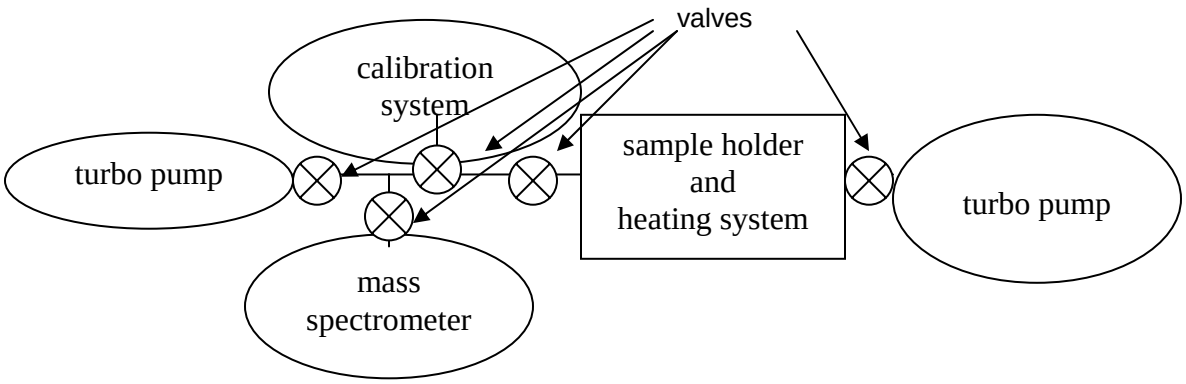

Fig. 1. Schematic of thermal helium desorption spectrometer.

Helium Detection

Helium detection in the THDS is preformed with a mass spectrometer equipped with a Channeltron type electron multiplier. A linear relationship exists between ion current in the mass spectrometer and helium partial pressure:

$$I(A) \propto P_{He}(torr)\,. \tag{1}$$

The helium desorption rate from a sample is described by:

$$L(t) = \frac{dN}{dt} = \frac{dP(t)}{dt} + \frac{S}{V}P(t) = \frac{dP(t)}{dt} + \frac{P(t)}{\tau}, \tag{2}$$

where *L(t)* is the helium desorption rate,*N* is the number of helium atoms,*P(t)* is the partial pressure of helium,*S* is the pumping speed (L s^{-1}),*V* is the chamber volume (L), and τ = *V/S*, the pumping time constant (s).

The THDS system can operate in two modes, either a static or a dynamic mode. In the static mode, the $P(t)/\tau$ term in Eq. (2) is minimized, with no pumping on the sample holder chamber. In the dynamic mode, the $dP(t)/dt$ term in Eq. (2) is minimized, and τ is adjusted by the valve to the turbo-drag pump. We plan to operate the THDS system in the dynamic mode.

The mass spectrometer will be calibrated by releasing a known small amount of He into the system to determine a calibration factor:

$$Q = {\#\,He\ atoms}/{I} \tag{3}$$

Sample Heating

The samples will be heated radiatively by a resistively (150 A, 20 V) heated tungsten filament. A type C thermocouple is used for temperature measurement. Proportional integral derivative (PID) temperature control will be implemented with LabVIEW™. Different heating schedules can be programmed with the system, with either linear heating or linear-step heating (i.e., heating to T1, cooling to room temperature, heating to T1 + 50 K, cooling to room temperature; this is continued in ΔT steps until the maximum

desired temperature is reached) used initially. LabVIEW™ is also used for recording all system data during a desorption experiment (temperature, pressure, He partial pressure, and time).

Data Analysis

The first-order rate of He desorption from a sample is given by:

$$\frac{dN}{dt} = -N\nu \exp\left(\frac{-Q}{kT}\right), \tag{4}$$

where N is the number of helium atoms, Q is the activation enthalpy, ν is the attempt frequency, T is temperature, and k is Boltzmann's constant. With a linear heating rate, the temperature at which the desorption rate is maximum is:

$$-\frac{Q}{kT_{\max}^2} = \frac{\nu}{\beta}\exp\left(-\frac{Q}{kT_{\max}}\right), \tag{5}$$

where T_{max} is the temperature at which the desorption rate is a maximum and β is the heating rate. Eq. 5 is used to calculate the activation enthalpy, Q. The attempt frequency, ν, is usually taken as the Debye frequency, 1×10^{13} s^{-1}, which is on the order of the atomic vibration frequency in solids.

Linear-step heating experiments can provide further information about helium release mechanisms. By considering the first part of the release curve where the change in N is very small, the slope of a release curve, when plotted in an Arrhenius plot, gives the activation enthalpy, Q. The attempt frequency, ν, can also be calculated, instead of assuming a value. A calculated attempt frequency lower than the expected Debye frequency value indicates multi-step activated processes in which first-order reaction kinetics do not apply. Examples of both linear heating and linear-step heating THDS experiments are presented in Ref. [8].

We anticipate multiple He interactions govern the He desorption, which make data analysis more complicated than simple first-order kinetics. The planned THDS experiments will be closely coupled to multiscale simulation models currently being developed.

Progress

The procurement of all required equipment for the THDS system is complete. The vacuum system is assembled, and vacuum levels of 10^{-8} torr have been demonstrated. The next planned steps to prepare the system for experiments include attaching the mass spectrometer, testing the sample heater, and installing the calibration system.

Future Work

The THDS system is planned for initial operation by the beginning of June 2005. We will soon begin helium implanting iron specimens with an ion gun for use in system validation. After the system is operating and validated, we will begin experiments to provide data on helium diffusion trapping mechanisms and energetics in iron.

Acknowledgments

This work has been supported by the Office of Fusion Energy Sciences, U.S. Department of Energy, under Grant DE-FG02-04ER54750.

References

[1] R. Vassen, H. Trinkaus, and P. Jung, Phys. Rev. B 44 (1991) 4206.
[2] K. Morishita, R. Sugano, and B. D. Wirth, J. Nuc. Mater. 323 (2003) 243.
[3] K. Morishita, R. Sugano, B. D. Wirth, and T. Diaz de la Rubia, Nuc. Inst. Meth. Phys. Res. B 202 (2003) 76.
[4] P. A. Redhead, Vacuum (1962) 203.
[5] A. A. van Gorkum and E. V. Kornelsen, Vacuum 31 (1981) 89.
[6] E. V. Kornelsen and A. A. van Gorkum, Vacuum 31 (1981) 99.
[7] E. Kautto, O. P. Kahkonen, J. Kuhalainen, M. Manninen, Nuc. Inst. Meth. Phys. Res. B 103 (1995) 376.
[8] P. M. G. Damen, A. van Veen, F. Labohm, H. Schut, and M. A. van Huis, J. Nuc. Mater. 306 (2002) 180.

HELIUM – SELF-INTERSTITIAL ATOM INTERACTION IN FERRITIC ALLOY—L. Ventelon and B. D. Wirth (University of California, Berkeley), C. Domain (Electricite de France)

OBJECTIVE

The objective of this work was to determine the effect of interstitial and substitutional helium atoms on the behavior of self-interstitial atoms and self-interstitial atom clusters in ferritic alloys.

SUMMARY

Atomistic simulations have been performed to investigate the effect of He impurities on the properties and behavior of self-interstitial atom clusters in Fe. Ferritic alloys are candidate fusion energy first wall and breeding blanket structural materials, and will be exposed to high levels of radiation damage and transmutation products in a 14 MeV peaked fusion neutron spectrum. A comparison is made of the interaction energies between interstitial He atoms and a single self-interstitial atom (SIA) obtained with *ab-initio* electronic structure and semi-empirical interatomic potentials using molecular dynamics and conjugate gradient molecular statics calculations. The results provide insight into the validity of semi-empirical interatomic potentials and a basis for extrapolating *ab-initio* results from small to larger system sizes. We also present the results of MD investigation into the migration behavior of SIAs and SIA clusters in the presence of interstitial and substitutional He. The MD simulations reveal a strong interaction between He and SIA clusters, often resulting in SIA – vacancy reactions that spontaneously eject helium into interstitial sites, and provide quantitative information on the interaction radii, trapping – binding energetics and migration behavior of mixed He-SIA clusters.

PROGRESS AND STATUS

Introduction

Associated with the development of long-lived and high-performance fusion materials, one key challenge is dealing with the high-level of helium generated from (n,α) reactions in the first wall and blanket structures. Amongst its harmful consequences, helium has a strong tendency to precipitate into thermally stable helium – vacancy clusters and helium bubbles, which is detrimental to the mechanical properties of metals and alloys [1]. Moreover, helium assists the nucleation and growth of cavities in irradiated materials, leading to swelling [2]. Finally, helium migration and precipitation in the form of grain boundary bubbles can produce high temperature embrittlement. Thus, we are investigating the He diffusion mechanisms in ferritic alloys, including by substitutional and interstitial migration and diffusion by vacancy – helium clusters. Possible reactions that must be incorporated into damage accumulation models of fusion materials performance include trapping/de-trapping interactions with a large number of microstructural defects, including dislocations, grain boundaries, precipitate interfaces, vacancies and self-interstitial atom (SIA) clusters and clustering (precipitation) interactions with vacancy, and possibly even SIA clusters. The primary focus of this work is on the interactions between helium and SIA and SIA clusters.

Interatomic Potentials and Simulation Methods

Atomistic simulations have been performed, using semi-empirical Fe-He potentials, using both molecular dynamics (MD) and molecular statics (MS) methods by conjugate gradients. The Fe-Fe interaction is described by the Ackland version of the Finnis-Sinclair potential [3], which predicts a $\langle 110 \rangle$ dumbbell as the stable self-interstitial atom, with a metastable $\langle 111 \rangle$ dumbbell. The isolated SIA migrates according to this potential by rotation of the $\langle 110 \rangle$ mono-interstitial to the $\langle 111 \rangle$ configuration with an activation energy of about 0.2 eV, followed by a fast migration in the $\langle 111 \rangle$ direction [4]. It is important to note that recent *ab-initio* calculations [5–6] and a semi-empirical potential recently developed for Fe [7], predict a larger energy difference between the $\langle 110 \rangle$ and the $\langle 111 \rangle$ configurations, namely 0.7 eV. However, for larger clusters, the $\langle 111 \rangle$ orientation of the dumbbells within the SIA cluster is energetically preferred for both semi-empirical potentials. Thus, in terms of qualitative analysis of the behavior of SIA and SIA clusters,

the performance of these two potentials are comparable and the use of this new potential will likely only change our quantitative results slightly, but again the focus here is on determining the governing mechanisms which give us insight into material behavior. Such mechanisms likely are much less sensitive to the specific details of the selected interatomic potential. The Fe-He interaction is described by the Wilson and Johnson potential [8], a purely repulsive pair-wise potential. For the He-He interaction, we have used the Beck potential [9], also a semi-empirical pair-wise potential.

Ab-initio calculations have been performed with the Vienna Ab-initio Simulation Package VASP [10–12]. The calculations implement a plane-wave basis set, using pseudo-potential within the PAW formalism to describe the electron-ion interaction. Electron exchange and correlation are described by the Perdew-Zunger functional, adding a non-local correction in the form of the generalised gradient approximation (GGA) of Perdew and Wang. All the calculations were performed with the spin polarised GGA pseudo-potentials from the VASP library. Brillouin zone (BZ) sampling is performed using the Monkhorst-Pack scheme. Point defects as well as pure phases are investigated using the super-cell approach with periodic boundary conditions. The defect calculations are performed at constant volume, thus relaxing only the atomic position in a super-cell dimensioned with the equilibrium lattice parameter for Fe. Calculations with 54 (respectively, 128) atom super-cells are done with a BZ sampling of 125 (respectively, 27) k points and a cut-off energy of 400 eV.

The MD simulations have been performed using a computational box size of $50a_0 \times 50a_0 \times 50a_0$ (containing 250,000 atoms), where a_0 is the Fe lattice parameter, with periodic boundary conditions. The cell size has been systematically varied from $3a_0 \times 3a_0 \times 3a_0$ to $20a_0 \times 20a_0 \times 20a_0$ in the conjugate gradient simulations, using the same interatomic potentials. The conjugate gradient scheme is employed in relaxing the atomic positions, and takes several steps to relax the atoms, allowing the whole relaxation process to be fully automated. Volume relaxation turned out to have a small effect on the binding and formations energies as long as conjugate gradient scheme allows for atomic relaxation around the defect. The MD simulations provide insight into the dynamic mechanisms governing He – point defect interactions, while the static simulations provide the formation and binding energies. For static simulations using semi-empirical potentials and *ab-initio* simulations, we have calculated the binding energy between two entities, A and B, in a bcc iron matrix, containing N atoms as follows. The energy E(N - 1 + A) of a super-cell containing only defect A is added to that E(N - 1 + B) of the super-cell containing only defect B. From this sum, one subtracts the energy E(N - 2 + A + B) of the same super-cell containing A and B interacting, and the reference state (E_{ref}) of the super-cell containing no defect. Thus, $E_b(AB) = [E(N - 1 + A) + E(N - 1 + B)] - [E(N - 2 + A + B) + E_{ref}]$. This method can be extended to three, four and so on entities, as follows:

$$E_b(A_1A_2 \ldots A_n) = \sum_{i=1}^{n} E(A_i) - \left[E(A_1 + A_2 + \ldots + A_n) + (n-1)E_{ref}\right]$$

For substitution energy, the reference state for He is the fcc crystal structure. Details of the calculation methods of the formation and binding energies are described in Ref. [2] for static simulations using semi-empirical potentials, and in Ref. [13] for *ab-initio* simulations.

Results and Discussion

It is believed that helium initially resides in interstitial positions in metallic alloys with a very high mobility [14]. As helium diffuses by an interstitial mechanism in a metal with high vacancy super-saturation, as during irradiation, it will become deeply trapped at a vacancy and the diffusion of the now substitutional helium occurs via a vacancy mechanism. Atomistic simulations within the framework of the multiple frequency diffusion model of Le Claire [15] revealed an effective activation energy of 2.35 eV for thermal helium diffusion and showed that substitutional helium can exchange with a second nearest neighbor vacancy with an activation energy of 0.66 eV [16]. According to the semi-empirical potentials, interstitial He diffuses from octahedral to neighboring octahedral sites with an activation energy of about 0.1 eV, where the migrational saddle point consists of the tetrahedral site. Notably, recent *ab-initio* results show a reversal of the octahedral-tetrahedral site stability, but do reveal similar high mobility (low migrational

activation energy) as an interstitial [6–7]. Further, both this set of semi-empirical potentials and the recent *ab-initio* calculations reveal a strong trapping of substitutional He at vacancies, SIAs and SIA clusters.

The He trapping effect upon SIA clusters has been investigated by both dynamic and static simulations. Figure 1 shows a comparison of the diffusivities of a 20 SIA cluster in pure iron and in the presence of a high concentration of substitutional He. The SIA cluster diffusivity was obtained from MD simulations at 600, 800 and 1000 K in pure Fe and in an Fe alloy containing 2500 atomic parts per million (ppm) of randomly distributed substitutional He. As seen in Fig. 1, the low, practically athermal activation energy of one-dimensional SIA cluster migration changes only slightly as a result of He. This indicates that the fundamental migration mechanism remains the same. However, the diffusivity pre-factor decreases by about one order of magnitude, and indicates that He does slow the net SIA cluster migration. The degree of trapping observed depends on the relative positions of both the He and SIA cluster.

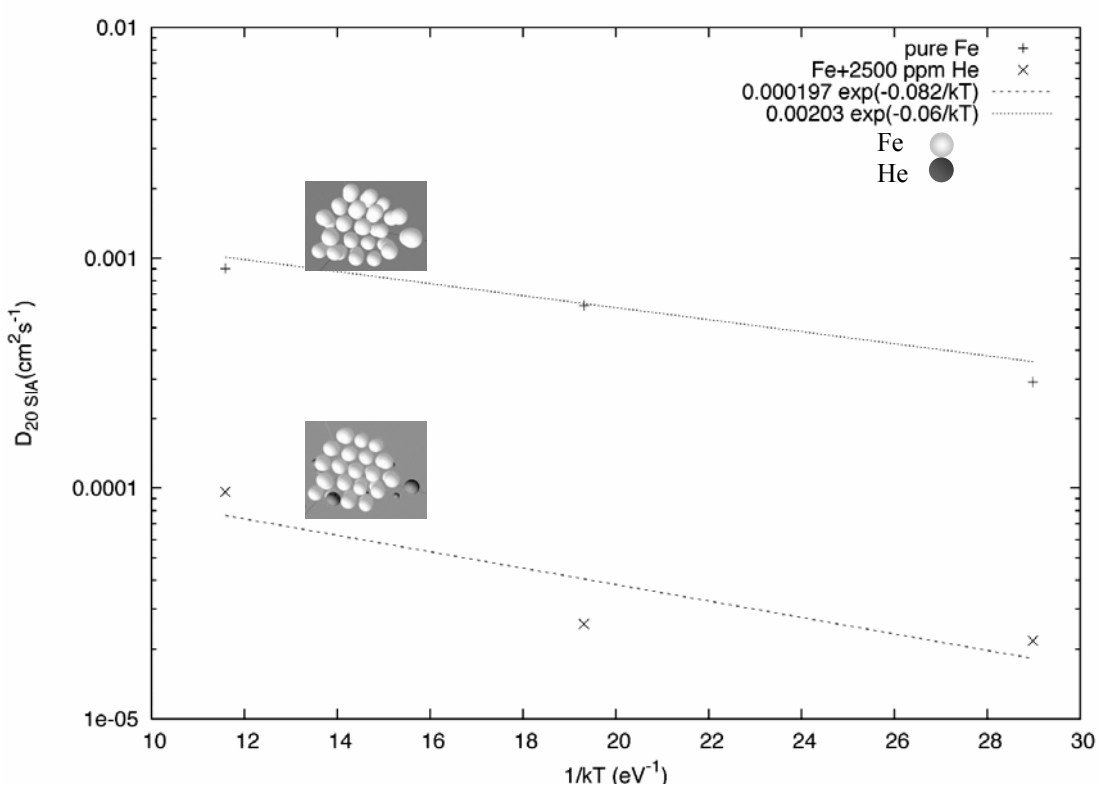

Fig. 1. Comparison of the diffusivities of a 20 SIA cluster in pure iron and in the presence of a high concentration of substitutional He.

Another MD simulation performed at 1000 K in a defected region of otherwise perfect bcc iron containing a high concentration of substitutional He has revealed a large number of interaction phenomena, as shown in Fig. 2. In this figure, a 9 SIA – 2 He cluster, a single vacancy, an isolated SIA, an interstitial He atom and 2 substitutional He atoms from the overall simulation are in close proximity (Fig. 2a). The isolated SIA is about 2.3 nm away from the substitutional He atom. Over several picoseconds, the SIA migrates three-dimensionally with multiple changes of orientation, generally moving towards the nearby helium atom. Upon reaching a separation of about 1.4 nm from the helium in the [111] direction, a fast and spontaneous recombination – replacement reaction occurs (Fig. 2b). In this reaction, the SIA enters the vacant lattice site, recombining with the vacancy and ejecting the helium atom from a substitutional to an interstitial position. The resulting interstitial He rapidly diffuses to and binds with a nearby substitutional He atom for a period of 10 ps, before finally de-trapping (Fig. 2c). Considering the 9 SIA – 2 He cluster, it remains effectively trapped for about 43 ps before the 9 SIA cluster de-traps from the di-He and migrates one-dimensionally towards the isolated vacancy, with which it annihilates (Fig. 2d). Subsequently, the de-

trapped interstitial He migrates to and traps the 8 SIA cluster (Fig. 2e). This simulation has shown a variety of recombination, trapping and de-trapping processes involving He and SIA clusters which merits further study.

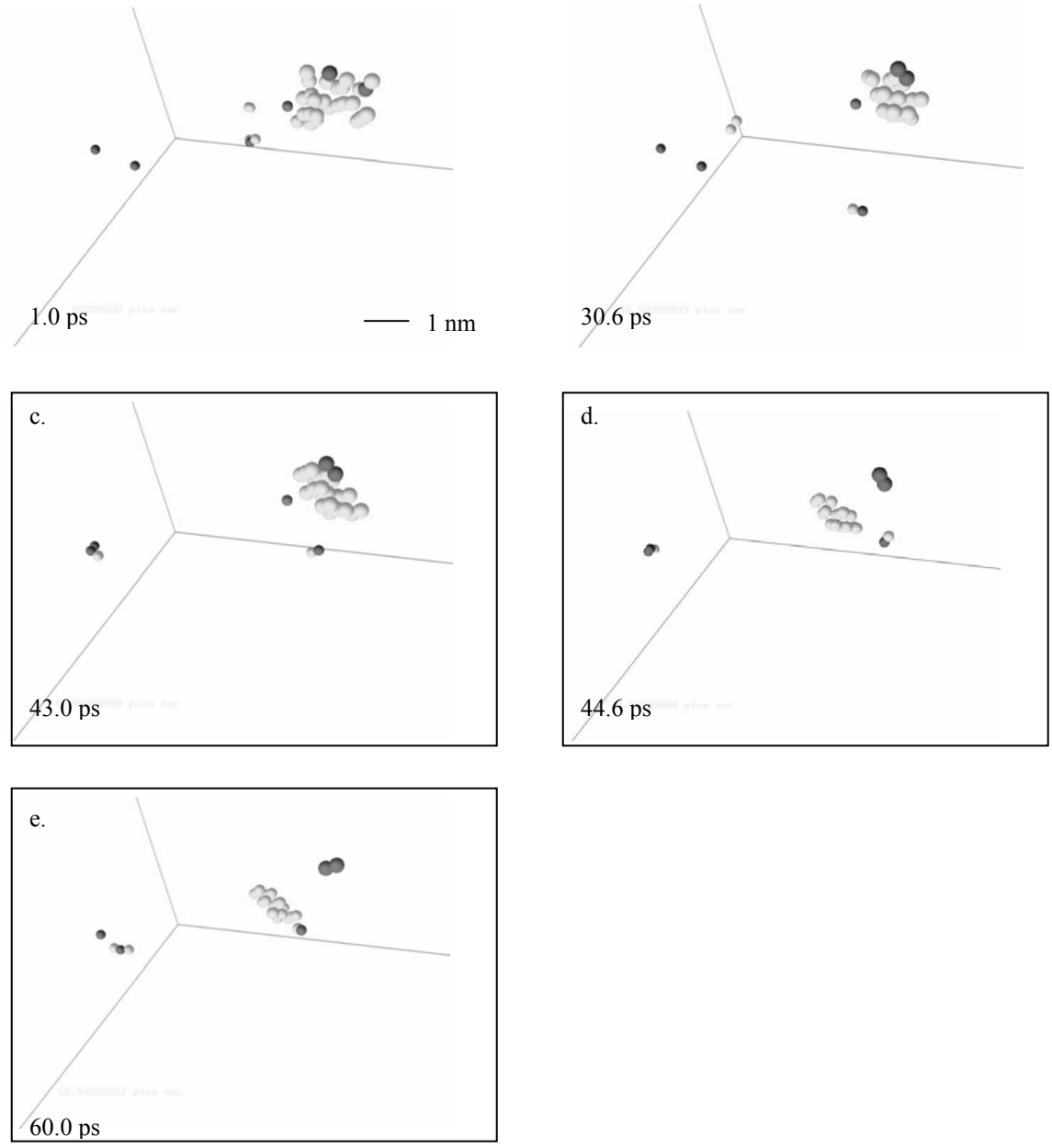

Fig. 2. Series of MD snapshots showing the interaction between SIA and SIA cluster (light gray circles) and neighboring substitutional He atoms (dark gray circles) at 1000K. This simulation shows a fast and spontaneous recombination – replacement reaction (2.a, 2.b), He – He complex formation (2.c), SIA de-trapping from the di-He (2.d) and migration of the de-trapped interstitial He to the SIA cluster (2.e).

Figure 3 shows a series of snapshots in time from an MD simulation at 1000 K showing the interaction between an 11 SIA cluster and 4 substitutional He – 2 vacancy cluster. The 11 SIA cluster, initially about 8 nm away from the He cluster in the [111] direction, migrates one dimensionally along the ⟨111⟩ direction with a net drift towards the He – vacancy cluster (Fig. 3a). When the SIA cluster reaches a separation of about 2 nm from the helium – vacancy cluster, the SIA cluster is spontaneously attracted to the vacancy

cluster complex, where it annihilates (recombines with) the 6 vacant lattice sites and ejects the 4 substitutional He atoms into interstitial positions (Fig. 3b). The SIA cluster and the 4 He interstitial cluster rapidly coalesce to form a 5 SIA – 4 interstitial He cluster (Fig. 3c). The resulting SIA – He cluster is strongly bound and, although the SIA cluster continually attempts to migrate by detaching from the cluster, it is unable to overcome the binding interaction and remains trapped over the time scale of the MD simulation. Notably however, the 5 SIA – 4 interstitial cluster does rotate from its initial ⟨111⟩ direction to a different ⟨111⟩ direction (Fig. 3d).

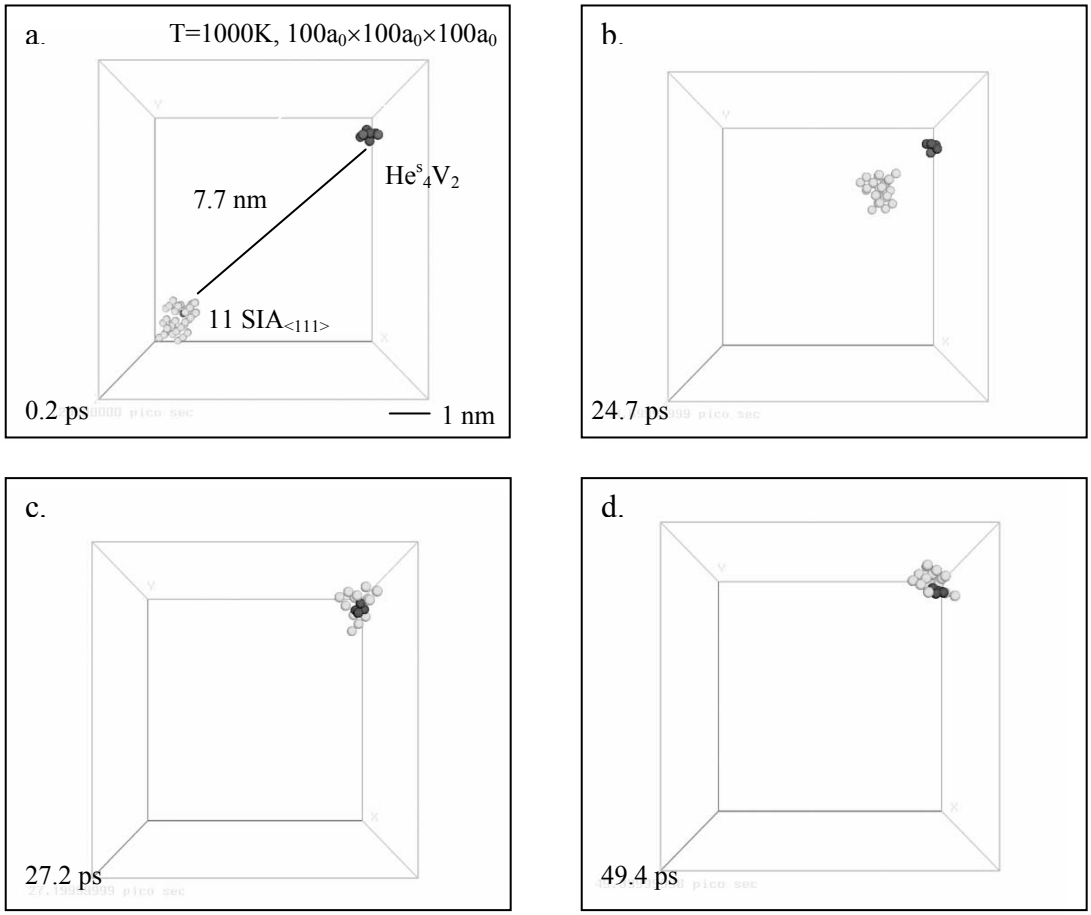

Fig. 3. Series of snapshots from an MD simulation at 1000 K showing the interaction between an 11 SIA cluster (light gray spheres) and 4 substitutional He – 2 vacancy cluster (dark gray spheres). The SIA cluster is spontaneously attracted to the vacancy cluster complex and the resulting SIA – He cluster is strongly bound.

To summarize, our dynamic simulations reveal a long-range interaction between one-dimensionally gliding SIA clusters and substitutional He as well as small He – vacancy clusters, leading to substitutional He – SIA recombination kick-out mechanism that ejects He atoms into interstitial positions. The dynamic simulations also reveal that SIA cluster – He interstitial complexes can be moderately to strongly trapped, depending on the relative size of each cluster. However, the dynamic simulations do not provide the recombination – replacement radii or the trapping – binding energetics. Therefore, we performed molecular statics (MS) calculations using the conjugate gradients method to investigate the energetics of interstitial helium – SIA cluster complexes. The MS results have been interpreted by considering the strain field interactions between the defects. Thus, ⟨111⟩ split interstitial dumbbells, whether isolated or as part of a small SIA cluster loop, have a large anisotropic stress field, compressive along its ⟨111⟩ orientation and tensile along a perpendicular ⟨110⟩ direction. The displacement field of interstitial He is

compressive and roughly spherical. The anticipated stress field interaction between these defects is expected to produce an attractive interaction along the ⟨110⟩ direction perpendicular to the dumbbell(s) orientation and a repulsive interaction along the ⟨111⟩ direction.

Therefore, to provide a quantitative assessment of the binding energy between SIA clusters and interstitial He atom clusters, the He has been displaced along a ⟨110⟩ direction, perpendicular to the ⟨111⟩ orientation of the dumbbells within the cluster. Figure 4 shows the calculated defect energy of a 20 SIA – He^i_1 cluster as a function of the distance between the center of mass of the SIA cluster and of the He atom. Well separated, the pair has a formation energy of 48.11 eV. As the He is moved towards the loop in the conjugate gradient calculations, a slightly positive binding energy of a few hundredths of an eV is obtained. As the He is moved closer to the cluster, a sharp decrease in the total defect energy (increase in binding energy) is observed as the He approaches the loop periphery. The maximum binding energy for He at the loop periphery (distance from center of cluster of approximately 0.5 nm) is 1.25 eV when the He is on a perfect loop ledge, and increases to 1.39 eV when the He is close to the jog point of the loop. Presumably, the increase in binding energy is due to the higher strain energy of the cluster at the jog point. As expected, further motion of the He into the loop interior results in highly negative binding energies. The trapping radius has been assigned by considering the interstitial He trapped when the binding energy exceeds the kinetic energy of the He corresponding to the internal energy of a monoatomic ideal gas, namely when the binding energy is equal to 3/2kT. This is approximately 0.11 eV over the temperature range of 400–700 °C. Notably, especially considering the dynamic simulation results, the interaction or trapping radii obtained from this analysis are quite small, ranging from 0.8 to 1.2 nm, depending on the specific orientation of the interaction between the interstitial helium and the 20-member SIA cluster loop. The relatively strong binding energies of the trapped He^i_1 – 20 SIA complex are large enough to influence microstructural evolution. Assuming that the de-trapping rate is given by a standard Arrhenius form, $k = \nu_o \exp(-(E_b + E_m)/kT)$ where k is the de-trapping rate, E_b the binding energy, E_m the migration energy of the (most) mobile species of about 0.1 eV, with an intrinsic vibrational attempt frequency of 10^{13} s^{-1}, the observed binding energies correspond to mean lifetimes for the trapped complex on the order of 100 ps at 700ºC and 1 μs at 500ºC.

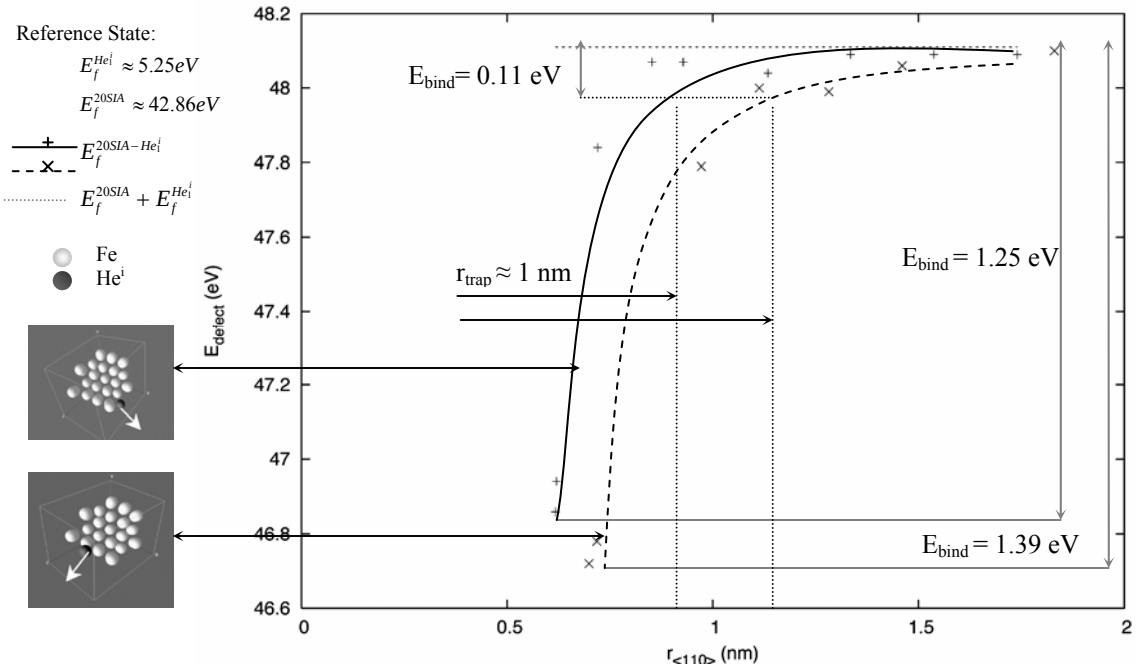

Fig. 4. Calculated defect energy of a 20 SIA – He^i_1 cluster as a function of the distance between the center of mass of the SIA cluster and of the He atom.

Figure 5 shows the results of similar calculations performed for 20 SIA – He^i_2 and – He^i_4 configurations. As expected, the binding energies increase with increasing size of the helium interstitial clusters and depend on the specific geometry of the interaction (e.g., the binding energies are strongest at the loop jog point). The trapping radii are increased slightly over the single interstitial helium but are still quite short, on the order of 1.3 – 1.5 nm. The mean lifetimes calculated at 500 °C for such strongly trapped complexes are on the order of one hour with 2 He atoms and one year with 4 He atoms. These calculations indicate SIA – He^i_n is strongly bound. However, it is again interesting to note that static calculations reveal moderate to high trapping/binding energies, but relatively small interaction/trapping radii. The underlying reasons for the relatively small trapping radii and in particular the apparently smaller values obtained in static vs. dynamic simulations are not known and will require further study. Figure 6 plots the results of our conjugate gradient MS calculations to investigate the binding energies of complexes containing 1, 2, and 4 interstitial helium with 1, 2, 6, 11, and 20 SIA clusters. Although, there is a large amount of scatter in the data, which we believe to result from the specific details of the geometric configurations investigated, the general trends are an increasing binding energy with increasing SIA and He cluster size.

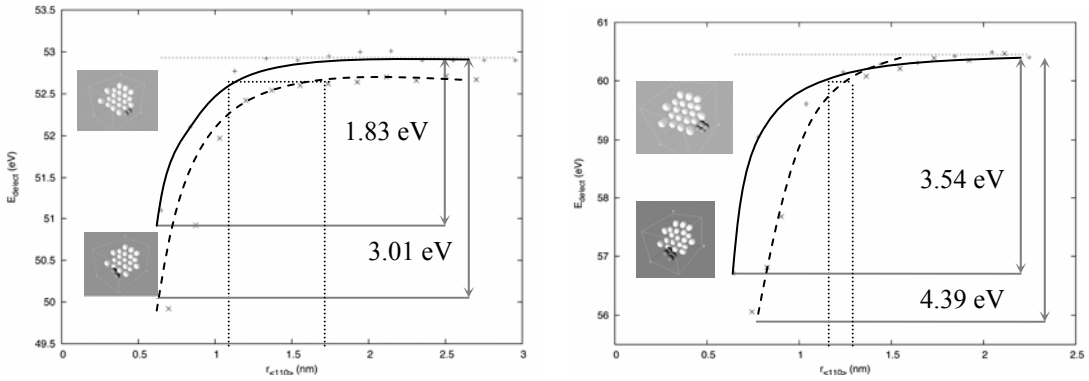

Fig. 5. Similar calculations performed for 20 SIA – He^i_2 and – He^i_4 configurations.

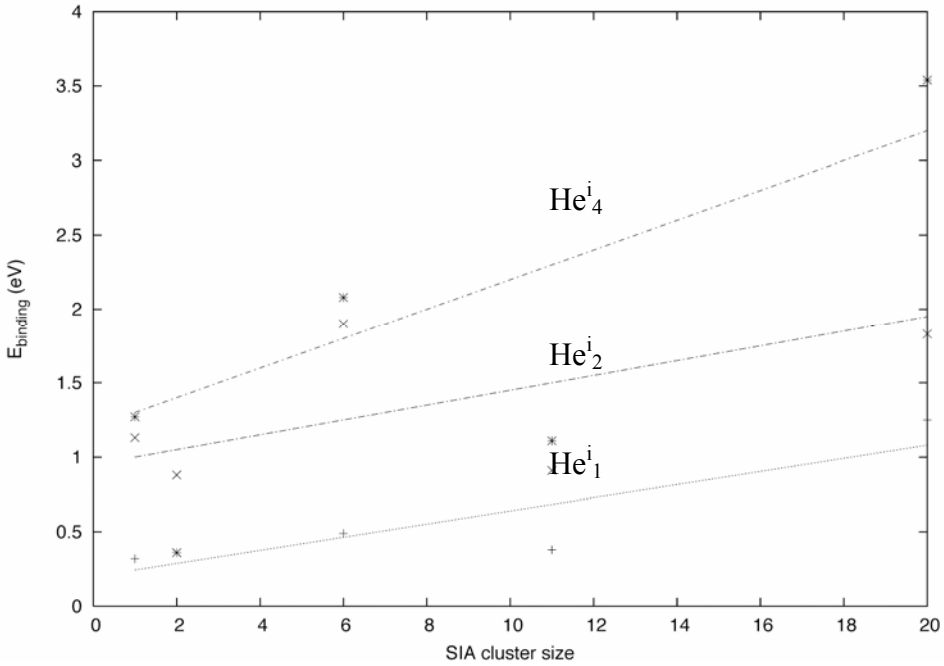

Fig. 6. Conjugate gradient MS calculations investigating the binding energies of complexes containing 1, 2, and 4 interstitial helium with 1, 2, 6, 11, and 20 SIA clusters.

Therefore, we conclude that moderate to strong binding interactions and trapping are expected to occur between SIA/SIA clusters and interstitial He. Surprisingly, the trapping radii governing the interaction are rather small, on the order of 1 nm, and found to be smaller in static than dynamic simulations. We conclude size strain effects are dominant in controlling the strong trapping/binding observed in our simulations.

However, a key question to ask is about the adequacy of the semi-empirical potentials used in this work. Thus, we have compared the interaction energies obtained from our semi-empirical MS simulations to *ab-initio* electronic structure calculations. Besides the previously mentioned reversal in the octahedral-tetrahedral stability of interstitial He in the bcc Fe lattice, the semi-empirical results using a 50×50×50 unit cell are in reasonably good agreement with the VASP calculations performed in a 3×3×3 computational cell, as shown in Table 1.

Table 1. Comparison of formation energies for He – defect configurations between *ab-initio* and semi-empirical potential calculations

Configuration	VASP 54 atoms	Semi-empirical results 250,000 atoms
	He occupation site	
He^s_1	E_f=4.26 eV	E_f=3.25 eV
He^i_1	E_f=4.63 eV E_m=0.2 eV He^i Tetrahedral Octahedral saddle	E_f=5.25 eV E_m=0.1 eV He^i Octahedral Tetrahedral saddle
	He^i_1 - He^i_1 Binding Energy (eV)	
cfg1	0.27	0.43
cfg2	0.38	0.75
	He^i - He^s Binding Energy (eV)	
He^i_1 - He^s_1 ⟨100⟩	1.83	2.18
⟨110⟩	1.91	2.11
He^i_2 - He^s_1	3.62	4.28
He^i_3 - He^s_1	4.97	5.53
He^i_4 - He^s_1	6.62	8.09
He^i_5 - He^s_1	8.38	9.72
	He^s_1 – Vacancy Binding Energy (eV)	
1 nn	0.79	0.33
2 nn	0.51	0.19

The formation energies of substitutional and interstitial He atoms, as well as the binding energies between He atoms are comparable. For both the semi-empirical and *ab-initio* calculations, the interaction (binding) energy between two interstitial He atoms is about 0.5 eV. Although the semi-empirical results give slightly higher binding energies, the two methods predict the same relative stability. In this specific calculation, the interstitial helium pair is on tetrahedral sites in the VASP calculation, whereas the positions have been shifted to octahedral sites for the semi-empirical MS calculation, as shown in Fig. 7. We have also compared the binding energies between a substitutional He atom with one to five neighboring interstitial He atoms. Again, in this case, the interstitial He atoms are inserted on tetrahedral sites using VASP and octahedral sites in the MS calculations. As listed in Table 1, both approaches show the same trend, namely an increasing binding energy with increasing number of interstitial He atoms within the cluster, from about 2 eV up to about 9 eV. Once again, the binding energies obtained from the semi-empirical results are slightly higher than the VASP calculations. We have also compared the energy and configurations of a substitutional He atom with a nearest neighbor vacancy (at either first or second nearest neighbor positions). Both methods predict that the He^s – nearest neighbor complex is energetically preferred and that the He atom prefers to be located away from the lattice site of either vacancy. The VASP results predict stronger binding energy between the substitutional helium – vacancy complex compared to the semi-empirical potential. We conclude from this comparison that the semi-

empirical potentials are performing well in representing helium – point defect interactions, although the quantitative comparison is not quite so favorable.

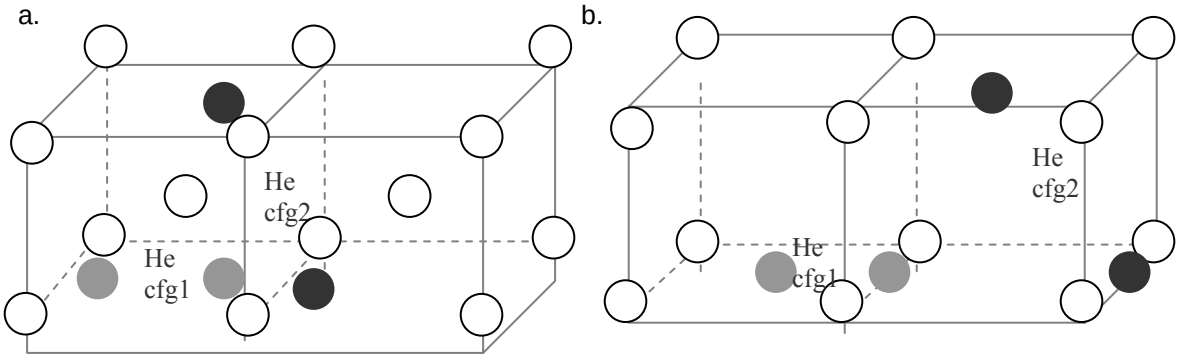

Fig. 7. Interstitial helium pair on tetrahedral sites in the VASP calculation (7.a) and positions shifted to octahedral sites for the semi-empirical MS calculation (7.b).

To complete the comparison, we have considered specifically the binding energy between a ⟨110⟩-oriented Fe SIA and a neighboring interstitial He atom. Three different configurations for the interstitial – self-interstitial atom were used, as shown in Fig. 8. The *ab-initio* calculations were performed with a 54 atom ($3a_0 \times 3a_0 \times 3a_0$) and 128 atom ($4a_0 \times 4a_0 \times 4a_0$) unit cells, while we have performed the semi-empirical MS calculations by systematically varying the cell-size from $3a_0 \times 3a_0 \times 3a_0$ (54 atoms) to $20a_0 \times 20a_0 \times 20a_0$ (250,000 atoms). Table 2 presents the results obtained for computational cell sizes of 54 and 128 atoms. As can be seen, both methods predict configuration 3 to be the most stable, although the semi-empirical potentials predict a change in stability in going from 54 to 128 atoms. However, the absolute agreement between the results presented in Table 2 is not as good as for the previous results presented in Table 1. Perhaps this should not be surprising for situations involving a single SIA, since the *ab-initio* calculations predict a lower formation energy for the ⟨110⟩ split-dumbbell than this semi-empirical potential and a much larger energy difference between the ⟨110⟩- and ⟨111⟩-orientations of the SIA. Moreover, He has been introduced on octahedral sites in the *ab-initio* calculation, even though the preferred configuration for (isolated) interstitial He is the tetrahedral site.

Finally, Fig. 9 presents the results of the size scaling study on the SIA – He interstitial binding energy for each of the three configurations. The results clearly indicate a strong cell-size effect at small cell sizes that does not diminish until larger system sizes on the order of $10a_0 \times 10a_0 \times 10a_0$ are reached. The difference in calculated binding energy for the configurations in increasing the cell size from a $3 \times 3 \times 3$ unit cells to $20 \times 20 \times 20$ is found to be 0.12 ± 0.03 eV, averaged over all three configurations. The major conclusion of the cell-size study is to reinforce that care must be taken in comparing the results of *ab-initio* calculations performed in small super-cells to those of semi-empirical simulations performed at larger size, to properly account for strain field effects due to the periodic images.

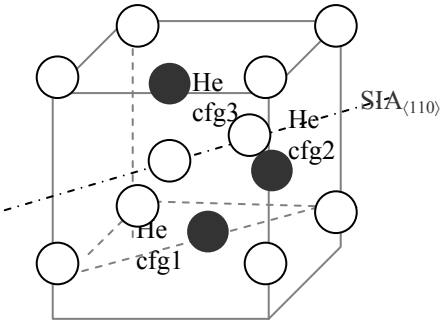

Fig. 8. Three different configurations for the interstitial – self-interstitial atom used for the calculations presented in Table 2.

Table 2. Comparison of *ab-initio* and semi-empirical MS calculations of the SIA – Helium interstitial atom binding energy, as a function of cell size

Configuration	VASP results 54 atoms	VASP results 128 atoms	Semi-empirical results 54 atoms	Semi-empirical results 128 atoms
He^{i}_{1} cfg1	-0.15	-0.09	0.32	0.34
He^{i}_{1} cfg2	-0.04	0.03	-0.15	-0.09
He^{i}_{1} cfg3	0.02	0.07	0.29	0.37

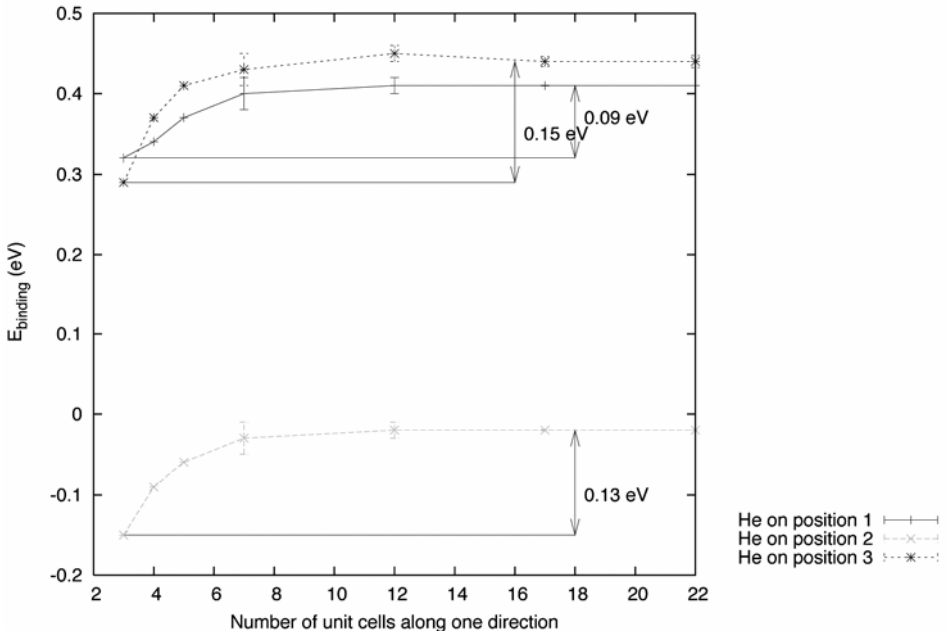

Fig. 9. Size scaling study on the SIA – He interstitial binding energy for each of the three configurations.

Conclusions

The results of atomistic calculations to investigate the effect of He impurities on the properties and behavior of self-interstitial atom clusters in Fe have been presented. The MD simulations using semi-empirical potentials to describe the Fe-He interactions reveal a high mobility of interstitial He in bcc Fe, a strong interaction between interstitial and substitutional He and SIA clusters and a spontaneous SIA – vacancy recombination and kick-out mechanism that ejects the substitutional He into interstitial position.

The MS calculations performed using the conjugate gradient method reveal relatively small interaction radii of about 1 nm between SIA and He cluster complexes, but with strong binding energies from about 1.3 to 4.4 eV. The strong binding interaction between He and SIA clusters effectively traps the otherwise highly mobile SIA clusters for times sufficient to influence the overall microstructural evolution under fusion neutron irradiation conditions. Overall, the results are in good qualitative agreement with *ab-initio* results and indicate that the helium – SIA interactions are governed by size (strain) effects. Future work will seek to clarify some of the issues raised in this study associated with the relatively small interaction radii observed in static vs. dynamic simulations, and will focus on the migration mechanisms and mobility of substitutional helium – vacancy cluster complexes using kinetic Monte Carlo simulations.

Acknowledgements

The authors would like to acknowledge Professor G. Robert Odette (UCSB) and Drs. Takuya Yamamoto (UCSB), Rick Kurtz, Howard Heinisch and Fei Gao (PNNL) and François Willaime and Chu Chun Fu (CEA-Saclay) for many helpful discussions during the course of this work. This work has been supported by the Office of Fusion Energy Sciences, U.S. Department of Energy, under Grant DE-FG02-04ER54750.

References

[1] K. Morishita, R. Sugano, B. D. Wirth, and T. Diaz de la Rubia, Nucl. Instrum. Methods B 202 (2003) 76–81.
[2] K. Morishita, R. Sugano, and B. D. Wirth, J. Nucl. Mater. 323 (2003) 243–250.
[3] G. J. Ackland, D. J. Bacon, A. F. Calder, and T. Harry, Philos. Mag. A 75 (1997) 713.
[4] B. D. Wirth, G. R. Odette, D. Maroudas, and G. E. Lucas, J. Nucl. Mater. 244 (1997) 185.
[5] C. C. Fu, F. Willaime, and P. Ordejón, Phys. Rev. Lett. 92 (2004) 175503.
[6] F. Willaime, C. C. Fu, M. C. Marinica, and J. Dalla Torre, Nucl. Instrum. Methods *B* 228 (2005) 92–99.
[7] M. I. Mendelev, S. Han, D. J. Srolovitz, G. Ackland, D. Y. Sun, and M. Asta, Philos. Mag. 83 (2003) 3977.
[8] W. D. Wilson and R. D. Johnson, In P. C. Gehlen, J. R. Beeler Jr., and R. I. Jaffee (eds.), Interatomic Potentials and Simulation of Lattice Defects, Plenum (1972) 375.
[9] D. E. Beck, Mol. Phys. 14 (1968) 311.
[10] G. Kresse and J. Hafner, Phys. Rev. B 47 (1993) 558.
[11] G. Kresse and J. Hafner, Phys. Rev. B 49 (1994) 14251.
[12] G. Kresse and J. Furthmüller, Comput. Mater. Sci. 6 (1996) 15.
[13] C. Domain, C. S. Becquart, and J. Foct, Phys. Rev. B 69 (2004) 144112.
[14] K. Morishita, B. D. Wirth, T. Diaz de la Rubia, and A. Kimura, In S. Hanada, Z. Zhong, S. W. Nam, and R. N. Wright (eds.), Proceedings of the Fourth Pacific Rim International Conference on Advanced Materials and Processing (PRICM4), The Japan Institute of Metals (2001) 1383.
[15] A. D. Le Claire, J. Nucl. Mater. 69&70 (1978) 70.
[16] B. D. Wirth, G. R. Odette, J. Marian, L. Ventelon, J. A. Young-Vandersall, and L. A. Zepeda-Ruiz, J. Nucl. Mater. 329–333 (2004) 103–111.

DIFFUSION OF He INTERSTITIALS IN GRAIN BOUNDARIES IN α-Fe—F. Gao, H. L. Heinisch, and R. J. Kurtz (Pacific Northwest National Laboratory)

OBJECTIVE

The objective of this research is to study the migration and diffusion mechanisms of He atoms in grain boundaries in α-Fe using molecular dynamics and to assess the effects of different grain boundaries on activation energies and diffusion mechanisms of He interstitials.

SUMMARY

The migration and diffusion mechanisms of interstitial He atoms at two representative grain boundaries in α-Fe, Σ11<110> {323} and Σ3<110> {112}, are studied using molecular dynamics. The migration of He atoms was followed for 10 – 30 ns, at temperatures between 600 and 1200 K. The diffusion coefficient of He atoms is calculated using the mean square displacements of He atoms, and the effective migration energies were determined to be 0.32 and 0.44 eV for Σ11<110>{323} and Σ3<110>{112} GBs, respectively. He interstitial diffuse quickly in the Σ11 GB with one-dimensional behavior along the GB directions, while it migrates one-dimensionally at low temperature, two-dimensionally at intermediate temperature and three-dimensionally at higher temperature in the Σ3 GB. The different activation energies and diffusion mechanisms in these two representative grain boundaries suggests that the varying atomic structures of the grain boundaries are important for the diffusivity of He.

PROGRESS AND STATUS

Introduction

It is generally accepted that grain boundaries provide fast diffusion paths for He atoms, and their accumulation in both bulk and GBs have major consequence for structural integrity of first-wall materials. However, the detail knowledge of He diffusion in both bulk and GBs, trapping and detrapping, interaction of He with microstructures, the importance of small helium-vacancy cluster mobility and helium bubble nucleation processes represent important scientific and technological issues, which demand computer simulations to obtain insight and fundamental understanding of the complex atomic-level processes of He atoms controlling microstructural evolution in advanced ferritic steels. We have initiated a systematic study to characterize the interaction of He with extended defects (dislocations and GBs) in a fusion relevant structural material such as ferritic steel. The grain boundary structures and binding He to GBs in α-Fe have been explored previously using computer simulations [1]. Atomic calculations demonstrate strong binding of He to GBs in α-Fe, and both substitutional and interstitial He atoms are trapped at GBs. We report here on the results of MD simulations of helium migration and its diffusion mechanisms in grain boundaries studied using molecular dynamics methods. The correlation of these results with the binding properties of He atom at GBs is also discussed.

Modeling

The model consists of a two-part computational cell, rectangular in shape. The inner part, region I contains movable atoms, while region II supplies neighbors for region I, with a semi-rigid boundary condition. The equilibrium structures of GBs at 0 K are obtained via relaxation using molecular dynamics with an energy quench. The two grains are free to move and undergo homogenous displacement in all three directions, which occurs during relaxation via a viscous drag algorithm. Periodic boundary conditions are applied to the directions perpendicular to the normal direction of the GB plane. Two symmetric tilt GBs are employed to study He diffusion, all with a common <101> tilt axis. The two GBs are Σ3{112} Θ=70.53º and Σ11{323} Θ=50.48º, consisting of 18816 and 17976 atoms, respectively. MD simulations of He diffusion were performed in the temperature range from 600 K to 1200 K, and the migration of He atoms were followed for 10 – 30 ns, which depends on temperature. The diffusivity and self-diffusion coefficient of He atoms can be determined from summation of the mean square

displacements (MSD) of He atoms and the mean square displacements of all atoms N in the simulation cell, respectively. With self-diffusion coefficients obtained at different temperatures, the activation energy for He migration in GBs, E_m, can be estimated from the Arrhenius relation. In all cases the set of interatomic potentials due to Ackland[2], Wilson and Johnson[3], and Beck[4] were used for the Fe-Fe, Fe-He and He-He interactions, respectively.

Results

The lowest energy configurations of single He atom at the GBs were determined by the procedure described in the previous section. The most stable configuration of He interstitial in the Σ3 GB is found to form a $<\bar{1}11>$ crowdion defect with Fe atoms, while a tetrahedral He interstitial is the most stable con configuration in the Σ11 GB. These stable configurations are used as the initial starting configurations, and the migration of He interstitials was investigated at the temperature range of between 600 and 1200K. The mean square displacements (MSDs) of all the atoms and the He interstitial can be determined as a function of time. During the simulation, a large number of He jumps are observed, but the dynamic processes occasionally involve the jumps of Fe atoms. However, the contribution of Fe jumps to the total MSD is negligible. The diffusion coefficients estimated for the He interstitial in both GBs are given in Fig. 1 as a function of reciprocal temperature, where circle symbols represent the data calculated for the Σ3 GB and square symbols indicate the data obtained for the Σ11 GB. The data approximately follow an Arrhenius relationship, from which the corresponding activation energies, E_m, and preexponential factors, D_0, can be determined. The best fits to the data give the values of E_m and D_0 to be 0.32 eV and 2.15×10^{-3} cm^2/s for the Σ3 GB, and 0.44 eV and 2.3×10^{-3} cm^2/s for the Σ11 GB, respectively. It should be noted that the data at 1200 K in the Σ3 GB is excluded for the evaluation of activation energy because the He interstitial dissociates from the GB at this temperature, migrating three-dimensionally. This is consistent with the small binding energy of He interstitials to the Σ3 grain boundary. The migration energies of He interstitials in GBs are slightly higher than that of He interstitials in the bulk (0.08 eV). In the bulk of Fe, a He interstitial has very high mobility, and can migrate from one tetrahedral site to another before becoming deeply trapped as a substitutional helium in a radiation-induced or thermal vacancy. The activation energies obtained in the present work suggest that He interstitials are very mobile in the GBs, and grain boundaries provide fast diffusion paths for He interstitials along some specific directions.

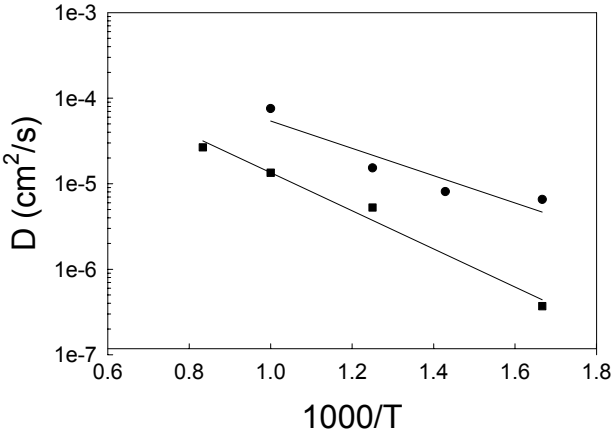

Fig. 1. Diffusion coefficients of He interstitial as a function of reciprocal temperature in Σ3 and Σ11 GBs in α-Fe, where reciprocal temperature is scaled by 1000.

The migration mechanisms of He interstitials in GBs have been studied by carefully analysis of the computer-generated trajectories. The trajectories of the He interstitial in the Σ3 GB are shown in Fig. 2(a)

for the temperature of 600 K, where gray spheres represent Fe atoms in three (110) atomic panes. The middle plane is the plane containing the initial starting site of the He interstitial. At 600 K, the He interstitial mainly migrates along the <110> direction that is parallel to the tilt axis, but some displacements are observed along the $<1\bar{1}1>$ direction. This can be also demonstrated by plotting the components of the MSD along <110>, $<1\bar{1}1>$ and $<\bar{1}12>$ directions as a function of time, and the large increase in the MSD is due to the contribution of the <110> component. These results suggest that the He interstitial mainly migrates with one-dimensional behavior at low temperature. However, the migration path of the He interstitial changes from one-dimensional (1D) diffusion to two-dimensional (2D) diffusion with increasing temperature. The trajectories of the He interstitial at 800 K are shown in Fig. 2(b). The further increase in temperature (up to 1200K) leads to the dissociation of the He interstitial from the Σ3 GB because of its small binding energy to that GB. In fact, the He interstitial has the lowest binding energy in the Σ3{112} shown in Fig. 2, among all the GBs calculated.[1]. Dissociation from this GB allows for the He interstitial to also migrate along the $<\bar{1}12>$ direction, resulting in three-dimensional (3D) diffusion. It is important to point out that the activation energy obtained for He migration in the Σ3 GB is an effective activation energy. The temperature dependence of the MSD along different directions suggests that the migration barrier along the <110> direction should be lower than that along the $<\bar{1}12>$ direction.

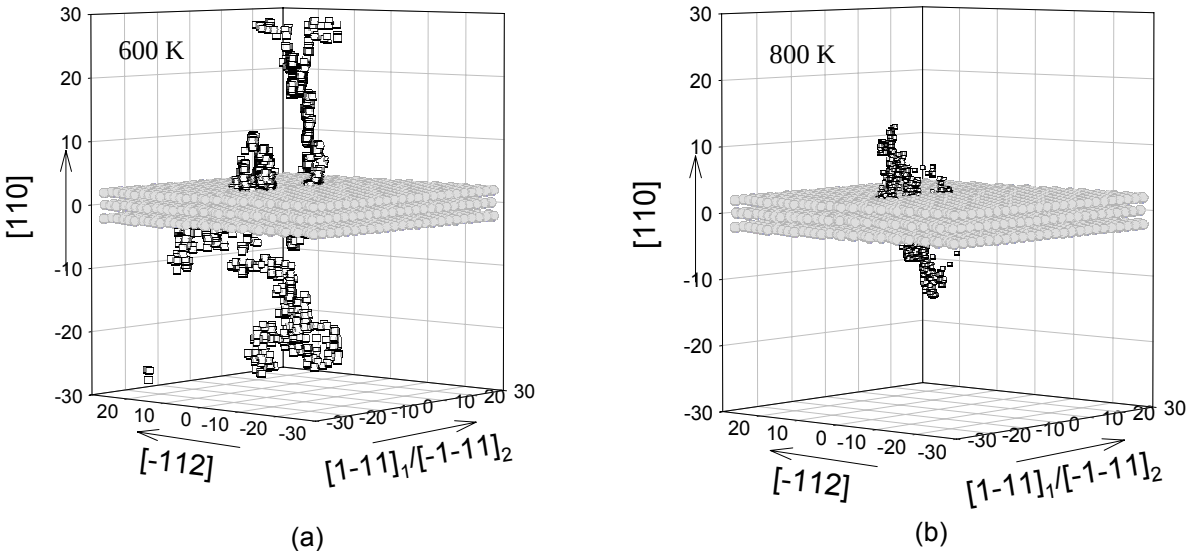

Fig. 2. Trajectories of He interstitial at 600 K (a) and at 800 K (b) in Σ3 GB, where three (110) atomic planes at the boundary are presented, as indicted by light spheres.

The trajectories of He interstitials and their MSD along three independent directions in the Σ11 GB at 1000 K are shown in Figs. 3(a) and (b), respectively. Similar to the plots in Fig. 2, only three atomic planes normal to the tilt axis are presented in Fig. 3(a). Although the He interstitial can move in the spaces between three planes, it is strongly bound to the middle plane on which the initial starting position of the He interstitial is allocated. It is of interest to note that the He interstitial migrates one-dimensionally along the $<1\bar{1}3>$ direction, even at higher temperature. Also, the MSD in Fig. 3(b) indicates that the He interstitial migrates only along $<1\bar{1}3>$, giving rise to the increase in the MSD.

Although only two GBs have been used in these simulations of the diffusion of He interstitials, the results have indeed demonstrated that He diffusion and the corresponding migration mechanisms depend significantly on the atomic structures of the GBs. Earlier studies showed that there is a strong correlation between the binding energy of an interstitial He atom and the excess atomic volume in the GB [1]. The Σ3

GB has the smallest excess atomic volume and the smallest maximum binding energy for He. In the Σ3 GB He atoms demonstrate an ability to migrate three-dimensionally, including hopping out of the boundary into the matrix. On the other hand, the Σ11 GB has about eight times more excess volume, He atoms have binding energy three times greater than in the Σ3 GB, and they are restricted to one-dimensional migration within the GB. One might expect that this variation in diffusion mechanisms of He interstitials in GBs should have significant effects on bubble nucleation at different GBs.

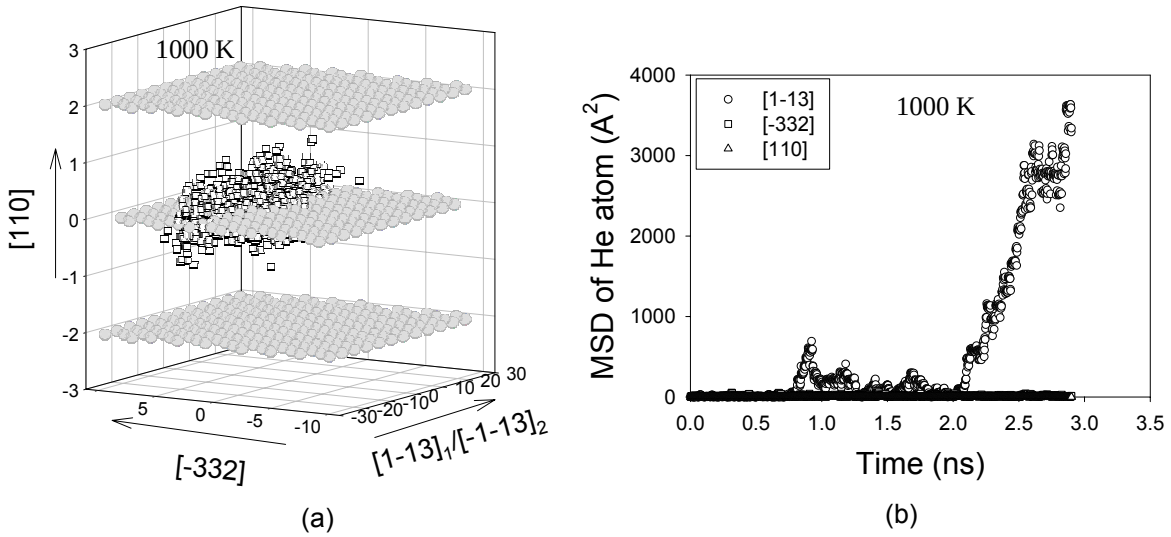

Fig. 3. (a) Trajectories of He interstitials at 1000 K in a Σ11 GB, where three (110) atomic planes are presented, as indicted by light spheres, and (b) MSD of He interstitials along <$1\bar{1}3$>, <$\bar{3}32$>, and <110> directions at the same temperature.

Conclusions

Helium diffusion along the GBs in α-Fe has been studied using molecular dynamics methods, and two grain boundaries, Σ11<110>{323} and Σ3<110>{112}, were used for the current investigations. The migration of He atoms were followed for 10–30 ns, at temperatures between 600 and 1200 K. The diffusion coefficient of He atoms is calculated using the mean square displacements of He atoms, and the effective migration energies were determined to be 0.32 and 0.44 eV for Σ11<110>{323} and Σ3<110>{112} GBs, respectively. We found that in the Σ11 GB, where excess volume is larger and He binding energy is high, He atoms easily diffuse one-dimensionally along specific directions, with a few directional changes observed at higher temperatures. However, He atoms migrate one-dimensionally at low temperature, two-dimensionally at intermediate temperature and three-dimensionally at higher temperature in the Σ3 GB, where excess atomic volumes are smaller and the binding energy of a He atom is lower. The different activation energies and diffusion mechanisms in these two representative grain boundaries suggests that the varying atomic structures of the grain boundaries, particularly regarding excess atomic volume, are important for the diffusivity of He atoms.

References

[1] R. J. Kurtz and H. L. Heinisch, J. Nucl. Mater. 329–333 (2004) 1199.
[2] G. J. Ackland, D. J. Bacon, A. F. Calder, and T. Harry, Philos. Mag. A75 (1997) 713.
[3] W. D. Wilson and R. D. Johnson: Interatomic Potential and Simulation of Lattice Defects, Plenum, (1972) 375.
[4] D. E. Beck, Mol. Phys. 14 (1968) 311.

10. DOSIMETRY, DAMAGE PARAMETERS, AND ACTIVATION CALCULATIONS

No contributions.

11. MATERIALS ENGINEERING AND DESIGN REQUIREMENTS

No contributions.

12. IRRADIATION FACILITIES AND TEST MATRICES

IRRADIATION PROGRESS OF MFE-RB-17J EXPERIMENT—D. K. Felde and R. L. Wallace (Oak Ridge National Laboratory)

OBJECTIVE

The objective of this work is to irradiate mostly vanadium alloy specimens in direct contact with lithium at temperatures of 450°C, 600°C and 700°C in a europium-shielded RB position of the High Flux Isotope Reactor (HFIR). Some steel and ceramic specimens are included but are isolated from the primary lithium bath.

SUMMARY

The 17J experiment has been irradiated for 3 of 10 planned cycles in the HFIR. The upper capsule has been operating 20 to 50°C below the target temperature of 700°C for the last two cycles. The cause has not been determined. The middle capsule has operated at its target temperature of 600°C. A partial blockage of the purge gas line observed in the first cycle of irradiation led to a reduction in the target temperature for the lower capsule to ~425°C (from an original target of 450°C). Further degradation of this blockage has caused some operational difficulties resulting in this capsule running at slightly lower temperatures, ~418°C average, for part of cycle 402.

PROGRESS AND STATUS

Background

The MFE-RB-17J irradiation experiment was described in an earlier report [1] and the initial operating cycle is described in the previous progress report [2]. Three axially stacked specimen holders are contained within a common inner containment housing, which is itself contained in an outer containment housing tube. The two upper holders are made from the molybdenum alloy TZM and the lower holder is made from stainless steel. The holders are designed to irradiate three sets of metallurgical and ceramic test specimens in lithium baths at 700°C, 600°C and 450°C, in order from top to bottom within the experiment.

The temperatures of the three holders are controlled independently by adjusting the mixture of inert gases flowing between the holders and the inner housing, which effectively controls the thermal conductivity and consequently the temperature difference across the gas gap between the holder and the inner housing. Gas supply lines can feed helium, neon or argon or a mixture of either helium and neon or helium and argon to the plenums below each of the three holders. Gas from lower holders become part of the mixture for upper holders, so while the temperature of the zones can be independently controlled, they are dynamically coupled.

A helium gas supply line, referred to as a purge line, is routed to the lower holder lower plenum at the base of the inner housing. Helium flows through this line passing upward past the specimen holders and out an effluent line opening at the top of the inner containment. The purge line remains open at all times and the flow is automatically increased in response to detected off-normal operating conditions while all other gas flows are stopped, ensuring that holder temperatures decrease.

As described in the previous report [2], an apparent temperature dependent plugging of the helium purge line that discharges below the lower (450°C) subcapsule was observed. After completion of operating cycle 400, the purge line and control gas line supplying the lower zone were switched at the control cabinet. Further plugging of the tube in this configuration would result in lower temperatures as argon flow would be restricted rather than helium.

Operation

HFIR operating cycles 401 and 402 were conducted during the reporting period. Cycle 401 was initiated on July 16, 2004 with shutdown on August 9, 2004. A plot showing temperatures for the three zones along with reactor power is shown in Fig. 1. A more detailed look at the startup portion of the cycle is shown in Fig. 2. Of particular note is the lower temperature for the 700°C zone. It was not possible to reach the 700°C average that was obtained during cycle 400, even with higher argon gas percentages in the mixture. Average temperatures closer to 670–680°C were reached during the early portion of the cycle. Somewhat higher temperatures were reached as the cycle progressed due to normal power shifting in the reactor. The temperature transients observed during the early startup portion are believed to be caused by argon gas flow instabilities at the high argon flow rates in the upper capsule region. Argon flow rate was raised well above 100 sccm in an attempt to increase the temperature in the upper zone and it is believed that these flows were high enough to push argon into the middle zone, resulting in a rapid temperature increases in that zone. It was necessary to cut argon flow and increase helium flow rates in order to regain temperature control of the middle capsule.

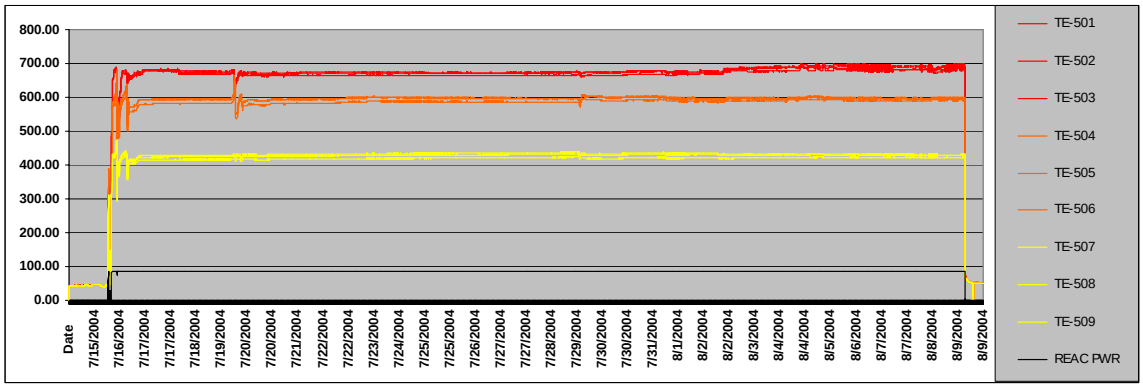

Fig. 1. 17J temperature and power history for HFIR cycle 401.

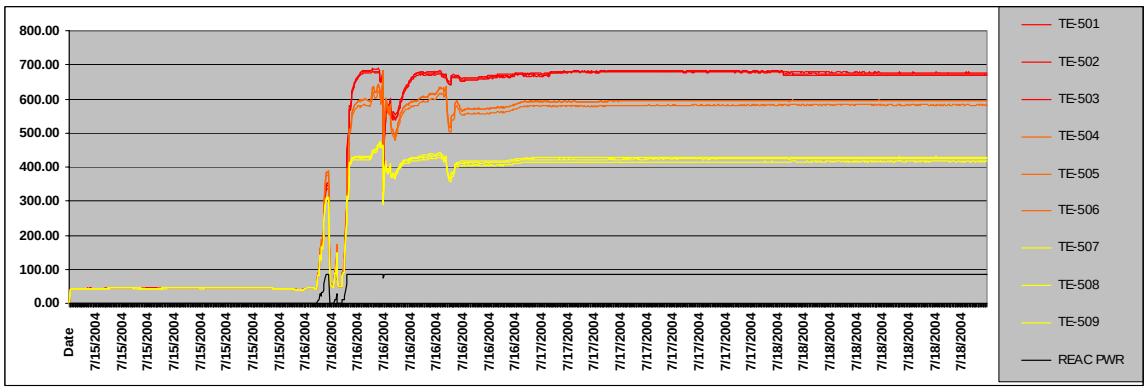

Fig. 2. 17J – Startup portion of HFIR operating cycle 401.

Cycle 402 was initiated on September 28, 2004. The cycle was shutdown after 10 days for administrative reasons and was restarted on November 10, 2004. The cycle was completed on November 23, 2004. The temperature and power history are shown in Fig. 3 where the two portions of the interrupted cycle are referred to as cycle 402A and 402B. The startup portion of cycle 402A is shown in Fig. 4 and the startup of cycle 402B is shown in Fig. 5.

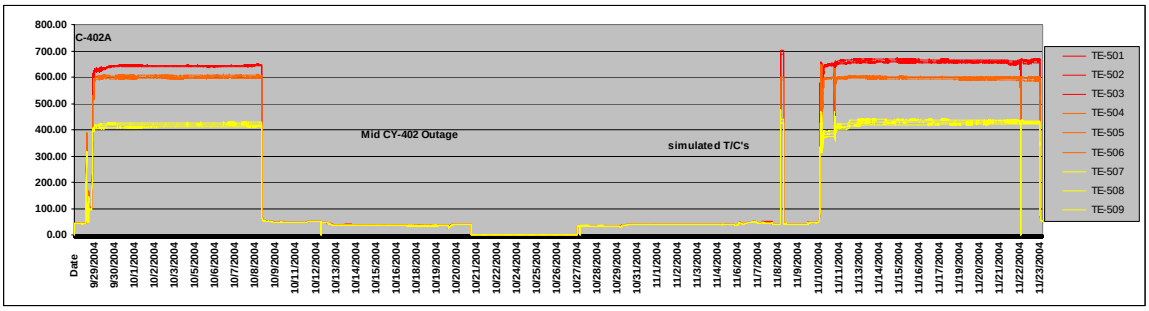

Fig. 3. 17J temperature history for HFIR cycle 402.

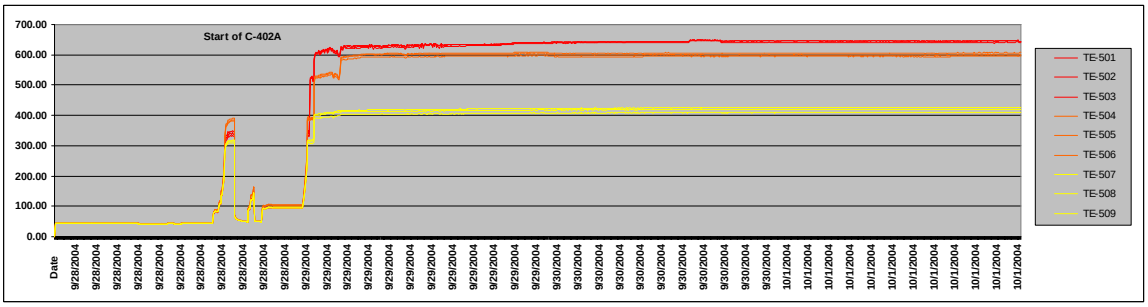

Fig. 4. 17J startup portion temperature history for HFIR cycle 402A.

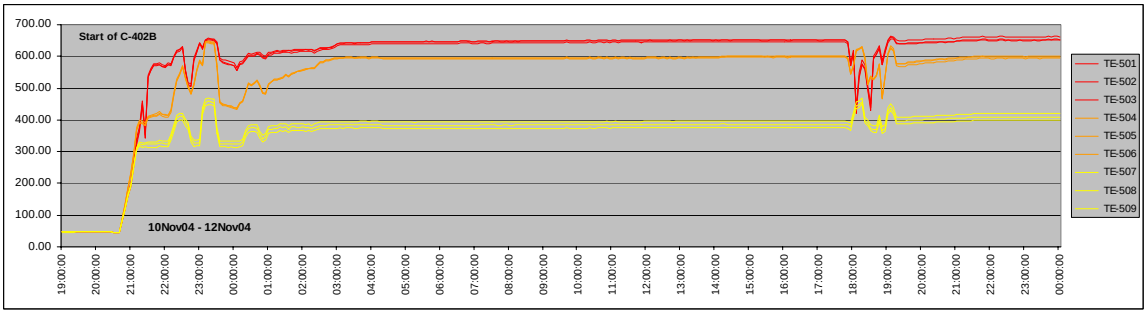

Fig. 5. 17J startup portion temperature history for HFIR cycle 402B.

Of particular note is the further decrease in the temperature achievable for the 700°C zone, where the maximum average temperature reached at the beginning of cycle 402A is ~650°C. The cause for the downward trend in temperature has not been determined. The partially restricted line carrying argon to the lower 450°C zone also showed some degradation in flow capacity from the previous cycle. For cycle 401, approximately 15 sccm of argon was used to maintain the average temperature at 428°C. At the start of cycle 402A, argon flow was restricted to <10 sccm. This limited the temperature in the lower capsule to an average of ~418°C at the start of the cycle.

During the outage between cycle 402A and 402B, the purge line and gas control line were switched back to the original configuration, with the helium purge gas flowing through the restricted line. Further degradation of the line, however, caused operational problems early in the startup portion of cycle 402B, as indicated by the temperature transients shown on Fig. 5 and so the lines were switched back. The solenoid valve on the control gas line was also bypassed to give more flexibility in operation. It was possible to maintain an average temperature of ~425°C in the lower zone during cycle 402B.

The 17J experiment has been irradiated for 3 full cycles in the HFIR. The estimated peak displacements per atom in vanadium for the RB* position is 0.74/cycle. The power history timeline for cycles 401 and 402 is shown in Tables 1 and 2, respectively. This provides information on low power portions of the cycle where specimens are not at temperature (e.g., startup, operator training, etc.).

References

[1] A. L. Qualls et al., Assembly of the MFE-RB-17J Experiment, Fusion Materials Semiannual Progress Report for Period Ending December 31, 2003, DOE/ER-0313/35, U.S. Department of Energy, pp. 242–249.
[2] D. K. Felde et al., Irradiation Start of MFE-RB-17J Experiment, Fusion Materials Semiannual Progress Report for Period Ending June 30, 2004 (to be published).

Table 1. Power history for HFIR Operating Cycle 401

CYCLE #	Begin Time	End Time	Elapsed Time	Reactor Power	Integrated Power	COMMENTS	
(days)	(m/d/y hh:mm)	(m/d/y hh:mm)	(hours)	(MW)	(MWD)		
SOC 401	7/15/04 2134	7/15/04 2137	0.0	0.0	0		
	7/15/04 2137	7/15/04 2152	0.3	0.0	0		
	7/15/04 2152	7/15/04 2209	0.3	8.5	0		
	7/15/04 2209	7/15/04 2220	0.2	25.5	0		
	7/15/04 2220	7/15/04 2228	0.1	34.0	0		
	7/15/04 2228	7/15/04 2232	0.1	42.5	1		
	7/15/04 2232	7/15/04 2239	0.1	59.5	1		
	7/15/04 2239	7/15/04 2241	0.0	76.5	1		
	7/15/04 2241	**7/15/04 2307**	**0.4**	**85.0**	**3**	Training SU	
	7/15/04 2307	7/15/04 2328	0.4	0.0	3		
	7/15/04 2328	7/15/04 2338	0.2	0.0	3		
	7/15/04 2338	7/15/04 2354	0.3	8.5	3		
	7/15/04 2354	7/16/04 0000	0.1	25.5	3	Training SU	
	7/16/04 0000	7/16/04 0017	0.3	0.0	3		
	7/16/04 0017	7/16/04 0026	0.1	0.0	3		
	7/16/04 0026	7/16/04 0042	0.3	8.5	3		
	7/16/04 0042	7/16/04 0046	0.1	25.5	3		
	7/16/04 0046	7/16/04 0049	0.0	34.0	3		
	7/16/04 0049	7/16/04 0051	0.0	42.5	3		
	7/16/04 0051	7/16/04 0056	0.1	59.5	3		
	7/16/04 0056	7/16/04 0059	0.0	76.5	3		
	7/16/04 0059	7/16/04 0447	3.8	85.0	17		
	7/16/04 0447	7/16/04 0453	0.1	76.5	17	Setback per MFE request	
	7/16/04 0453	**8/9/04 1000**	**581.1**	**85.0**	**2075**		24.41520833
EOC 401	8/9/04 1000	9/28/04 1140	1201.7	0.0	0	Extended outage due to PISA concerns	

Table 2. Power history for HFIR Operating Cycle 402

CYCLE # (days)	Begin Time (m/d/y hh:mm)	End Time (m/d/y hh:mm)	Elapsed Time (hours)	Reactor Power (MW)	Integrated Power (MWD)	COMMENTS	
SOC 402	9/28/04 1140	9/28/04 1214	0.6	9.9	0		
	9/28/04 1214	9/28/04 1228	0.2	17.8	0		
	9/28/04 1228	9/28/04 1235	0.1	24.8	1		
	9/28/04 1235	9/28/04 1240	0.1	33.4	1		
	9/28/04 1240	9/28/04 1245	0.1	40.5	1		
	9/28/04 1245	9/28/04 1248	0.0	59.3	1		
	9/28/04 1248	9/28/04 1251	0.0	74.3	1		
	9/28/04 1251	**9/28/04 1516**	**2.4**	**85.0**	**10**		
	9/28/04 1516	9/28/04 1529	0.2	9.1	10		
	9/28/04 1529	9/28/04 1535	0.1	17.3	10		
	9/28/04 1535	9/28/04 1638	1.1	23.6	11		
	9/28/04 1638	9/28/04 2038	4.0	9.9	12		
	9/28/04 2038	9/28/04 2043	0.1	17.8	13		
	9/28/04 2043	9/28/04 2048	0.1	25.3	13		
	9/28/04 2048	9/28/04 2053	0.1	33.5	13		
	9/28/04 2053	9/28/04 2058	0.1	42.4	13		
	9/28/04 2058	9/28/04 2102	0.1	59.2	13		
	9/28/04 2102	9/28/04 2105	0.0	74.4	13		
	9/28/04 2105	**10/8/04 2010**	**239.1**	**85.0**	**860**		242.8077647
EOC 402A	10/8/04 2010	11/10/04 1541	787.5	0.0	860		
SOC 402B	11/10/04 1541	11/10/04 1549	0.1	8.5	860		
	11/10/04 1549	11/10/04 1552	0.0	17.0	860		
	11/10/04 1552	11/10/04 1554	0.0	25.5	860		
	11/10/04 1554	11/10/04 1558	0.1	34.0	860		
	11/10/04 1558	11/10/04 1602	0.1	42.5	860		
	11/10/04 1602	11/10/04 1607	0.1	59.5	860		
	11/10/04 1607	11/10/04 1609	0.0	76.5	861		
	11/10/04 1609	**11/23/04 1527**	**311.3**	**85.0**	**1963**		554.2894314
EOC 402B	11/23/04 1527						311.4816667